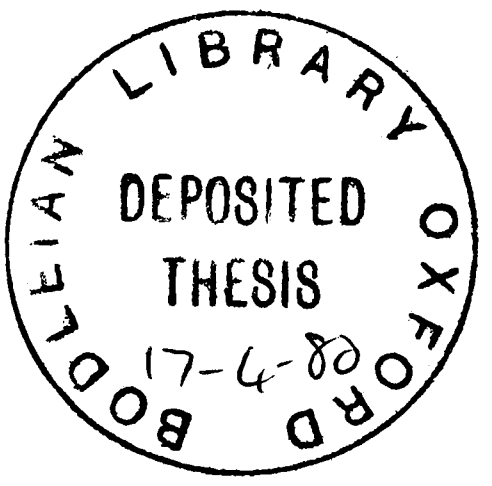
Angle Resolved Auger Electron Spectroscopy

by

P. Carr

Wolfson College



A dissertation submitted for the degree of Doctor of Philosophy

in the University of Oxford.

October 1979.

To Jane

There was an electron in gold
who said,"Shall I do as I'm told?
Shall I snuggle down tight
with a brief flash of light
or be Auger outside in the cold?"

-A Random walk in Science

R.L.Weber and E.Mendoza

Inst. of Physics 1975

Preface

This thesis describes the research carried out independently by the author in the Department of Metallurgy and Science of Materials, University of Oxford, since October 1975. The results presented are original and no part of the thesis has been submitted for any degree in this or any other University. Appropriate references are given where the work of others has been used to aid the present investigation.

The author also wishes to thank :-

Professor Sir Peter Hirsch F.R.S. for the provision of laboratory facilities.

Dr. M.J. Whelan F.R.S. for his careful supervision of the work and valuable comments on the manuscript.

Dr. R.J. Reid for introducing me to practical Auger spectroscopy.

Mr. D. Pinfold, Mr. D. Tansley and Mr. J. Stead for the construction of many intricate pieces of apparatus.

Mr. J. Short for introducing me to workshop practice and his many helpful suggestions.

Mr. R. Cripps and Mr. G. Dixon-Brown for their assistance with practical electronics.

Mr. S. Bowers and Mr. A. McKnight for photographic services.

The S.R.C. for a maintainance grant from October 1975 to October 1978.

The National Physical Laboratory for financial support from October 1978 to October 1979.

Mrs. Valerie Perry for her careful typing of the manuscript.

My parents for their support and encouragement through the years.

Abstract of thesis entitled, "Angle Resolved Auger Electron Spectroscopy", by P.CARR, Wolfson College, submitted for the degree of Doctor of Philosophy, Michaelmas term 1979.

This thesis describes a study of angular effects in Auger electron emission from solid surfaces using a specially developed instrument, based on a static high resolution electron energy analyser, that allows Auger currents to be measured with almost any combination of incident beam angles and emission angles.

The rate of Auger production as a function of depth was first of all examined by measuring the Auger emission angular distributions, from clean non-crystalline surfaces, using a wide variety of incident beam conditions. The rate of Auger production was found to be constant within the escape depth providing $2{\cdot}5 \leqslant E_p/E_c \leqslant 24$. Further experiments on various surfaces, with overlayers present, showed that the form of the Auger emission angular distributions could be used to determine whether or not the overlayer was uniform, and also to estimate it's thickness.

The angular variations of each part of the copper $M_{2,3}VV$ doublet were measured for the first time from a single crystal copper surface. It was shown that the initial state of the Auger electron profoundly affects the emission angular distributions and this provided evidence that band structure effects could not be ignored when describing the initial state of the Auger electron. The lack of structure in the silicon $L_{2,3}VV$ emission angular distributions was thought to be partly due to Auger electron originating in different types of surface site in the silicon surface.

The angular distributions of the high energy Auger signals exhibited pronounced structure, independent of the initial state of the Auger electrons, that could be correlated with the Kikuchi patterns and channeling patterns obtained at similar energies. Much of the structure in these signals could be qualitatively understood using the dynamical theory of electron diffraction.

Finally these techniques were used to study the growth forms of various evaporated metal films.

Contents

	Preface	i
	Abstract	ii
	Contents	iv
Chapter 1	Auger Spectroscopy	1
Chapter 2	Instrument Development	11
Chapter 3	Angular Distributions of Auger Electrons from Clean and Adsorbate Covered Non-Crystalline Surfaces	29
Chapter 4	Angular Distributions of Low Energy Auger Electrons from Clean Single Crystal Surfaces	54
Chapter 5	Angular Distributions of High Energy Auger Electrons from Clean Single Crystal Surfaces	80
Chapter 6	Effects of the Incident Beam Direction on Auger Electron Emission	97
Chapter 7	An Investigation of the Growth Forms of Thin Metallic Films using Angle Resolved Auger Spectroscopy	116
Chapter 8	Summary and Conclusions	141
	Appendix A	
	References	

Chapter 1

Auger Spectroscopy

		page
1.1	Historical Remarks	1.
1.2	The Auger Process and Notation	1.
1.3	Auger Energies	2.
1.4.1	Solid State Effects	3.
1.4.2	Valence Band Effects	3.
1.4.3	Chemical Shifts	4.
1.4.4	Energy Loss Processes	4.
1.5	Escape Depths	5.
1.6.1	A General Formula for Auger Production	5.
1.6.2	Estimates of $\sigma(E)$	7.
1.6.3	Fluorescent Yield	8.
1.6.4	Estimates of $I(E,\theta,\phi)$	8.
1.7	The Measured Auger Current	9.
1.8	Recent Developments and Scope of This Work	9.

1.1. Historical remarks

Auger (1925, 1926) was the first person to observe those electrons originating from the radiationless de-excitation of ionised atoms. The ions were created by x-ray irradiation inside a Wilson cloud chamber and paired electron tracks were seen originating from the x-ray paths. One track was due to the photoelectron emitted following ionisation and the other was due to the Auger electron created with the filling of the atomic vacancy.

The application of this technique to surface analysis had to wait thirty years until Lander (1953) noticed the presence of Auger peaks in the secondary electron spectrum created by electron irradiation of the surface. However poor vacua and a lack of sensitivity impeded further development until 1967 when Tharp and Scheibner (1967) showed that the secondary electron emission spectrum could be recorded using the LEED instrument that was then gaining in popularity. It was then shown by Harris (1968) that the sensitivity could be dramatically increased by differentiating electronically the N(E) signal that contained small Auger peaks on a large, often sloping, background. Thus it became possible to obtain chemical information using Auger spectroscopy and structural information using LEED from the same instrument. Further improvements in signal to noise and resolution were then achieved by Palmberg (1969) using an energy dispersive cylindrical mirror analyser (CMA). This type of analyser coupled with electron guns having spot sizes from $\sim$ 1mm, down to 100Å is probably the most popular configuration currently in use.

1.2. The Auger Process and Notation

Following the ionisation of a core level, denoted A in figure 1. 1(a), by x-rays or electrons the ion can de-excite by emitting a photon of energy $h\nu = E_a - E_b$ as in figure 1. 1(b) or by emitting an Auger electron from level C of energy $E_a - E_b - E_c$ as in figure 1(c). In the usual notation this would be referred to as an ABC transition. Conventionally the atomic levels are identified using x-ray notation in extreme j-j coupling. Therefore in this

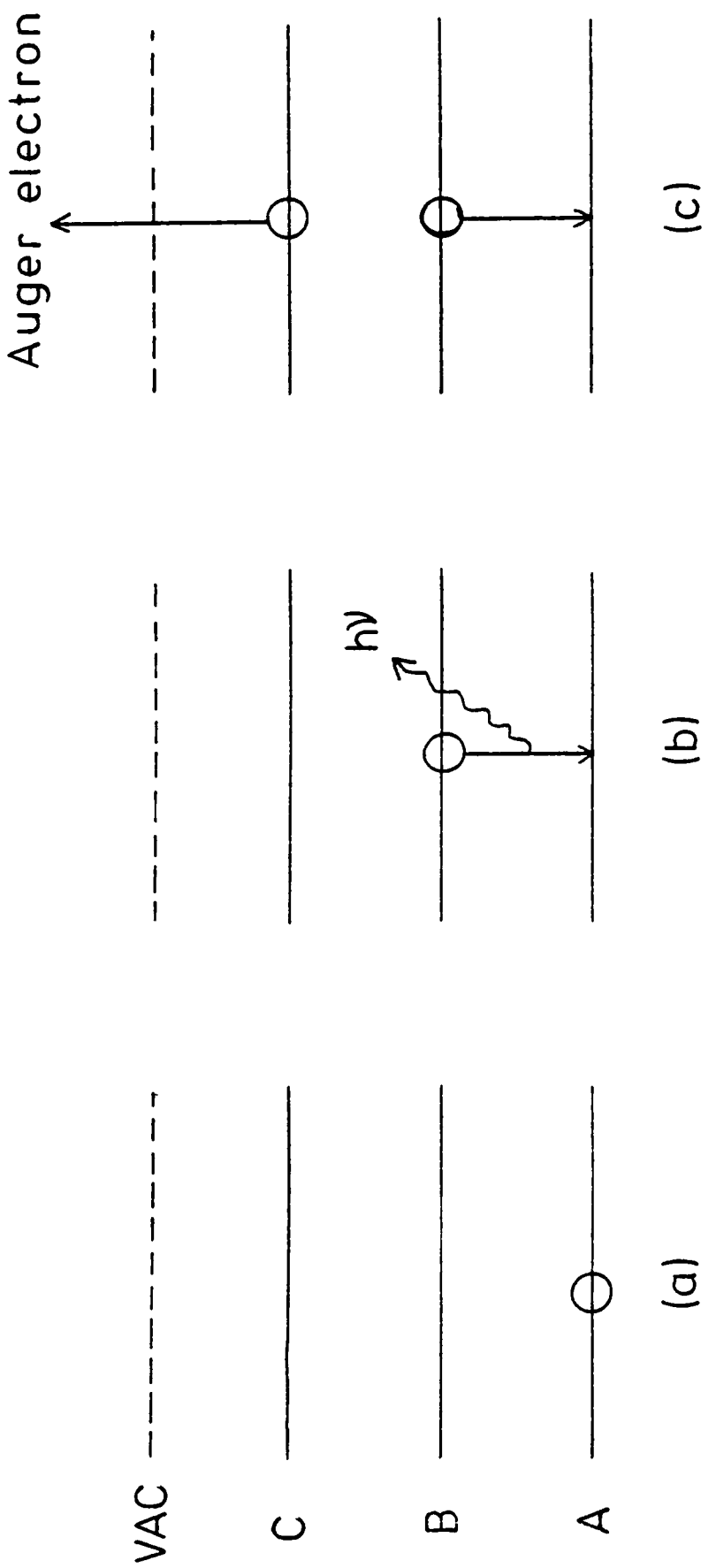


Fig.1.1 The Auger Process

scheme an Auger transition in which the initial hole is in level K and the "up" and "down" electrons in levels $L_{2,3}$ leads to a K $L_{2,3}$ $L_{2,3}$ Auger electron. This classification leads to a total of six lines in the KLL series but experiments by Hörnfeldt et al (1962) showed the existence of nine lines for z = 38,40 and 42. This can be correctly described in an intermediate coupling scheme where the nine lines are given by;

$KL_1L_1(^1S_0)$, $KL_1L_2(^1P_1)$, $KL_1L_2(^3P_0)$, $KL_2L_2(^1S_0)$, $KL_1L_3(^3P_1)$, $KL_1L_3(^3P_2)$, $KL_2L_3(^1D_2)$, $KL_3L_3(^3P_0)$, $KL_3L_3(^3P_2)$. This type of structure is not always seen in solid state Auger spectra due to various mechanisms that broaden or otherwise change the spectrum. In solids the low energy levels that combine to give the valence bands are simply designated as V leading to notations such as LVV.

1.3 Auger Energies

In Auger spectroscopy the presence of a particular element on a surface is indicated by the energies at which the corresponding Auger electrons appear. A first approximation to the electron energy following an abc transition is given by

$$E_{abc}(z) = E_a(z) - E_b(z) - E_c(z) \quad \text{——— (1)}$$

(the z in brackets is the atomic number)

This expression is generally very innaccurate partly because the Auger electron is leaving an ion where the energy levels will be slightly different from those of the neutral atom. Thus a more accurate expression is given by

$$E_{abc}(z) = E_a(z) - E_b(z) - E_c(z+1) \quad \text{——— (2)}$$

where the binding energy of a level c in the atom with atomic number (z+1) is taken as an approximation to the binding energy of the ion with atomic number z. Chung and Jenkins (1970), after noting that the Auger transitions abc and acb are quantum mechanically indistinguishable, proposed the following formula.

$$E_{abc}(z) = E_a(z) - \tfrac{1}{2}\left(E_b(z) + E_b(z+1) + E_c(z) + E_c(z+1)\right) \quad \text{——— (3)}$$

In practice this formula is found to have an accuracy of about 5eV which is

as good, if not better than, calculations of Auger energies from first principles. To further ensure that the assignment of Auger lines are correct tables of standard spectra have been compiled that show the differential spectra of most elements (Palmberg et.al.(1972)).

1.4.1. Solid State Effects

Unlike the sharp narrow features found in gas phase Auger emission, the spectra from the solid state environment are often broadened and shifted in a number of ways.

1.4.2. Valence Band Effects

In a solid the discrete outer levels of the atom combine to form the valence bands and the effect this has on the Auger transition will be illustrated with the $L_{2,3}VV$ silicon transition shown in figure 1.2. Assuming that electrons at any energy in the band can participate in the Auger transition the width of the line can be found by considering the Auger electron energies at the extremities of the band

$$E_a(1) = EL_{2,3} - 2E_1 \quad \text{and}$$
$$E_a(2) = EL_{2,3} - 2E_2$$

therefore the line width is given by

$$E_a(1) - E_a(2) = 2(E_2 - E_1)$$
$$= 2\xi$$

where ξ is the valence band width.

The shape of the Auger line can be calculated as follows. The probability of finding two electrons at $\varepsilon + \Delta$ and $\varepsilon - \Delta$ in the band is given by $\rho(\varepsilon + \Delta)\,\rho(\varepsilon - \Delta)$ and the corresponding probability of a transition occurring is proportional to

$$\left|M(\varepsilon, \Delta)\right|^2 \; (\varepsilon + \Delta) \; (\varepsilon - \Delta)$$

where $M(\varepsilon, \Delta)$ is the matrix element for this transition. Therefore the total probability of producing an Auger electron of energy $E_{L_{2,3}} - 2\varepsilon$ is given by

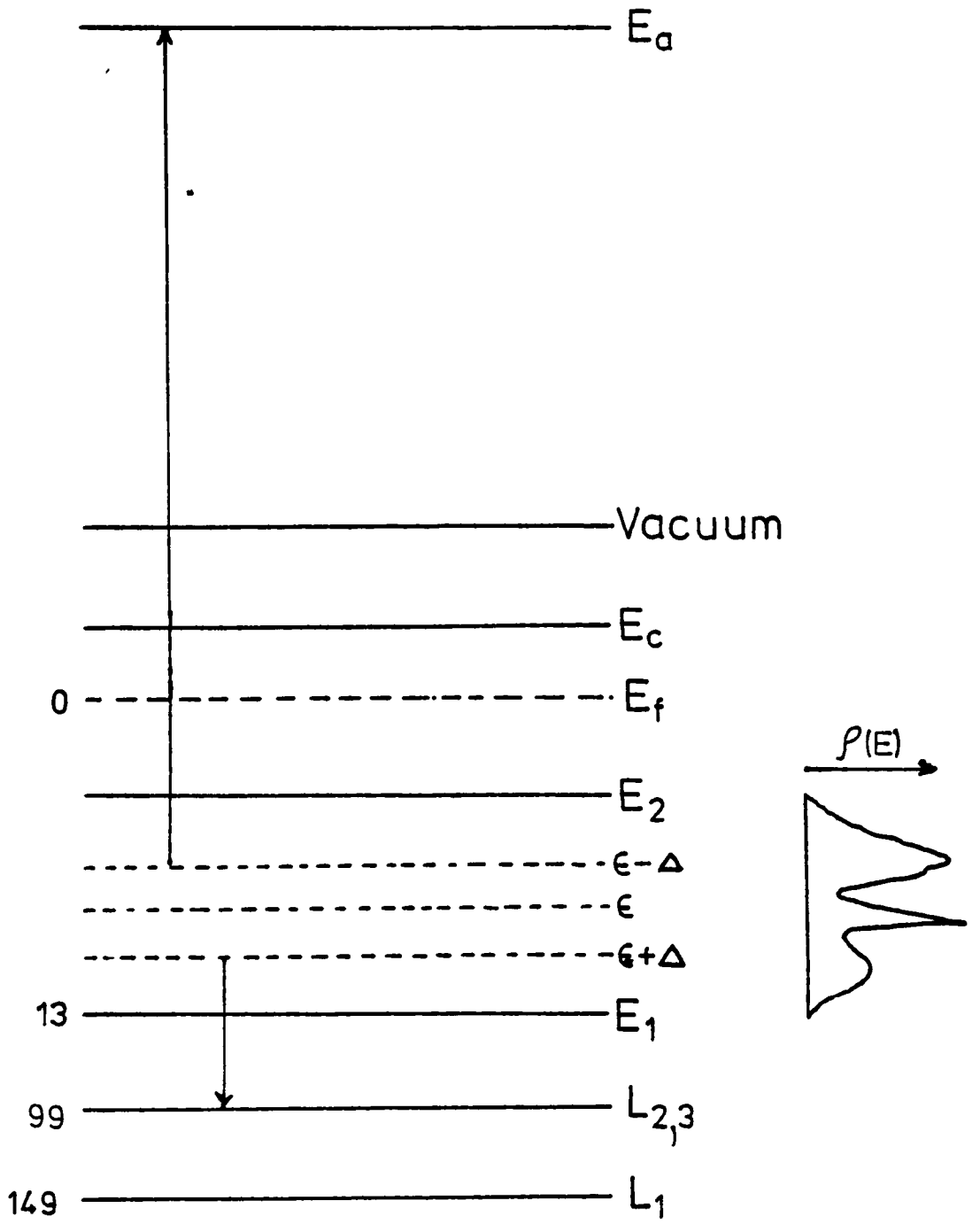


Fig.1.2 The formation of the silicon $L_{2,3}VV$ Auger electron of energy E_a

$$f(\varepsilon) = \int_0^{\xi} |M(\varepsilon, \Delta)|^2 \quad \rho(\varepsilon+\Delta)\, \rho(\varepsilon-\Delta)\, d\Delta \quad \text{---} \quad (4)$$

Thus it is in principle possible to obtain $\rho(\varepsilon)$ by deconvoluting the measured Auger spectrum providing the matrix element is uniform across the band.

1.4.3. Chemical Shifts

In the technique of ESCA (Electron spectroscopy for chemical analysis) the change of binding energy that occurs after the formation of a chemical bond is directly observable in the changes of kinetic energy of the photo-emitted electron. This has been exploited to great effect in the identification of the chemical species present. In the case of an Auger electron the kinetic energy is determined by the energies of the three levels involved in the transition and when the valence band is also involved the change in $\rho(E)$ may also affect the line shape. Little systematic work has been done on this effect in Auger emission but in the case of the carbon KLL spectrum it is possible to differentiate between carbon in SiC, MoC, Graphite and diamond by the line shape change (Haas et.al.(1972)). In other cases such as the oxidation of aluminium there are large shifts of up to 15eV in the $L_{2,3}VV$ peak (Powell, (1973)). Recent work by Rye et.al. (1978) shows promise in being able to provide "fingerprint" spectra for various chemical groupings that may allow their identification in subsequent work.

1.4.4. Energy Loss processes

The dominant energy loss process that broadens an Auger peak is the creation of bulk or surface plasmons by the escaping Auger electron (Raether (1965)). The inelastic tail created in this way may well extend 20 or 30 eV from the Auger peak and where groups of peaks occur the relative intensities of the various peaks have to be determined after correction for inelastic scattering. The extraction of the true Auger line shape from the measured data involves deconvoluting the measured spectrum with an inelastic function

generally obtained by measuring the inelastic tail on the backscattered primary electrons, at the Auger electron energy. As the angle of emergence of the Auger electron will alter the ratio of surface to bulk plasmon losses it is always difficult to ensure that the inelastic function used is relevant to the situation.

1.5. Escape Depths

All the energy loss processes put to together ensure that the inelastic mean free path for low energy electrons in solids is very short. A compilation of inelastic mean free paths expressed in monolayers is given in fig.1.3 (taken from Seah, 1978). The sharp increase in the inelastic mean free path at energies of less than 10eV is due to the low energy threshold for plasmon creation occurring at about this energy. The scatter of experimental points about this line is very large and no systematic trends with elements, or compounds have been found. The actual escape depth depends on the angle of emergence of the Auger electron and is equal to $\lambda \cos \theta$ where λ is the inelastic mean free path and θ is the angle between the electron path and the surface normal.

1.6.1. A General formula for Auger production

The discussion so far has concentrated mainly on the qualitative aspects of Auger spectroscopy. To develop a quantitative technique it would be best to have formulae relating the collected Auger current to the primary beam current for any given surface composition and experimental arrangement. This degree of generality has certainly not been achieved and any attempts made at quantitative analysis are based on comparison of standard samples with those being studied. However, to try and identify the most important factors affecting the Auger yield, a number of authors (Meyer and Vrakking (1972), Fiermans and Vennik (1977), Bishop and Rivière (1969)) have studied the case of an adsorbed layer of atoms on a substrate. This approach will be used here although the

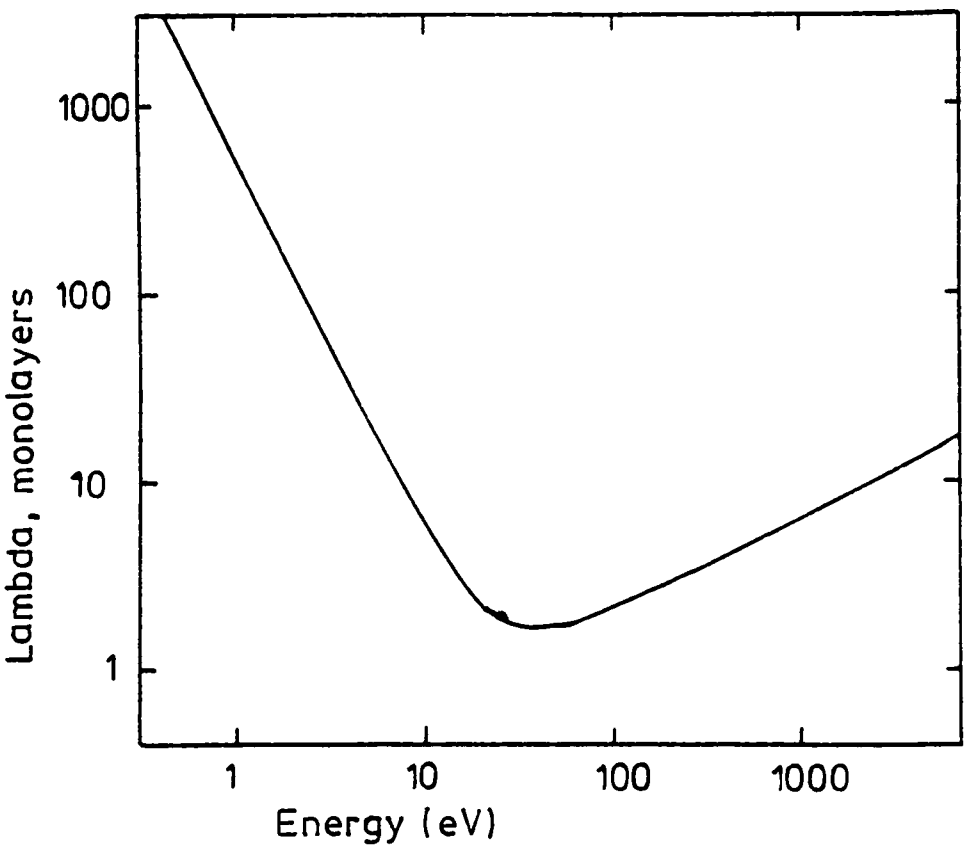


Fig.1.3 Electron inelastic mean free paths taken from Seah(1978)

emphasis will be placed on slightly different aspects.

The total Auger current from the absorbed layer will be divided into the contribution from the unscattered primary beam I_a^p and the contribution from all the backscattered electrons I_a^b. The Auger current due to the primary beam alone can be written as

$$I_a^p = I_p . \sigma(E_p) . N . (1-\omega) . F(\theta_p . \phi_p) \text{ ---- (5)}$$

I_p - primary beam current

$\sigma(E_p)$ - ionisation cross section at energy E_p

N - number of surface atoms per cm^2

ω - fluorescent yield

θ_p - polar angle of incidence (measured from surface normal)

ϕ_p - azimuthal angle

In the case of a non-crystalline specimen $F(\theta_p, \phi_p)$ is generally taken (Meyer and Vrakking (1972)) as sec θ_p to account for the increasing path length of the primary electrons in the surface layer as θ_p increases. In a crystalline specimen the ionisation may vary with both θ_p and ϕ_p due to diffraction of the incoming beam.

The dividing line between the backscattered and primary electrons is a rather difficult one to draw, and Bishop and Rivière (1969) assume that no significant elastic or inelastic scattering occurs in the overlayer itself, and therefore the backscattered contribution is due solely to inelastic and elastic scattering in the substrate. An alternative more exact definition is to say that any electron not travelling with $E = E_p$, $\theta = \theta_p$ and $\phi = \phi_p$ in the overlayer belongs to the backscattered current $I_b(E,\theta,\phi)$. The Auger current in the overlayer created by the backscattered current can be written

$$I_a^b = \int_{E_c}^{E_p} \int_{\theta} \int_{\phi} I_b(E,\theta,\phi) . \sigma(E) . N . (1-\omega) . F(\theta,\phi) . dE \sin\theta \, d\theta d\phi \text{ ----- (6)}$$

E_c - energy of core level

Again in the non crystalline case $F(\theta,\phi)$ is taken as sec θ and it is not necessary to take I_b as a function of ϕ. The total Auger current due to primary and backscattered electrons is given by

$$I_a = I_a^p + I_a^b = I_p\,\sigma(E_p)N(1-\omega)F(\theta_p,\phi_p) + \text{---}$$
$$\int_{E_c}^{E_p}\int_{\theta}\int_{\phi} I_b(E,\theta,\phi)\sigma(E).N(1-\omega)F(\theta,\phi)dE\,\sin\theta\,d\theta.d\phi \quad \text{---} \quad (7)$$

A backscattering factor r can be defined as

$$r = \frac{I_a^p + I_a^b}{I_a^p} \quad \text{---} \quad (8)$$

and the total Auger current can be rewritten from equation (7) as

$$I_a = I_p\ \sigma(Ep).F(\theta_p,\phi_p).\ r.\ N(1-\omega) \quad \text{---} \quad (9)$$

Alternatively the total Auger current may be written as

$$I_a = \int_{E_c}^{E_p}\int_{\theta}\int_{\phi} I(E.\theta.\phi)\ \sigma(E).\ F(\theta,\phi),\ N(1-\omega)\ dE\,\sin\theta\,d\theta.d\phi \quad \text{---} \quad (10)$$

where $I(E.\theta.\phi)$ is the total current distribution in the overlayer from whatever source.

It can be seen that even in this simplified derivation the situation is complex and extending this type of analysis to include arbitrary distributions of atoms in the surface layers or rough surfaces would be very difficult. The various factors appearing in equation (7) will now be discussed.

1.6.2. Estimates of $\sigma(E)$

Theoretical estimates of $\sigma(E)$ have been made by a number of authors (Worthington and Tomlin (1956), Gryzinski (1959, 1965)). They agree in the general form of $\sigma(E)$ and the peak value occurs for a primary energy of about three times the energy of the level to be ionised. The formula due to Worthington and Tomlin (1956) is :-

$$(E_p) = \frac{2\pi e^2}{E_p E_c}\ b\ \ln\left(\frac{4E_p}{B}\right) \quad \text{---} \quad (11)$$

b = 0·35 for K electrons

$$B = 1{\cdot}65 + 2{\cdot}35\ \exp\left(1 - \frac{E_p}{E_c}\right)\ E_c$$

This implies that the primary beam conditions should be adjusted to ensure that the maximum in the energy spectrum of $I(E,\theta,\phi)$ occurs at about three times the ionisation potential of the core level.

1.6.3. Fluorescent Yield

Having ionised the atom the ion can decay by Auger or photon emission. Bishop and Rivière (1969) show that the probability of photon emission is $\leqslant 3\%$ following the ionisation of core levels of energy ~ 2keV and hence $(1-\omega)$ can be taken as unity in this range. This upper limit of ~ 2keV implies that the fluorescent yield will become significant following K shell ionisation for $z \geqslant 15$, L shell ionisation for $z \geqslant 36$ and so on through the various possible shells.

1.6.4. Estimate of $I(E,\theta,\phi)$

This term should be taken in conjunction with $F(\theta,\phi)$ to give a measure of the current distribution that is effective in ionising surface atoms. In non crystalline substrate $F(\theta,\phi)$ is usually taken as sec θ and $I(E,\theta,\phi)$ is accounted for in terms of the backscattering factor r calculated either using the Monte Carlo method (Bishop and Rivière (1969)) or more recently, by solution of the Boltzmann transport equation (Fathers and Rez (1979)). Unfortunately these methods are more reliable above ~ 5keV and few calculations have been performed at the low energies often used in Auger spectroscopy. Experimental estimates of $I(E,\theta,\phi)$ can be made (Meyer and Vrakking (1972)) if the backscattered electron distribution in the overlayer is assumed equal to the backscattered electron distribution leaving the surface. In the case of silicon r was found to lie between 1·2 and 1·4 for $\frac{E_p}{E_c} = 5$, so the backscattering contribution can be an important one.

In the crystalline case the Auger yield has been shown to be a function of both ϕ_p (Baines et.al.1975) and θ_p (Rusch et.al.(1973)) indicating that the diffraction of the incoming electrons can change the effective current in a crystal. In both these experiments clean surfaces were used so that the terminology used to describe the overlayer case is no longer valid.

1.7. The measured Auger current

The formula quoted for I_a give the total Auger current produced in an overlayer and this will be considerably different from the current i_a measured at the output of the energy analyser. i_a can be related to I_a by :-

$$i_a = I_a \frac{\Delta\Omega}{4\pi} .T. \; G(\theta_e,\phi_e) \quad \text{---- (12)}$$

$\Delta\Omega$ - solid angle subtended by the analyser entrance aperture

T - analyser transmission

$G(\theta_e,\phi_e)$ accounts for intensity changes with emission angle. It is very difficult to obtain an accurate value of T, the analyser transmission, at the energy of interest but this is usually circumvented by the use of standard samples and experimental conditions. The solid angle $\Delta\Omega$ subtended by the analyser aperture is relatively easily found although in the case of the CMA the Auger electrons are collected in a conical annulus that spans a wide range of θ_e and ϕ_e. Although the factor $G(\theta_e,\phi_e)$ can clearly affect the number of Auger electrons collected by an analyser its effect is seldom included (e.g. Meyer and Vrakking (1972)) in semi-quantitative derivations of Auger yields. In the case where electrons are collected in a large solid angle (e.g. R.P.A.) this may not be a serious omission but with the increasing use of analysers with narrow collection angles an understanding of $G(\theta_e,\phi_e)$ becomes essential.

1.8. Recent Developments and Scope of this work.

Auger Spectroscopy is now firmly established as a very useful surface analytical technique and is currently being developed in many ways. The RPA is rapidly being superseded by the energy dispersive CMA and CHA analysers, and electron probes of down to $\sim 100\text{Å}$ diameter allow high spatial resolution, elemental maps to be obtained. The limited acceptance angles of the CMA, and especially the CHA, mean that terms such as $G(\theta_e,\phi_e)$, appearing in equation (12), must be explicitly included when analysing spectra or comparing results between instruments with different geometries. In a similar way

different incident beam directions demand an understanding of terms like $F(\theta_p,\phi_p)$ in equation (9). These considerations become particularly acute in scanning Auger Microscopy where instrumental considerations demand rather extreme geometrical arrangement (e.g. Browning et.al. (1977)) and the topography of the surface itself also changes the effective values of θ_e and θ_p.

Recent work on single crystal surfaces (e.g. Noonan et.al. (1976)) has shown that, in certain materials, the Auger angular distributions exhibit large amounts of structure. From the standpoint of obtaining quantitative information these angular distributions must be understood and corrected for when necessary. However, the possibility also exists that the site of the emitting atom may be determined from the angular distributions, in a way similar to that already demonstrated at higher energies (Tomlinson and Howie (1968)). Recent calculations (e.g. Lindsay and Kinniburgh (1977)) performed at the appropriate energies tend to support this view although considerable problems concerning the initial state of the Auger electrons remain unsolved.

The main purpose of this work has been to investigate the variations in Auger current as a function of emission angle, both to provide information essential for the quantification of the technique and to explore the possibilities of obtaining structural information from the angular distributions. Results to be described later show that it is not always valid to consider the emission angular distributions as independent of the incident beam conditions, and this has led to a more detailed study of incident beam effects and in particular variations in Auger yield as a function of incident beam directions.

Chapter 2

Instrument Development

		page
2.1	The Vacuum System	11
2.2	Magnetic Field Compensation	11
2.3	The Ion Gun	12
2.4.1	The Electron Energy Analysers	12
2.4.2a	The Retarding Potential Analyser (R.P.A.)	12
2.4.2b	Electronics for the R.P.A.	14
2.4.3	The Concentric Hemispherical Analyser (C.H.A.)	14
2.4.4	Theory of Operation	14
2.4.5	Signal Collection using the C.H.A.	16
2.4.6	Signal to Noise Considerations	17
2.4.7	Electronics for the C.H.A.	18
2.5.1	Performance of the R.P.A.	18
2.5.2	Performance of the C.H.A.	18
2.5.3	Summary of C.H.A. Performance	20
2.6	The Electron Guns	20
2.7.1	Equipment Specifically Designed for Angle Resolved Work	21
2.7.2	Miniature Electron Gun	21
2.7.3	Internal Geometry of Electron Gun	22
2.7.4	Final Design	23
2.8	New Specimen Stage	24
2.9	Tests and Overall Performance of the Instrument	25
2.10	Summary	28

2.1. The Vacuum System

The first requirement of an electron spectrometer for surface studies is a vacuum chamber capable of pressures less than $\sim 10^{-10}$ torr.

The system used in this work was purchased from Vacuum Generators and is shown schematically in figure 2.1. The main chamber has a base pressure of less than $4x10^{-11}$ torr. A gas handling line is provided so that five gases can be bled into the main system via a leak valve.

The RF (radial field) pump, an AEI Triostat 400, was provided for two reasons. Firstly to seperately pump the gas handling line when changing gases etc, and secondly to pump the main chamber after inert gases had been bled in for ion bombardment. Unfortunately it took up to 8 hours to evacuate the main chamber from $\sim 5x10^{-5}$ torr to $\sim 10^{-9}$ torr using this pump.

To overcome this problem a trapped diffusion pump was installed in place of the RF pump to provide non-selective pumping of inert gases in the chamber or gas handling line. The pump used was an Edwards E02 diffusion pump with a Vacuum Generators CCT50 cold trap, Figure 2.2 shows the arrangement used.

Residual gas analysis is performed using a quadrupole mass spectrometer, the Q7b manufactured by VG Micromass.

2.2 Magnetic Field Compensation

Magnetic fields of up to 600mG were measured in the main chamber, using a Bell 620 gaussmeter. The specimen to analyser distance is $\sim$10cm and 20eV electrons would be deflected by $\sim$7mm in the entrance plan of the analyser by this magnetic field.

To reduce the magnetic fields to a more acceptable level three orthogonal pairs of square coils were mounted outside the chamber. The size was chiefly determined from the practical consideration of being able to remove

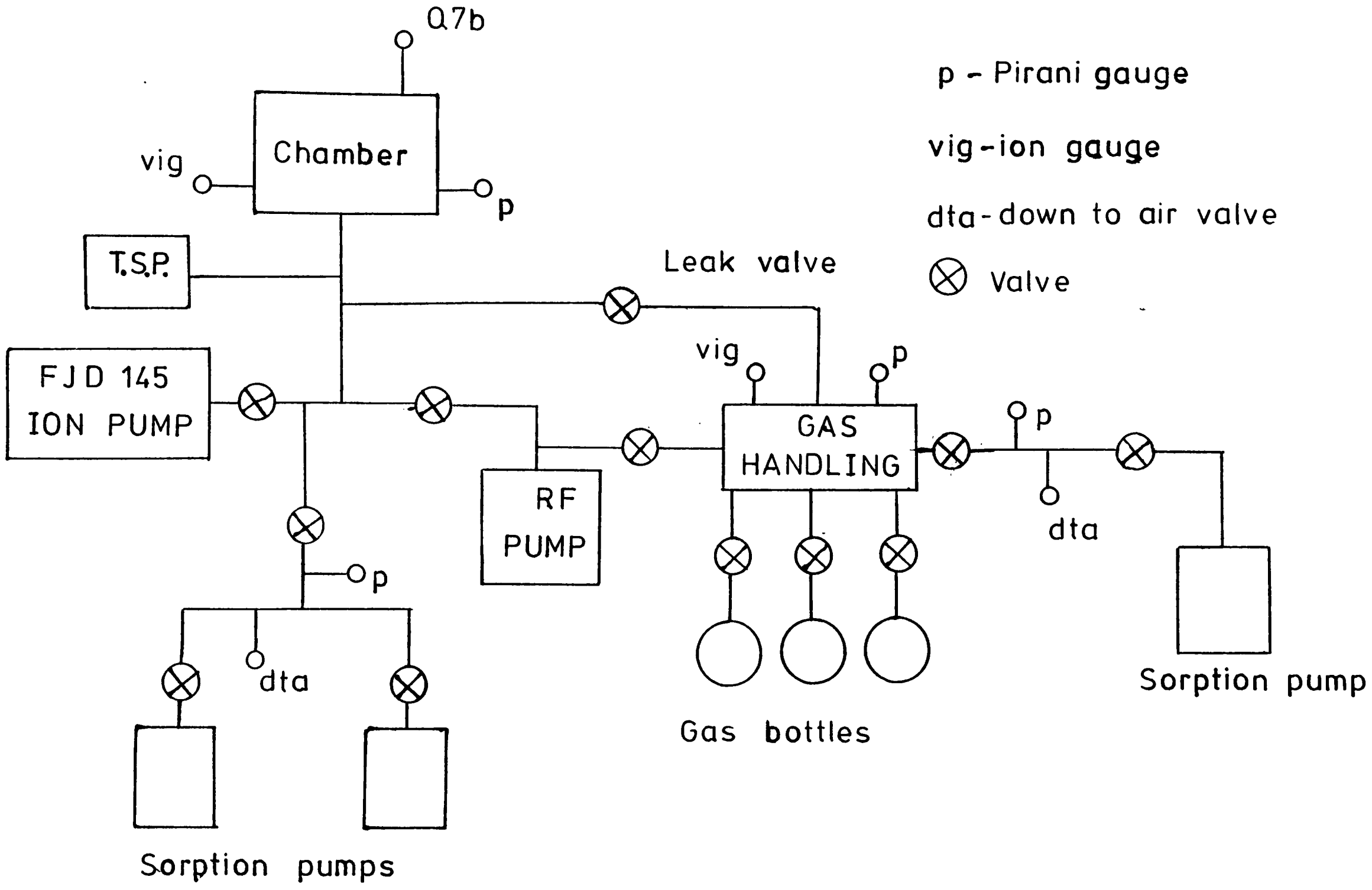


Fig.2.1 The vacuum system

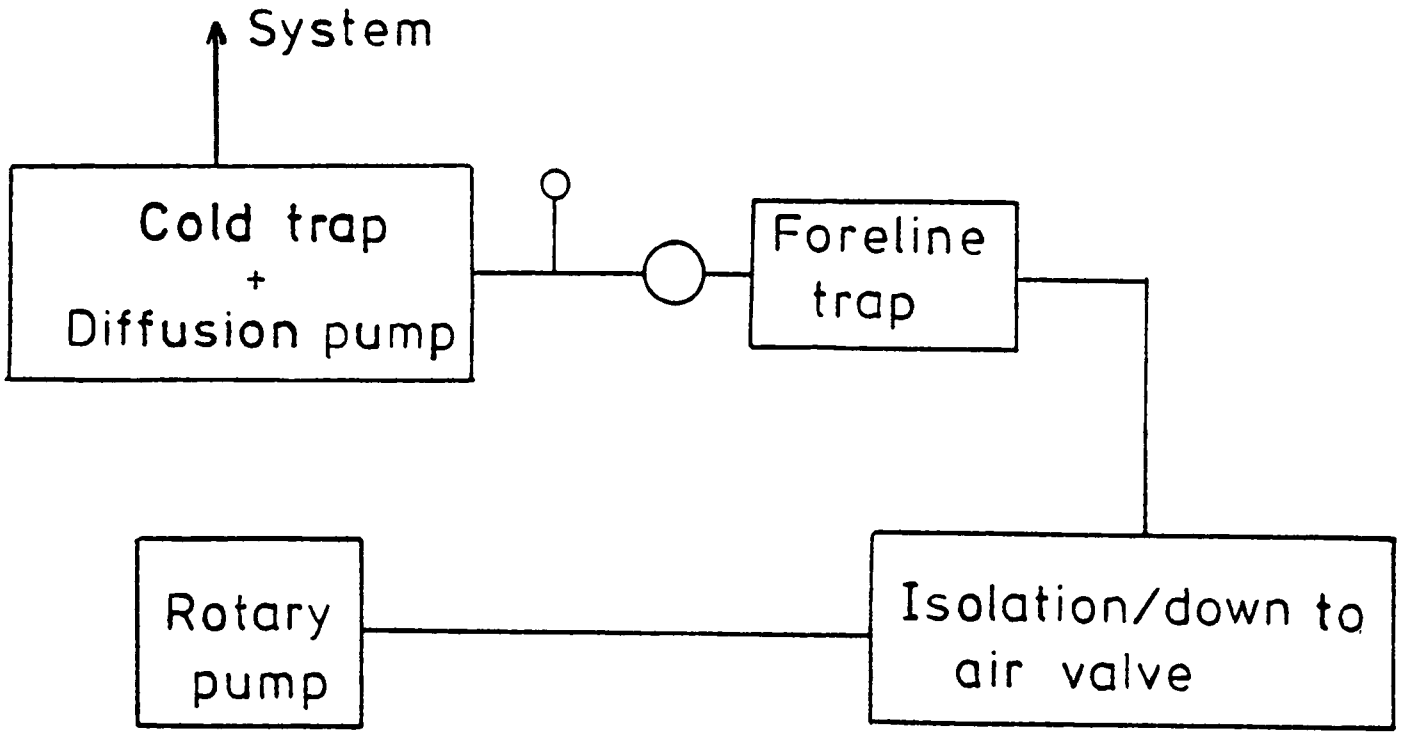


Fig.2.2 Trapped diffusion pump used in place of R.F. pump

the coils for bakeout. Each pair of coils was seperately controlled from a power supply built by the author. The circuit is shown in appendix A.

The magnetic fields were reduced to $\sim$ 20mG in the region between the specimen and the energy analyser. This reduces the deflection for 20eV electrons to $\sim$ 0·2mm in the plane of the analyser.

2.3. The Ion Gun.

It is essential to have a method of cleaning the specimen inside the vacuum chamber. This is generally done by a combination of inert gas ion bombardment and heat treatment.

Therefore an ion gun and power supply were designed and constructed by the author. The ion gun is mounted on a linear motion drive so that it can be retracted from the specimen area when experiments are in progress. The arrangement shown in figure 2.3 produces about 5μA cm^{-2} at 5x10^{-5} torr of Argon, with an electron emission of $\sim$20mA.

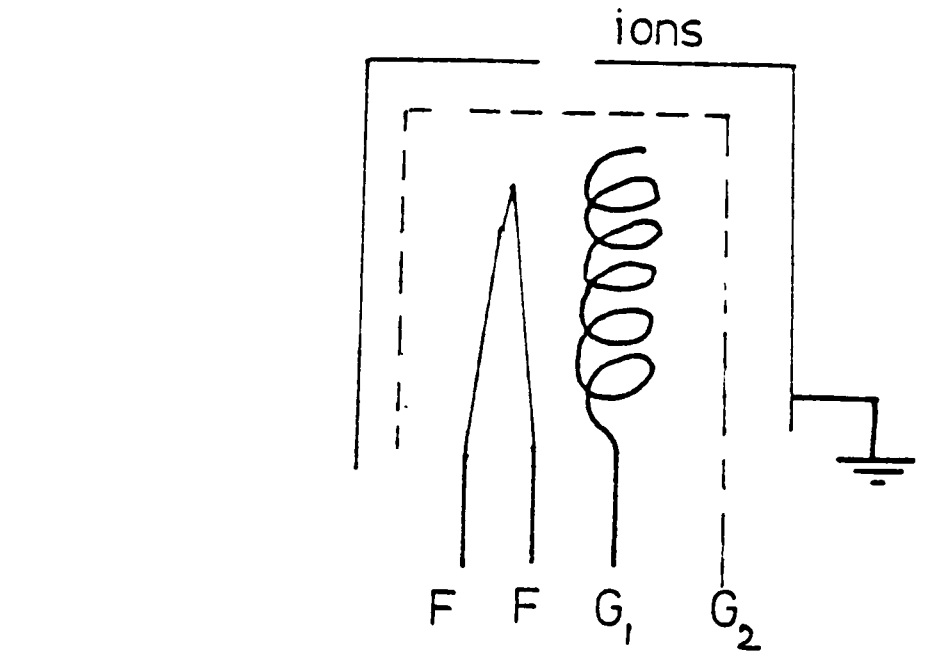
2.4.1. The Electron Energy Analysers

Before discussing each analyser in detail the general geometry within the vacuum chamber will be described with reference to figure 2.4. The position marked B is the specimen position for the Retarding Potential Analyser (RPA) and position A is the specimen position for the Concentric Hemispherical Analyser (CHA).

2.4.2.(a)The Retarding Potential Analyser, (R.P.A.)

This analyser was built by Vacuum Generators and the electronics were mostly built in the Laboratory. A schematic diagram of this device can be seen in figure 2.5.

To use this instrument for the display of LEED patterns the middle two grids are held slightly positive of the cathode potential thus transmitting



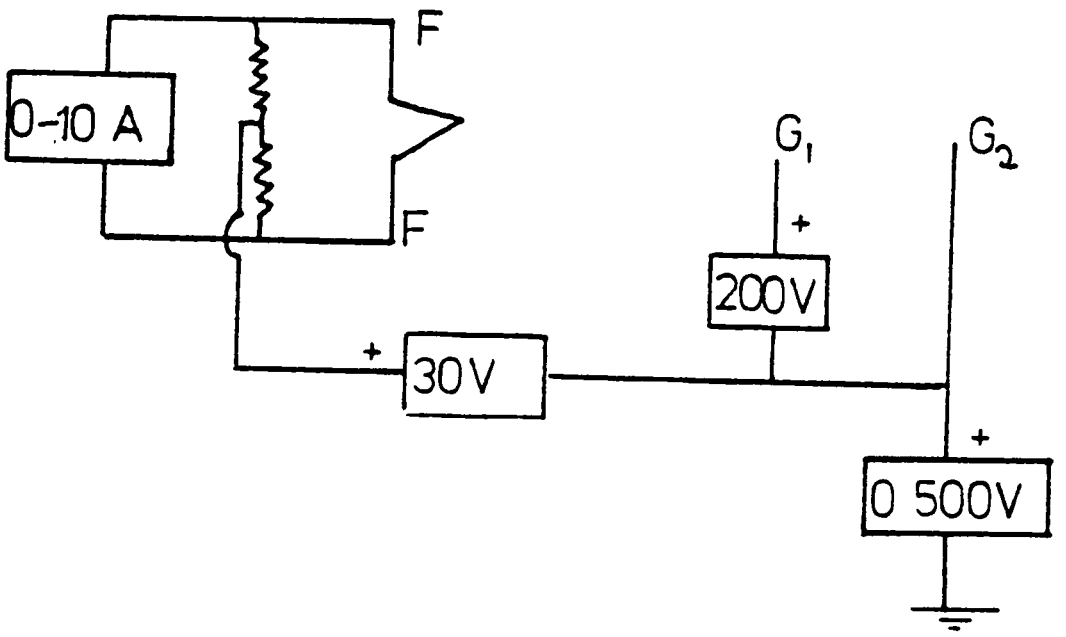


Fig.2.3 The ion gun and power supply

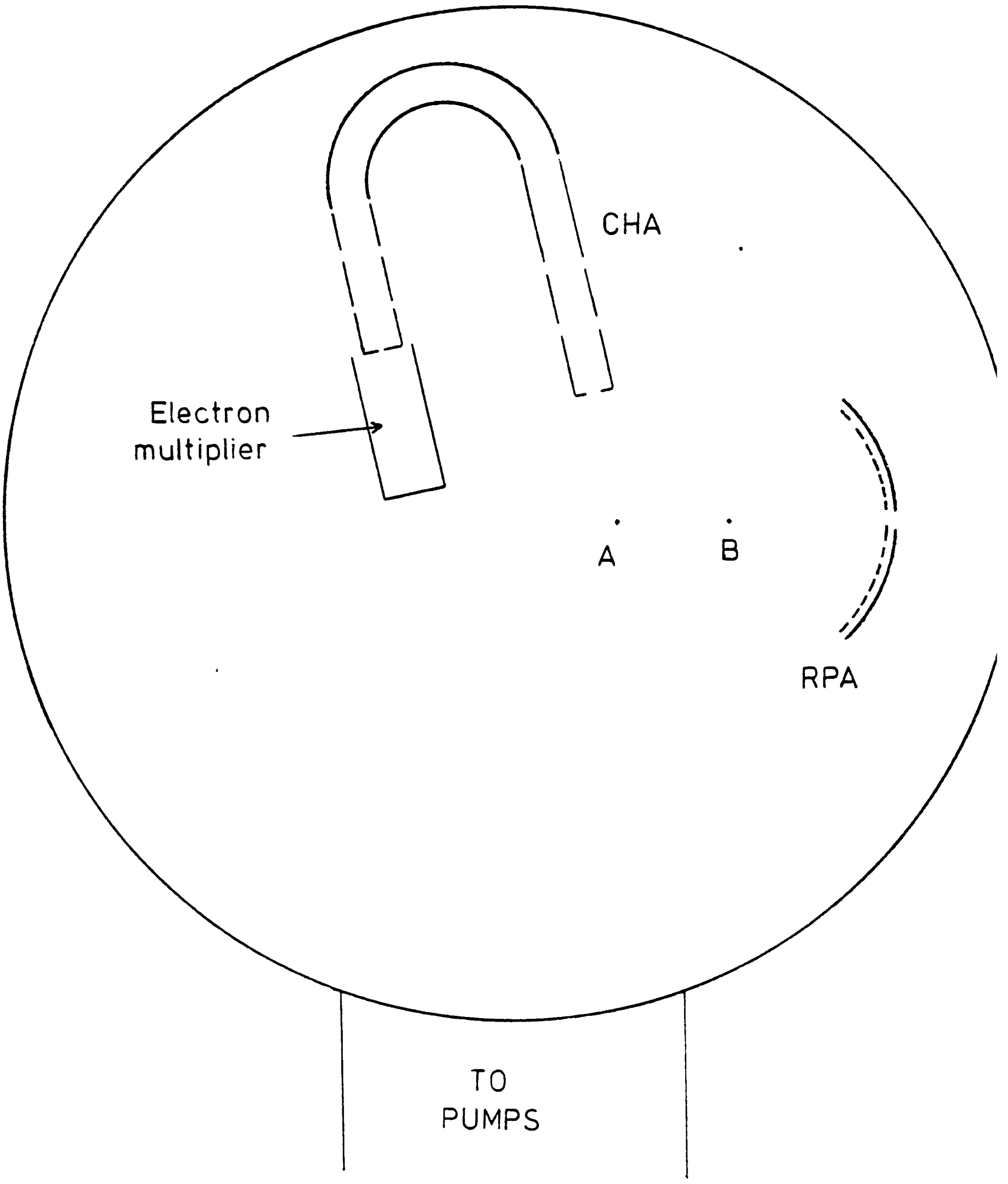


Fig.2.4 The general arrangement

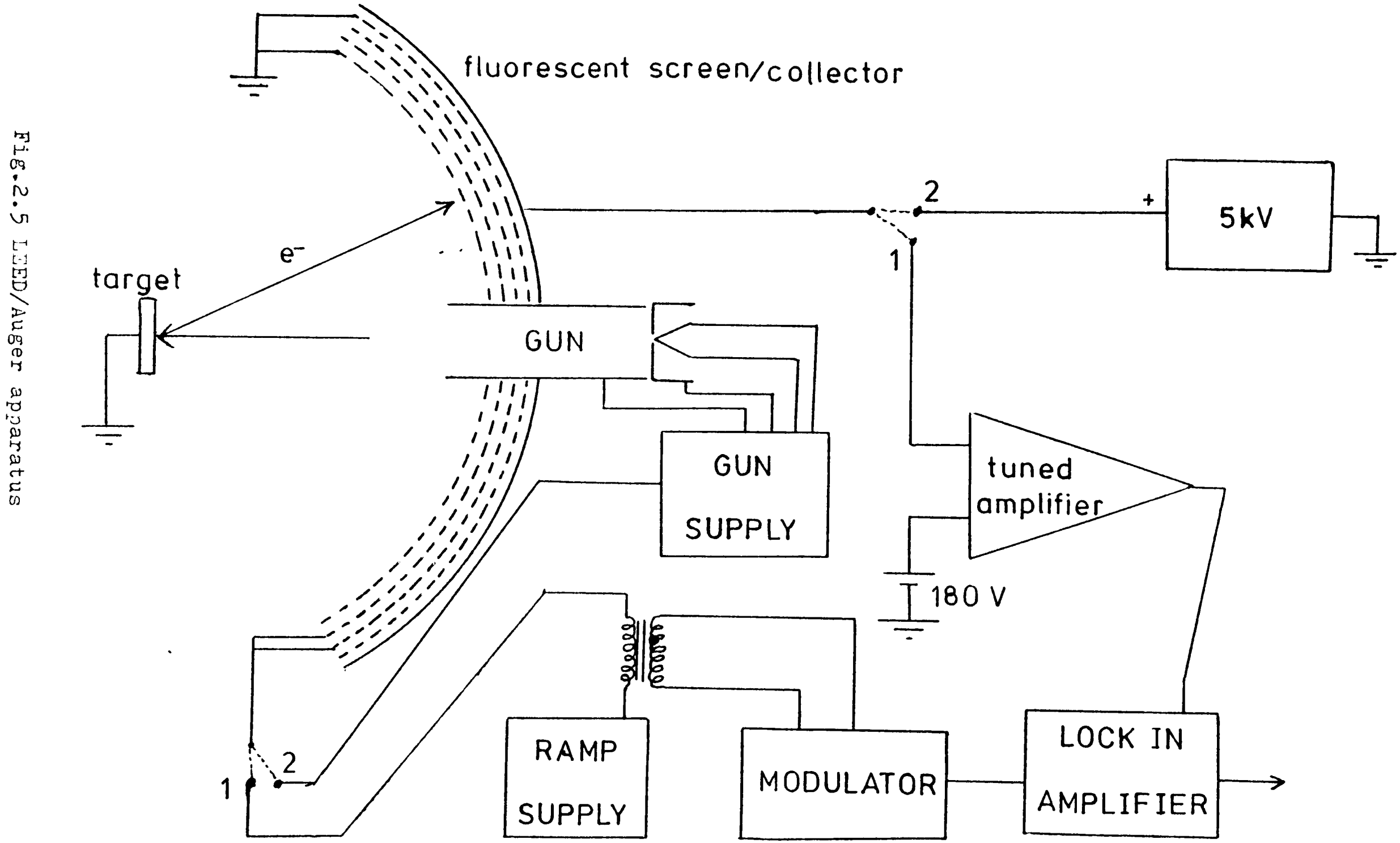


Fig.2.5 LEED/Auger apparatus

only the elastically reflected electrons which are then accelerated by 5kV to produce a spot pattern on the fluorescent screen. In this mode the gun at the centre of the screen is used.

The instrument can also be operated as an energy analyser as follows. If the middle two grids are scanned in voltage, by setting the switch in fig. 2.5 to position 1, the current reaching the collector I(E) is given by

$$I(E) = \int_{E_a}^{E_p} N(E)dE$$

where E_p is the primary electron energy and E_a is the energy of the slowest electrons transmitted. However it is generally N(E), or for AES, $N^1(E)$ that is required. The signal I(E) can be differentiated electronically by applying a modulation voltage to the middle two grids such that $\Delta E = K\sin\omega t$. The signal reaching the screen, $I(E+\Delta E)$, can be written as a Taylor series (The primes denote differentiation with respect to E)

$$I(E+\Delta E) = I(E) + I^1(E)\Delta E + \frac{I^{11}(E)}{2}(\Delta E)^2 + \frac{I^{111}(E)(\Delta E)^3}{3} + \text{---}$$

and by rearranging and collecting terms (see for example Taylor (1969)) this becomes

$$I(E+\Delta E) = I(E) + \left[I^1(E)K + \frac{I^{111}(E)K^3}{8} + \text{---}\right] \sin\omega t$$

$$- \left[\frac{I^{11}(E)K^2}{4} + \frac{I^{1V}(E)K^4}{48} \text{---}\right] \cos 2\omega t \text{ ---}$$

Thus by neglecting terms in K^3 and above

$$I(E+\Delta E) = I(E) + I^1(E)K \sin\omega t - \tfrac{1}{4} I^{11}(E)K^2 \cos 2\omega t + \text{-----}$$

Therefore the signal detected at frequency ω is to a good approximation $I^1(E) = N(E)$ and at 2ω is $I^{11}(E) = N^1(E)$. It has been shown (Bishop and Rivière (1969)) that the contribution of the second and subsequent terms to each harmonic is less than 10% if the modulation amplitude is less than half the Auger peak width.

2.4.2.(b) Electronics for the R.P.A.

Figure 2.5 shows the main features and detailed circuits can be found in appendix A. The electronics used are fairly conventional for this type of analyser except perhaps in two areas. The method of decoupling the signal from its high (180v) voltage at the collector involves the use of an operational amplifier with an isolated input, the Ancom 15A-71A. Secondly the method used to cancel the capacitivily induced signal at the collector uses a phase shifter, an attenuator and a unity gain subtractor (See appendix A for details). The output from the tuned amplifier is fed into one terminal of the subtractor (the Analog AD 520K). The modulation voltage is fed into the other terminal of the subtractor having been adjusted, using the phase shifter and attenuator, to be the same amplitude and phase as the capacitive signal. In this way the capacitivily induced signal can be cancelled out.

2.4.3. The Concentric Hemispherical Analyser (CHA)

The main part of the experimental work was done using this analyser which will therefore be described in detail.

The analyser was built, but unfortunately not tested, by A.E.I. at their Harlow factory to a design similar to that published by Bassett et.al. (1972,1974). A diagram of the analyser can be seen in figure 2.6. and a photograph (fig.2.7) shows the analyser with the mumetal shield removed.

2.4.4. Theory of Operation

The operation of a spherical condenser as an electron energy analyser was described in detail by Purcell in 1938. The type of spectrometer used in these studies, using a hemispherical deflector and focussing lenses on the input and output, was subsequently described by Kuyatt and Simpson (1967) in the form of a monochromator.

A $\frac{1}{r^2}$ electrostatic field is produced between the two hemispheres by setting

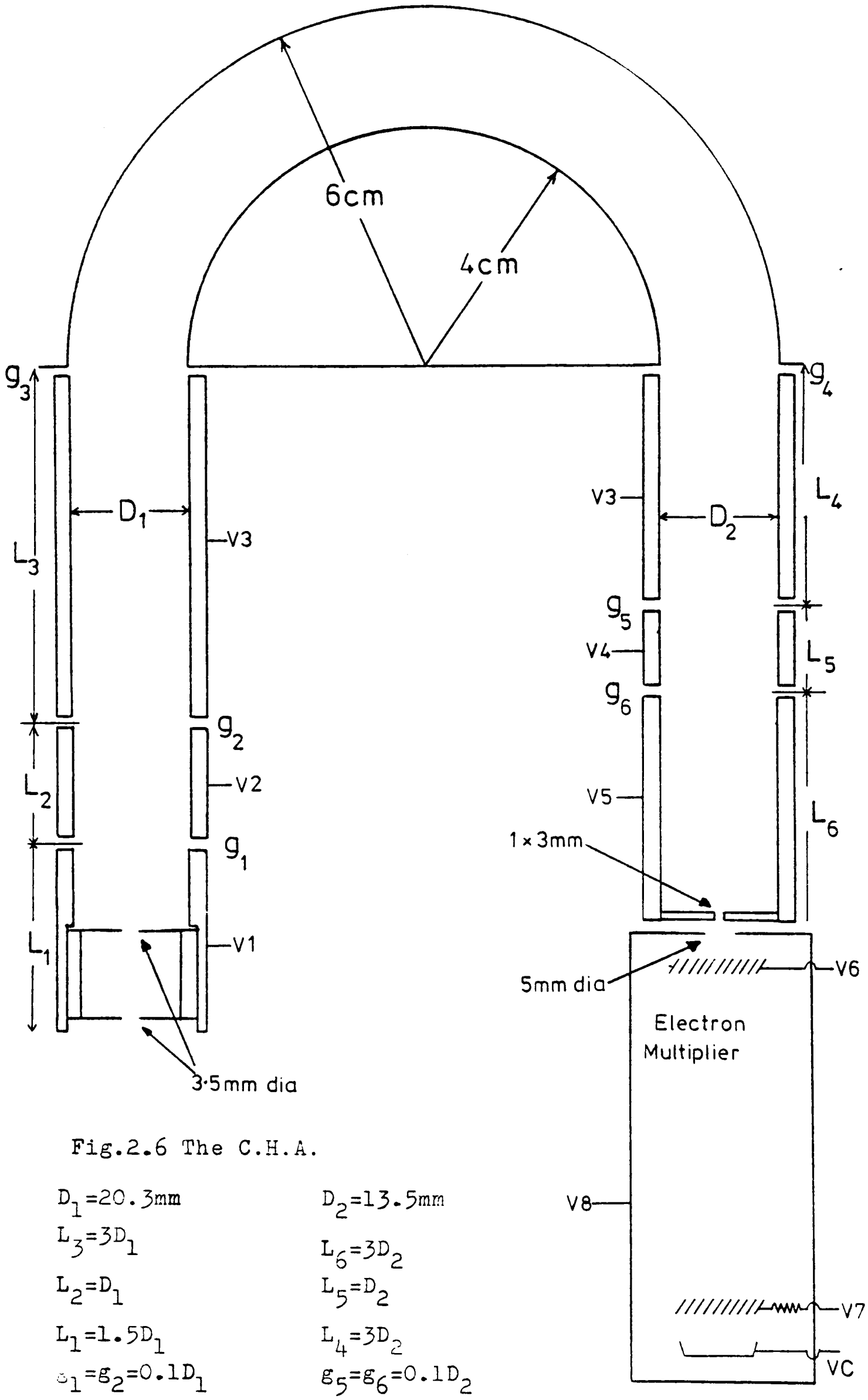


Fig.2.6 The C.H.A.

$D_1 = 20.3\text{mm}$ $\quad D_2 = 13.5\text{mm}$

$L_3 = 3D_1$ $\quad L_6 = 3D_2$

$L_2 = D_1$ $\quad L_5 = D_2$

$L_1 = 1.5D_1$ $\quad L_4 = 3D_2$

$g_1 = g_2 = 0.1D_1$ $\quad g_5 = g_6 = 0.1D_2$

$g_3 = 0.5\text{mm}$ $\quad g_4 = 0.5\text{mm}$

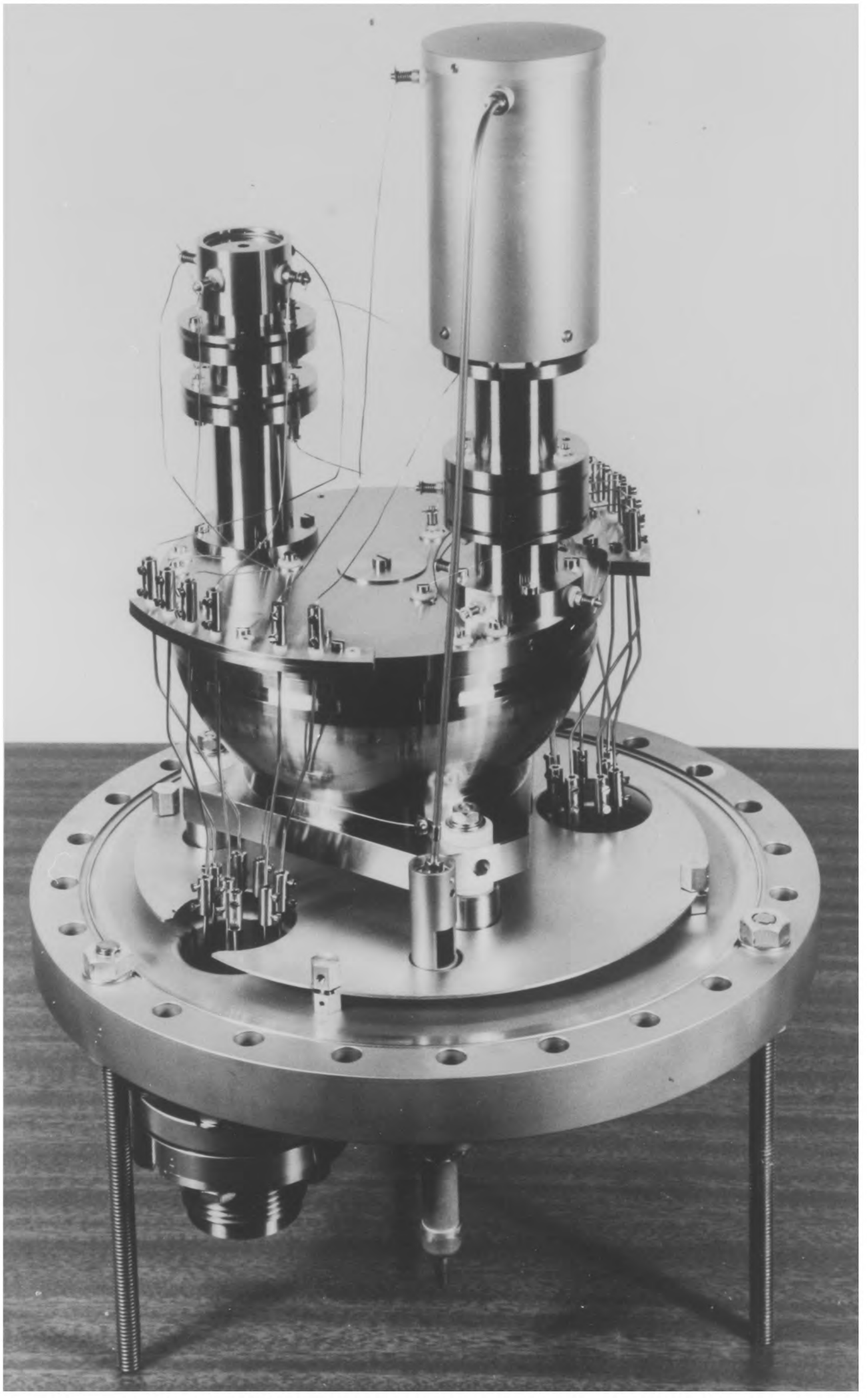


Fig.2.7 The C.H.A.

$$V1H = V_o \left(3 - 2\frac{R_o}{R_1}\right)$$

and $$VOH = V_o \left(3 - 2\frac{Ro}{R_2}\right) \quad \text{where} \quad R_o = \tfrac{1}{2}(R_1 + R_2)$$

If the electron energy $E_o = eV_o$ then electrons entering the deflector midway between the two hemispheres will travel on a circle radius R_o. The resolving power $\rho_h = \frac{Eo}{\Delta E}$ of the hemispheres is given by

$$\frac{1}{\rho_h} = \frac{S}{2R_o} + \alpha_h^2 \qquad \text{——— (1)}$$

S - entrance and exit slit width

α_h - the angular divergence of electron paths entering the hemisphers.

In this case both are virtual slits, the only real slits are at the entrance to the electron multiplier.

A further decrease in ΔE can be obtained by increasing ρ_h, and hence the analyser size, or by decreasing E_o at the entrance to the hemispheres by using a retarding input lens. Thus by using a retardation $R = \frac{E}{E_o}$, where E is the electron energy at the entrance to the input lens, the overall resolution ρ is given by $\rho = \rho_h R$. The effective size S at the input to the hemispheres is Md, where M is the input lens magnification and d is the source size at the specimen. Thus the overall resolving power is given by

$$\rho = \frac{2R_o}{Md} \cdot \frac{V_1}{V_3} \qquad \text{——— (2)}$$

where $\frac{V_1}{V_3} = R$ and $\alpha_h^2 < \frac{1}{2\rho_h}$ (Bassett et.al. 1972)

To evaluate this expression, M, the input lens magnification was calculated using information found in Harting and Read (1976). Thus inserting the values

$R_o = 50\text{mm}$

$d = 1\text{mm}$

$R = 10$

$M = 0{\cdot}5$

into equation (2) gives $\rho = 2000$

This derivation assumes that, S - the virtual slit width, is equal at

the entrance and exit to the hemispheres. The virtual slit at the exit plane is determined by the real slit width at the entrance to the electron multiplier, and the output lens magnification. Calculations using data in Harting and Read (1976) shows the magnification to be 0·5. Therefore the real slit of 1mm produces a virtual slit of 2mm at the exit to the hemispheres. Putting Md = 2mm (equivalent to a source of 4mm dia) leads to a value for ρ of 500.

Therefore with virtual slits of 0·5mm the resolution is 2000 whereas with virtual slits of 2mm the resolution is 500.

2.4.5. Signal Collection using the CHA

The current reaching the collector in the CHA can be written as

$$I(E) = C \Delta E \, N(E)$$

C is a constant

and since $\rho = \frac{E}{\Delta E}$

$$I(E) = \frac{C}{\rho} EN(E)$$

Therefore if the analyser is operated with ρ constant (by using a constant retardation) the output current $I(E) \alpha EN(E)$. This type of analyser can also be operated in a "constant ΔE" mode when a spectrum is scanned by changing the input retardation and in this mode $I(E) \alpha N(E)$. However the analyser used in this work has a three element input lens and scanning a spectrum by changing the input retardation would have involved programming the focus electrode V_2 in a non-linear way and this was not attempted.

In certain applications it is sufficient to plot I(E) directly but often it is desirable to obtain spectra in differential form. As with the RPA the current reaching the collector can be modulated (in ways to be described later) by an amount $\Delta E = K \sin \omega t$ and as before using a Taylor Expansion (Chattarji (1976))

$$I(E + K \sin \omega t) = I(E) + I^{1}(E) \, K \sin \omega t + I^{11}(E) \frac{K^2 \sin^2 \omega t}{2!} + \text{----}$$

Thus the amplitude of the first harmonic current is given by

$$I(\omega) = K\, I^{1}(E) = KC \frac{d}{dE}\left(\frac{EN(E)}{\rho}\right)$$
$$= \frac{KC}{\rho}\left(N(E) + EN^{1}(E)\right)$$

Except for very low energies the $N^{1}(E)$ term dominates because of the multiplication by E.

The most obvious way to modulate I(E) would be to apply a sinusoidal voltage to the CHA element. However due to the large number of elements present there is a tendency for the voltages on different elements to vary out of phase producing distortion (Bassett et.al. (1972)). To overcome this problem either the specimen potential or the primary beam energy is modulated. Modulating the specimen produces spectra containing the Auger features and any other features referenced to the specimen Fermi level. Modulating the beam energy produces an energy loss spectrum.

A third modulation technique is possible by applying a square wave to the wehnelt cylinder on the electron gun thus chopping the electron beam. The signal then detected is simply I(E) and by a suitable choice of time constants in the lock in amplifier, the signal to raise ratio can be improved over that available by straight amplification of I(E).

2.4.6. Signal to Noise Considerations

For a given collected current i_c the noise current $i_n = (2ei_c \Delta f)^{\frac{1}{2}}$ A (see Bassett et.al. 1972). An estimate of i_c can be obtained as follows. Assuming a primary beam current of 1μA and a surface reflectivity of $\sim 0.1\%$ implies that the reflected elastic current is $\sim 10^{-9}$A. Only that fraction of the current entering the 3·5mm analyser aperture is collected giving $i_c = 10^{-9} \times 10^{-4} = 10^{-13}$A. Thus $i_n = (2ei_c)^{\frac{1}{2}} (\Delta f)^{\frac{1}{2}} = 1{\cdot}2 \times 10^{-16} \times (\Delta f)^{\frac{1}{2}}$A. The bandwidth of the system, when using the oscilliscope display is primarily determined by the isolation amplifier giving $\Delta f = 200$Hz and therefore $i_n = 1{\cdot}7 \times 10^{-15}$A. Providing ΔE is greater than the intrinsic energy spread of

the beam i_c is a reasonable estimate of the collected current and therefore the signal to noise ratio of the elastic peak at ~1KeV where $\Delta E \simeq 1eV$ is simply $\frac{i_c}{i_n} \simeq 60$. Experiments described later show that the measured signal to noise ratio is about 80 for the elastic peak at 1KV indicating that the analyser is working satisfactorily in this context.

2.4.7. Electronics for the CHA

Figure 2.8 shows the general arrangement used for the CHA. The CHA control box (shown in detail in appendix A) contains a number of resistor chains that provide the correct potentials to the hemispheres and lenses. Retardation ratios of 10, 8 and 2 are available. The ramp voltage applied to the CHA control box is derived from an operational power supply that is controlled from the programmer box. This allows the selection of scan times ranging from 1ms to 3000 seconds.

The signal from the electron multiplier is fed straight into the head amplifier floating at ~ 2·5KV. The signal is then referenced to ground using the isolation amplifier. A number of variations of this were tried, including a tuned amplifier, but overall this arrangement seemed satisfactory. Full circuit details are given in Appendix A.

Before going on to describe the facilities for angle resolved studies the performance tests of the analysers will be reviewed.

2.5.1. Performance of the RPA

The resolution of the RPA was measured using the elasticilly reflected signal from a silicon specimen placed at position B (figure 2.4). The f.w.h.m. of the elastic peak was plotted as a function of energy and the resolution ρ was found to be about 250.

2.5.2. Performance of the CHA

This analyser was tested using two different types of source at

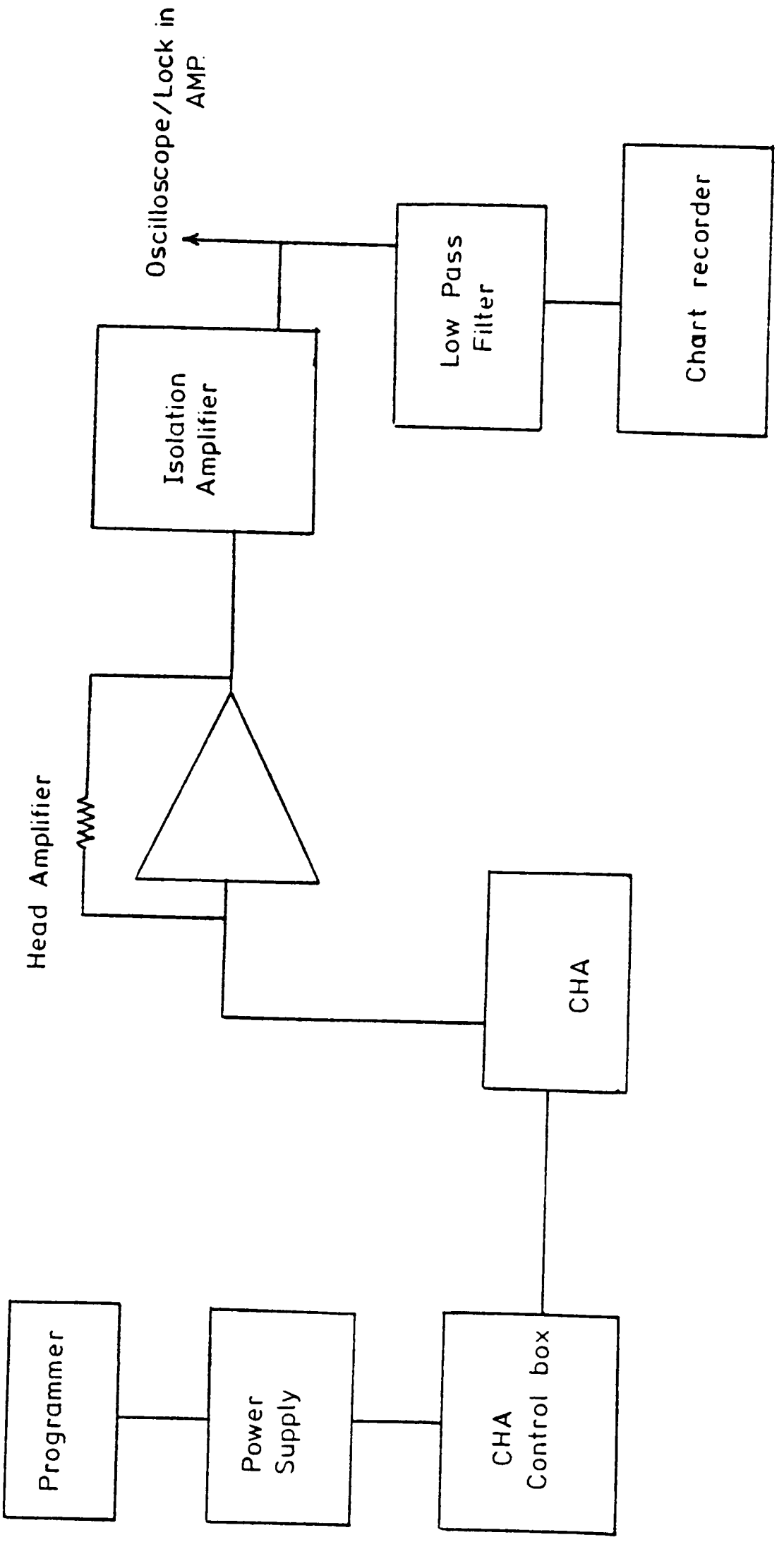


Fig.2.8 The C.H.A. electronics

position A (fig. 2.4).

The first was simply a hot filament and wehnelt cylinder assembly removed from an electron gun. Following the recommendations in (Bassett et.al. (1972)) a decelerating output stage had been incorporated to try and suppress spurious secondary peaks. However after much experimentation it became apparent that the focus on the output lens was the most critical factor for the removal of secondary peaks. Consequently an accelerating output stage was tried by grounding the final element (V_5) of the output lens. At first this was unsuccessful due to limited range of voltages then available for the focus electrode V_4. After suitable rewiring of the CHA control box the accelerating output was found to operate very well with no spurious peaks, provided the lens was properly focussed.

This modification resulted in reduced system noise essentially because one end of the electron multiplier could be grounded along with much of the shielding within the vacuum chamber. Secondly the analyser could be operated successfully down to 9eV (before retardation) with a retardation of 10, compared to about 40eV with the previous arrangement. (Due to the energy dependent electron multiplier gain)

The resolution was measured by plotting the f.w.h.m. of the energy distribution of electrons emitted from the filament as a function of electron energy. This showed that the resolution ρ was 900, less than the theoretical estimate of 2000 obtained when the source is assumed to be $\sim$1mm in diameter.

A second test of resolution was then performed using electrons elastically reflected from a silicon (111) surface using the arrangement shown in figure 2.9. In this case the measured value of ρ was 570. The source size d in this case is due to an electron beam $\sim$1mm dia at 65° from the surface normal resulting in an elliptical source with a maximum dimension of 2·5mm. Putting d = 2·5mm in equation (2) results in ρ = 800.

Therefore it appears that the source size is an important factor in

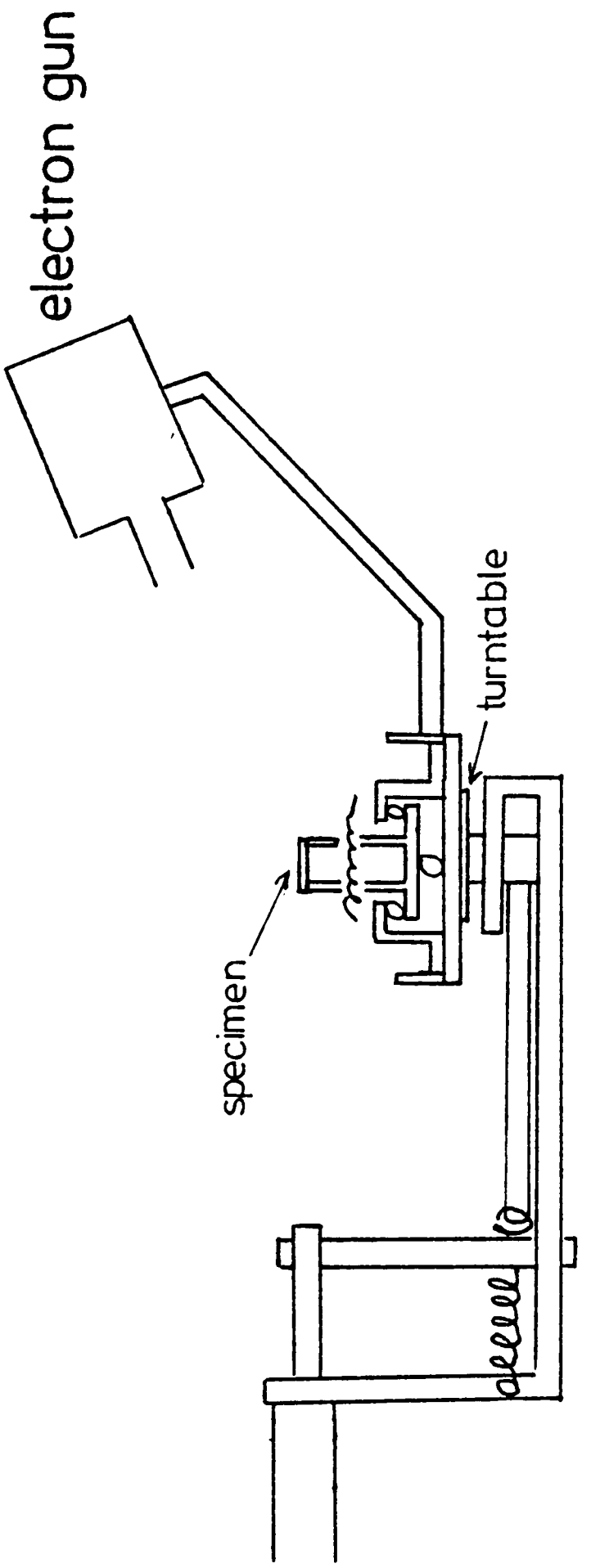


Fig.2.9 Original specimen stage

determining the resolution of the CHA.

A further possibility has been suggested by Browning et.al. (1977), where field penetration into the first lens was thought to change the magnification of the input lens used on the analyser described by Bassett (1974) an analyser very similar to the one discussed here. Some improvement in might have been possible by reducing the size of the output slit and hence making the input and output virtual slits of equal size. However the doubts cast by Browning et.al. (1977) on the validity of the theoretical values of M seemed to imply a rather time consuming empirical search for the optimum slit width and since ρ was adequate for the studies envisaged the matter was not pursued.

2.5.3. Summary of CHA performance

The instrument can be adjusted to optimum performance in a few minutes and the resolution has been measured to be at least 570, producing for the 90eV Si Auger peak an energy window of 0·16eV. This performance was considered satisfactory and the development of equipment for angle resolved studies was embarked upon.

2.6. The Electron Guns

Initially this equipment was provided with two electron guns. The gun used for LEED work is an integral part of the RPA system (shown schematically in fig. 2.5) and it provides $\sim 1\mu A$ beam current using an LaB_6 cathode. The electronics were built by the author in the Laboratory and the general form can be seen in fig.2.10. The focussing potentials are derived from a series of resistor chains with a constant 2KV across them.

A second gun providing a higher beam current was generally used for routine AES. This is a Superior Electronics SE 3K/SU gun using either an oxide or tungsten cathode. The focussing potential is applied to the middle element of an einzel lens using a floating power supply as shown in figure 2.11.

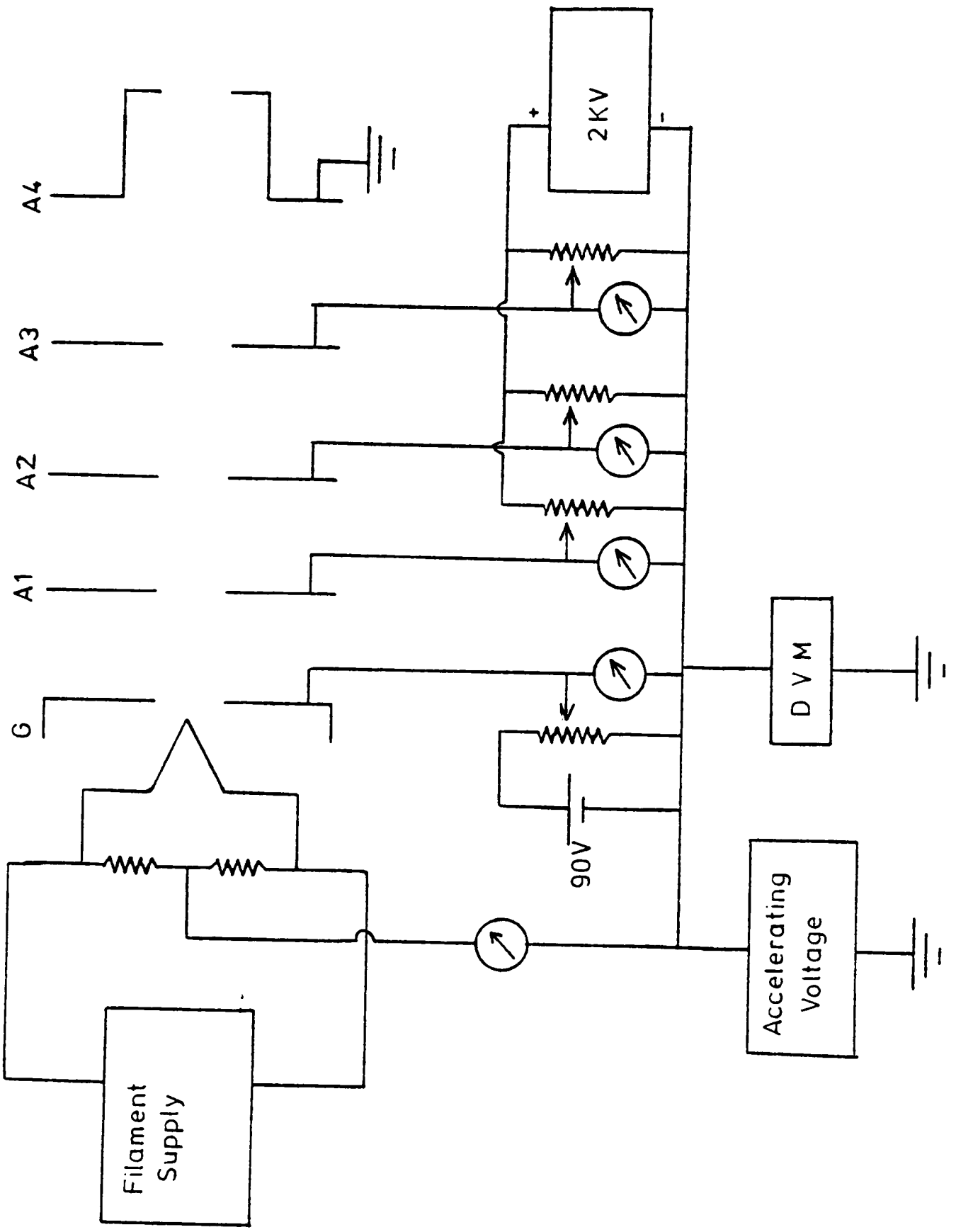


Fig.2.10 LEED gun and power supplies

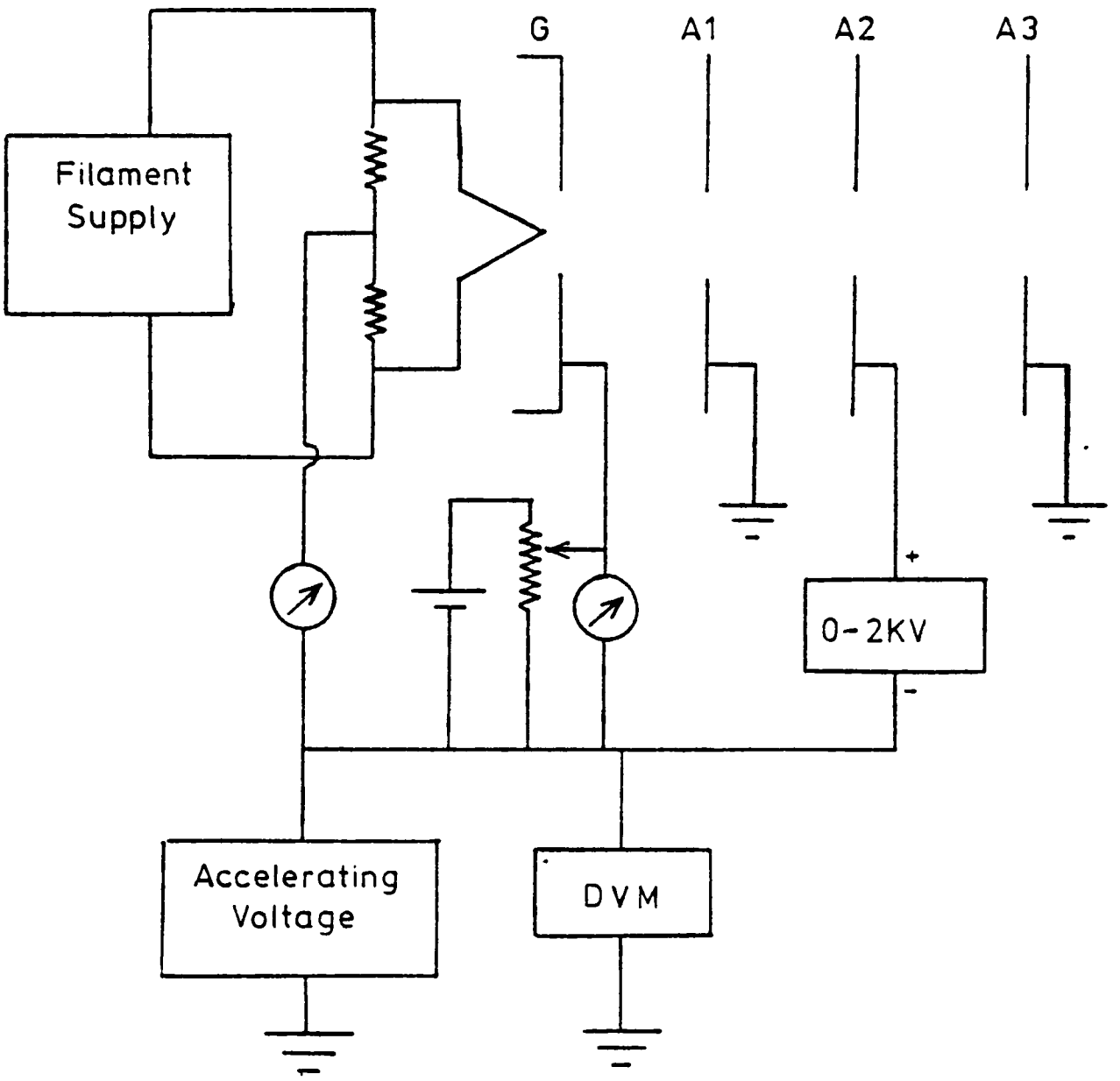


Fig.2.11 Auger gun and power supplies

The third electron gun was one specifically designed for angle resolved studies and it will be described along with the goniometer of which it was an integral part.

2.7.1. Equipment Specifically Designed for Angle Resolved Work

The diagram in figure 2.4 shows that the CHA is permanently fixed to the vacuum chamber. Therefore to study the effects of emission angle on Auger intensity it is necessary to rotate the specimen relative to the analyser. Manipulators to perform this task are readily available but because the electron gun is also attached to the chamber, any measured intensity variation at the CHA aperture will be due to changes in the incident beam direction as well as the angle of emission. To overcome this problem it was necessary to design a manipulator that would allow the electron gun to move with the specimen whilst changing the specimen orientation relative to the CHA. This in turn introduced a severe limitation on the overall size (especially length) of the electron gun as the specimen to analyser distance was only 6cm. at the closest point.

Unfortunately no commercialy available electron gun was suitable and consequently a miniature electron had to be designed and constructed by the author.

2.7.2. Miniature Electron Gun

The design of this electron gun was divided into two parts. Firstly the internal geometry was designed to be as small as possible and a prototype was constructed that would easily permit any alterations suggested by experiment. The second part was to design a body that would obstruct as small a fraction of the solid angle surrounding the specimen as possible.

2.7.3. Internal geometry of Electron Gun

Two types of cathode were considered, a tungsten hairpin and an indirectly heated oxide cathode. The latter was chosen for two main reasons, firstly that the flat emitting surface would be less prone to misalignment problems than the tungsten hairpin and secondly that the low heater current would allow the use of fine gauge wiring. (of importance when considering the overall size of the gun and the fact that it moves in the chamber) For ease of construction, design and wiring an einzel lens was used to focus the beam onto the specimen.

Inevitably as the internal diameter of the lenses decreases the aberrations for a given beam divergence increases. For the case of an einzel lens estimates of the spherical aberration coefficient can be found in (Harting and Read (1976)). However it is the size of the image at the specimen that is of interest and this is proportional to $C_s \alpha_o^3$,

where C_s - spherical aberration coefficient

α_o - beam divergence

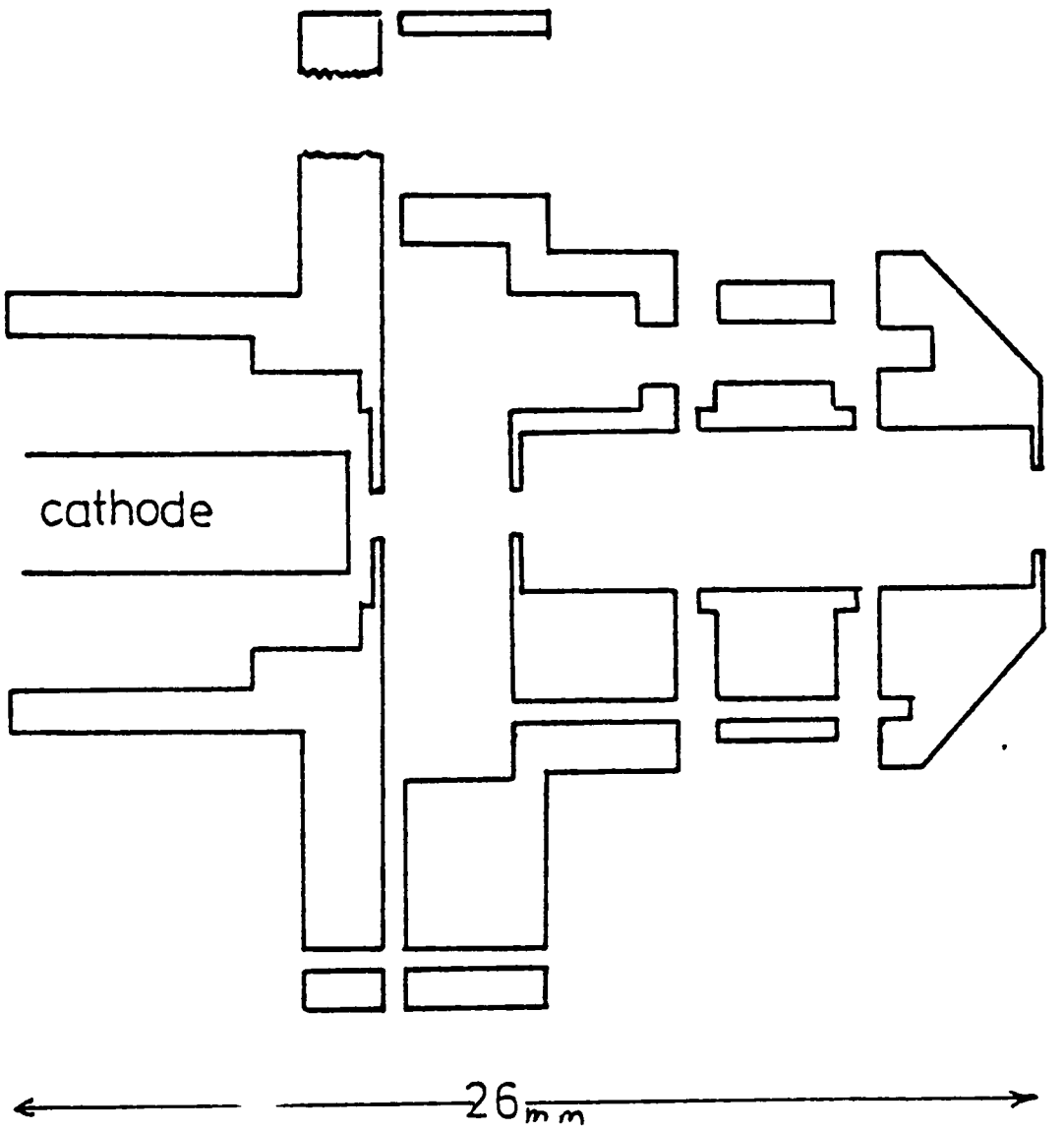
α_o is determined by the aperture at the entrance to the einzel lens (see fig. 2.12(a)).

The minimum acceptable beam current must now be considered, because reducing α_o and potentially the gun size also reduces the beam current. At this stage the design was directed toward a minimum beam current of 1μA and a maximum spot size of 1mm.

It was possible using data given by H.Moss (1968), to estimate the available beam current for certain geometries of cathode, wehnelt cylinder and beam defining aperture, and hence to obtain a minimum value of α_o giving in turn a maximum value on C_s.

The maximum value of C_s acceptable was then used to determine, using the information in Harting and Read (1976), the minimum lens diameter of 4mm used in the prototype gun of fig. 2.12(a).

a) PROTOTYPE ELECTRON GUN



b) Second Electron Gun

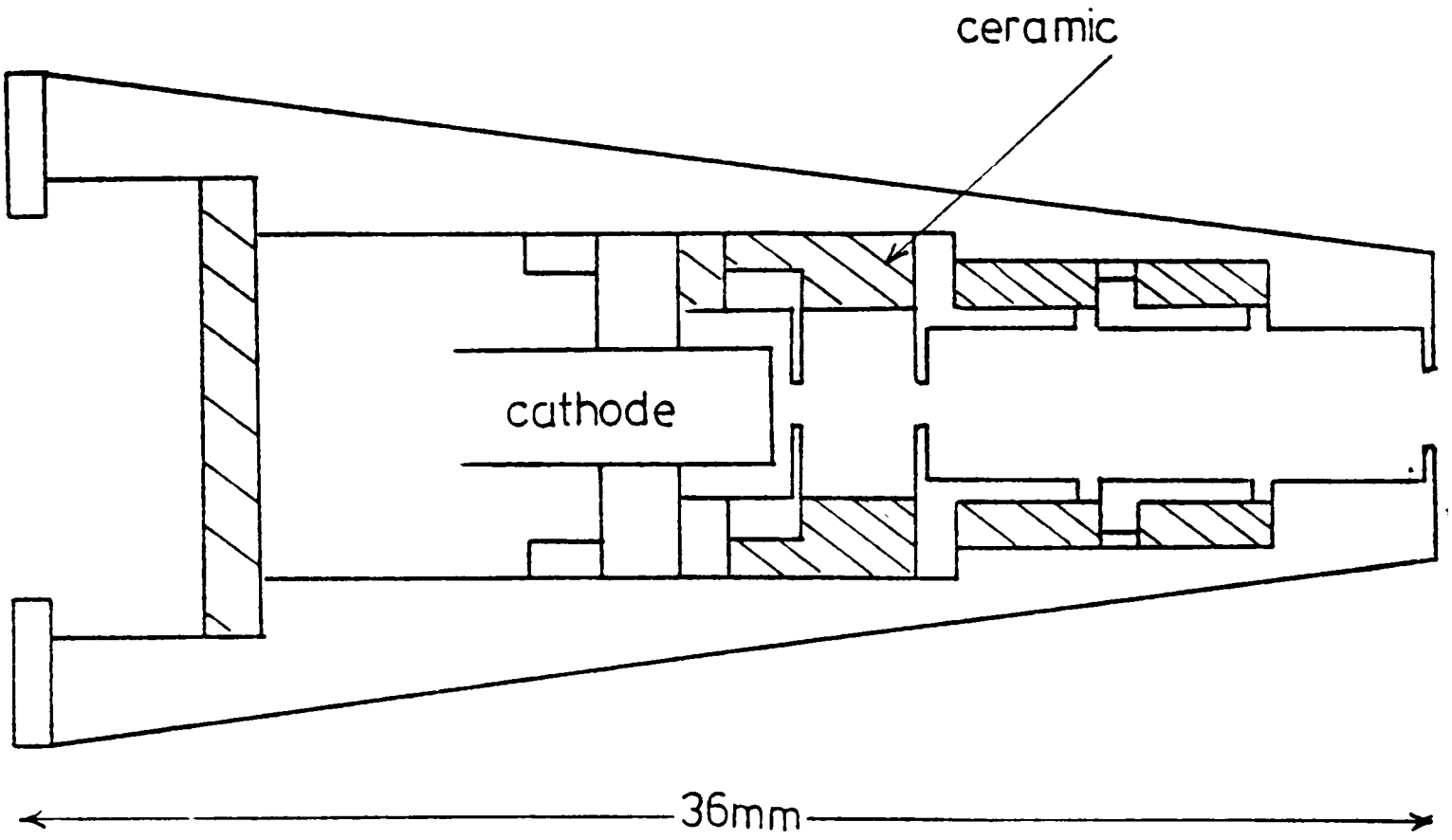


Fig.2.12 Miniature electron guns

This gun was constructed from non magnetic stainless steel and the lens elements were seperated using sapphire balls. Tests were conducted using a fluorescent screen and a Faraday cup in the energy range ~100eV to 3KV. The beam current increased with energy but even at 100eV ~1μA was available in a 1mm spot and 1KV 3μA was available in a 1mm spot. This performance was considered satisfactory and further experimentation on the prototype was not pursued.

2.7.4. Final Design

The final task was to house these lenses etc. in a small body at the same time ensuring that all the leads were electrically shielded to prevent electric fields in the specimen area. The lens elements were mounted using a machinable glass ceramic (MACOR trade name) in a conical stainless steel body. A diagram of the final device is shown in figure 2.12(b). The minature electron gun has now been in use for about two years and has proven reliable in service.

Auger spectroscopy was first done using the minature gun by mounting it rigidly on the turntable of a Vacuum Generators UMD-2 manipulator as shown in figure 2.9. As can be seen from the diagram this arrangement ensures that the incident beam direction is fixed relative to the specimen but it has no facility for adjusting the direction in situ. In principle this arrangement would allow variations of the takeoff angle θ (the angle between the surface normal and the axis defined by the input aperture of the analyser and the centre of the specimen) as well as the azimuthal angle ϕ.

In practice this arrangement was only suitable for static measurements because of the gross backlash associated with the o rotation and the large eccentricity of the θ rotation. In view of these problems and the obvious limitations imposed on the choice of incident beam direction a new specimen stage was designed by the author, and built in the laboratory.

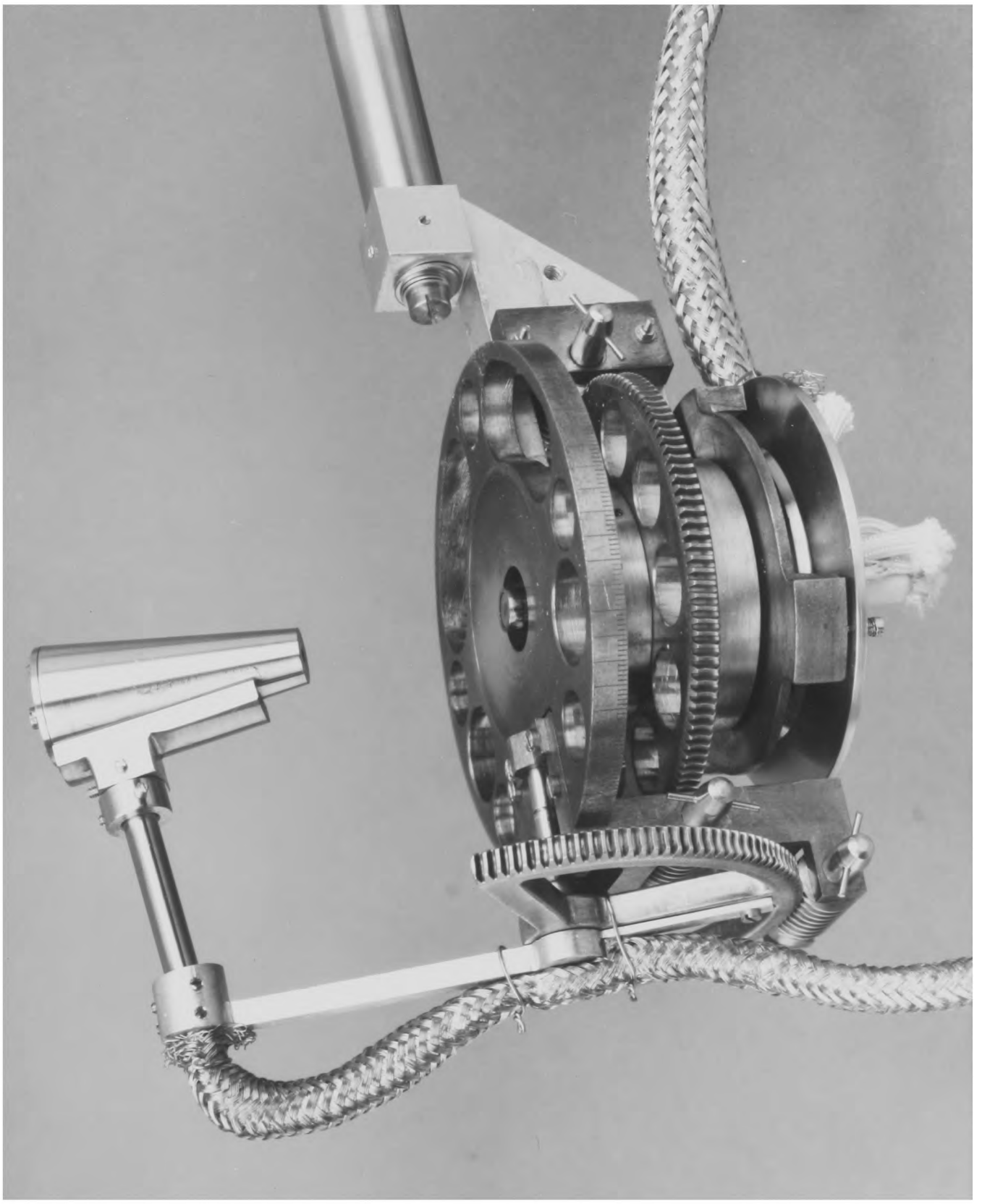
2.8. New Specimen Stage

A full study of geometrical effects in Auger spectroscopy requires an instrument that will collect electrons emitted from a specimen in any particular direction for any given incident beam direction. The photograph and diagram of 2.13 and 2.14 show the goniometer that includes the minature electron gun. The whole goniometer was mounted on the end of a $\frac{3}{8}$" dia. shaft that could be translated using the X,Y and Z drives of a Vacuum Generators UMD manipulator. The shaft was rotated using a Torvac rotary feedthrough mounted as shown in figure 2.15. The extra bearing was required to ensure that the specimen could be rotated accurately (to ± 0·2mm) about its own centre. In the later stages of the work the Torvac feedthrough became very unreliable and it was replaced by a Vacuum Generators RD1-S rotary motion drive.

This device allows the gun to be set in any desired orientation relative to the specimen, and once set, the specimen gun assembly can be put into almost any orientation relative to the analyser. The various rotations are operated by engaging the T bar, attached to the worm drives, with a rotatable shaft and coupling provided at right angles to the main shaft supporting the goniometer.

The nomenclature used for the various rotation axes can be seen in fig. 2.16. Figure 2.16(a) considers only the movement of the specimen relative to the CHA and Figure 2.16(b) shows only the movement of the gun relative to the specimen. The takeoff angle θ is controlled by the Torvac rotary feedthrough. The intensity versus can be plotted directly onto a chart recorder (see appendix for details). The azimuthal angle ϕ is adjusted using worm drive A (fig.2.14). One turn of worm A moves the turntable by 6^{o}. It should be emphasised here that adjusting worm drive A does not change the orientation of the gun relative to the specimen only that of the specimen relative to the analyser.

Fig.2.13 The specimen goniometer



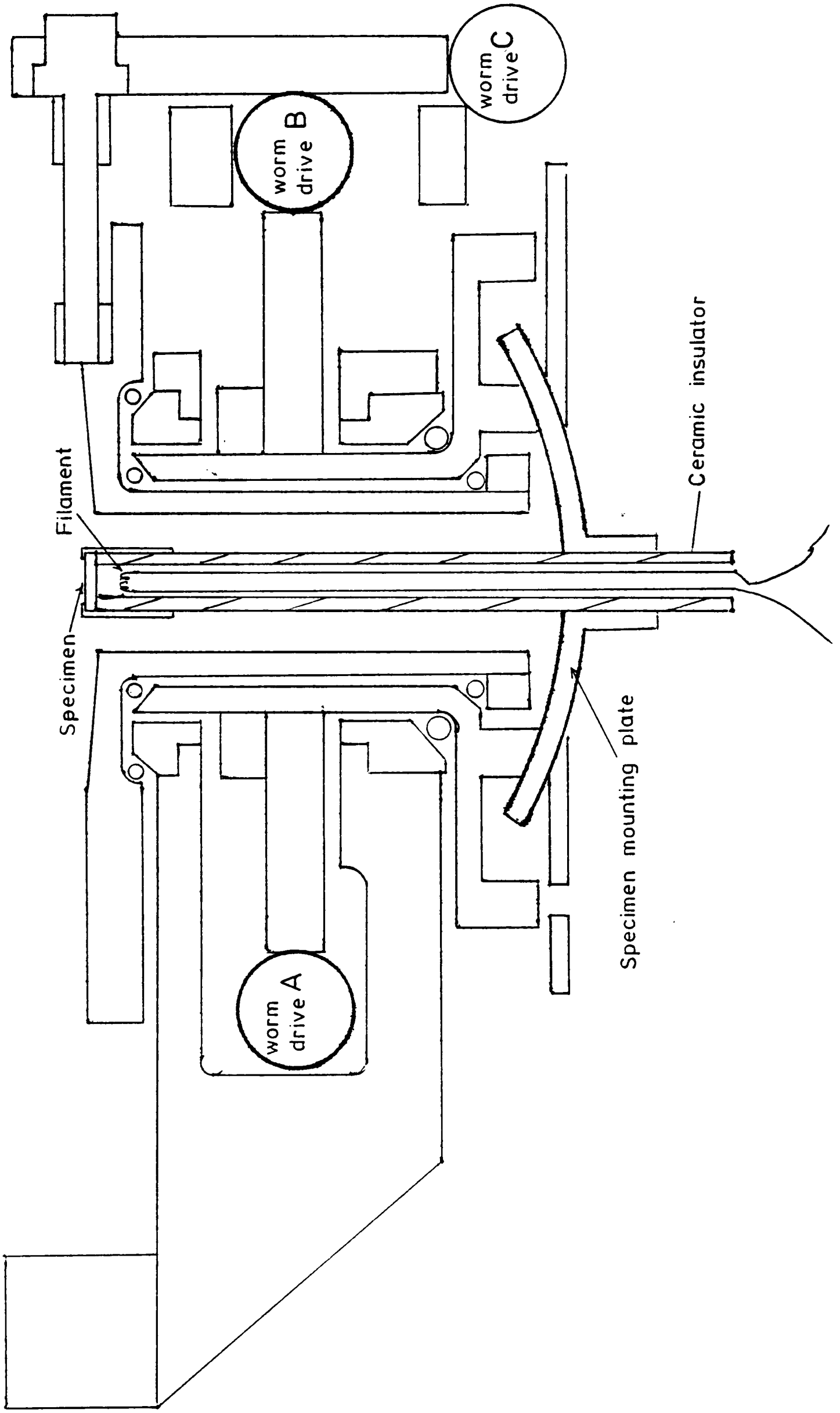


Fig.2.14 Cross section of specimen goniometer

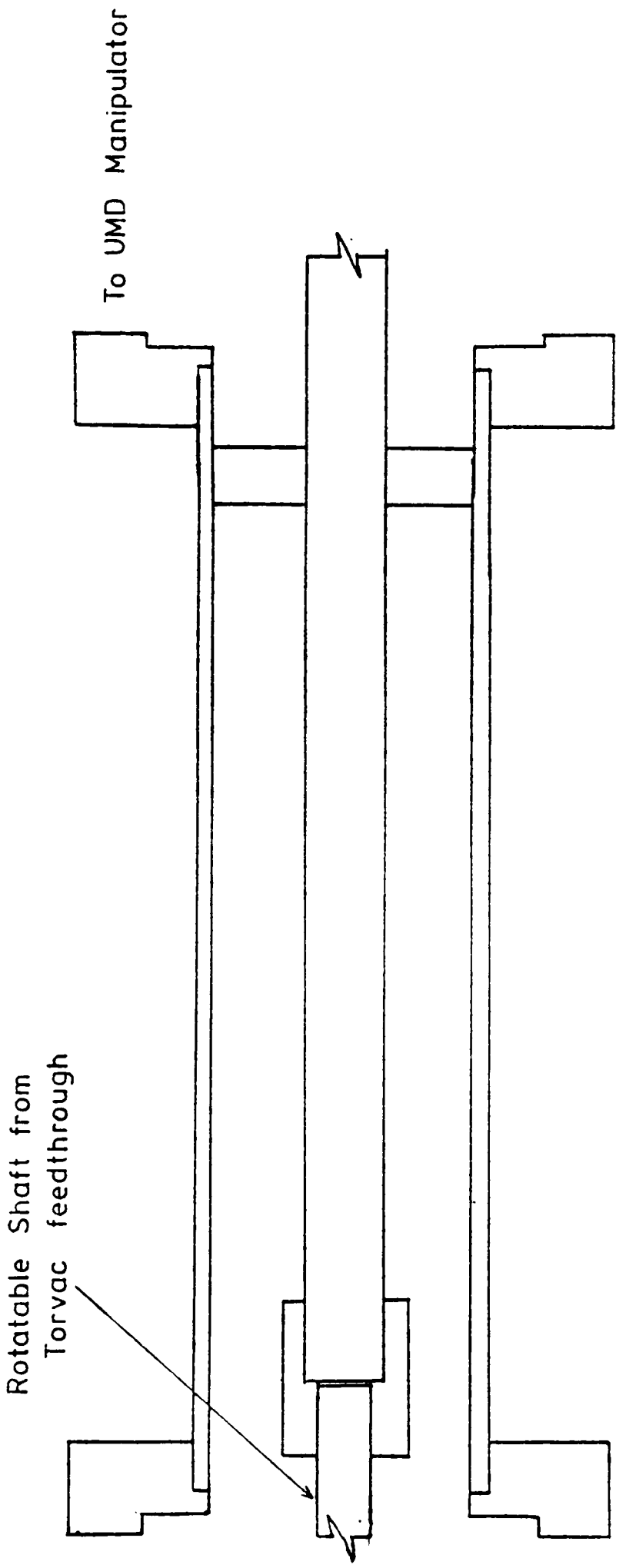
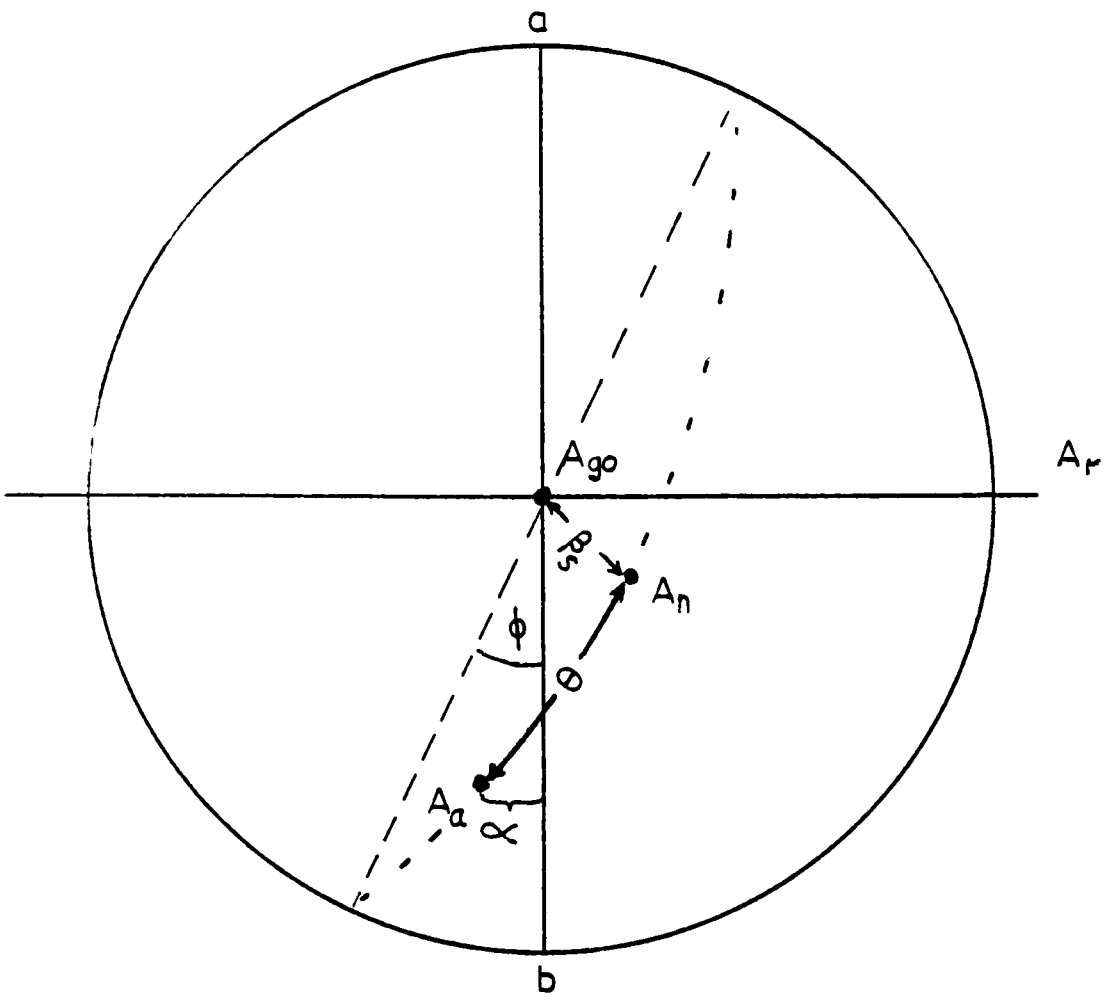


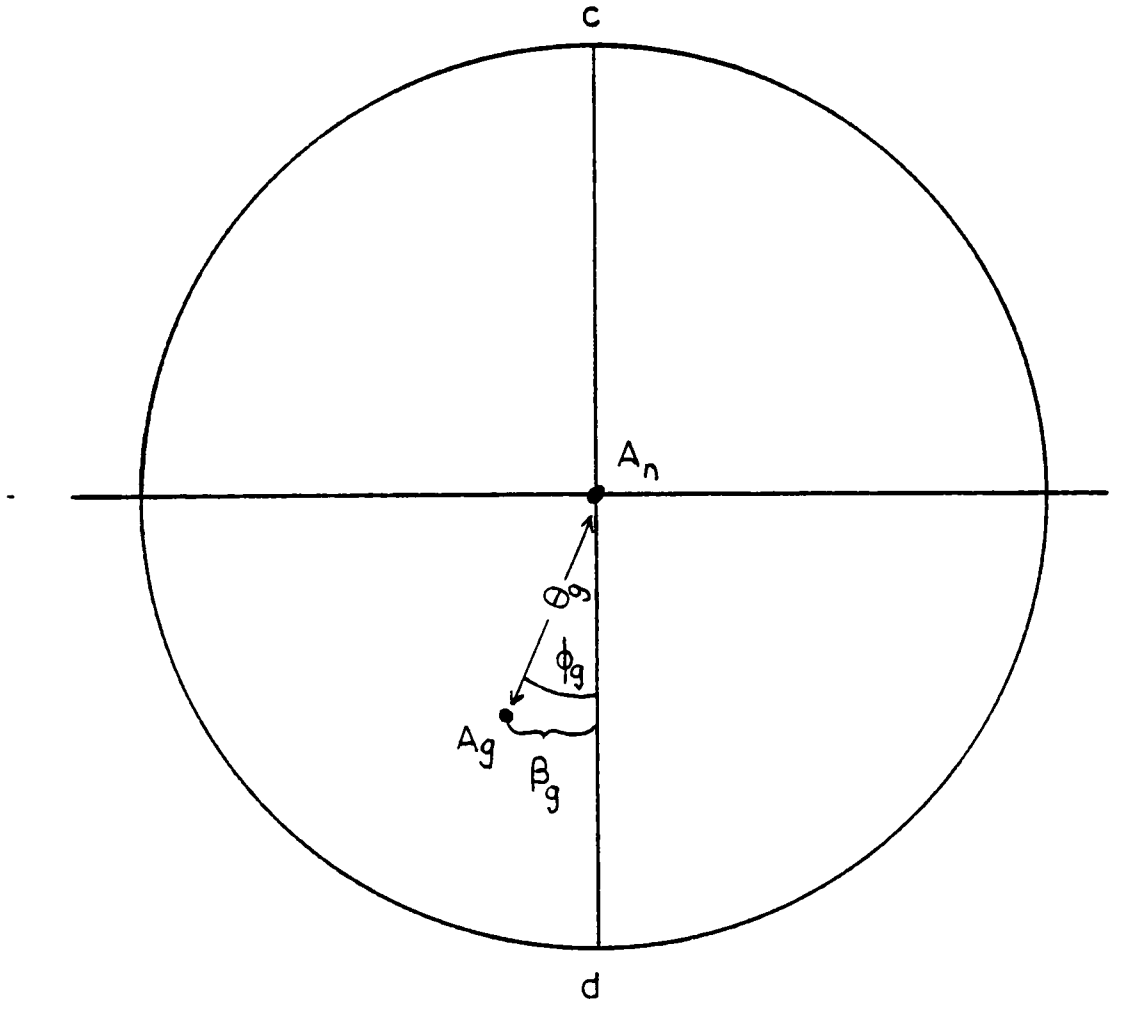
Fig.2.15 Shaft mounting

Fig.2.16 Definition of various angles associated with the goniometer

A_{go}-azimuthal rotation axis of the goniometer
A_n-normal to specimen surface
A_a-axis defining input to the C.H.A.
A_r-axis about which whole goniometer rotates
θ-takeoff angle
ϕ-azimuthal angle
β_s-angular error between A_n and A_{go}
α-angular error between planes of movement of A_a and A_{go}
A_g-axis of miniature electron gun
θ_g-incident beam angle
ϕ_g-azimuthal angle of incident beam
β_g-angular error between plane of movement of A_g and plane defined by c,d,and. A_n



a) Angles between specimen, goniometer and analyser



b) Angles between specimen and electron gun

Should the specimen normal A_n not be aligned with A_{go} this can be corrected by moving the specimen mounting plate (fig.2.14). The specimen is mounted at the centre of curvature of the mounting plate and hence only the angle β_s is altered but not the specimen position. A misalignment of up to 5^o in any plane can be corrected for in this way.

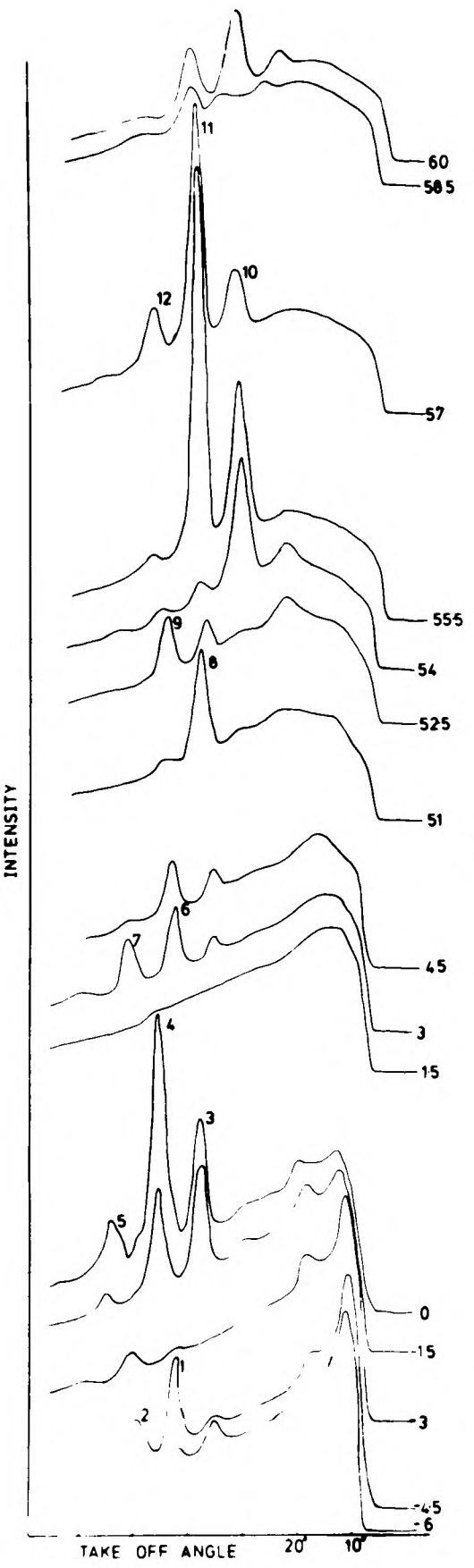
The angle α can be adjusted to equal 0^o by adjusting the tilt controls on the UMD manipulator. This ensures that for any given azimuth at $\theta = 0$ the specimen normal A_n will lie along A_a.

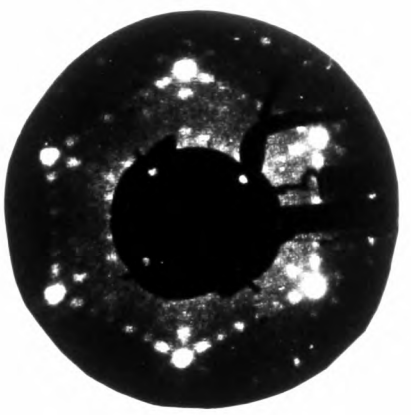
The angle between the incident beam and the surface normal θ_g is controlled by worm drive C and worm drive B is used to adjust ϕ_g allowing the incident beam direction to lie in any chosen azimuth relative to the specimen.

2.9. Tests and overall performance of the instrument

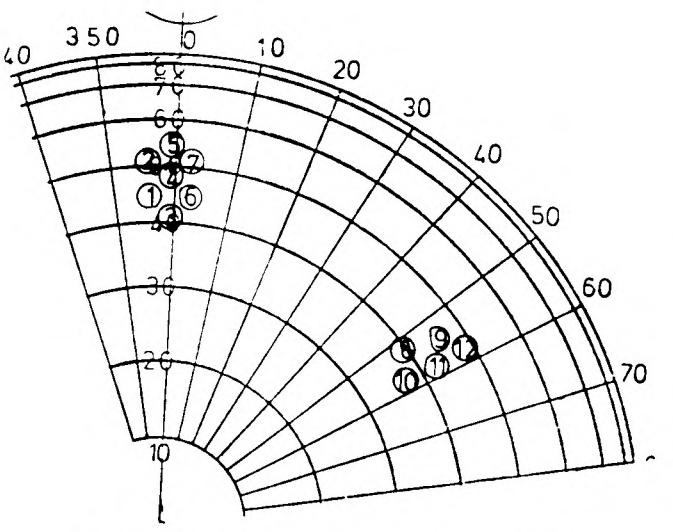
Before mounting a specimen in the goniometer it was necessary to ensure that the electron beam would hit the centre of the specimen for any incident beam direction θ_g. To check this a fluorescent screen was made and mounted in the specimen position shown in figure 2.14. The position of the gun was varied until the 1mm spot was at the centre of the screen and then θ_g was varied to ensure that the spot did not move across the specimen. Both faults were initially present but by adjusting the bracket holding the gun and the height of the specimen both faults were corrected. Neither adjustment could be performed in situ and consequently this initial setting up was time consuming but once set no further adjustment is required.

Further tests were performed using a silicon (111) specimen, prepared as in Chang (1970). The specimen was cleaned by electron bombardment heating until a sharp LEED pattern of the type shown in figure 2.17 was obtained. The data was collected in N(E) form by setting the analyser transmission energy on the feature of interest and varying the takeoff angle. The data were plotted directly as intensity versus angle on a chart recorder.





LEED PATTERN 39eV



Peak positions from angular profiles

angular profiles of elastic peak in various azimuths

Fig.2.17 Data from silicon(111) surface at 39eV

Figure 2.18 shows the results obtained by analysing the elastic peak at 800eV reflected from the specimen surface. The photograph was taken with the specimen at position B (fig. 2.4) and the angular profiles were plotted with the specimen at position A. The photograph of the Kikuchi pattern shows clearly the three fold symmetry of the Si (111) surface.

For the purpose of checking the specimen orientation relative to the goniometer the Kikuchi pattern is very convenient because features in the pattern are fixed relative to the specimen rather than to the incident beam direction.

Only if the axis A_{go} and the surface normal A_n lie on the same axis will features related by symmetry appear at the same position on angular profiles of the type shown in figure 2.18. Therefore by measuring the angular position of corresponding points in the plot labelled a,(a); b,(b); c,(c); the two axis can be shown to be aligned to within $\pm 1{\cdot}5^{\circ}$ ie $\beta_s < 1{\cdot}5^{\circ}$ in fig. 2.16.

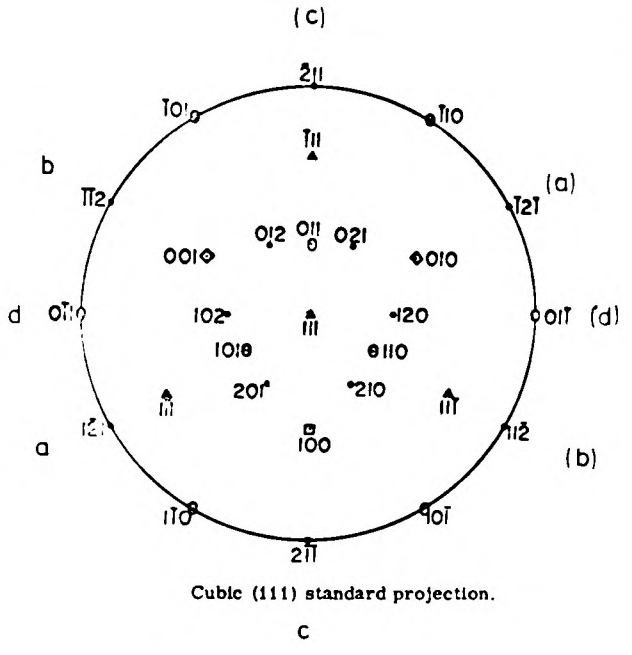
The spectrum labelled d,(d) was obtained by scanning at right angles to a mirror plane. A movement in ϕ of $1{\cdot}5^{\circ}$ or less in either direction produces a significant assymmetry and in practice this has been found the most accurate way of determining the specimen azimuth.

If angle $\alpha = 0^{\circ}$ in fig.2.16 then profiles identical to d,(d) should appear at 60° intervals in ϕ. However if $\alpha \neq 0^{\circ}$ then these spectra, although still symmetric, will differ from one another because A_n the specimen normal will never lie in line with A_a the analyser axis.

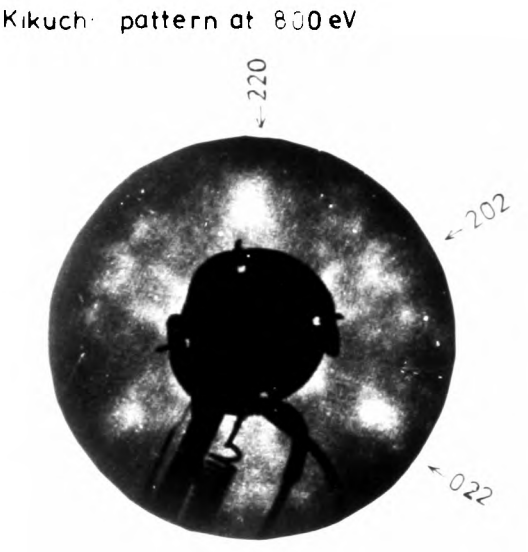
Therefore the expected asymmetry relating the azimuthal directions of type d(d) will be broken indicating $\alpha \neq 0^{\circ}$. Although the method of checking α is possible it is rather time consuming because for each adjustment made to the tilt controls three scans of the type d(d) must be made.

A more convenient method of checking α is to tilt the gun to allow the features at $\theta = 0^{\circ}$ to be observed. Only if A_n lies on A_a will the intensity

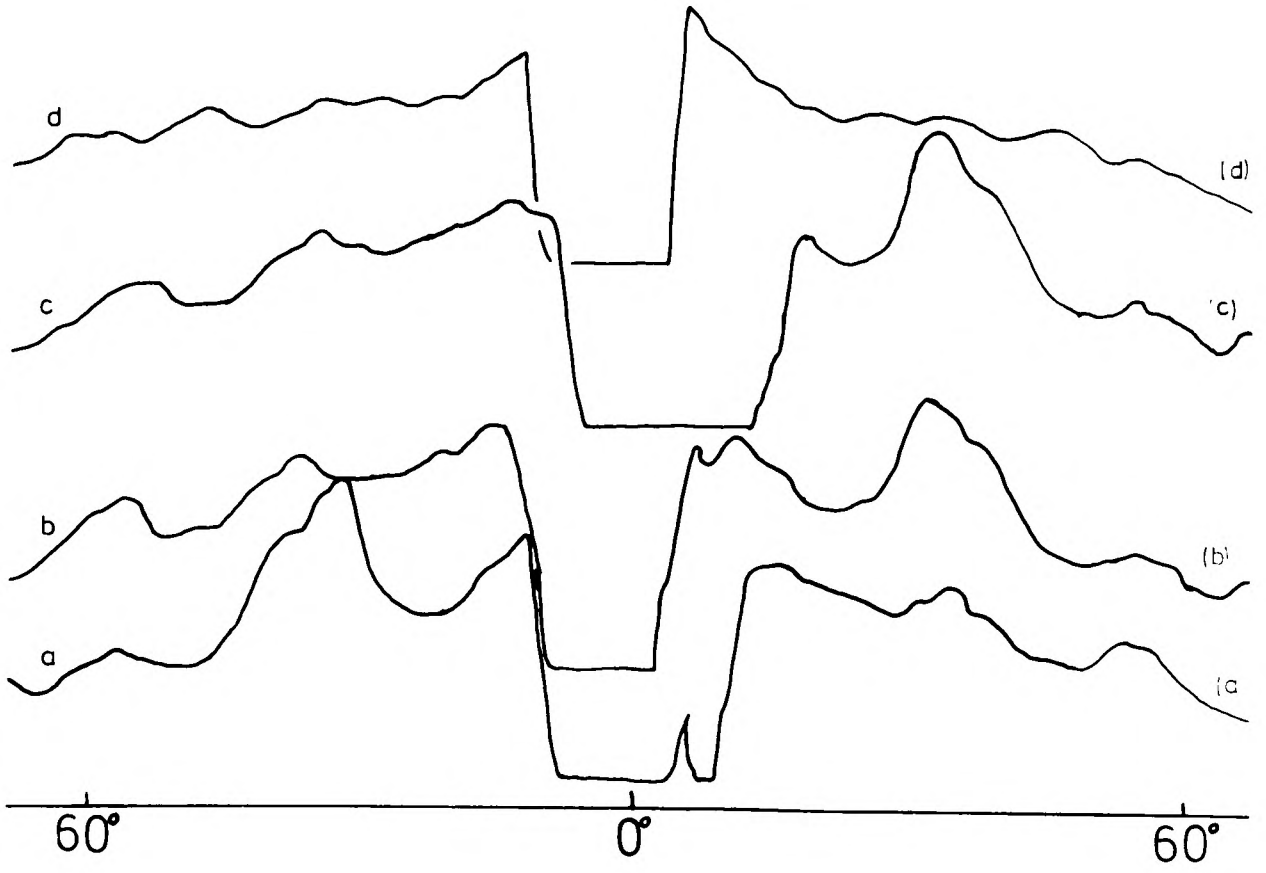
Fig.2.18 Data from the silicon(111) surface
at 800eV



Cubic (111) standard projection.



Angular Profiles of Elastic Peak at 800 eV in four azimuths



Emission angle

at $\theta = 0^{\circ}$ remain constant while ϕ is varied. This provides fairly quick a way of testing α to an accuracy of $\pm 1{\cdot}5^{\circ}$.

Therefore using these tests it is possible to align the various rotation axis of the specimen with the analyser axis to within 3°. The accuracy limitation of $\pm\ 1{\cdot}5^{\circ}$ will be largely due to the angular aperture of the analyser at the specimen being $\sim 2^{\circ}$. If such results are to be reproducible it is important to always scan θ in one direction only to avoid introducing errors due to the large backlash of $\sim 7^{\circ}$ present on the rotary feedthrough. At a later stage of the work the Torvac rotary feedthrough was replaced by a Vacuum Generators RDI-S rotary feedthrough which greatly improves the angular repeatability.

The final alignments to be checked are the rotation axis of the electron gun and specimen. For this purpose the data of fig. 2.17, obtained from the same Si (111) specimen as before at a primary energy of 39eV, was used. A visual check was made, using the fluorescent screen, to ensure that the beam did not move about on the specimen whilst changing the angle θ_g (fig.2.16(b)) (using worm drive B (fig.2.14)).

Providing the axis of the electron gun A_g lies along the specimen normal A_n the bright spots shown in the photograph of figure 2.17 should all appear at the same angular position θ. The angular profiles of figure 2.17 were used essentially to plot out the LEED pattern seen in the photograph. The numbers labelling the various peaks allow them to be identified with the various diffraction spots. In this case the spots 4 and 11 ought to appear at $\sim 35^{\circ}$ from the specimen normal for $\theta_g = 0.^{\circ}$ Having already determined the direction of the specimen normal from fig. 2.18 the fact that the spot labelled 4 appears at 48° from the specimen normal, indicates that the incident beam is 13° from the surface normal in the azimuth labelled 0°. Similarly spot 11 lying at 42° from the surface normal indicates $0_g = 7^{\circ}$ in the azimuth labelled $\sim 57^{\circ}$.

In the azimuth labelled 0^{o}, θ_g can be adjusted in situ using worm drive C. In the azimuth at right angles to this, β_g must be adjusted by opening the vacuum chamber, but again this adjustment is only performed once whereas θ_g can often be changed in the course of an experiment. Again the accuracy of these adjustments is $\pm$ 1·5^{o}.

2.10. Summary

The construction and testing of an instrument to study angular effects in Auger electron spectroscopy has been described. The use of a high resolution, energy dispersive, electron energy analyser is a major improvement over the narrow angle, retarding field type of analyses that have been used previously (eg. M^{c}Donnel et.al. (1975), Zehner et.al. (1976)). The instrument is also extremely flexible in that almost any range of emission angles can be studied while still allowing complete freedom in the choice of incident beam directions.

The basic design philosophy of using a static energy analyser in conjunction with a versatile goniometer could easily be used to modify other existing Auger spectrometers for angle resolved studies avoiding the need to purchase new equipment with a movable energy analyser.

Chapter 3

Angular Distributions of Auger Electrons from Clean and Adsorbate Covered Non-Crystalline Surfaces

		page
3.1	Introduction	29
3.2	Theory for Clean Non Crystalline Surfaces	30
3.3	Experimental	32
3.4	Results and Discussions for Clean, Non Crystalline Surfaces	33
3.5	Theory for Non Crystalline Surfaces with Overlayers Present	38
3.6	Experimental	40
3.7.1	The Angular Distribution of the Argon LMM Auger Electrons from Ion Bombarded Silicon (111)	40
3.7.2	The Angular distributions of the Silicon LVV, the Argon LMM and the Carbon KLL Auger electrons from Ion Bombarded Silicon (111)	43
3.8.1	The Oxidised Silicon Surface	47
3.8.2	Experimental	48
3.8.3	Results from Oxidised Silicon Surface	49
3.8.4	Discussion	49
3.9	Summary	52

3.1. Introduction

The theory outlined in chapter 1 included the derivation of a formula (equation (12)) to predict the collected Auger current i_a emitted from an adsorbed monolayer. The main purpose of this chapter is to investigate in detail the variation of the Auger current as a function of emission angle. This requires an extension of the model used in chapter 1 to include possible variations in the rate of Auger production with depth that can arise when systems other than an adsorbed monolayer are considered. These variations can arise because of a variation in the rate of ionisation with depth or because of a concentration gradient of impurity atoms. In the unfortunate case where both these mechanisms contribute to an overall variation of Auger production with depth it would be impossible to draw any quantitative conclusion about the concentration of impurity atoms at the surface or strictly speaking in the top 50Å or so.

In principle it should be possible to calculate the rate of Auger production at a depth z in the specimen by using equations of the type shown as (10) in chapter 1. When dealing with more than the surface monolayer it is necessary to evaluate the Auger current $i_a(z)$ created in layer dz at depth z and equation (10) becomes

$$i_a(z) = \int_{E_c}^{E_p}\int_{\theta} I(E,\theta,z)\,\sigma(E)\,N(1-\omega)\,\sec\theta\,dE\,\sin\theta d\theta \,. \qquad \text{——— (1)}$$

(the dependence on ϕ does not have to be included in a non-crystalline specimen)

This in turn requires a knowledge of the energy and angle distribution of the total current $I(E,\theta,z)$ at each element of depth. At higher incident beam energies ($\sim$10KV) Monte Carlo calculations have been performed to calculate the rate of ionisation as a function of depth in a crystal (Shimizu et.al. (1977)). However at lower energies no such calculations have yet been done and even supposing such calculations were performed it is very difficult to actually measure the rate of ionisation with depth to check the theoretical predictions.

To circumvent this problem the approach adopted in this work has been to measure the variation in Auger current as a function of emission angle from a pure specimen, and then to derive the depth distribution of $i_a(z)$ from the measured angular distribution of the Auger electrons. To allow the use of simple theoretical models non crystalline samples were used. Having determined how $i_a(z)$ behaves, the possibility then arises of determining the relationship between the emission angular distributions and the depth distribution of the species in question. The rest of the chapter will describe the theoretical and experimental methods used and provide general formulae relating the emission angular distributions to $i_a(z)$, for non crystalline samples.

3.2. Theory for clean non-crystalline surfaces

Any theory concerned with predicting the variation in Auger yield with emission angle must have as its starting point some model for $i_a(z)$. Harris (1969) was among the first to consider this problem and he assumed that $i_a(z) = i_a(0) \exp\left(-\frac{l}{\lambda_p}\right)$ where λ_p is an effective attenuation length for the primary electrons and l is the undeflected path length of the primary beam to the depth considered. However, Bishop and Rivière (1969) suggested that $i_a(z)$ would initially increase with depth, reaching a maximum at a depth greater than the escape depth for the Auger electrons. They considered the assumption that $i_a(z)$ is constant would be a better approximation than the one used by Harris. Seah (1972) assumed that $i_a(z)$ was constant within the Auger escape depth, whereas most recently Matsudaira (1978) again assumed that $i_a(z)$ decayed exponentially with depth.

The effect that $i_a(z)$ can have on the emission angular distribution will be examined using the following simple model. The physical situation can be seen in figure 3.1. and the following assumptions were made.

1) The Auger electrons are emitted isotropically from the ion
2) The attenuation of the electrons within the sample follows an exponential decay

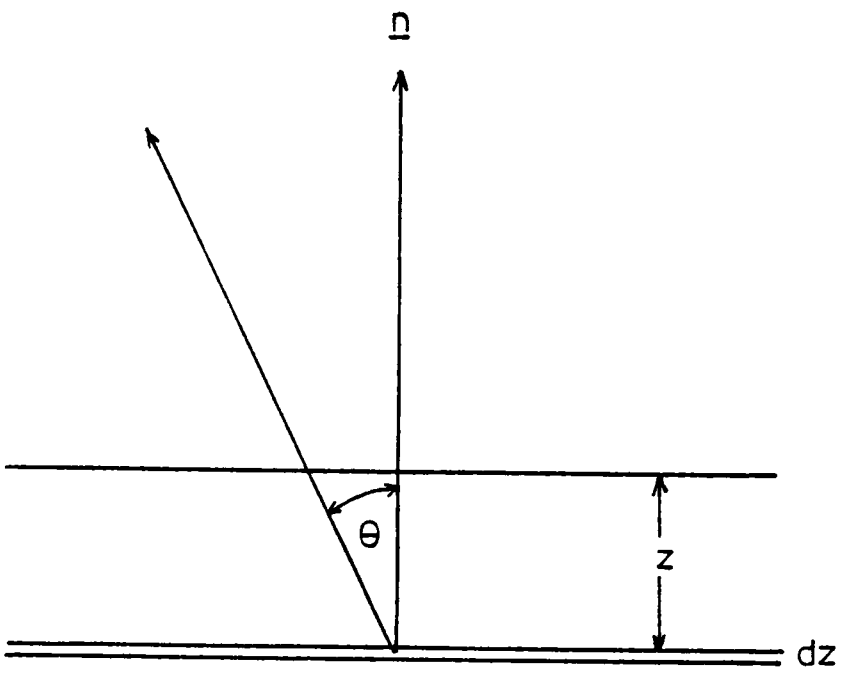


Fig.3.1 The clean surface model

3) surface roughness is ignored.

4) All electrons emitted along the direction specified by θ can be detected by the analyser with an acceptance solid angle $\Delta\Omega$

5) refraction at the surface is ignored.

Thus the Auger current collected by the analyser set at an angle θ from the surface normal can be written as :-

$$i_a(\theta) = \int_0^\infty i_a(z) \exp\left(-\frac{z}{\lambda_a \cos\theta}\right) dz \frac{\Delta\Omega}{4\pi} \quad \text{---} \quad (2)$$

The factor T has been omitted since all the work to come will refer to ratios of collected current where T would simply cancel out and the subscript e on θ has been omitted for convenience in this chapter.

λ_a is the inelastic mean free path. The actual path length travelled by the electron will be slightly greater than $\frac{z}{\cos\theta}$, but because the inelastic scattering cross section is much greater than the elastic cross section the error caused by this assumption can be shown to be less than 3% (Seah and Dench (1978)).

The general behaviour of $i_a(\theta)$ can be examined by inserting the various types of functions suggested for $i_a(z)$. Since the Auger current is usually measured in arbitrary units the normalised version of $i_a(\theta)$ is used ie. $\frac{i_a(\theta)}{i_a(0)}$. Therefore following Harris (1969) and putting $i_a(z) = i_a(0) \exp\left(-\frac{z}{\lambda_p}\right)$ into equation (2) will result in

$$\frac{i_a(\theta)}{i_a(0)} = \frac{\left(\frac{\lambda_p}{\lambda_a} + 1\right) \cos\theta}{\frac{\lambda_p}{\lambda_a} + \cos\theta} \quad \text{---} \quad (3)$$

putting $i_a(z) = i_a(0)$, a constant, gives

$$\frac{i_a(\theta)}{i_a(0)} = \cos\theta \quad \text{---} \quad (4)$$

The form of $i_a(z)$ suggested by Bishop and Rivière (1969) can be approximated by letting $i_a(z) = i_a(0)\ (1 + Bz)$. This assumes that the peak in the ionisation rate mentioned by Bishop occurs below the escape depth for Auger electrons.

This approximation gives

$$\frac{i_a(\theta)}{i_a(0)} = \frac{\cos\theta + B\lambda a \cos^2\theta}{1 + B\lambda_a} \quad \text{——} \quad (5)$$

Thus if $B\lambda_a \gg 1$

$$\frac{i_a(\theta)}{i_a(0)} = \cos^2\theta \quad \text{——} \quad (6)$$

and if $B\lambda_a \ll 1$

$$\frac{i_a(\theta)}{i_a(0)} = \cos\theta \quad \text{——} \quad (7)$$

(in agreement with equation (4))

Plots of $\frac{i_a(\theta)}{i_a(0)}$ versus θ for equations 3, 4 and 5 are shown in figure 3.2.

The curves labelled (1) and (2) are plotted from equation (3) where for curve (1) $\lambda_p = \lambda_a$ and for curve (2) $\lambda_p = 2\lambda_a$. Curve (3) is simply $\cos\theta$ and curve (4) is $\cos^2\theta$. Therefore the general picture to emerge is that if $i_a(z)$ increases with depth the Auger emission will be peaked about $\theta = 0$. Conversely if $i_a(z)$ decreases with depth the peak at $\theta = 0$ will be much less prominent. Finally if $i_a(z)$ is approximately constant with depth then a $\cos\theta$ angular distribution will result. The ranges of validity of these various formulae have been tested using a silicon specimen as described below.

3.3. Experimental

A 5·5mm diameter disc was cut from a silicon (111) wafer using an ultrasonic drill and the specimen was prepared as described in Chang (1970), before mounting in the vacuum chamber. After baking the system to obtain a base pressure less than 5×10^{-11} torr the specimen was cleaned in situ by heating it to $\sim 1200^{\circ}C$ by electron bombardment ($\sim$1000eV at 4mA emission). The non-crystalline surface used in these experiments was created by bombarding the surface with 500eV Argon ions at normal incidence for about 5 mins using $\sim 2\mu A$ beam current.

After this treatment the Kikuchi type structure normally observed in

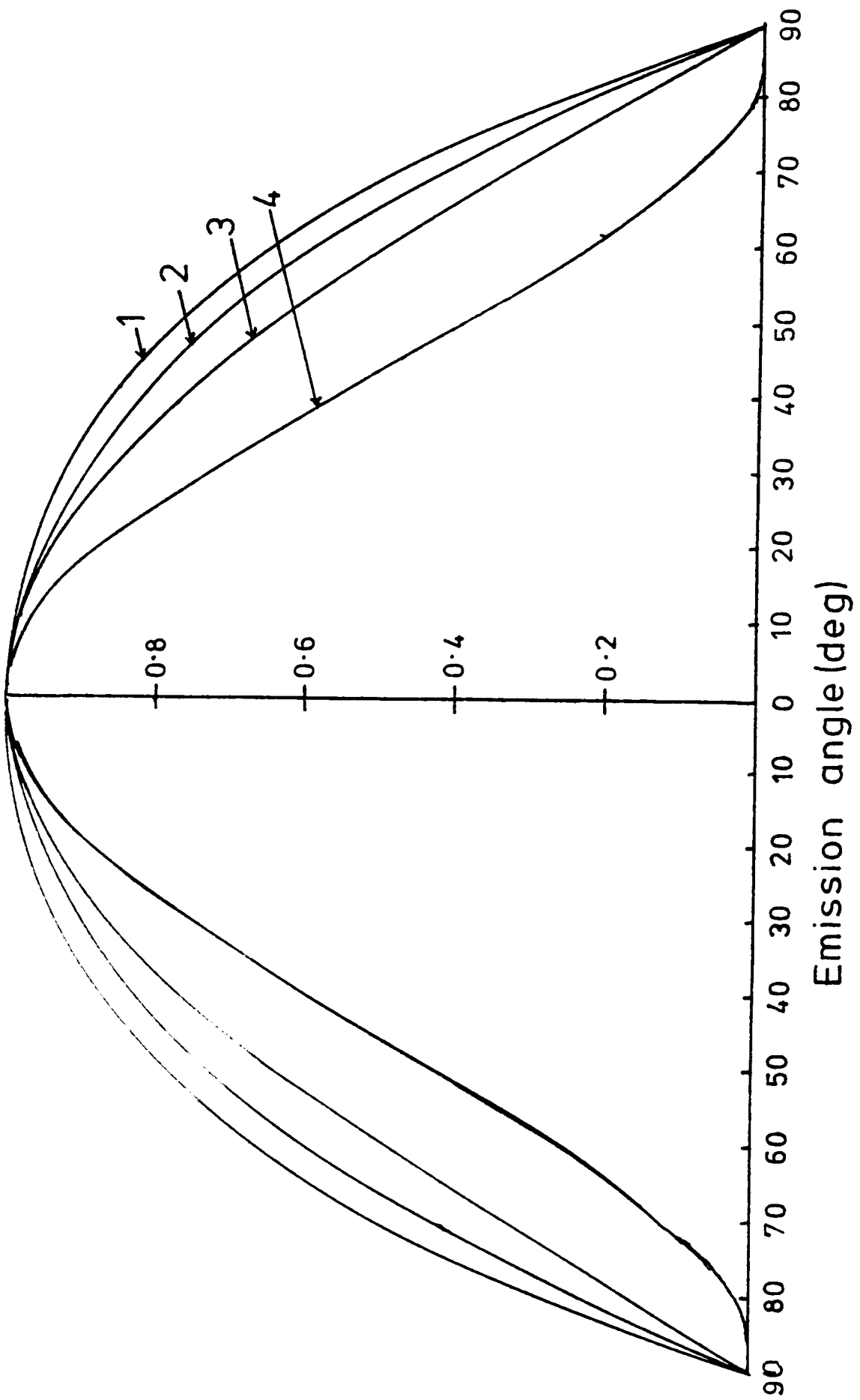


Fig.3.2 Theoretical predictions of $\frac{i_a(\theta)}{i_a(0)}$ for various $i_a(z)$

the elastic peak at 1000eV was totally obliterated, indicating the non-crystalline nature of the surface. A typical Auger spectrum obtained using this method of preparation can be seen in figure 3.3. The data was obtained using a primary beam of 1kV at normal incidence with an emission angle of 20^{o}. The carbon peak at 272eV is less than $1/80$ of the silicon peak at 92eV and the Argon peak at $\sim$215eV is about $1/32$ of the silicon 92eV peak.

Where possible the angular distributions of the silicon LVV peak was plotted using data in the E.N(E) form. A typical plot in this mode is shown in figure 3.4.

The intensity of the Auger feature is assumed proportional to the intensity measured at B substracted from the intensity at A. Thus the angular distribution of the Auger peak is obtained by plotting the angular distribution of the intensity at B and subtracting it from the angular distribution obtained at A. The angular distributions at A and B are plotted directly as a function of takeoff angle by setting the analyser pass energies at A or B and rotating the goniometer as described in chapter II. Unfortunately the background slope becomes too large for this mode of operation especially when using low primary beam energies and consequently the derivative mode has to be used. In this mode spectra are simply recorded at discrete values of emission angle and the peak to peak height of the derivative spectrum is taken to be proportional to the signal strength. The derivative form of the Si LVV spectrum form the ion bombarded silicon (111) surface has already been shown in figure 3.3.

3.4. Results and Discussion for clean non-crystalline surfaces

The angular distributions of the silicon LVV transition were measured for the following set of incident beam conditions.

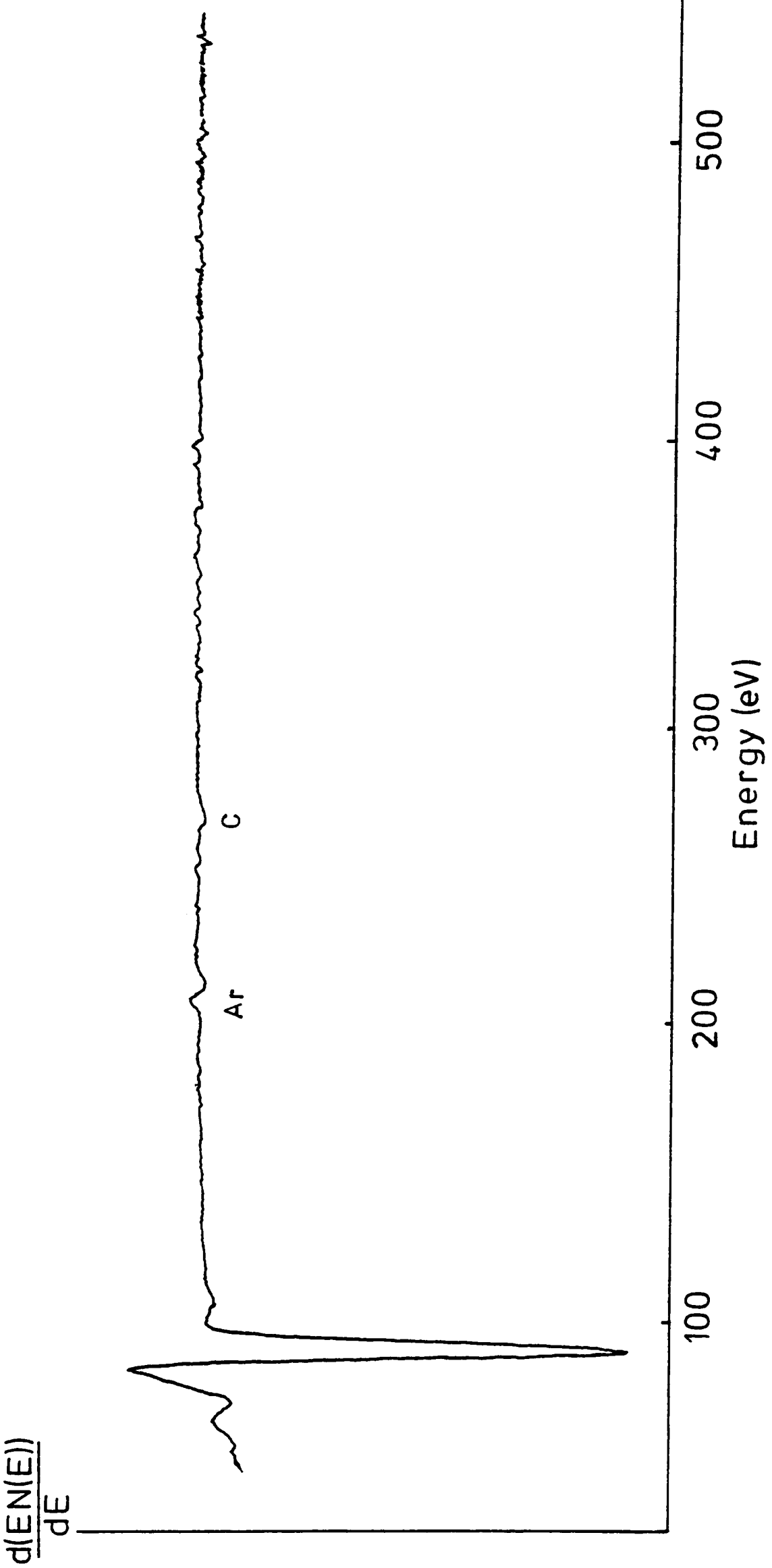


Fig.3.3 Auger spectrum from ion bombarded silicon(111) specimen E_p=1000eV

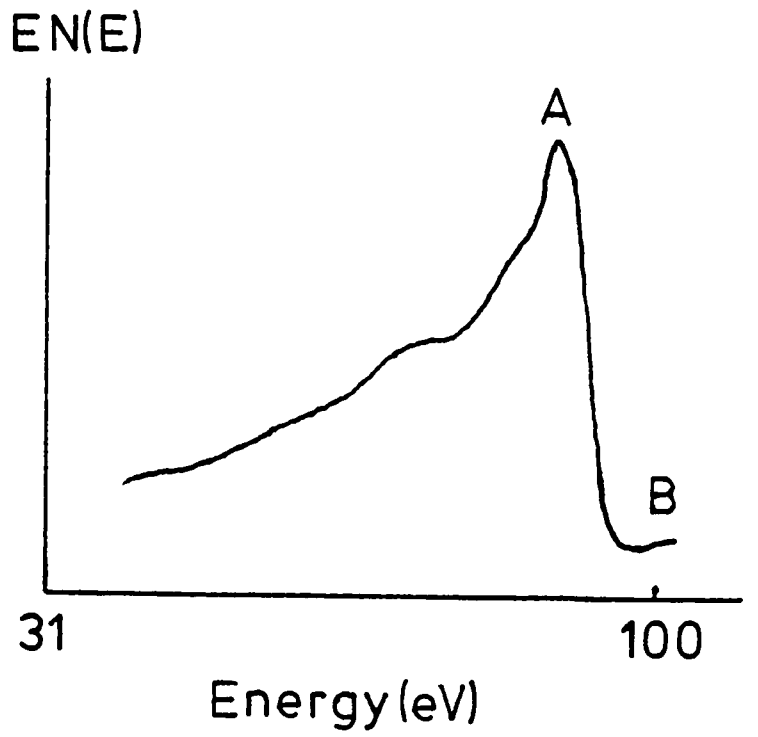


Fig.3.4 Silicon LVV peak from ion bombarded silicon(111) surface E_p=1000eV

Table 3.1.

Primary Energy (eV)	Angle of incidence (degrees)
2200	0
1900	0
1000	0
1000	30
1000	60
400	60
250	72
130	72

The angular distribtion at E_p = 1000eV and an angle of incidence of 30^o is shown in figure 3.5. Figure 3.6 shows the angular distribution obtained using $E_p = 250^o$eV with the angle of incidence at 72^o and finally figure 3.7 shows the angular distribution with E_p = 130eV and the angle of incidence at 72^o. The data shown in figure 3.5 were collected in E N(E) form whereas the data shown in figures 3.6 and 3.7 were both recorded in $\frac{d(E\ N(E))}{dE}$ form. The crosses indicate the experimental errors.

It was found that the angular distributions were always close to cosine θ, (where θ is the emission angle measured from the surface normal) except in the last case when E_p was 130eV. For this reason only the angular distributions of figures 3.5 and 3.6 have been included as examples. The middle dashed curve of figure 3.5 is given by cosine θ and the dashed curve in figure 3.6 is also cos θ. It has already been shown by equation (4) that a constant rate of Auger production within the Auger escape depth will produce a cosine θ angular distribution and hence the assumption made by Seah (1972) seems to be largely justified.

The experimental errors inevitably introduce an uncertainty about the form of $i_a(z)$ and this has been estimated as follows. In figure 3.5 curves have been drawn to lie inside and outside the data points, within the error bars, to provide extreme forms of the angular distribution consistent with the data.

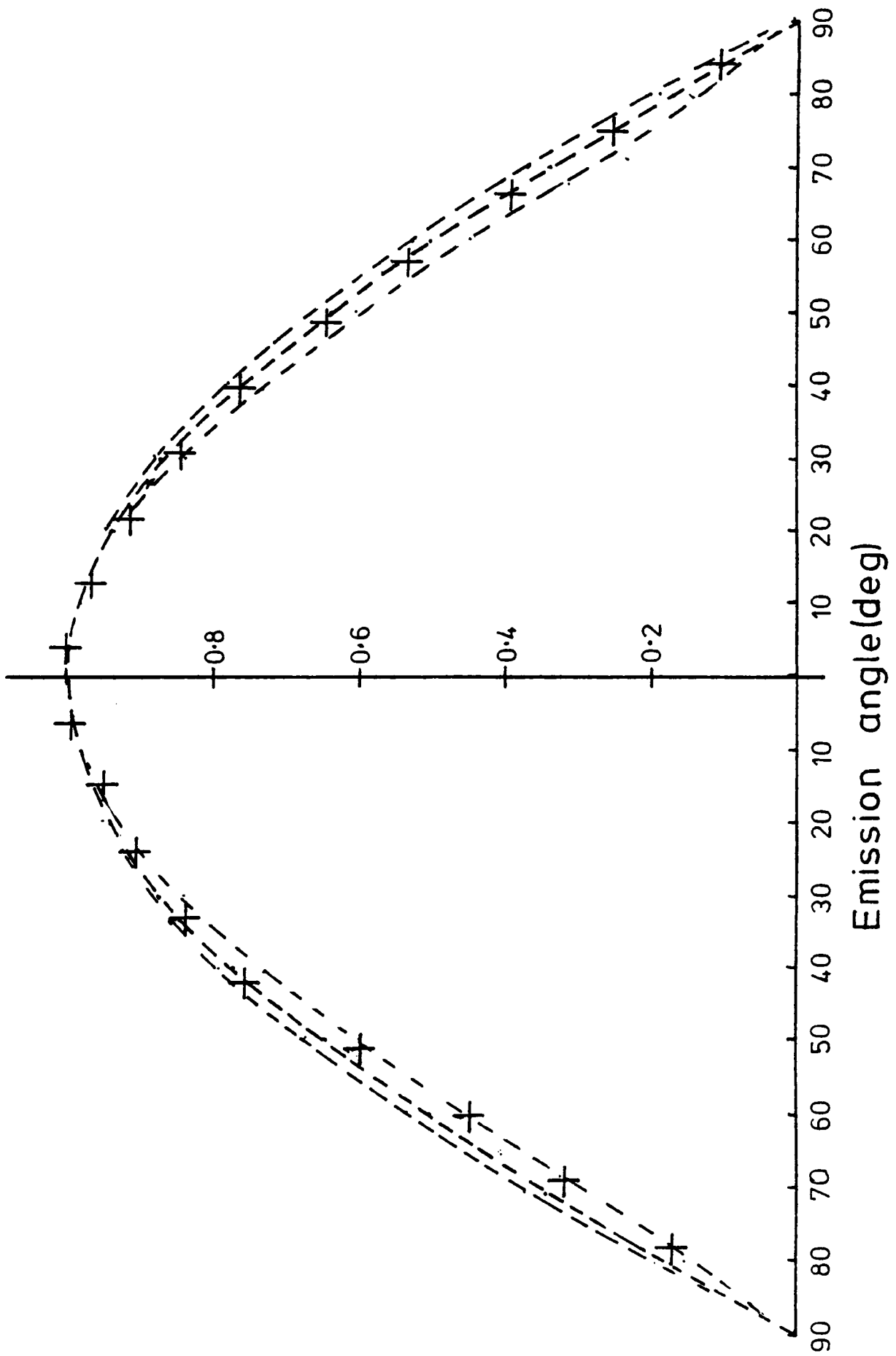


Fig.3.5 Angular distribution of silicon LVV signal from ion bombarded silicon(111) E_p=1000eV, θ_p=30°

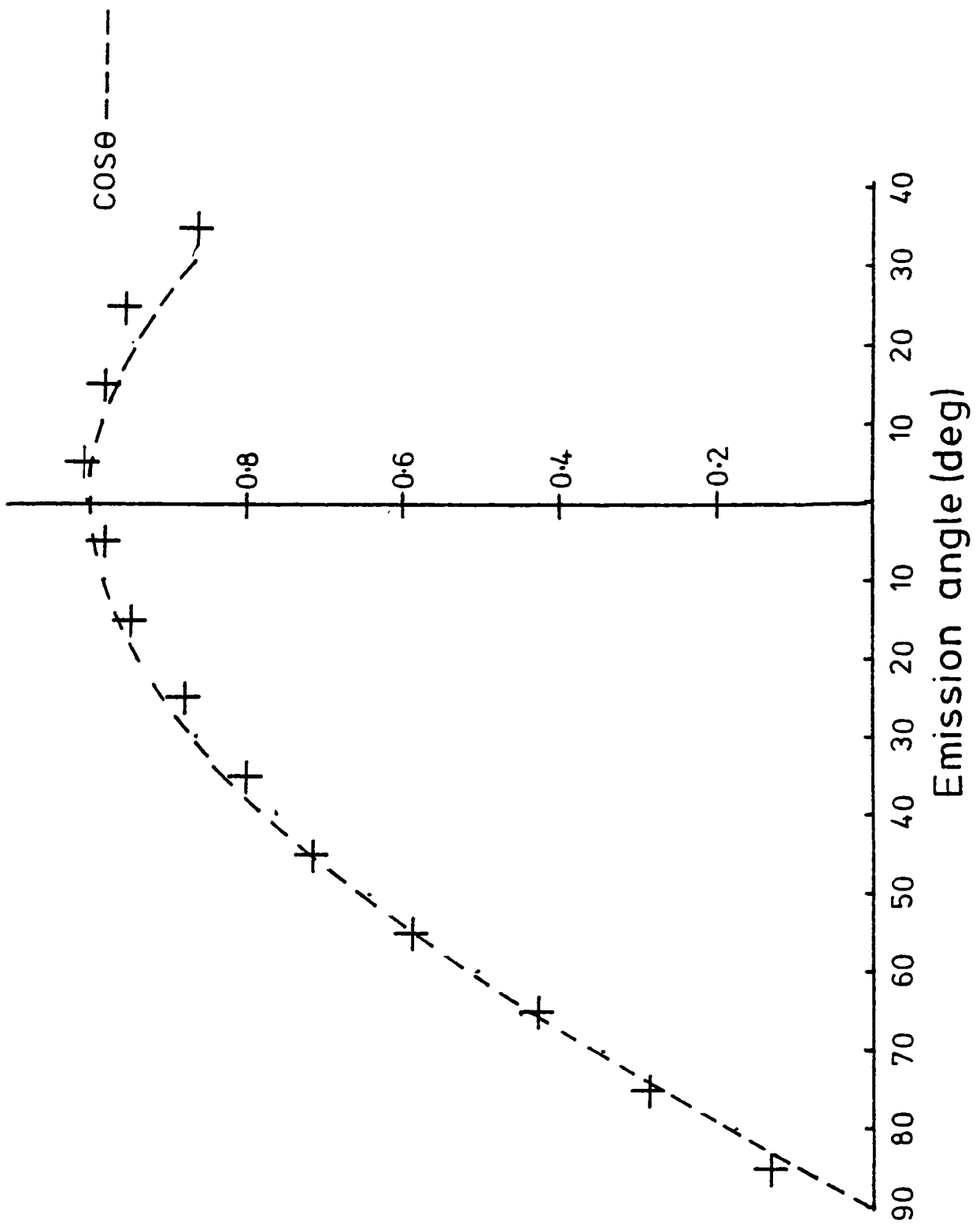


Fig.3.6 Angular distribution of silicon LVV signal from ion bombarded silicon(111) E_p=250eV, θ_p=72°

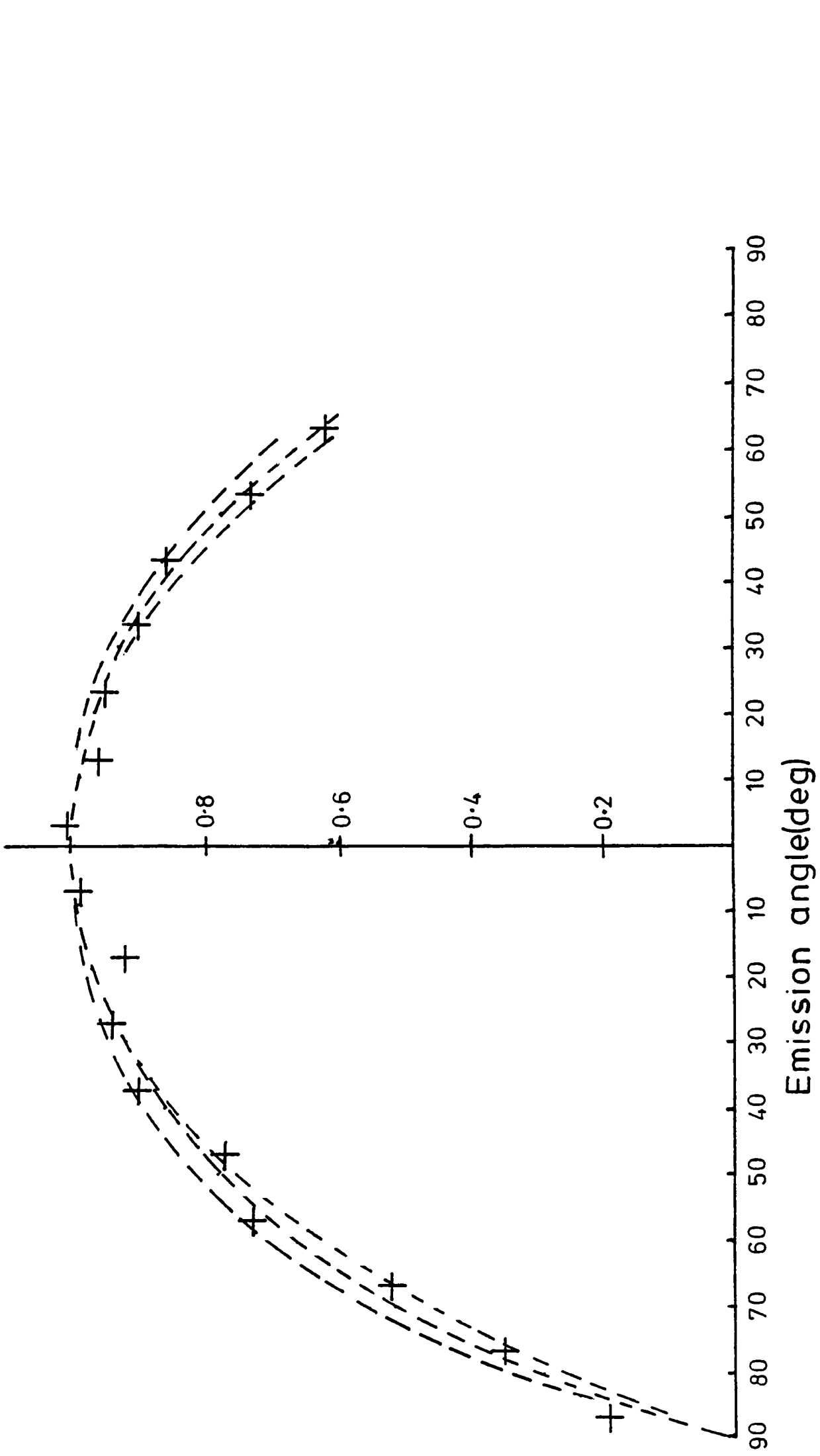


Fig.3.7 Angular distribution of silicon LVV signal from ion bombarded silicon(111) E_p=130eV, θ_p=72°

The outside dashed curve in figure 3.5 was generated by putting $\lambda_p = 7{\cdot}4\,\lambda_a$ in equation (3). The rate of Auger production assumed in the derivation of equation (3) was $i_a(z) = i_a(0)\exp\left(-\frac{z}{\lambda_p}\right)$, therefore at depth λ_a in the specimen

$$i_a(\lambda_a) = i_a(0)\exp\left(-\frac{\lambda_a}{7{\cdot}4\lambda_a}\right)$$
$$= 0{\cdot}87\, i_a(0)$$

The inside curve in figure 3.5 was generated by putting $B\lambda_a = 0{\cdot}25$ in equation (5). In the approximation for $i_a(z)$ used to derive equation (5) the Auger current at depth λ_a in the specimen is

$$i_a(\lambda_a) = 1{\cdot}25\, i_a(0)$$

Therefore the Auger current at depth λ_a in the specimen must lie in the range

$$0{\cdot}87\, i_a(0) \leqslant i_a(\lambda_a) \leqslant 1{\cdot}25\, i_a(0)$$

The angular distribution obtained with an incident beam energy of 130eV, shown in figure 3.7 has been analysed in a similar way using equation (3). The outside dashed curve was generated by putting $\lambda_p = 0{\cdot}7\,\lambda_a$ in equation(3), the middle curve by putting $\lambda_p = \lambda_a$ and the inside curve by putting $\lambda_p = 1{\cdot}7\,\lambda_a$. Thus $i_a(\lambda_a)$ for the three cases is given by respectively

$$i_a(\lambda_a) = i_a(0)\exp\left(-\frac{\lambda_a}{0{\cdot}7\,\lambda_a}\right)$$
$$= 0{\cdot}24\, i_a(0)$$

$$i_a(\lambda_a) = i_a(0)\exp\left(-\frac{\lambda_a}{\lambda_a}\right)$$
$$= 0{\cdot}37\, i_a(0)$$

$$i_a(\lambda_a) = i_a(0)\exp\left(-\frac{\lambda_a}{1{\cdot}7\,\lambda_a}\right)$$
$$= 0{\cdot}55\, i_a(0)$$

Therefore for all data presented in figure 3.7 the Auger current at depth λ_a must lie in the range

$$0{\cdot}24\, i_a(0) \leqslant i_a(\lambda_a) \leqslant 0{\cdot}55\, i_a(0)$$

The conclusions arrived at here are important for a number of reasons.

To allow the determination of concentration gradients in the near surface region from angular spectra of the type recorded here it is essential to work in the regime where the Auger production is constant within the Auger escape depth. The results presented here would indicate that this will be the case providing $\frac{E_p}{E_c} > 2.5$ and the angle of incidence is less than $\sim 72^o$

E_c - energy of core level being ionised

Possible charges in $i_a(z)$ occurring at $E_p \gg E_c$ have not been observed but this point will be discussed later. From the point of view of quantitative analysis the above criterion for constant $i_a(z)$ must also be obeyed since in the case illustrated by figure 3.7 where $i_a(\lambda_a) \leqslant 0.55\ i_a(0)$ any concentration determined resulting from atoms at distance λ_a below the surface would be in error.

This type of effect at low values of $\frac{E_p}{E_c}$ could also be exploited to yield at least qualitative information about the depth distribution of the atoms where Auger electrons are being analysed by essentially increasing the ratio of surface to bulk ionisations. It is important to emphasise that λ_p bears no simple relationship to the inelastic mean free path of the primary electrons it is simply a factor describing the rate of change of the Auger current with depth due to a change in the rate of ionisation with depth.

The type of effect observed here for low values of $\frac{E_p}{E_c}$ has been independently observed by Matsudaira (1978) for the case of 850eV nickel Auger electrons from polycrystalline nickel with E_p = 2000eV at an angle of incidence of $\sim 70^o$, in this case $\frac{E_p}{E_c} \sim 2.4$. These results were interpreted on the basis of a model similar to the one used here to interpret the results obtained at E_p = 130eV. It therefore seems likely that the criterion suggested here for ensuring a constant rate of Auger production with depth would also apply at higher incident beam energies.

In the experiment performed here on the silicon surface the maximum value of $\frac{E_p}{E_c}$ used was 24 for the silicon LVV transition and no deviation from

the cosine θ distribution was observed. However Matsudaira (1974) say that the angular distribution of 45eV iron Auger electrons from an ion bombarded iron surface was proportional to $\cos^2 \theta$ with a primary energy of 2000eV at 70° from normal incidence. They offered no explanation of this observation. The value of $\frac{E_p}{E_c}$ for this situation is 37, much higher than was used in the experiments on the silicon performed here. Equation (6) predicts a $\cos^2 \theta$ angular distribution with $B \lambda_a \gg 1$ and it therefore seems likely that the results from the iron surface can be understood by letting the iron Auger current be described by $i_a(z) = i_a(0)\ (1 + Bz)$. This explanation would be compatible with the suggestion made by Bishop and Rivière (1969) that the Auger production initially increases with depth.

Thus it seems now to be possible to distinguish three distinct types of behaviour of $i_a(z)$. Firstly that $i_a(z)$ decreases with depth, secondly that $i_a(z)$ is constant with depth and thirdly that $i_a(z)$ increases with depth. These types of behaviour refer to depths less than the Auger escape depth.

Figure 3.8. illustrates the three forms of $i_a(z)$ described here. Depth is measured in units of λ_a and $i_a(z)$ is measured in units of $i_a(0)$. Curve (1) is given by $i_a(z) = i_a(0) \exp\left(-\frac{z}{\lambda_a}\right)$, this form of $i_a(z)$ was used to describe the data shown in figure 3.7. Curve (2) is given by $i_a(z) = i_a(0)$, the data in figures 3.6 and 3.7 were analysed using this form of $i_a(z)$. Curve (3) is given by $i_a(z) = i_a(0)\ (1 + \frac{3z}{\lambda})$. This form of $i_a(z)$ may be appropriate to describe the results of Matsudaira (1974) on the ion bombarded iron surface.

Thus it appears that the ratio of the incident beam energy to the energy of the core electron, $\frac{E_p}{E_c}$, can be used to predict the form of $i_a(z)$ within the Auger escape depth. The results are summarised in Table 3.2 for the case when the angle of incidence is $\sim 70^\circ$ from the surface normal.

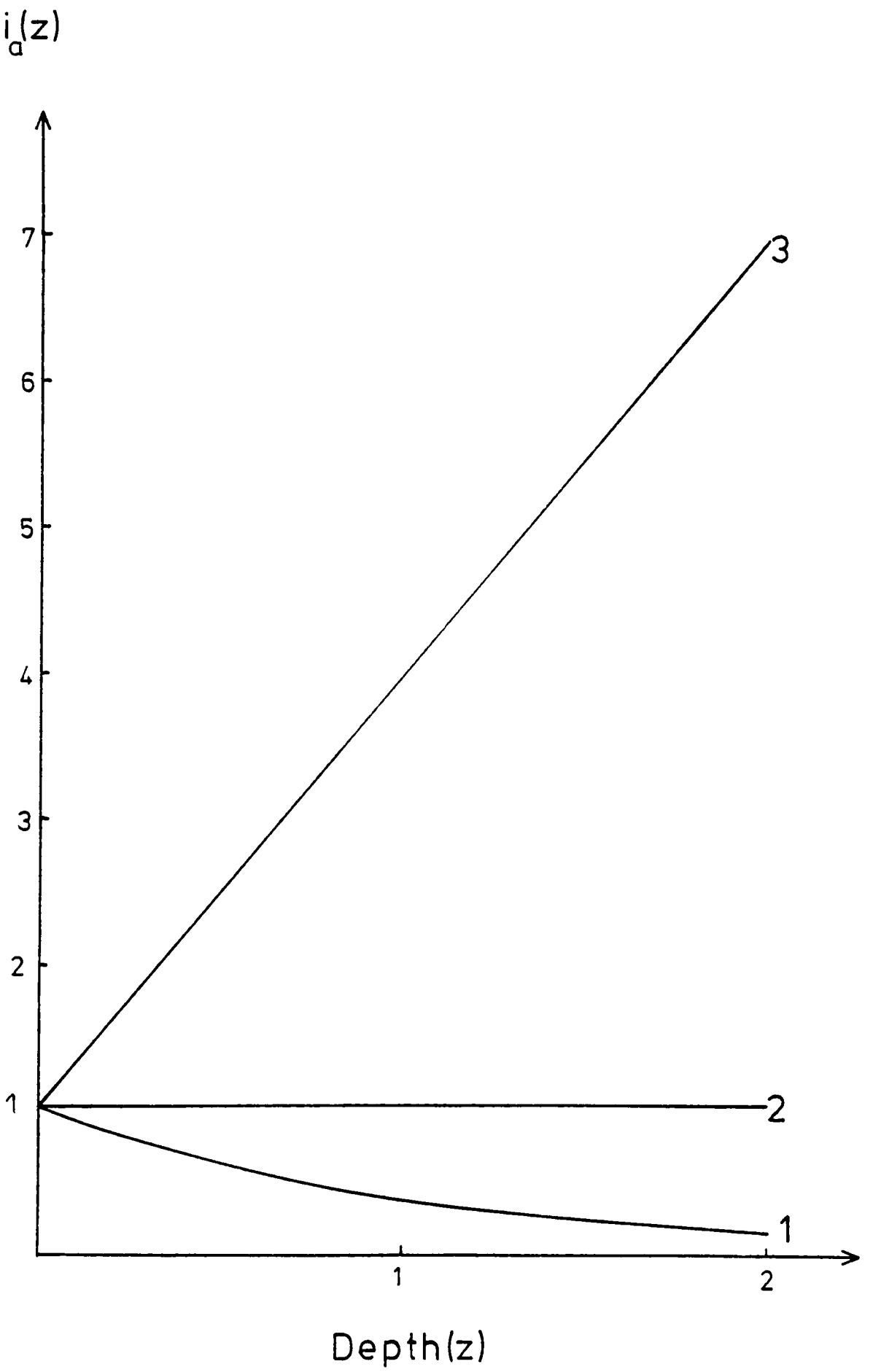


Fig.3.8 The three forms of $i_a(z)$ discussed in text

Table 3.2

$\frac{E_p}{E_c}$	$i_a(z)$
$\frac{E_p}{E_c} \leqslant 2.5$	$i_a(0) \exp -\frac{z}{\lambda_p}$
$2.5 \leqslant \frac{E_p}{E_c} \leqslant 24$	$i_a(0)$
$\frac{E_p}{E_c} \geqslant 37$	$i_a(0)\ (1 + Bz)$

There exists a transition region for $24 \leqslant \frac{E_p}{E_c} \leqslant 37$ where no data are at present available and it is therefore impossible to say where the approximation of constant $i_a(z)$ breaks down at higher energies.

The analysis of these results has relied upon a theory based on an atomically flat surface model. Ion bombardment inevitably damages the surface, as illustrated by the loss of crystallinity, and this may effect the experimental results. However in the case of silicon, Argon ion bombardment has been shown (Bean et.al. (1977)) to produce parallel ledges about 2500Å long and 250Å high with the edges lying at $\sim 60^\circ$ to one another. It therefore seems reasonable to expect the flat surface model to produce valid results except for very high angles of emission of the order of $90^\circ - \tan^{-1}(\frac{250}{2500}) = 84^\circ$ where the emitted Auger electron would interact with neighbouring ledges.

In the following section concerning the Auger angular distributions from overlayers the assumption of constant ionisation rate with depth will be made and the experiments are designed to ensure that this assumption is valid.

3.5. Theory for Non-Crystalline Surfaces with Overlayers Present

The model to be used for the case of an overlayer on a substrate is similar to the clean substrate model and all the assumptions made there are made here. Further assumptions made in this derivation are that $i_a(z)$ is constant with depth and that the overlayer is of even thickness all over the

substrate. A sketch of the situation envisaged is shown in figure 3.9.

Consider now the angular variation of substrate Auger electrons with an overlayer thickness n present. If the Auger current at depth z in the substrate is given by $i_a^s(z)$. (The superscript s refers to the substrate and the origin for z is at the substrate overlayer interface) then the substrate Auger current emerging at angle θ is given by

$$i_a^s(\theta) = \int_0^\infty i_a^s(z) \exp\left(-\frac{z}{\lambda_s^s \cos\theta}\right) \exp\left(-\frac{n}{\lambda_s^o \cos\theta}\right) dz \frac{\Delta\Omega}{4\pi} \quad \text{-----(8)}$$

where λ_s^s is the inelastic mean free path of substrate Auger electrons in the substrate and λ_s^o is the inelastic mean free path of substrate Auger electrons in the overlayer. Letting $i_a^s(z) = i_a^s(0)$ and integrating, $i_a^s(\theta)$ becomes

$$i_a^s(0) \exp\left(-\frac{n}{\lambda_s^o \cos\theta}\right) \lambda_s^s \cos\theta \frac{\Delta\Omega}{4\pi}$$

Therefore the normalised form of $i_a^s(\theta)$ is

$$\frac{i_a^s(\theta)}{i_a^s(0)} = \cos\theta \exp\left[-\frac{n}{\lambda_s^o}(\sec\theta - 1)\right] \quad \text{-----} \quad (9)$$

In equation 8 the total path length of an electron, emitted at depth z, to the surface is given by $\frac{z}{\cos\theta} + \frac{n}{\cos\theta}$ and the attenuation is described in the usual way by an exponential factor. Thus the effect of an overlayer is to modify the cos θ distribution expected from a clean surface by the factor $\exp\left(-\frac{n}{\lambda_s^o}(\sec\theta - 1)\right)$ which describes the extra attenuation in the overlayer. If $\frac{n}{\lambda_s^o} \ll 1$ then $\frac{i_a^s(\theta)}{i_a^s(0)}$ tends towards cos θ as expected.

The angular distribution of the Auger electrons emitted in the overlayer will now be considered. In this case the origin of z is taken at the overlayer / vacuum interface. The Auger current emitted at an angle θ from the surface normal is given by

$$i_a^o(\theta) = \int_0^n i_a^o(z) \exp\left(-\frac{z}{\lambda_o^o \cos\theta}\right) dz \frac{\Delta\Omega}{4\pi} \quad \text{-----} \quad (10)$$

where λ_o^o is the inelastic mean free path of overlayer Auger electrons in the

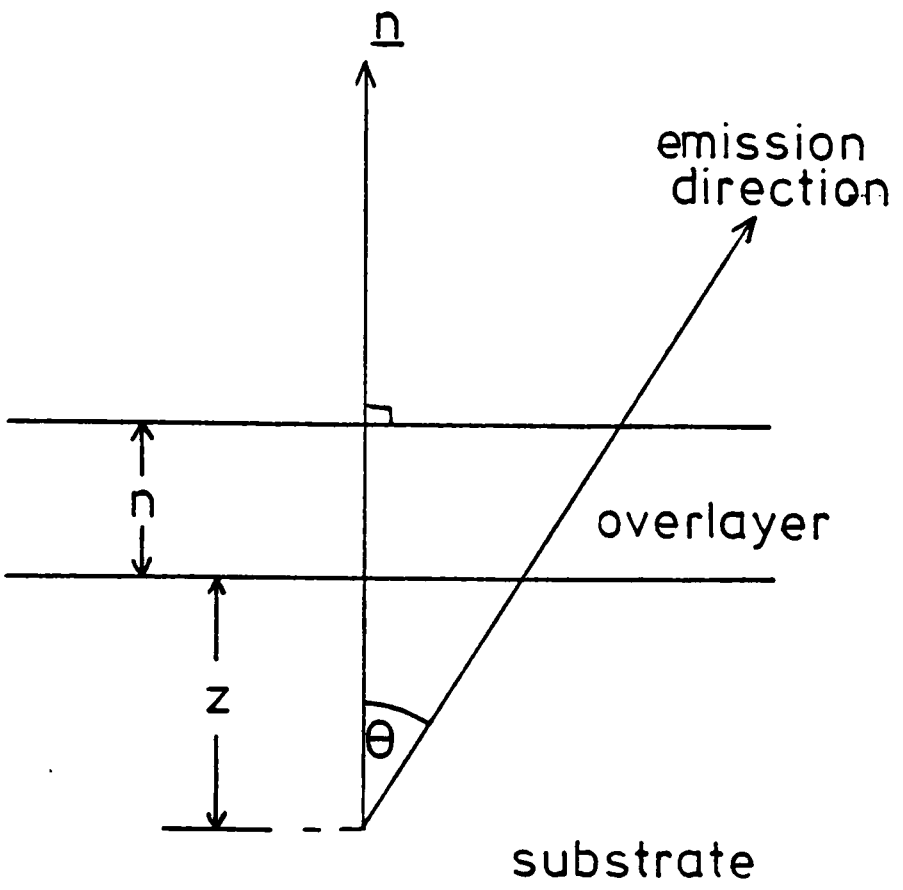


Fig.3.9 The overlayer model

overlayer. Integrating equation (10) and putting $i_a^o(z) = i_a^o(0)$

$$i_a^o(\theta) = i_a^o(0)\ \lambda_o^o\ \cos\theta \left(1 - \exp\left(-\frac{n}{\lambda_o^o \cos\theta}\right)\right) \frac{\Delta\Omega}{4\pi}$$

Therefore the normalised form of $i_a^o(\theta)$ becomes

$$\frac{i_a^o(\theta)}{i_a^o(0)} = \cos\theta \left[\frac{1 - \exp\left(-\frac{n}{\lambda_o^o \cos\theta}\right)}{1 - \exp\left(-\frac{n}{\lambda_o^o}\right)}\right] \quad \text{——} \quad (11)$$

The behaviour of equations 9 and 11 can be see in figure 3.10 where equation 9 has been plotted with $n = 2{\cdot}1\ \lambda_s^o$ as curve (1) and equation 11 has been plotted with $n = 2{\cdot}1\ \lambda_o^o$ as curve (2). If $\lambda_s^o = \lambda_o^o$ then the two curves shown would correspond to the situation where an even layer of thickness $2{\cdot}1\ \lambda_s^o$ was present on a substrate. Curve (2) in this situation is fairly close to cos θ and for larger values of $\frac{n}{\lambda_o^o}$ would become indistinguishable from cos θ. These theoretical predictions will now be used to explain the following results from non crystalline surfaces.

3.6. Experimental

The specimens were prepared as described previously and ion bombarded with 500eV Argon ions at approximately normal incidence. The spectrum shown in figure 3.3 would be typical for such a surface showing an argon peak about 1/32 the size of the silicon LVV peak.

3.7.1. The Angular Distribution of the Argon LMM Auger Electrons from Ion Bombarded Silicon (111)

The first "overlayer" system to be examined was the silicon (111) surface immediately after Argon ion bombardment. The peak to peak height of the major Argon LMM peak, the shape of which is shown in figure 3.11, was plotted as a function of emission angle. A primary beam energy of 1000eV was used and the angle of incidence was 48^o from the surface normal. In this case $\frac{E_p}{E_c} = 3$ and therefore the rate of Auger production should have been constant with depth. The resulting angular distribution is shown in figure 3.12.

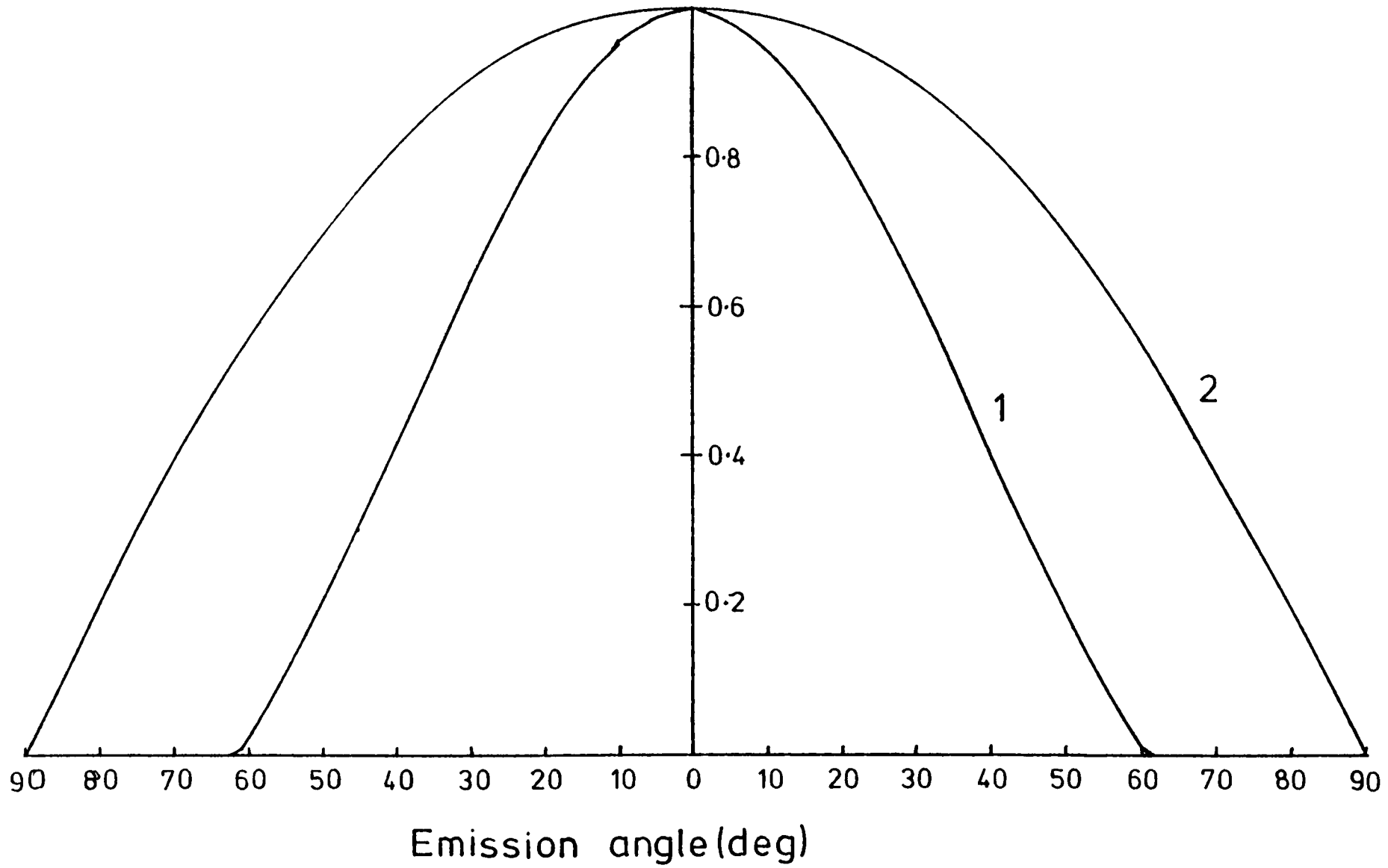


Fig.3.10 Theoretical angular distributions for substrate(1) and overlayer(2) Auger electrons with $n=2.1\lambda_s^o=2.1\lambda_o^o$

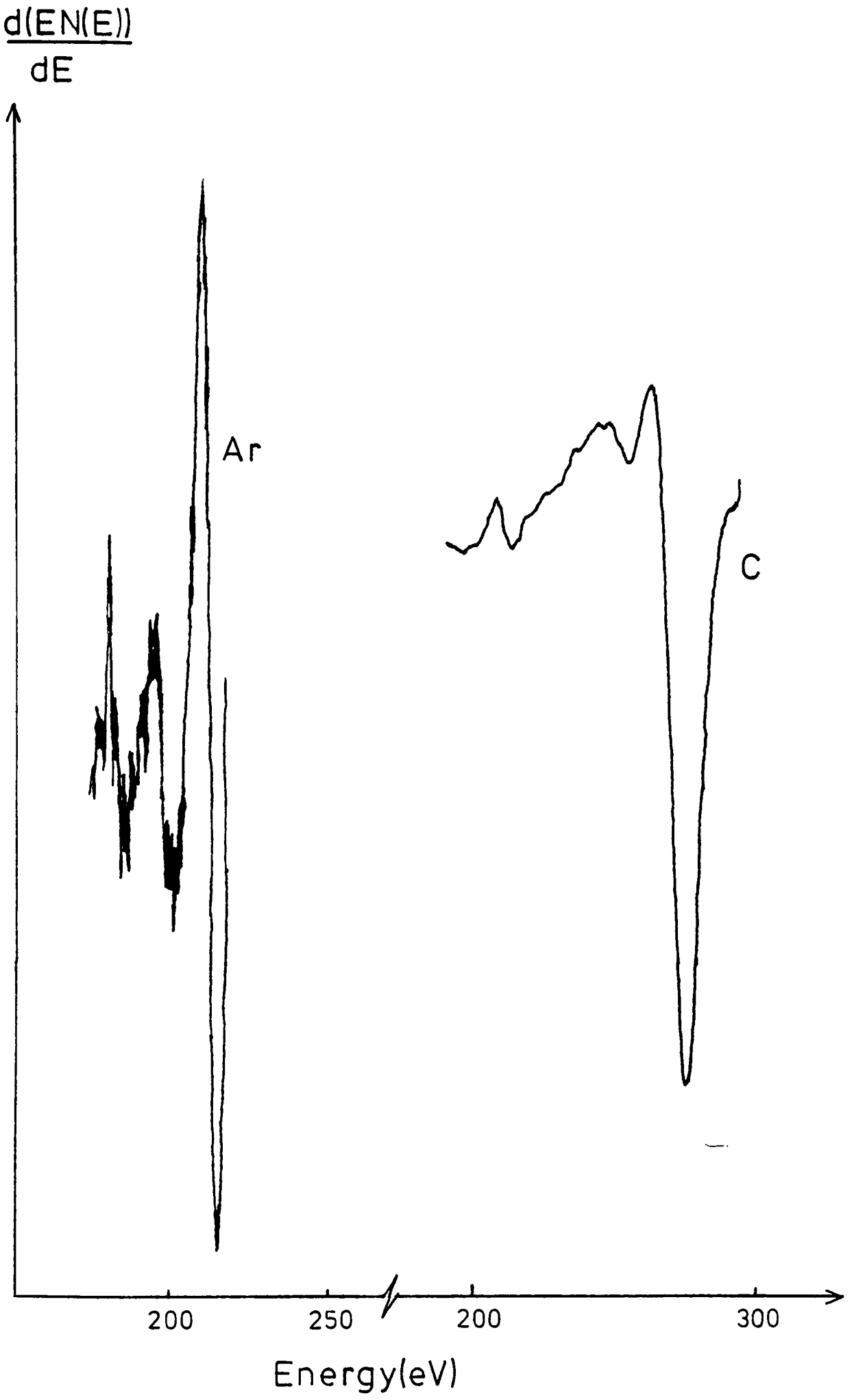


Fig.3.11 The Argon LMM and Carbon KLL line shapes from contaminated,ion bombarded silicon(111) surface

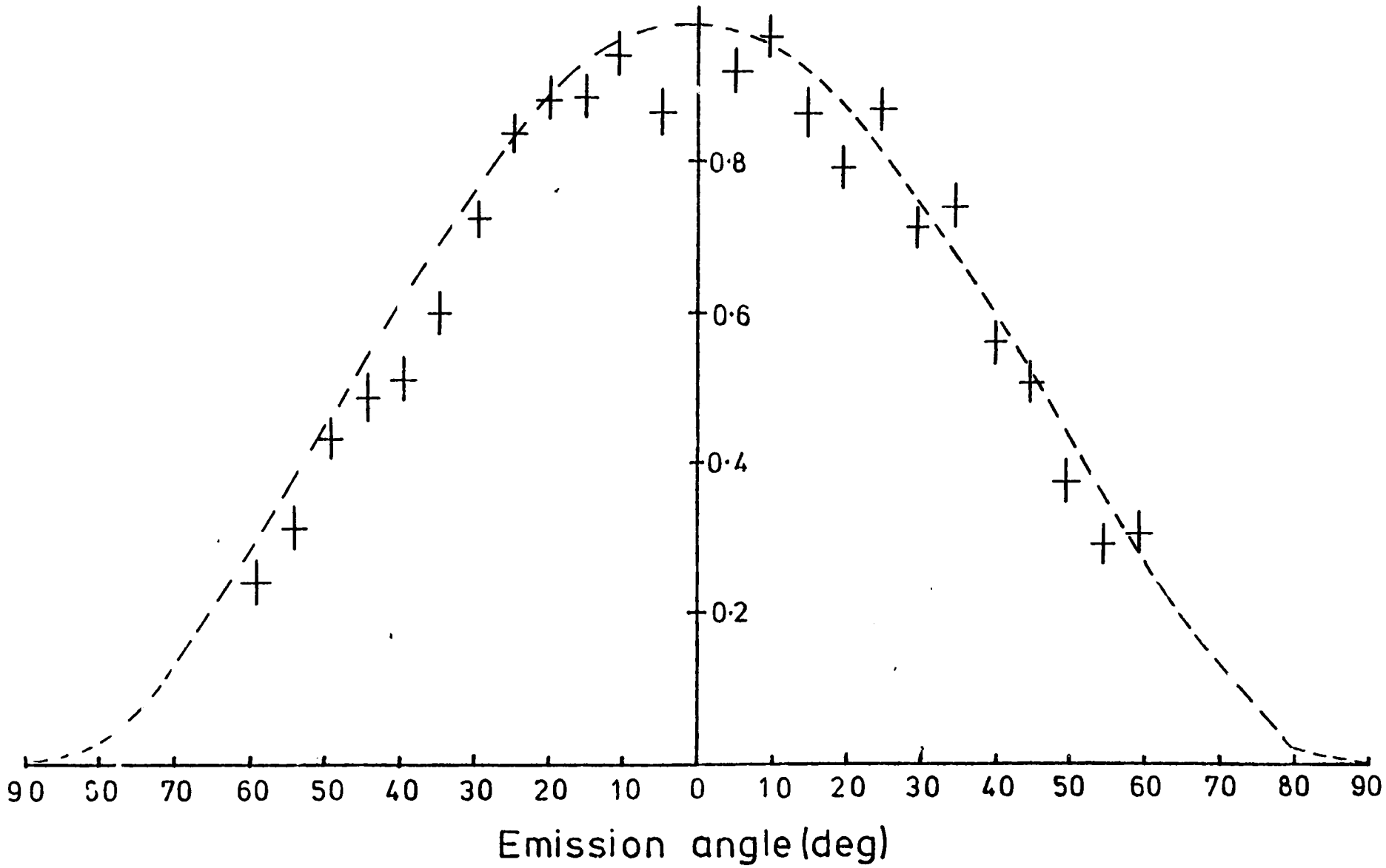


Fig.3.12 Angular distribution of Argon LIII peak from ion bombarded silicon(111) surface
E_p=1000eV, θ_p=42°

The peak to peak heights have been normalised by setting the peak to peak height equal to one at an emission angle of 0^{o}.

The data in this case were not analysed using equations 9 and 11 because it seems inappropriate to think of the abrupt onset of an Argon signal at a certain depth in the crystal. A more appropriate model would be based on equation (2) where

$$i_{Ar}(\theta) = \int_0^{\infty} i_{Ar}(z) \exp\left(-\frac{z}{\lambda_{Ar}\cos\theta}\right) dz \; \frac{\Delta\Omega}{4\pi} \quad \text{---} \quad (12)$$

and $i_{Ar}(\theta)$ is the Argon Auger current emitted at angle θ from the surface normal, $i_{Ar}(z)$ is the Argon Auger current at depth z in the crystal and λ_{Ar} is the inelastic mean free path for Argon Auger electrons. Assuming that the probability of producing an Argon Auger electron per Argon atom is constant with depth then $i_{Ar}(z)$ can be used to describe the number of argon atoms at depth z. Following the same analysis as before for the clean surface and putting $i_{Ar}(z) = i_{Ar}(0)\ (1 + Bz)$ in equation (12) results in an angular distribution described by

$$\frac{i_{Ar}(\theta)}{i_{Ar}(0)} = \frac{\cos\theta + B\lambda_{Ar}\cos^2\theta}{1 + B\lambda_{Ar}} \quad \text{---} \quad (13)$$

The dotted curve in figure 3.12 is given by putting $B = \frac{4}{\lambda_{Ar}}$ in equation (13).

This curve is in fact indistinguishable from $\cos^2\theta$ at the signal to noise levels present in these spectra so in fact $\frac{4}{\lambda_{Ar}}$ is a lower limit on B, ie $B \geqslant \frac{4}{\lambda_{Ar}}$. The inelastic mean free path of Argon Auger electrons at $\sim$ 215eV can be obtained from Seah and Dench (1978) where $\lambda_{Ar} = 8\text{Å}$ this implies that $B \geqslant \frac{1}{2}\ \text{Å}^{-1}$. Therefore the Argon atom concentration is proportional to

$$i_{Ar}(z) = i_{Ar}(0)\ (1 + \tfrac{z}{2}) \quad \text{---} \quad (14)$$

where z is measured in Angstroms. It is important to note here that this model will only apply to the first $\sim 20\text{Å}$ of the surface and that the overall depth distribution of the Argon atoms will extend to perhaps as far as 500Å (Bean et.al. (1977)) with a maximum Argon concentration occuring somewhere

in between.

The effect of this type of concentration profile on quantitative Auger spectroscopy can be profound for a number of reasons. In general it might not at first sight be apparent that the concentration gradient exist at all and therefore the assumption will be made that the species in question is evenly distributed within the escape depth of the Auger electrons, thus leading to an underestimate of the concentration. In the case where a CMA is used with a takeoff angle of $\sim 46^{o}$ the signal actually observed at this angle will be lower by a factor of $\frac{\cos^2 46^{o}}{\cos 46^{o}} = 0{\cdot}7$ than in the case where the concentration is constant with depth.

In the case considered here where $i_{Ar}(z) = i_{Ar}(0)\left(1 + \frac{4z}{\lambda_{Ar}}\right)$ it is possible to calculate the underestimate of the Argon content, within $2\lambda_{Ar}$ of the surface, that would arise if the signal measured parallel to the surface normal were taken as resulting from Argon evenly distributed within the surface layer. The situation envisaged is shown in figure 3.13. Only about 14% of any Auger electrons created at a depth greater than $2\lambda_{Ar}$ will reach the surface and therefore the model used here should be relatively insensitive to what happens to the Argon concentration below this depth. A given number of Argon atoms existing between the surface and the depth $2\lambda_{Ar}$ can be distributed with a concentration per unit area at depth z of

$$n_{Ar}(z) = n_{Ar}(0)\left(1 + \frac{4z}{\lambda_{Ar}}\right) \quad \text{---- (15)}$$

$$\text{or} \quad n_{Ar}(z) = 5n_{Ar}(0) \quad \text{----- (16)}$$

These concentration gradients will in turn give rise to an Argon Auger current emerging parallel to the surface normal proprtional to respectively

$$\int_0^{2\lambda_{Ar}} n_{Ar}(0)\left(1 + \frac{4z}{\lambda_{Ar}}\right) \exp\left(-\frac{z}{\lambda_{Ar}}\right) dz \quad \text{------ (17)}$$

$$\text{and} \quad \int_0^{2\lambda_{Ar}} 5n_{Ar}(0) \exp\left(-\frac{z}{\lambda_{Ar}}\right) dz \quad \text{------ (18)}$$

Equation (17) gives a value of $3{\cdot}2\, n_{Ar}(0)\, \lambda_{Ar}$ and equation (18) gives a value of $4{\cdot}3\, n_{Ar}(0)\, \lambda_{Ar}$ for the Argon signals. Thus the Argon Auger

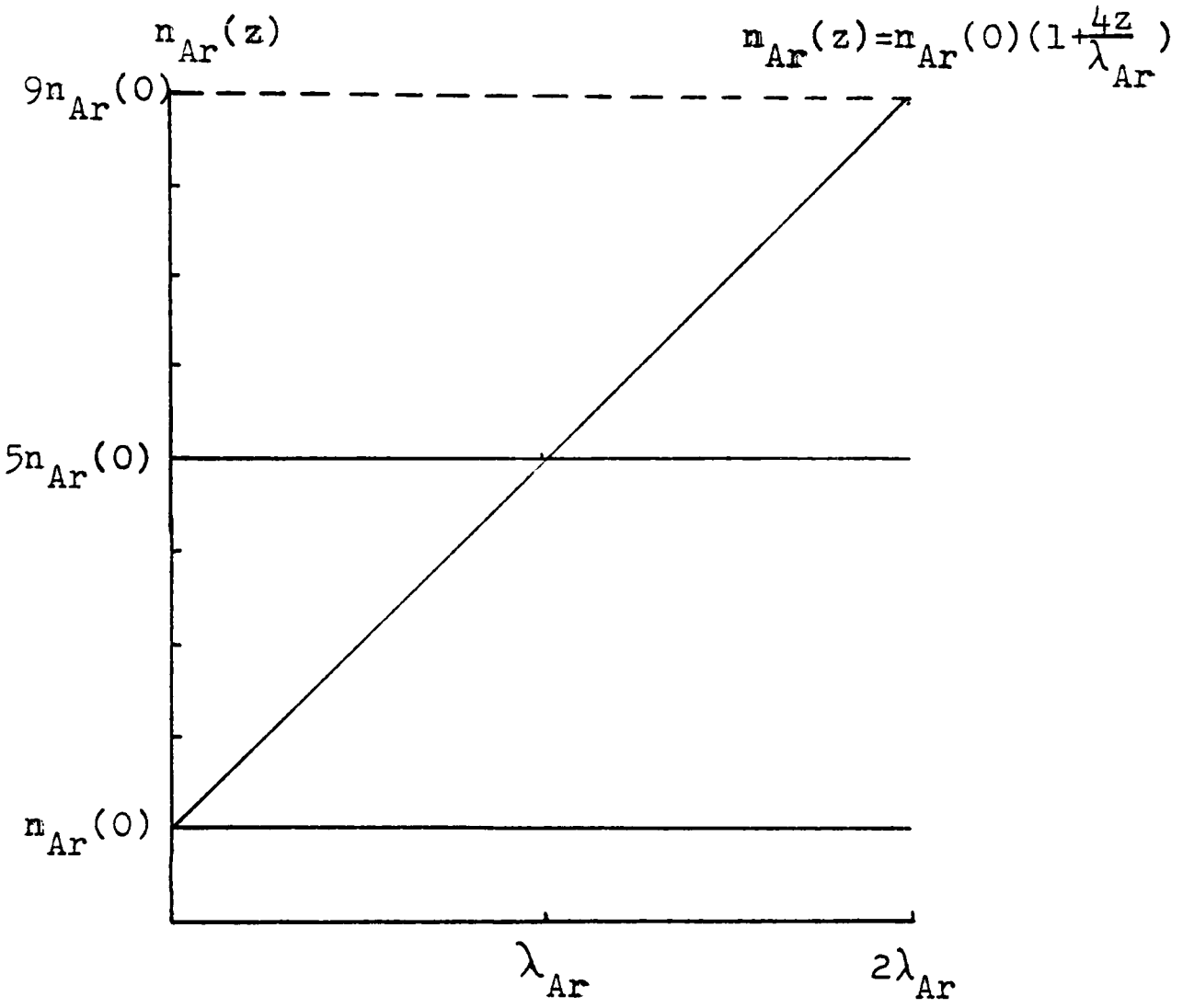


Fig.3.13 Two possible depth distributions of a given number of Argon atoms

signal arising from atoms distributed in the way described by equation (15) will be about 0·7 $\frac{3\cdot2\, n_{Ar}(0)\,\lambda_{Ar}}{4\cdot3\, n_{Ar}(0)\,\lambda_{Ar}}$ of the signal from the same number of argon atoms distributed in the way described by equation 16. This implies that an underestimate of 30% would be made in the Argon concentration for this system if the depth distribution were not accounted for. Furthermore if the popular CMA were used to measure the intensities then the underestimates would be about 50% for this particular system.

3.7.2. The Angular Distributions of the Silicon LVV, the Argon LMM and the Carbon KLL Auger Electrons from Ion Bombarded Silicon (111)

An Argon ion bombarded silicon (111) surface prepared in the same way as the one just discussed was left in the vacuum chamber for about 3 days until some carbon contamination was observed. Using a primary beam energy of 1500eV at 48° from the surface normal and detecting the signals in the differential mode the Argon LMM peak to peak height was found to be about γ_{43} of the silicon LVV peak to peak height and the carbon KLL peak to peak height was about γ_{68} of the silicon LVV peak to peak height. Typical lineshapes of the Argon and carbon peaks are shown in figure 3.11.

The angular distribution of the carbon KLL transition is shown in figure 3.14. The incident beam conditions were Ep= 1500eV and the angle of incidence was 48° again ensuring that the rate of ionisation of carbon atoms with depth would be constant. The outer curve of figure 3.14 was generated by putting $n = 0\cdot6\,\lambda_o^o$ in equation (11) and the inner curve was generated by putting $n = 1\cdot1\,\lambda_o^o$ in equation (11). A value for λ_o^o -(the inelastic mean free path for carbon Auger electrons at 272eV), can be found from Seah and Dench (1978) to be ~9Å and therefore n, the overlayer thickness must lie in the range $5\cdot4\text{Å} \leqslant n \leqslant 10\text{Å}$. Taking the carbon atomic radius as 0·7Å this implies a carbon overlayer containing about 5 or 6 monolayers.

According to the theory leading to equation (9) the substrate Auger

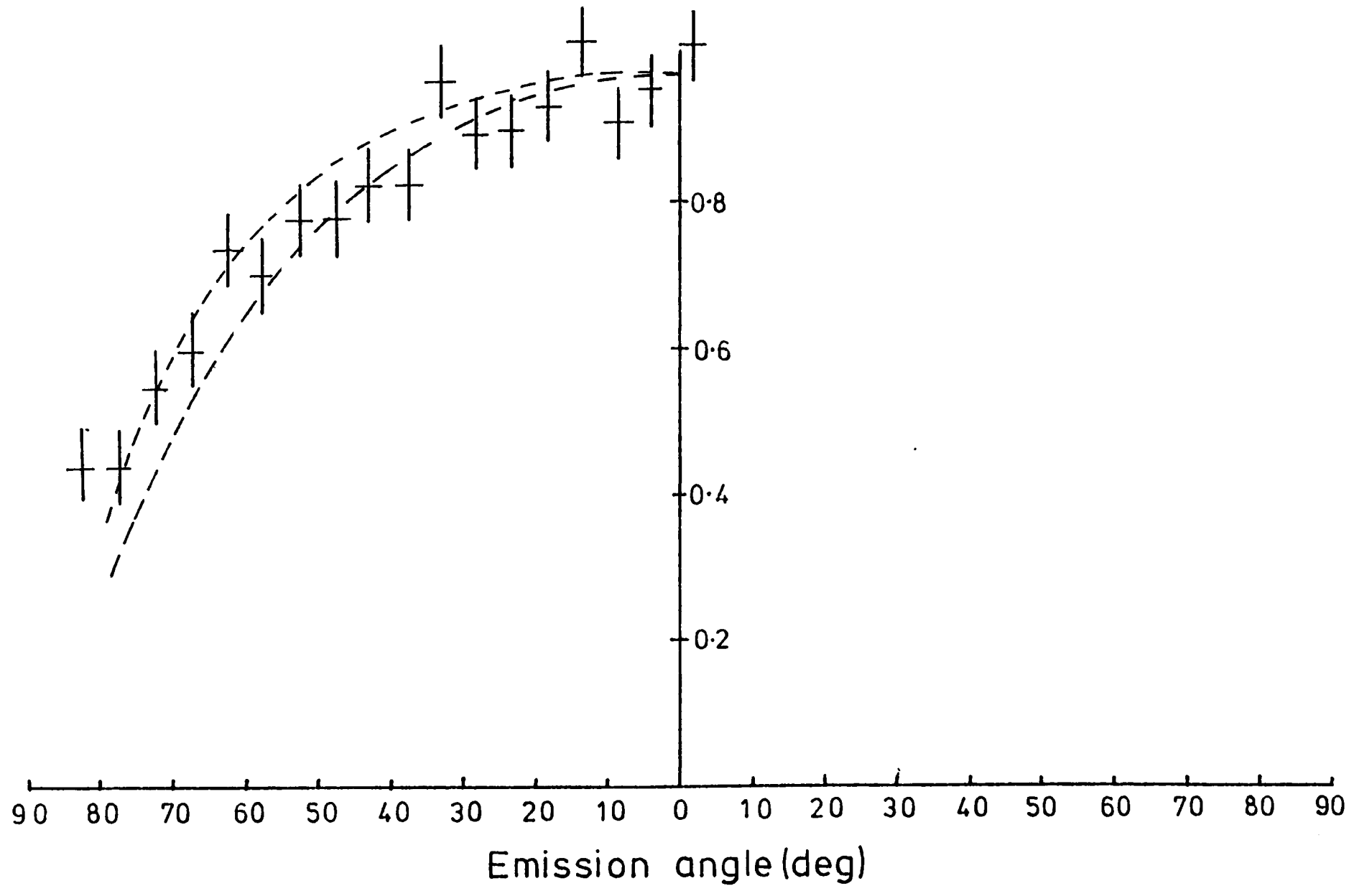


Fig.3.14 Angular distribution of Carbon KLL signal from ion bombarded silicon(lll) surface
E_p=1500eV, θ_p=48°

angular distribution ought to be modified in the presence of an overlayer. In this case, with an overlayer of $8 \pm 2\text{Å}$, equation (9) describing the substrate angular distribution becomes

$$\frac{i_a^s(\theta)}{i_a^s(0)} = \cos\theta \exp\left(-\frac{8}{\lambda_s^o}(\sec\theta - 1)\right) \quad \text{---} \quad (19)$$

λ_s^o for the silicon LVV transition at 92eV can be found from Seah and Dench (1978) to be $\sim 5{\cdot}5\text{Å}$ leading to a value of $\frac{n}{\lambda_s^o} = 1{\cdot}4$.

The angular distribution of the silicon LVV transition from this system is shown in figures 3.15. As can be seen the data points are very close to cosθ. The lower dotted curve is given by putting $\frac{n}{\lambda_s^o} = 0{\cdot}6$ in equation (9) implying an overlayer thickness of only $\sim 3\text{Å}$. The value of n derived from the carbon angular distribution leading to $\frac{n}{\lambda_s^o} = 1{\cdot}4$ would give a much narrower distribution for the silicon LVV angular distribution than the one shown for $\frac{n}{\lambda_s^o} = 0{\cdot}6$. Thus it is clear that an even overlayer of carbon 8Å thick is incompatible with the substrate results.

To try and confirm that the behaviour of the silicon substrate emission was not in some way anomalous the Argon LMM angular distribution from the substrate was measured and is shown in figure 3.16. Within the noise levels present this angular distribution is the same as the Argon angular distribution recorded in figure 3.12 from the amorphous surface with no carbon overlayer present. The dotted curve in figure 3.16 is given by $\cos^2\theta$ but as mentioned earlier this is indistinguishable from equation (13) with $\frac{B}{\lambda_{Ar}} = 4$ with the noise levels present. Thus it seems that the substrate angular distributions are unaffected by the presence of the carbon overlayers in the system.

A rough estimate of the carbon concentration can be obtained by applying the formulae given in Palmberg et.al. (1972) that is

$$C_c = \frac{I_c}{S_{c,Ag}} \quad \frac{1}{\sum_a \frac{Ia}{S_{a,Ag}}} \quad \text{---} \quad (20)$$

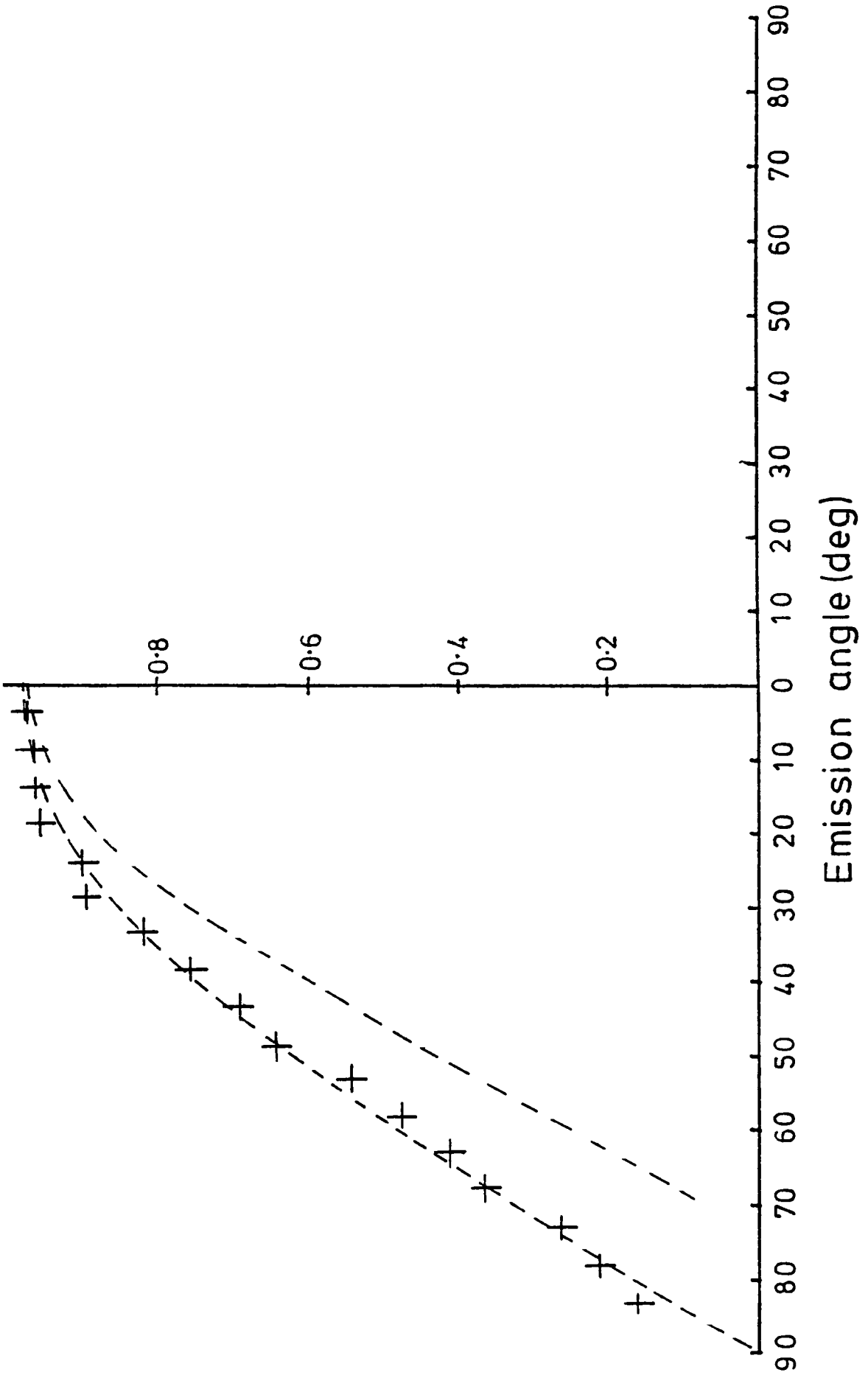


Fig.3.15 Angular distribution of Silicon LVV signal from ion bombarded silicon(111) surface with carbon contamination present. E_p=1500eV, θ_p=48°

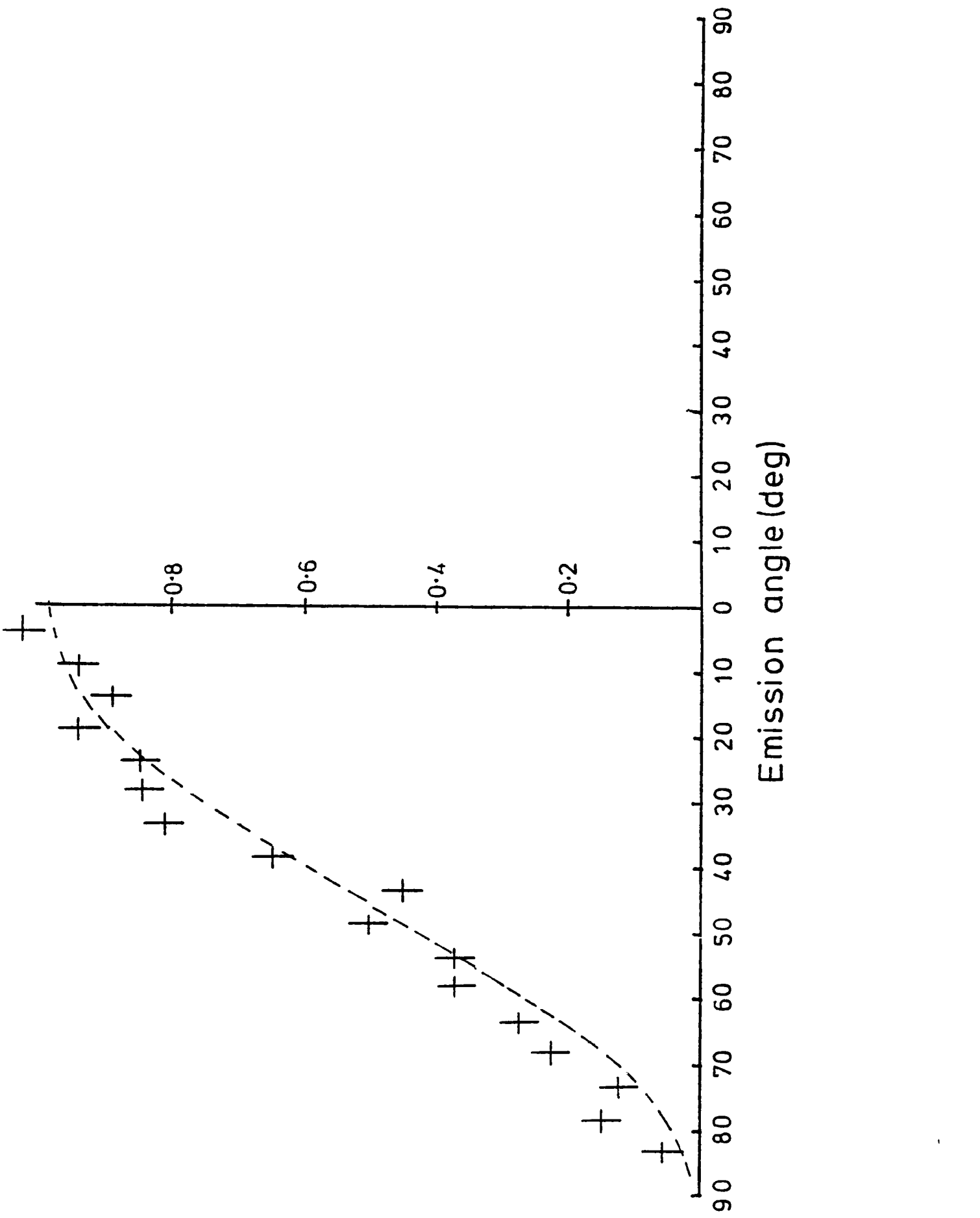


Fig.3.16 Angular distribution of Argon LMM signal from ion bombarded silicon(111) surface with carbon contamination present. E_p=1500eV, θ_p=48°

where :- C_c - is the atomic concentration of carbon

I_c - the peak to peak height of the C transition

$S_{c,Ag}$ - the relative sensitivity of carbon to silver

(to be found in Palmberg et.al. (1972))

The summation over a is over all the element involved in the spectrum, in this case silicon, argon and carbon. Unfortunately it is impossible to obtain a value for $S_{Ar,Ag}$ from the handbook (Palmberg et.al. (1972)) and therefore the argon contribution in the summation will be ignored on the following grounds. The silicon LVV peak dominates the summation and ignoring the Argon contribution will introduce an error in the summation of $\sim 3\%$

From the handbook $S_{c,Ag} = 0{\cdot}1$

and $S_{Si,Ag} = 0{\cdot}5$

Therefore the concentration of carbon can be estimated as

$$C_c = \frac{3{\cdot}7}{0{\cdot}1} \times \frac{1}{\frac{25{\cdot}4}{0{\cdot}5} + \frac{3{\cdot}7}{0{\cdot}1}}$$

$$= 0{\cdot}07$$

Care must be taken in interpreting this concentration figure Equation 20 is based on the idea that

$$C_c = \frac{I_c}{I_c^b} \quad \text{——} \quad (21)$$

where I_c is the carbon Auger signal measured in the specimen and I_c^b is the carbon signal measured from a bulk standard under identical conditions. This assumes that all the electron scattering properties of the sample are identical to those of the standard. Thus the figure of $C_c = 0{\cdot}07$ means that only 7% of the carbon atoms present in a sample of both carbon are present in the silicon sample observed here and therefore the next assumption is that this figure of 7% can be applied to the case of carbon in silicon. In other words for every 100 atoms in the sample observed here 7 are carbon atoms.

For this particular system however this figure of 7 at.% of carbon in silicon is rather meaningless in view of the evidence presented to indicate

that the carbon is present only on the surface of the silicon. It is therefore necessary to relate the carbon Auger signal observed to a concentration expressed in terms of monolayers to rather than atomic percent in the bulk. This can be done as follows.

The top monolayer of a homogeneous sample would give a signal corresponding to 7% of a monolayer (assuming one carbon atom fills the site of one missing silicon atom). The next monolayer down would give a carbon Auger signal corresponding to 7% x $\exp -\frac{z_2}{\lambda_c}$ of a surface monolayer, and so on through the sample. (z_2 is the depth of the second monolayer from the surface and λ_c is the inelastic mean free path of carbon Auger electrons). Therefore taking Is % as the percentage of a monolayer that would give the observed Auger signal the following equation can be written.

$$I_s\,\% = \sum_{n=1} 7 \exp\left(-\frac{nz_n}{\lambda_c}\right) \%$$

where n refers to the layer number and z_n is the depth of layer n.

Writing this as an integral gives

$$I_s\,\% = \int_0^\infty 7 \exp\left(-\frac{z}{\lambda_c^m}\right) dz\,\% \quad \text{---} \quad (22)$$

$$= 7\,\lambda_c^m\,\%$$

λ_c^m - carbon inelastic mean free path in monolayers and from Seah and Dench (1978) $\lambda_c^m = 3{\cdot}7$ monolayers therefore $I_s\% = 26\%$ of a monolayer. Thus under the assumption that the carbon is in monolayer form there would be 26% of a monolayer present.

However the angle resolved spectra from the carbon on silicon indicated that the carbon overlayer was about 5 or 6 monolayers thick whereas the intensity data indicate only 26% of a monolayer of carbon on the surface. These results and the fact that the substrate Auger emissions are unaffected by the carbon overlayer suggest that the silicon surface has about 10% or less of its surface covered by carbon islands about 5 or 6 monolayers thick. This would explain the absence of overlayer effects on the substrate Auger

angular distributions since 90% of the substrate emissions in fact arise from areas uncovered by carbon.

So far only the quantity and physical whereabouts of the carbon on the amorphous silicon has been discussed. However a certain amount of chemical information can also be obtained from Auger spectroscopy. In particular the Auger lineshapes from carbon in graphite, diamond, silicon carbide and molybdenum carbide have been examined in detail by Haas et.al. (1972). Comparing the lineshape shown in figure 3.11 with those of Haas et. al. it appears that the carbon lineshape shown here is in fact a mixture of the silicon carbide and graphite lineshapes shown by Haas et.al. (1972). The presence of the graphite type lineshape is what would generally be expected from carbon contamination in vacuum (Chattarji (1976) p.210). Silicon carbide can be formed from carbon on the surface of silicon by heating the silicon to between 800°C and 1100°C (Henderson et.al. (1971)) and this would seem the most likely origin of the silicon carbide Auger lineshape, as heating was generally the method used to clean the silicon surface prior to ion bombardment.

The results of this section can now be summarised. The angular distribution of the carbon Auger signal was interpreted to indicate the presence of a carbon overlayer some 5 monolayers thick. The discontinuity of this overlayer was inferred from the fact that the substrate Auger angular distributions were characteristic of a clean surface and also that an intensity analysis of the Auger intensities showed that 90% of the silicon surface was uncovered by carbon. The combination of these results seems to indicate that the carbon was present in islands about 5 monolayers thick covering about 10% of the silicon surface. In addition the chemical form of the carbon was shown to be a mixture of silicon carbide and graphite.

3.8.1. The Oxidised silicon surface

3.8.2. Experimental

The silicon (111) specimen was prepared as before by heating in vacuum followed by Argon ion bombardment. The Auger spectrum shown in figure 3.3 would again be typical. The oxidation was carried out in a manner similar to that described by Oertel and Weber (1977). The specimen was heated by electron bombardment to $\sim 700^{o}C$ and oxygen (BOC grade X) was admitted via a leak valve to a pressure of $\sim 10^{-4}$ torr, after having valved off all the vacuum pumps. The temperature in fact was only an estimate as the lower limit on the optical pyrometer used was $800^{o}C$ therefore the specimen temperature was set just less than $800^{o}C$. After about 40 minutes the heating current was switched off and then the oxygen was pumped out. An Auger spectrum recorded from this surface, at an emission angle of 0^{o} using a primary beam energy of 1000eV at 24^{o} to the surface normal, is shown in figure 3.17. The presence of the relatively large carbon peak in the spectrum of figure 3.17 is surprising in view of the fact that the carbon to silicon peak heights were in the ratio of 1 : 100 before the oxidation took place. It therefore seems that the carbon must have been introduced during the oxidation process while all the system pumps were valved off from the specimen chamber. A gas analysis during oxidation would have helped to confirm this suggestion but unfortunately the pressure of 10^{-4} is too high to allow the use of the Q7b mass spectrometer.

As it takes about one hour to build up angular profile for the signals shown in figure 3.17 it is necessary to ensure that the various signals involved will remain stable during the experiment. Following the treatment just described two sources of signal instability arise. Firstly the oxygen poisons the cathode of the electron gun and it takes about an hour of continuous running to stabilise the emission again. The second source of instability arises because of electron beam induced decomposition of the SiO_2 (Thomas (1974)) and subsequent desorption of oxygen. However the results in Thomas (1974) shows that after a certain electron irradiation time an equilibrium

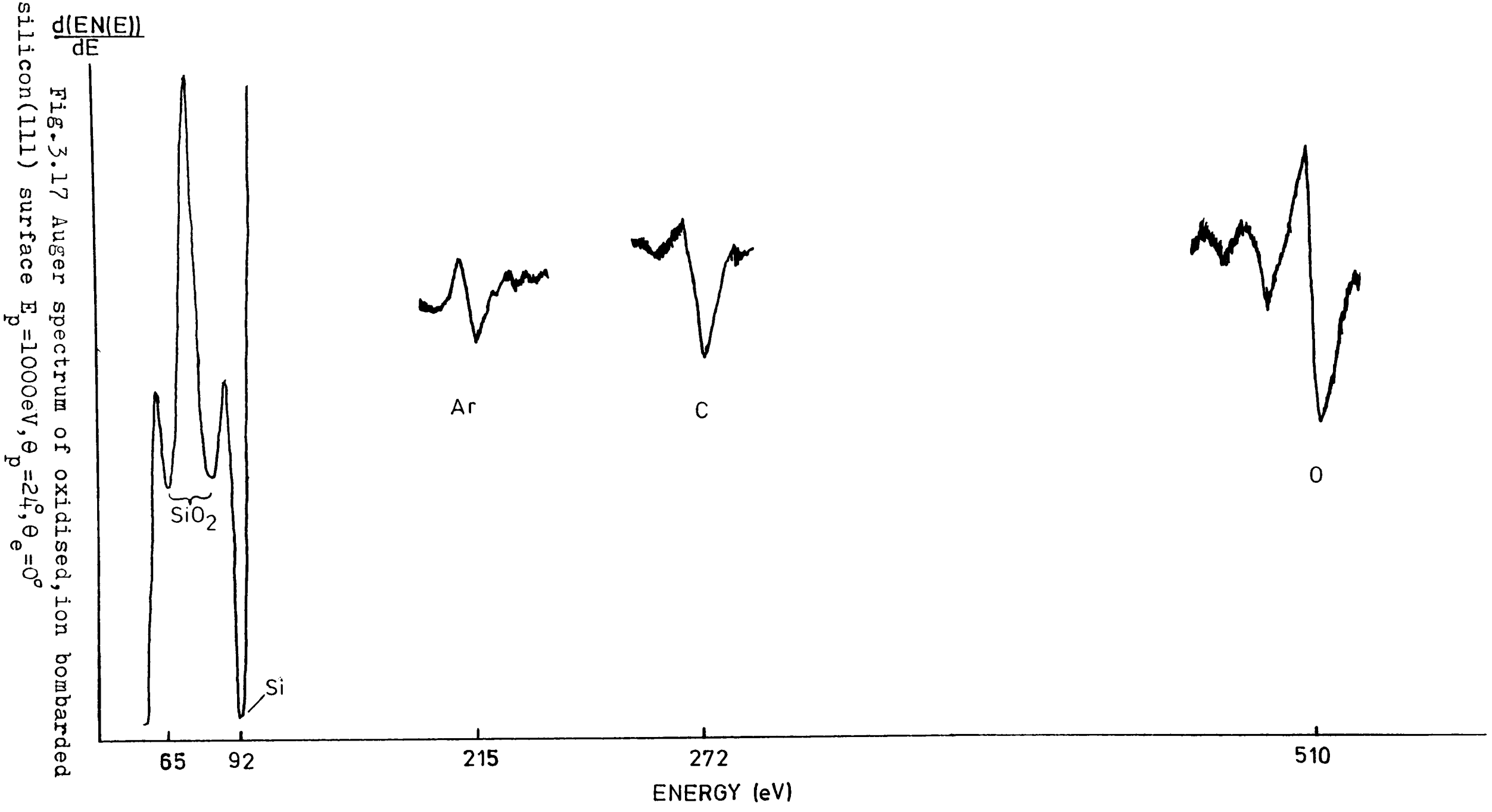


Fig.3.17 Auger spectrum of oxidised, ion bombarded silicon(111) surface E_p=1000eV, θ_p=24°, θ_e=0°

value of the SiO_2 signal at 76eV and the elemental Si signal at 92eV can be reached. To find this equilibrium value spectra of the type shown in figure 3.17 were recorded at ~10 minute intervals with the 1000eV ~1μA electron beam being left on all the time. After about 80 minutes the signals appeared to be stable with time and during this time the 92eV peak had increased by about 10% relative to the peak at 76eV. To reduce the time required to collect the data the Argon signal at 215eV was not recorded as a function of emission angle. The angular distributions of the other signals were obtained by recording spectra of the type shown in figure 3.17 at 5^o or 10^o intervals in emission angle.

3.8.3. Results from Oxidised Silicon Surface

The angular distributions of the SiO_2 peak at 76eV and the elemental Si peak at 92eV are shown in figure 3.18. The intensities were taken as being proportional to the peak to peak heights in the differential spectrum. Both sets of peaks are normalised to equal one at an emission angle of 0^o. The outside dotted line is generated from equation (11), describing overlayer angular distributions, with $\frac{n}{\lambda_8} = 1{\cdot}1$, the middle dotted line is generated from equation (9), describing substrate angular distribution, with $\frac{n}{\lambda_s^o} = 0{\cdot}6$ and the bottom dotted curve is generated from equation 9 with $\frac{n}{\lambda_s^o} = 1{\cdot}1$. The upper data points are from the 76eV signal and the lower ones from the 92eV signal. Figure 3.19 shows the oxygen 510eV signal plotted as a function of emission angle, the dotted curve is from equation (11) with $\frac{n}{\lambda_o^o} = 1{\cdot}1$. The carbon KLL peak is plotted as a function of emission angle in figure 3.20. The dotted curve derived from equation (11) with $\frac{n}{\lambda_o^o} = 1{\cdot}6$ is shown for comparison.

3.8.4. Discussion

In general terms it is immediately obvious from the data of figure 3.18 that the SiO_2 signal at 76eV originates in a layer on top of elemental silicon

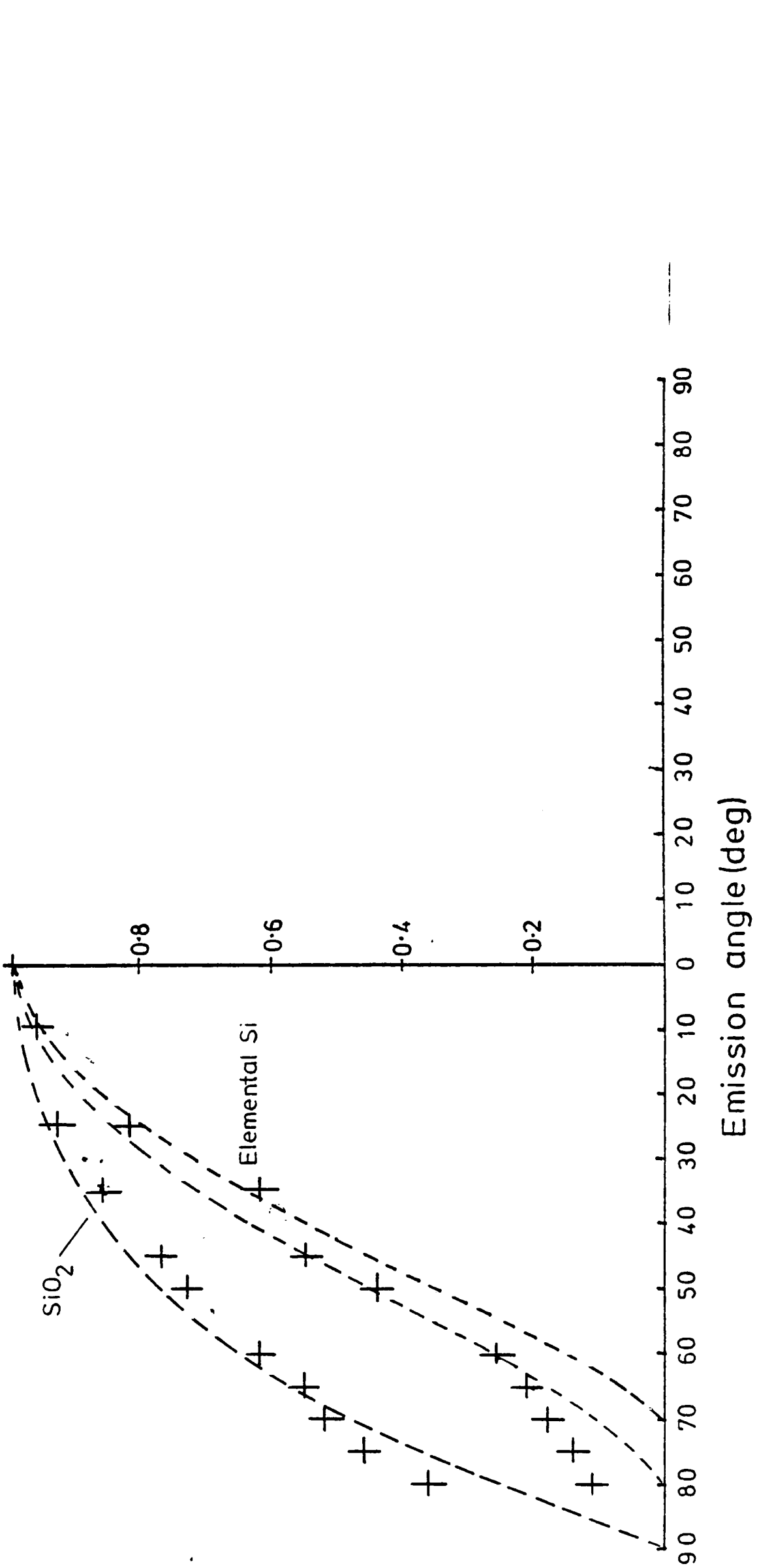


Fig.3.18 Angular distribution of elemental silicon signal at 92eV and chemically shifted silicon signal at 76eV. E_p=1000eV, θ_p=24°

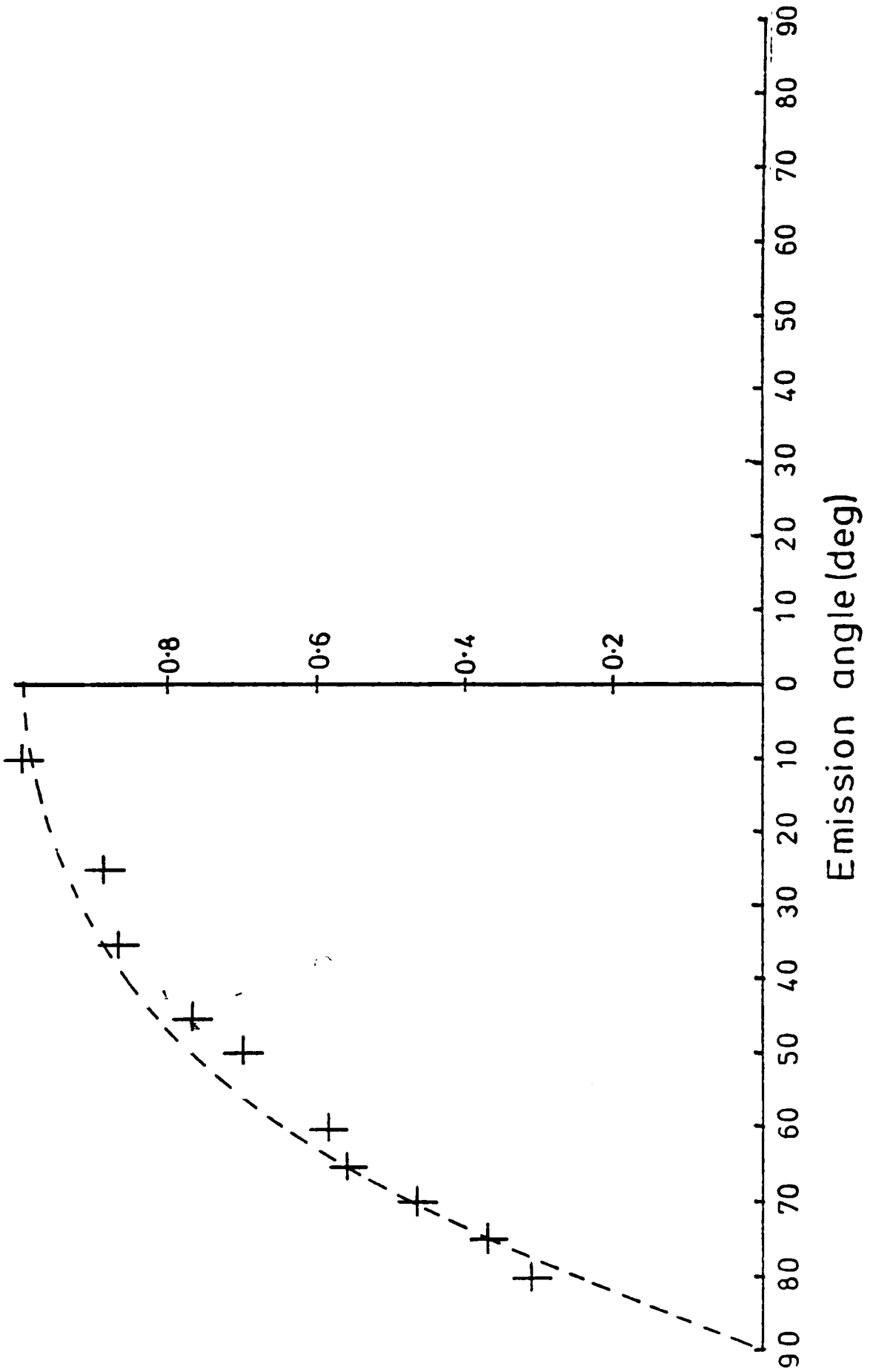


Fig.3.19 Angular distribution of oxygen 510eV signal from oxidised silicon. E_p=1000eV, θ_p=24°

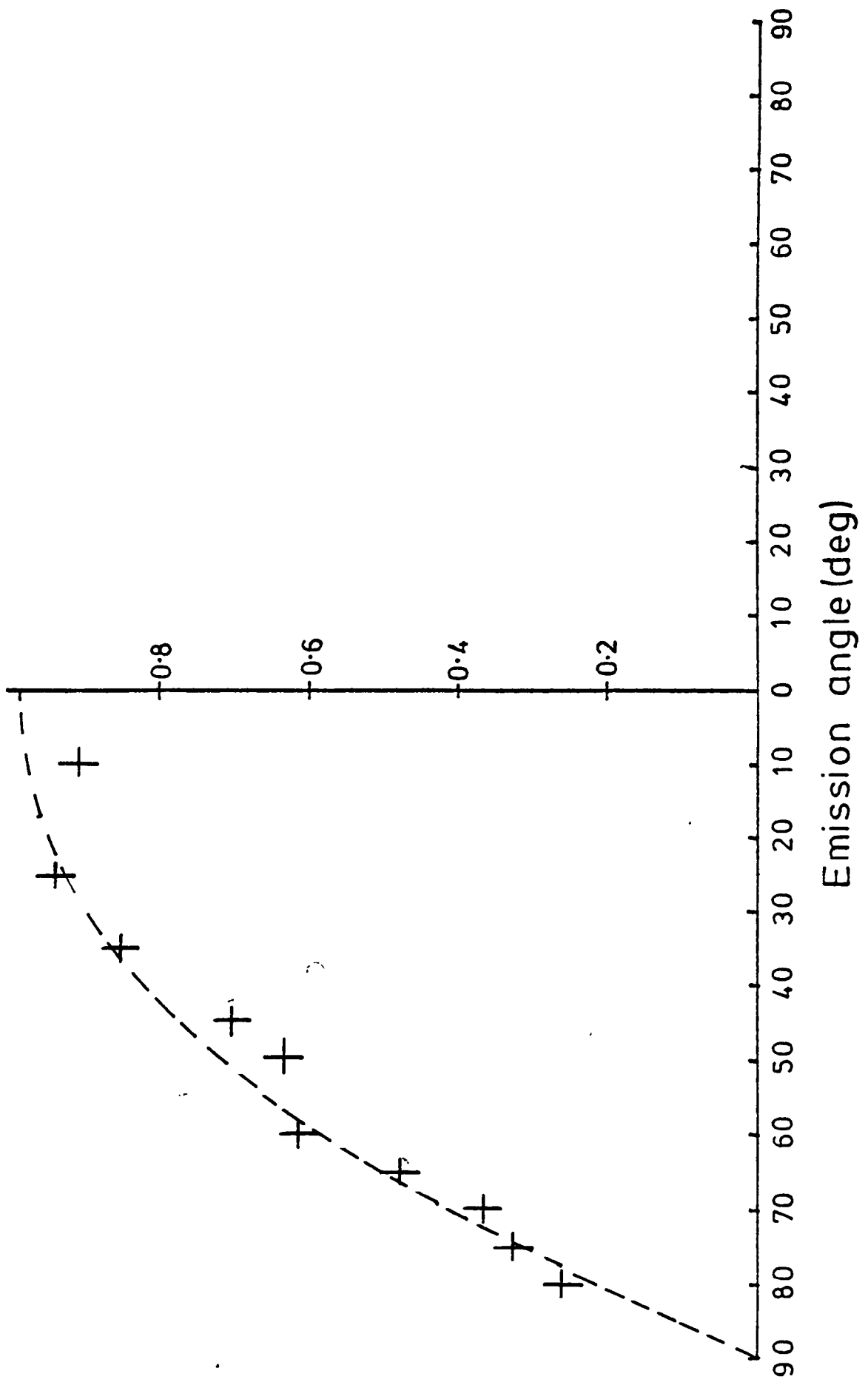


Fig.3.20 Angular distribution of carbon 272eV signal from oxidised silicon. E_p=1000eV, θ_p=24°

however a detailed comparison of the thoery with experiment leads to some problems of interpretation. The inelastic mean free paths of the 76eV electrons in the overlayer (λ_o^o), and of the 92eV electrons in the overlayer (λ_s^o) can be taken as being equal within the experimental error. Therefore the factor $\frac{n}{\lambda_s^o}$ appearing in equation 9 should be exactly equal since n is merely a measure of the overlayer thickness. This being so the top and bottom dotted curves in figure 3.18 ought to describe respectively the angular distributions of the overlayer and substrate Auger emissions with $\frac{n}{\lambda_s^o} = 1{\cdot}1 = \frac{n}{\lambda_o^o}$. The upper set of data points describing the overlayer emission are described reasonably well by the upper dotted curve but the angular distribution of 76eV substrate emission is less well described by the bottom curve. A slightly better fit to the angular distribution of the 76eV substrate emission may be obtained by putting $\frac{n}{\lambda_s^o} = 0{\cdot}6$ as shown by the middle dotted curve however the resulting inequality of $\frac{n}{\lambda_s^o}$ and $\frac{n}{\lambda_o^o}$ is rather unsatisfactory. It would probably be possible to obtain reasonable agreement with the angular distributions of both the substrate and overlayer Auger emissions by using an intermediate value of $\frac{n}{\lambda_s^o}$ and $\frac{n}{\lambda_o^o}$. However another possibility seems worth considering at this point.

It can be seen that for angles of emission greater than $\sim 65^o$ the intensity of the substrate emission starts to diverge rather markedly from either theoretical curve implying that the some reason the signal from elemental silicon at 92eV is not being attenuated as much as it should when travelling through a surface oxide layer of $\sim 10\text{Å}$ thick at an angle of more than $\sim 65^o$. It was mentioned earlier that before these angular experiments were performed the electron beam was left on the surface for about 80 minutes in which time the 92eV signal from elemental silicon increased by about 10% relative to the 76eV signal from SiO_2 indicating that somewhere in the overlayer elemental silicon was being reformed from the oxide. If this 10% increase in the number of elemental silicon atoms present were to occur primarily at the top of the oxide layer then at high angles of emission the

Auger signal from these surface silicon atoms would still be relatively strong and could account for the divergence of the elemental silicon Auger signal from the theoretical predictions. At lower angles of emission their effect would be noticed less as their contribution to the total 92eV signal would be reduced. From the results presented it is impossible to rule out for instance, surface roughness, as a contributing factor to the deviations occuring at high emission angles but the proposed mechanism does at least fit in with the angular results and the fact that SiO_2 is known to dissociate under an electron beam with a subsequent desorption of oxygen. (Thomas (1974))

Bearing this last point in mind, the film thickness will be estimated on the basis of $\frac{n}{\lambda_o^o} = \frac{n}{\lambda_s^o} = 1{\cdot}1$. Following Seah and Dench (1978) and putting $\lambda_s^o = 5{\cdot}5$ Å leads to a film thickness $n = 1{\cdot}1 \times 5{\cdot}5$ Å.

$$= 6\text{Å}$$

Alternatively if the value of λ_s^o derived by Oertel and Weber (1977) specifically for 76eV or 92eV electrons in SiO_2 is accepted then $\lambda_s^o = \lambda_o^o = 11 \pm 4$ Å and therefore $n = 11 \times 1{\cdot}1$

$$= 12\text{Å} \pm 4{\cdot}5\text{Å}$$

A third estimate of the film thickness can be made from the ratios of the 76eV and 92eV signals present in these spectra by comparing them with those of Oertel and Weber (1977). This leads to a value of n between 10Å and 20Å.

To summarise on the conclusions drawn from figure 3.18. Taking $\frac{n}{\lambda_s^o} = \frac{n}{\lambda_o^o} = 1{\cdot}1$, the values of n obtainable using different sources for λ_s^o and λ_o^o, lie in the range 6Å - 16Å. The film appears to be continuous with the possibility that some elemental silicon has been reformed at the top of the film.

Turning now to the angular distribution of the oxygen signal shown in figure 3.19. The dotted curve has again been derived from equation 11 with $\frac{n}{\lambda_o^o} = 1{\cdot}1$. In this case λ_o^o can be found from Seah and Dench (1978) to be 10Å leading to an estimate of the film thickness n = 11Å. Taking λ_o^o = 16Å

(from Oertel and Weber (1977)) leads to a film thickness n = 18Å. To rely on the oxygen angular distribution would however not be justified because the value of $\frac{E_p}{E_c}$ for the condition used here is only 1·8, and it was suggested earlier that a constant rate of ionisation rate with depth would only be a valid assumption for $\frac{E_p}{E_c} \geqslant 2{\cdot}5$. Thus the observed angular distribution from the 512eV oxygen auger electrons may be due to a variation in oxygen concentration with depth as well as a variation in ionisation rate with depth.

The final angular distribution recorded from this surface was that of the carbon 272eV transition. The results fitted by a dotted curve given by equation 11 with $\frac{n}{\lambda_o^o} = 1{\cdot}6$ is shown in figure 3.20. The film thickness deduced from this taking $\lambda_o^o = 10Å$ (Seah and Dench (1978)) is 16Å. This is on the upper limit of all the other derivations of film thickness. The application of equation 11 to this situation implies that the carbon is evenly distributed in the layer which may or may not be valid. If one assumes the film thickness is less than 16Å this would imply that the carbon concentration increases with depth toward the SiO_2 / Si boundary, but in the absence of a more accurate value of film thickness this cannot be confirmed.

The results from this investigation of the oxidised silicon surface shows the presence of a continuous oxide film ~10Å thick on a pure silicon substrate. It can also be suggested that a small amount of elemental silicon has been reformed at the top of the oxide layer due to the electron beam leading to an unexpected persistence of the elemental silicon signal at high emission angles.

3.9. Summary

The results of this chapter can be summarised as follows. Using clean specimens, the incident beam conditions that lead to a constant rate of Auger production with depth were examined and the conditions are summarised in Table 3.2. A variety of overlayer systems were then examined and it was shown

that systems exhibiting island growth could be distinguished from systems exhibiting continuous layer growth by careful analysis of the emission angular distributions from the substrate and overlayer. Similarly, concentration gradients as a function of depth could also be detected as in the case of ion implanted Argon. It is important to note that examination of only the signal ratios as a function emission angle could lead to ambiguous results since much of the information is contained in the form of the individual angular distributions. Finally it was shown that a knowledge of the depth distribution of the atoms in question was a prerequisite for quantitative analysis and in the case of ion implanted Argon, errors of 30% were shown to occur if the concentration gradient was not properly accounted for in the analysis.

Chapter 4

Angular Distributions of Low Energy Auger Electrons from Clean Single Crystal Surfaces.

		Page
4.1	Introduction	54
4.2.1	Theory	55
4.2.2	Diffraction of the Electron out of the Crystal	55
4.2.3	The Initial State of the Emitted Auger Electron	58
4.3.1	The Silicon (111) Surface	61
4.3.2.	Introduction	61
4.3.3	Experimental	61
4.3.4	Angular Profiles of the Silicon $L_{2,3}VV$ Transition using a Primary Beam Energy of 1000 eV	62
4.3.5	Discussion	63
4.4.1	Angular Profiles of the Silicon $L_{2,3}VV$ Transition using different Incident Beam conditions	65
4.4.2	Theory	65
4.4.3	Experimental details	66
4.4.4	Discussion and Conclusions	68
4.5.1	The Copper (111) Surface	70
4.5.2	Introduction	70
4.5.3	Experimental	71
4.5.4	Angular Profiles of the Copper M_1VV and $M_{2,3}VV$ Signals	72
4.5.5.(a)	Discussion	72
4.5.5.(b)	Transition Rates	74
4.5.5.(c)	The $M_{2,3}VV$ Signal in Copper	78
4.5.6	Conclusions	78
4.6	Summary	79

4.1 Introduction

Single crystal specimens present many more problems than polycrystalline ones when it comes to describing the effects of incident beam angle or emission angle on the measured Auger signals. This is simply because the diffraction of electrons into and out of the crystal must be described along the lines already developed in LEED theory. The overall process can be conveniently divided into two parts. The process leading up to the creation of the core hole and the subsequent emission of the Auger electron from the crystal. This chapter will concentrate on the second part of the problem by examining the processes that lead to the observed changes in Auger current with emission angle and it will usually be assumed that the rate of ionisation is constant within the detected volume. The discussion will be further restricted to include only the low energy Auger signals ($\sim$200eV) and discussion of the high (~1000eV) energy signals will be left till the next chapter.

It has already been observed that Auger electrons emitted from single crystal surfaces such as copper (McDonnel et.al. (1975), Noonan et.al. (1976), Zehner et.al. (1976), Zehner et.al. (1977), Noonan et.al. (1977), White et.al. (1978)), Nickel (Allie et.al. (1976), Aberdam et.al. (1978)), Iron (Matsudaira (1974)), Silver (Matsudaira and Onchi (1978)), MgO and NiO (Place and Prutton (1979)) can exhibit very large variations as a function of emission angle. This, however, is not the case for Aluminium (Allié et.al. (1976), Aberdam et.al. (1978)) and silicon (White et.al. (1978)) where the angular variations are less pronounced.

In terms of developing a quantitative analytical technique these angular variations are simply a nuisance and a simple technique of correcting for them is desirable (Chang (1977)). On the other hand it has been suggested (Woodruff (1975)) that the diffraction of the outgoing Auger electron will provide a way of determining the crystallographic site of the emitting atom. This type of effect has already been established for the emission of high energy (several

hundred KeV) β^- and β^+ particles from radioactive emitters introduced into single crystals (Domeij (1965), Uggerhoj (1966), Uggerhoj and Anderson (1968), Tomlinson and Howie (1968)) and has been interpreted by the dynamical theory of electron diffraction using the reciprocity principle of Von Laue (1935). In the case of Gold in lead it was possible (Tomlinson and Howie (1968) to determine whether the emission sites were interstitial or substitutional.

The main advantage in this type of approach to structural analysis over that of conventional LEED or RHEED is that an ordered overlayer is not required, the only requirement is that the atoms are located in a preferred type of surface site. Furthermore the signal comes directly from the atom of interest and not from the atom of interest plus the rest of the crystal surface, as in LEED, so the sensitivity may well be greater than for LEED.

4.2.1. Theory

Following the ionisation of a core level in an atom located in a crystal lattice the atom can decay to its ground state by emitting an Auger electron. Having left the atom the Auger electron will then be diffracted out of the crystal to be collected by a detector, providing no inelastic processes have occurred on the way. The theory used to describe the scattering of the Auger electron after leaving the atom will be described first and then the initial state of the Auger electron as it leaves the atom will be considered.

4.2.2. Diffraction of the Auger Electron out of the Crystal

The diffraction of low energy electrons up to an energy of about 400eV has already received considerable attention in the context of LEED (Pendry (1974)) and it has been shown by Pendry (1975) and Holland (1975) that the techniques of LEED theory can be adapted to treat the case of Auger emission. In this type of theory the crystal to be made up of the largest possible non overlapping spheres centred on each nucleus. Inside the spheres (or muffin tins as they are usually called) the potential is spherically symmetric and

outside, the potential is constant.

Both theories take as their starting point an outgoing wave ψ_e^o that can be expanded in the region outside the muffin tins as

$$\psi_e^o (\underline{r} - \underline{e}) = \sum_{l,m} b_{lm} h_e^+ (K|\underline{r} - \underline{e}|) Y_{lm} (\underline{r} - \underline{e}) \quad \text{---- (1)}$$

$\underline{e}$ is the emitter co-ordinate

h_l^+ is a Hankel function of the first kind

Y_{lm} are spherical harmonies

b_{lm} are the wave amplitudes

K satisfies the equation

$$\frac{\hbar^2 K^2}{2m} = E - V_o$$

V_o - uniform potential

E - electron energy

A plane is then drawn through the centre of the emitting atom parallel to the surface and the amplitudes $b_{\underline{g}}^{\pm}$ of the plane waves $\sum_{\underline{g}} b_{\underline{g}}^{\pm} \exp (i\underline{K}_{\underline{g}}^{\pm} \underline{r})$ emitted into the region of constant potential on either side of the layer are evaluated. (The + and - signs refer to waves propagating upwards and downwards from the layer).

In an angle resolved experiment the detector collects a narrow pencil of beams at a particular energy and angle relative to the surface. In the case of an unscattered wave this defines the momentum of the beam parallel to the surface $\underline{k}_{||}$. The indirect contribution to the measured intensity from waves that have been scattered by the crystal can only contain contributions from waves that differ from $\underline{k}_{||}$ by units of $\underline{g}$, the surface reciprocal lattice vectors. This means that the summation of plane waves is only over a discrete set of beams ($\underline{k}_{||} + \underline{g}$).

The final amplitude of a beam emerging from the crystal is then calculated by considering the multiple scattering of the plane waves leaving the layer containing the emitting atom from all the other layers in the crystal.

This calculation refers to one atom emitting and Auger electron in layer s in the crystal and it is necessary to add the intensities due to the various emitters. Thus the total intensity $I(\underline{k}_{||} + \underline{g})$ can be written as (Pendry (1975), Aberdam et.al. (1976))

$$I(\underline{k}_{||} + \underline{g}) = \sum_{s=1}^{\infty} P_s M_s \left| C_g(s) \right|^2 \quad \text{---} \quad (2)$$

$C_g(s)$ - amplitude for an emitter in layer s.

M_s - number of equivalent atoms in layer s

P_s - describes the rate of ionisation in layers s

Aberdam (1976) assumes that

$$P_s = \exp\left(- 2K_{\perp}^{im} d\,(s-1)\right)$$

where $K_{\perp}^{im}$ is the imaginary part of the normal component of the incident wave vector and d is the lattice spacing. Although the form of P_s is not expected to alter the shape of the observed angular distributions much, it would seem, from the work described in chapter 3, that taking P_s as a constant with depth would be a better approximation in most experimental situations.

To relate the value of $I(\underline{k}_{||} + \underline{g})$ to the current measured by a detector of angular aperture $d\Omega$ set at angle θ to the surface normal it is necessary to consider the number of beams collected. The area on the diffraction sphere determined by the detector is $K^2\, d\Omega$ therefore the projected area in $\underline{k}_{||}$ space is given by $K^2\, d\Omega \cos\theta$ and the number of states included in the angular aperture of the detector given by

$$K^2\, d\Omega \cos\theta \frac{L^2}{(2\pi)^2} \quad \text{---} \quad (3)$$

L^2 - the illuminated area

$\frac{L^2}{(2\pi)^2}$ - the density of states in $\underline{k}_{||}$ space

The current in each beam is proportional to the normal component of the wave-vector given by K cos θ and therefore the total collected current is given by (Pendry (1975))

$$I(\underline{k}_{||} + \underline{g})\, K^3 \cos^2\theta\, d\Omega \frac{L^2}{(2\pi)^2} \quad \text{---} \quad (4)$$

To compare the results of such a calculation with experiment requires an accurate description of $\psi_e^o(\underline{r} - \underline{e})$ and this will now be considered.

4.2.3. The Initial State of the Emitted Auger Electron

It was implicitly assumed in the previous section that a kinematical treatment of the scattering of the Auger electron out of the crystal would be inadequate. The first attempts to calculate the angular profiles of Auger electron emission were in fact kinematical (McDonnel et.al. (1975), Woodruff (1975)) and they also assumed that the source could be described as an isotropic emitter. The calculations by McDonnel et.al. (1975) were performed for the 62eV $M_{2,3}VV$ copper transition for the (100) and (111) surfaces of copper. The calculations did not generally produce very good agreement with the experimental profiles and this was attributed mainly to the use of a kinematical model for the scattering. Subsequently Davis and Kaplan (1976) tested this idea by performing a kinematical and a multiple scattering calculation for the same transition on the copper (100) face, again using an isotropic emitter model. There were many similarities between the angular profiles calculated using the kinematical and multiple scattering formalisms but in both cases the agreement with experiment was rather poor. The conclusion from this work is then to say that the choice of an isotropic emitter model is inappropriate for the copper $M_{2,3}VV$ emission and that a more complicated source wavefunction must be used. To circumvent this problem of a non-isotropic source it was suggested that Auger transitions involving only core levels should be used in the hope that an isotropic emitter model would be appropriate.

In the absence of theories that allow direct calculation of the initial state wavefunctions for Auger emission the next step is to try a number of simple anisotropic source wavefunctions. Aberdam et.al. (1976) calculated various angular profiles using different source wavefunctions described by individual values of (l,m) (cf eq^{n} 1). In the cases of the transition metals Iron, Nickel and Copper they set l,m = 2,0 and for Aluminium they set l,m = 1,0.

The theoretical angular profiles were very different from those calculated using an isotropic emitter (l,m = 0,0) but again the agreement with experiment was rather poor and it was concluded that many partial waves would have to be included to describe the source wavefunctions.

Lindsay and Kinniburgh (1977) adopted this approach in their study of the angular profile of Auger emission from Copper (100). For each value of l from 0 to 4 they calculated an individual angular profile by averaging over the possible values of m. Averaging over m was justified on the basis of work by Cleff and Mehlhorn (1974) who showed that the anisotropy resulting from the initial ionisation was less than 6%. As in the work of Aberdam et. al. (1976) there was poor agreement with experiment for any individual value of l. By summing the individual profile together with suitable weights it was however possible to reproduce the experimental data quite well. In the case of the $M_{2,3}VV$ profile in the ⟨010⟩ azimuth on copper (100) the weights attached to the various values of l were :-

Table 1

l	weight
0	0
1	0·348
2	0
3	1·856
4	0·172

On the (110) surface of copper in the $\langle \bar{1}10 \rangle$ azimuth the values were :-

Table 2

l	weight
0	0·006
1	0·350
2	0·802
3	1·859
4	0·174

Thus it can be seen that the l = 3 term always dominates but the best combination of l values for one face of copper does not always produce the best fit

on another face. Unfortunately this ad hoc treatment of the emitter wavefunction does not really answer the question of what composite wavefunction can be used to describe the copper $M_{2,3}VV$ emission under all circumstances. Lindsay and Kinniburgh (1977) suggest that a more accurate treatment of the surface barrier region may show that a pure $l = 3$ wavefunction can give as good agreement with experiment as the composite wavefunction. Aberdam et.al. (1978) extended this approach and calculated angular distributions for all the experimental data currently available for low energy Auger transitions and it was found that the best overall agreement for different faces or azimuths of a particular metal was to be found using single values of l for the source wavefunction. For copper and nickel the $l = 3$ source wavefunction gave best agreement with experiment, the $l = 1$ wavefunction was best for aluminium and $l = 2$ was best for iron. (in this context "best" means the smallest mean square error between theory and experiment). However in view of the large error for the iron case the authors preferred the $l = 3$ profile on the basis of peak positions alone. Aberdam et.al. (1978) also showed that these values of $l = 3$ for the Nickel, Iron and Copper $M_{2,3}VV$ transitions and $l = 1$ for aluminium $L_{2,3}VV$ transition could be predicted on the basis of transition rates calculated for isolated atoms by Asaad (1963) and McGuire (1971). Since the experiments were unable seperate the contributions from the M_2 ans M_3 holes (or L_2 and L_3 holes) the transition rates were calculated by summing the contribution from each hole.

Aberdam et.al. (1978) did however note that the line shape of the Nickel $M_{2,3}VV$ peak did change slightly with emission angle and the low energy part of the signal did produce an extra peak in the angular distribution at $\sim \pm 25^{o}$. Nevertheless they assumed that the angular distribution was correctly represented by recording the most intense part of the line at 56·25eV as a function of emission angle. Due to the lack of data with sufficiently high energy resolution they were unable to comment on the possibility of a similar effect in the case of the copper $M_{2,3}VV$ signal.

4.3.1. The silicon (111) surface

4.3.2. Introduction

Very little work has been done on the Auger angular distributions from the surfaces of single crystal silicon. White et.al. (1978) have measured the angular distribution of the LVV signal from the silicon (100) (2 x 1) surface and they found very little angular structure in the distributions. They attributed this to the effects of having more than one type of atomic site in the silicon lattice causing the measured angular distribution to be the sum of two or more angular distributions associated with the different atomic sites. On the other hand Aberdam et.al. (1978) preferred to explain the smooth angular profiles observed for the LVV Auger signal from Aluminium (100) and (110) on the basis of a small initial source anisotropy. Since the silicon and aluminium LVV signals both involve s-p valence bands it is quite possible that this explanation may apply to the results from silicon as well.

Detailed angular profiles have been obtained from the silicon (111) (7 x 7) surface for a variety of incident beam conditions and it will be shown how the angular profiles can be changed by changing the incident beam conditions and explanations of this based on the crystallography of the surface will be given.

4.3.3. Experimental

The silicon (111) specimen (24 parts per billion phosphorus) was prepared in the way described in chapter two before insertion into the vacuum chamber. The main contamination was usually carbon and this could be removed by heating the specimen to 1200^{o}C for a few minutes. This treatment reduced the carbon Auger signal at 272eV to less than one hundredth of the peak to peak height of the silicon LVV transition measured in the derivative mode and produced a sharp 7 x 7 LEED pattern characteristic of the clean surface.

After a number of such anneals triangular etch pits would appear on the surface but these would not be expected to alter the measurements other than to raise the level of the diffuse background, because of their irregular nature.

Before discussing the details of the angular spectra the main features in the silicon LVV Auger spectrum will be considered. Figure 4.1 shows two spectra recorded in the EN(E) mode at angles of emission of 15^{o} and 65^{o} from the surface normal in the $\langle 11\bar{2} \rangle$ azimuth. The spectra were recorded by modulating the wehnelt cylinder of the electron gun (§ 2.4.5) with a square wave of peak to peak amplitude of 4 volts, thus chopping the electron beam, and a lock in amplifier was used in the usual way. The line shape of the silicon LVV transition has already received considerable attention in the literature (Amelio (1970), Feibelman et.al. (1976), Houston et.al. (1977), Feibelman and McGuire (1978)). By deconvoluting the Auger spectrum with an inelastic loss function Houston et.al. (1977) were able to show that the Auger LVV feature itself has a width of only 20eV on the base line. The feature appearing at ~17eV from the main peak at 91eV in the upper curve of figure 4.1 can be identified as the bulk plasmon loss and the feature at ~ 10eV from the main peak in the lower curve is the surface plasmon loss. It can be seen from figure 4.1 that the surface plasmon loss is accentuated at large angles of emission due to the longer path length of the Auger electrons in the surface region. The peak at ~ 40eV can be assigned to the silicon $L_1L_{2,3}V$ Coster-Kronig transtion (Arnott and Hareman (1974)). Other than changes in the energy loss tail on the LVV signal, no changes in line shape were observed with changing angles of emission.

4.3.4. Angular profiles of the silicon $L_{2,3}VV$ transition using a primary energy of 1000eV

The angular profiles of the silicon $L_{2,3}VV$ transition from the silicon (111) surface in the azimuthal directions $\langle \bar{1}10 \rangle$ and $\langle \bar{1}\bar{1}2 \rangle$ can be seen in

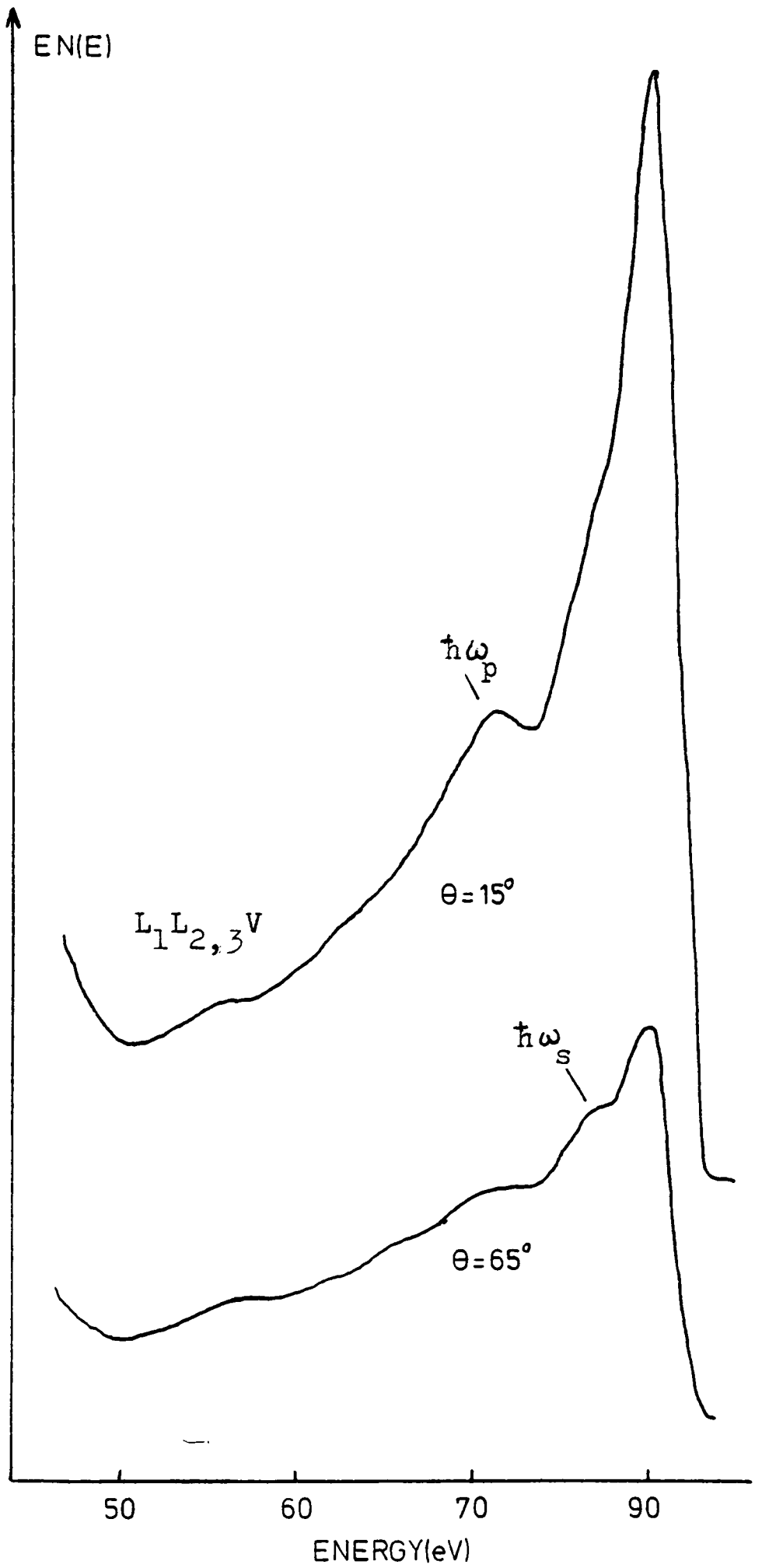


Fig.4.1 Silicon LVV line shapes at two angles of emission from silicon(111) surface in $\langle 11\bar{2} \rangle$ azimuth, E_p=1000eV, θ_p=60°

figures 4.2 and 4.3 (the experimental errors are indicated by the cross in the figures). The primary energy of 1000eV with the beam normal to the surface was chosen to ensure that the ionisation rate with depth would be constant within the Auger escape depth. The angular profiles were recorded by setting the analyser pass energy at the peak of the Auger spectrum at ~90eV and recording the angular profile of the Auger peak plus background directly onto the chart recorder. The pass energy was then set at ~ 94eV and the angular profile of the background was obtained, this was then subtracted from the previous angular profile to obtain the Auger angular profile. Angular profiles were also obtained by recording spectra at 5^{o} intervals and they all agreed within the experimental error. The data in the $\langle\bar{1}10\rangle$ azimuth shows two shoulders at $\pm 30^{o}$ correctly exhibiting the symmetry expected in this azimuth.

These structureless angular profiles are qualitatively similar to those already reported (White et.al. (1978), Allie et.al. (1976)) for the $L_{2,3}VV$ angular profiles for silicon (100) (2x1) and aluminium (001) and (110). In all these cases the angular profiles lie fairly close to $\cos^{2}\theta$ and this is shown for comparison in figure 4.2.

Attempts were made to obtain the angular distributions of the $L_1L_{2,3}V$ signal but the signal to noise ratios and the confusion between the inelastic tail of the $L_{2,3}VV$ signal and the $L_1L_{2,3}V$ signal made the collection of reliable data impossible.

4.3.5. Discussion

All the angular profiles so far observed for core-valence-valence Auger electrons of kinetic energy $\leqslant$ 150eV from transition metal crystals have shown strong angular structure whereas the angular profile of the Aluminium $L_{2,3}VV$ signal shows only weak structure. Aberdam et.al. (1978) suggest that this weak angular structure for Aluminium is due to the low source anisotropy associated with the l = 1 source wavefunction used in their calculations. There are many similarities in the form and origin of the silicon and aluminium

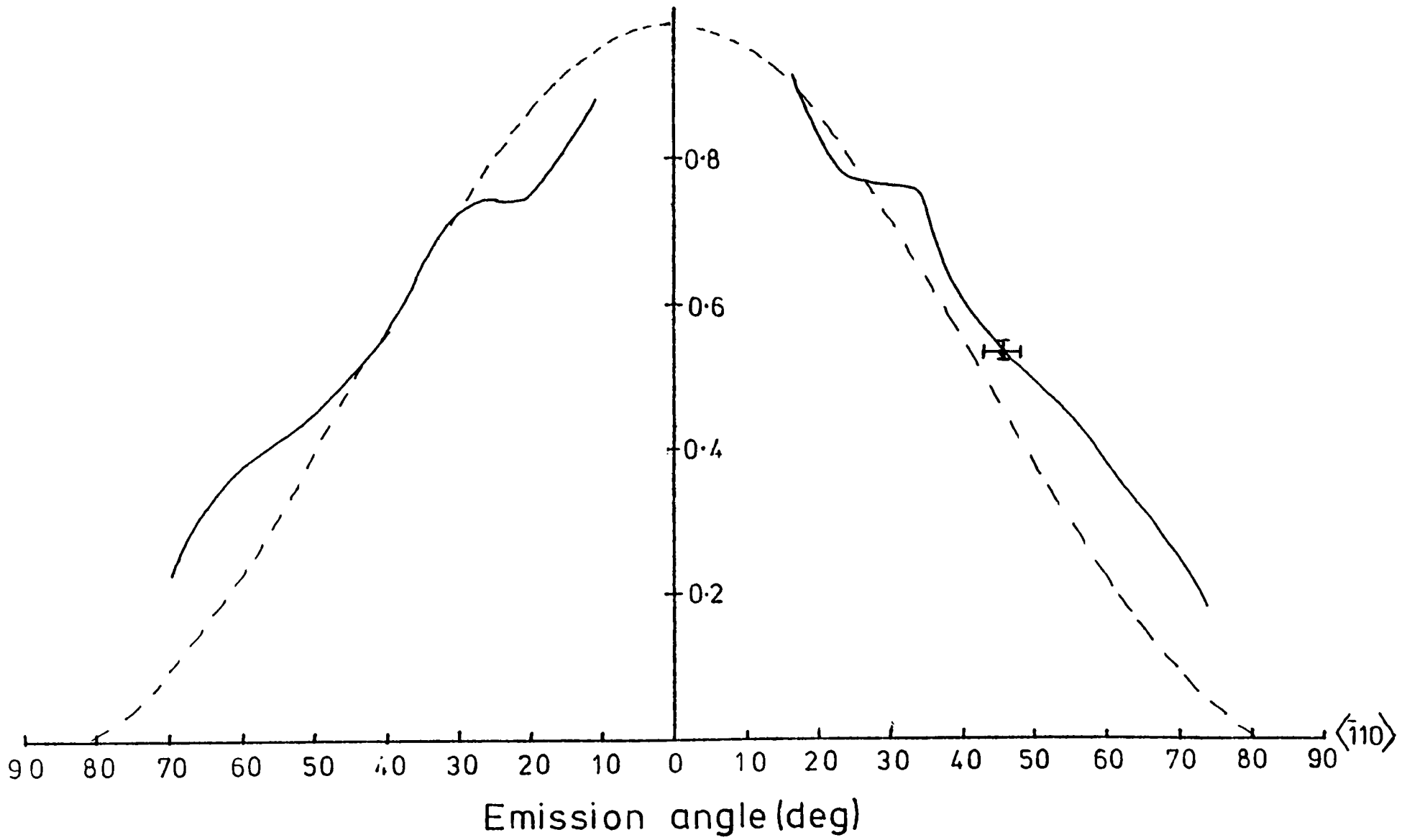


Fig.4.2 Angular distribution of silicon $L_{2,3}VV$ transition from silicon(111) in $\langle\bar{1}10\rangle$ azimuth E_p=1000eV, θ_p=0°

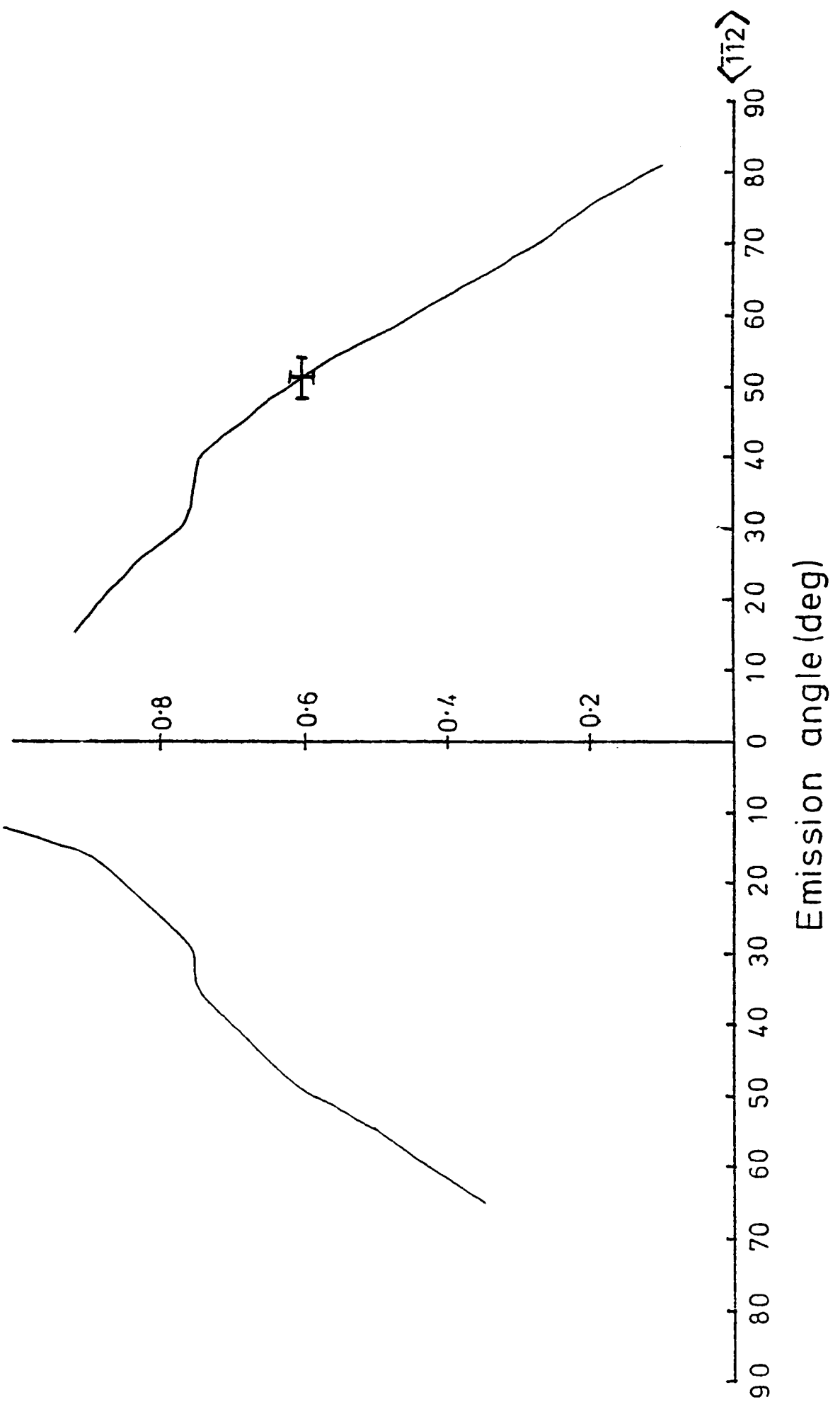


Fig.4.3 Angular distribution of silicon $L_{2,3}VV$ transition from silicon(111) in⟨1̄12⟩ azimuth.

E_p=1000eV, θ_p=0°

$L_{2,3}VV$ Auger lines. Both materials have their valence bands made up of s and p type states and in both cases the p type states contribute much more to the Auger line shape than the s type states (Feibelman et.al. (1976)). It is therefore reasonable to suppose that an l = 1 source wavefunction would also be appropriate to describe the silicon Auger electron wavefunction and hence the weak angular structure observed could also be attributed to low source anisotropy as in the case of aluminium.

However, White et.al. (1978) prefer to explain the weak angular structure they observed from the silicon (100) (2x1) surface in a rather different way. They point out that, if one ignores the surfaces, the fcc metal copper has only one type of atomic site whereas silicon with a diamond structure has two types of non equivalent site. Thus in the case of silicon the angular profiles result from Auger electrons emitted from two types of non equivalent site. The presence of the surface complicate matters still further, especially for silicon (100) where a (2x1) reconstruction occurs leading to four non equivalent surface sites. Thus, the authors argue, the observed angular profiles from silicon (100) (2x1) result from an incoherent sum of angular profiles for each non equivalent site resulting in the rather structureless angular profile that they observe. This type of argument can also be carried over to the silicon (111) (7x7) surface investigated here. As this surface structure is not known it is impossible to say how many non equivalent sites exist on this surface although the rumpling model of Mark et.al. (1977) would imply that the non-equivalent site introduced by the (7x7) reconstruction differ very little from each other leaving only two types of non-equivalent site.

Although this argument about non-equivalent sites in the surface layer may explain the weak angular dependence of Auger emission from silicon it does not explain the weak angular dependence found by Aberdam et.al. (1978) for aluminium which is an fcc metal just like copper, nickel and iron all of which show marked angular dependencies for Auger emission. Aberdam et.al. (1976)

also showed that the shape of the angular profiles calculated, including only the first layer for copper, nickel, iron and aluminium did not differ greatly from the profiles calculated including the whole crystal. If this type of calculation were to be performed on a reconstructed surface it seems likely that the reconstruction would cause the surface layer, taken in isolation, to give an angular profile significantly different from that of the whole crystal minus the surface layer and therefore the overall structure in the observed angular profile would be averaged out.

Therefore for the reconstructed silicon (100) (2x1) and silicon (111) (7x7) surfaces three possible reasons for the weak angular dependence of Auger emission can be postulated. Firstly the source anisotropy may be small as in the case of aluminium, secondly non-equivalent surface sites may average out each others contribution to the overall angular profile and thirdly,the reconstructed surface layer may interfere with the contribution from the rest of the crystal giving a structureless angular profile.

Experimentally it is very difficult to throw any light on the validity of the first two mechanisms but it is possible to change the contribution of the surface layer to the overall angular profile by altering the rate of ionisation with depth. The result of such an experiment will be described in the next section.

4.4.1. Angular profiles of the silicon $L_{2,3}VV$ transition using different incident beam conditions

4.4.2. Theory

It was shown in chapter 3 that the rate of Auger production with depth could be changed by changing the incident beam conditions. Using a primary beam of energy 130eV at 72° from the surface normal it was shown that the rate of Auger production with depth was proportional to $\exp\left(-\frac{z}{\lambda_a}\right)$ where z is the depth in the crystal and λ_a is the inelastic mean free path of Auger

electrons. Under normal circumstances when the Auger production is constant with depth the contribution to the total Auger signal of the first layer is given by

$$1 - \exp\left(-\frac{l}{\lambda_a}\right) \quad \text{---} \quad (7)$$

where l is the first layer thickness.

In the case of silicon (111) the distance between layers is 3·12Å and λ_a = 5·5Å (Seah and Dench (1978). Therefore the percentage contribution of the first layer to the overall Auger signal is ~45%. Using a primary energy of 130eV at 72° from the surface normal the rate of Auger production with depth is $\propto \exp\left(-\frac{z}{\lambda_a}\right)$ and hence the first layer contribution to the overall signal is given by :-

$$\frac{\int_0^l \exp\left(-\frac{2z}{\lambda_a}\right) dz}{\int_0^\infty \exp\left(-\frac{2z}{\lambda_a}\right) dz} = 1 - \exp\left(-\frac{2l}{\lambda_a}\right) \quad \text{---} \quad (8)$$

This shows that the contribution of the first layer to the overall signal is increased by 22% to give a 67% contribution. Thus it should be possible to detect changes in the angular profiles if the angular profile from the surface layer alone is significantly different to that of the sub-surface layers.

4.4.3. Experimental details

Operating at the low primary energy of 130eV reduces the Auger yield rather drastically as can be seen in the spectra shown in figure 4.4. The bottom curve (d) shows quite clearly the silicon $L_{2,3}VV$ signal using a primary beam energy of 1KeV. The upper three curves show the same energy range using primary energies of 130eV, 135eV and 140eV. The features that move with the changing primary energy are the bulk plasmon loss signals. It is obvious from this diagram that measuring the Auger signal in this mode is not feasible so the data was collected in the derivative mode. Figure 4.5 shows three Auger spectra obtained by modulating the specimen by 2 volts rms at primary

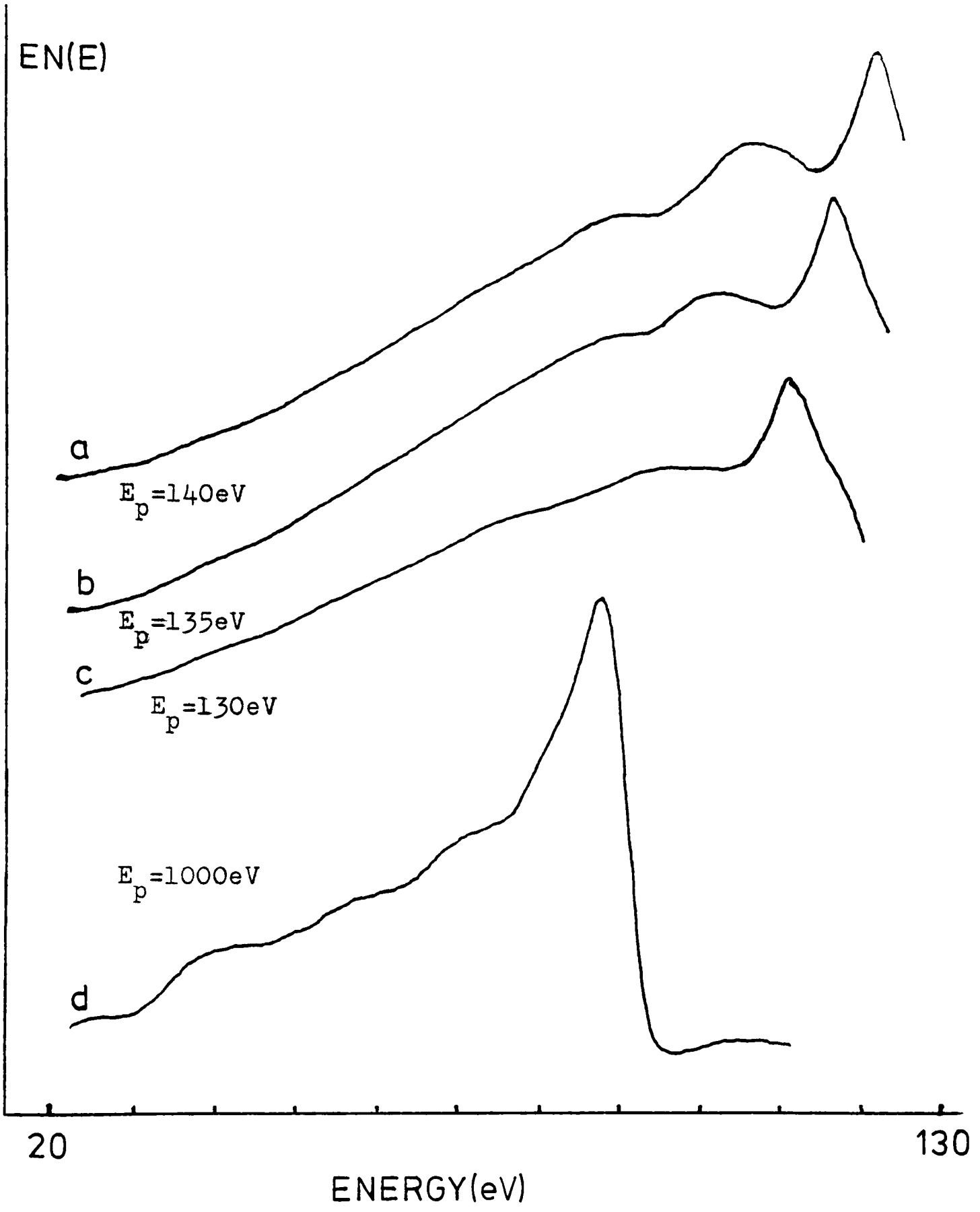


Fig.4.4 Auger spectra at various primary energies from silicon(111) surface. θ_p=72°

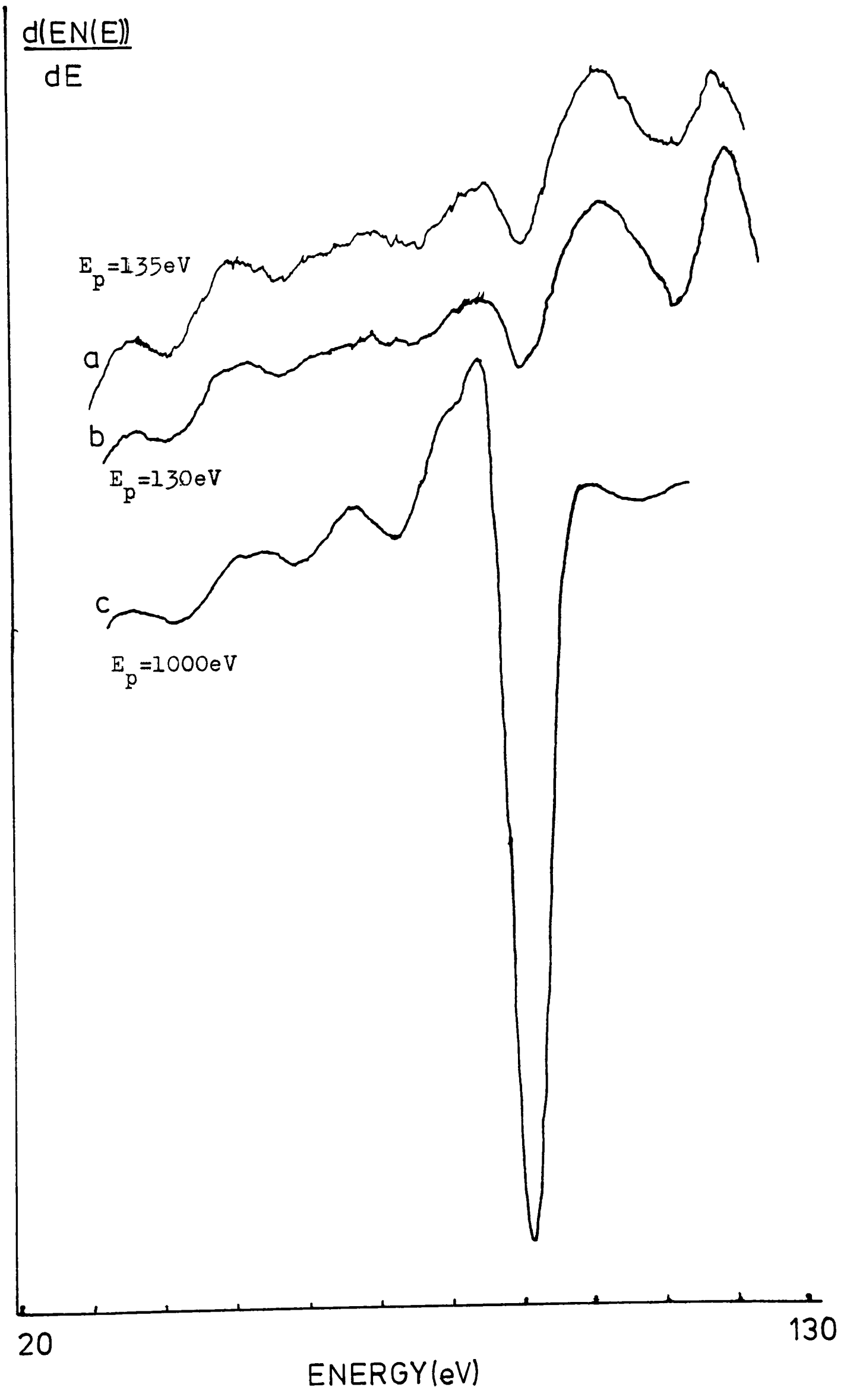


Fig.4.5 Auger spectra at various primary energies from silicon surface. $\theta_p=72^\circ$

energies of 1000eV, 135eV and 130eV.

The differential spectra obtained in this way (Stadler (1972), Gerlach et.al. (1970)) should contain only Auger features and any other features whose energies are referenced to the specimen Fermi level. However it was obvious from the data that other features related to the primary energy were appearing in these spectra. It can be seen in figure 4.5 that the large features above the Auger signal move with the primary beam energy. It is thought that these energy loss features appear in the spectra as a result of the small change in reflectivity with changing primary beam energy. This arises because the modulation voltage of 2Vrms applied to the specimen changes the energy of the electrons incident on the sample and any change in surface reflectivity over this range will cause the overall signal intensity entering the analyser to change and hence the overall signal is intensity modulated. As the energy of the primary beam is increased this effect becomes less noticeable, firstly because the loss features move away from the Auger features and secondly because the fractional change in beam energy becomes less for a given modulation amplitude.

By measuring spectra of the form shown in figure 4.5 at 10^{o} intervals using a primary energy of 130eV the angular profile of the $L_{2,3}VV$ silicon transition is shown in figure 4.6. It is immediately apparent that the angular structure is much more pronounced than in the angular profile shown in figure 4.2. Unfortunately the data in figures 4.2 and 4.6 are not directly comparable because of a 10^{o} error in the alignment of the $\langle\bar{1}10\rangle$ azimuth in figure 4.6, nevertheless the quantitative difference is still significant. Due to the close proximity of the plasmon loss features to the $L_{2,3}VV$ silicon Auger feature using a primary energy of 130eV a second set of data were recorded using a primary energy of 170eV and the resulting angular profile is shown in figure 4.7. This data was recorded in the same azimuth as that of figure 4.3 and again the angular profile obtained at low primary energy shows more angular structure. For comparison the angular profile of the elastic

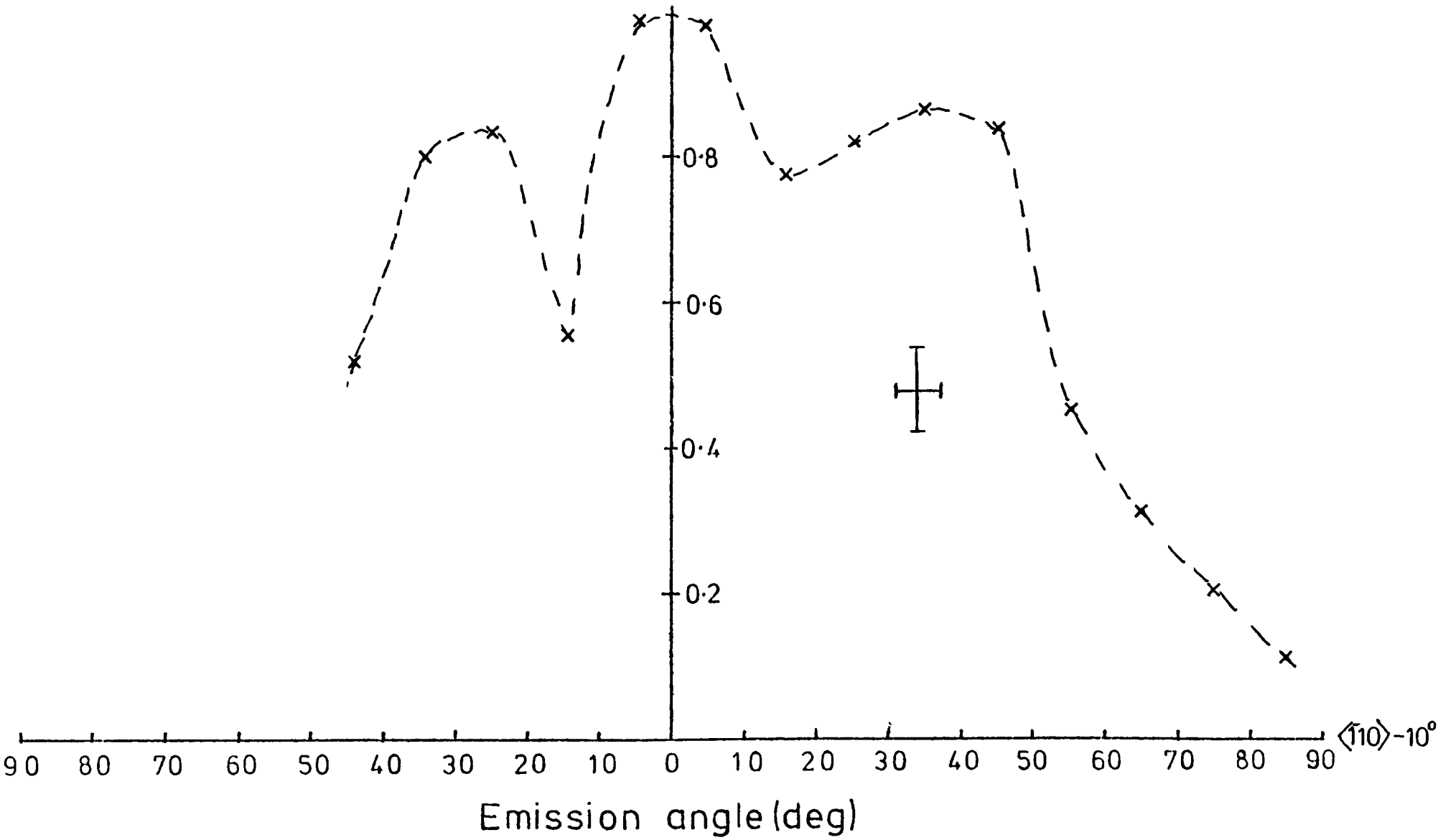


Fig.4.6 Angular distribution of silicon $L_{2,3}VV$ signal from silicon(111) surface close to⟨$\bar{1}$10⟩ azimuth. E_p=130eV, θ_p=72°

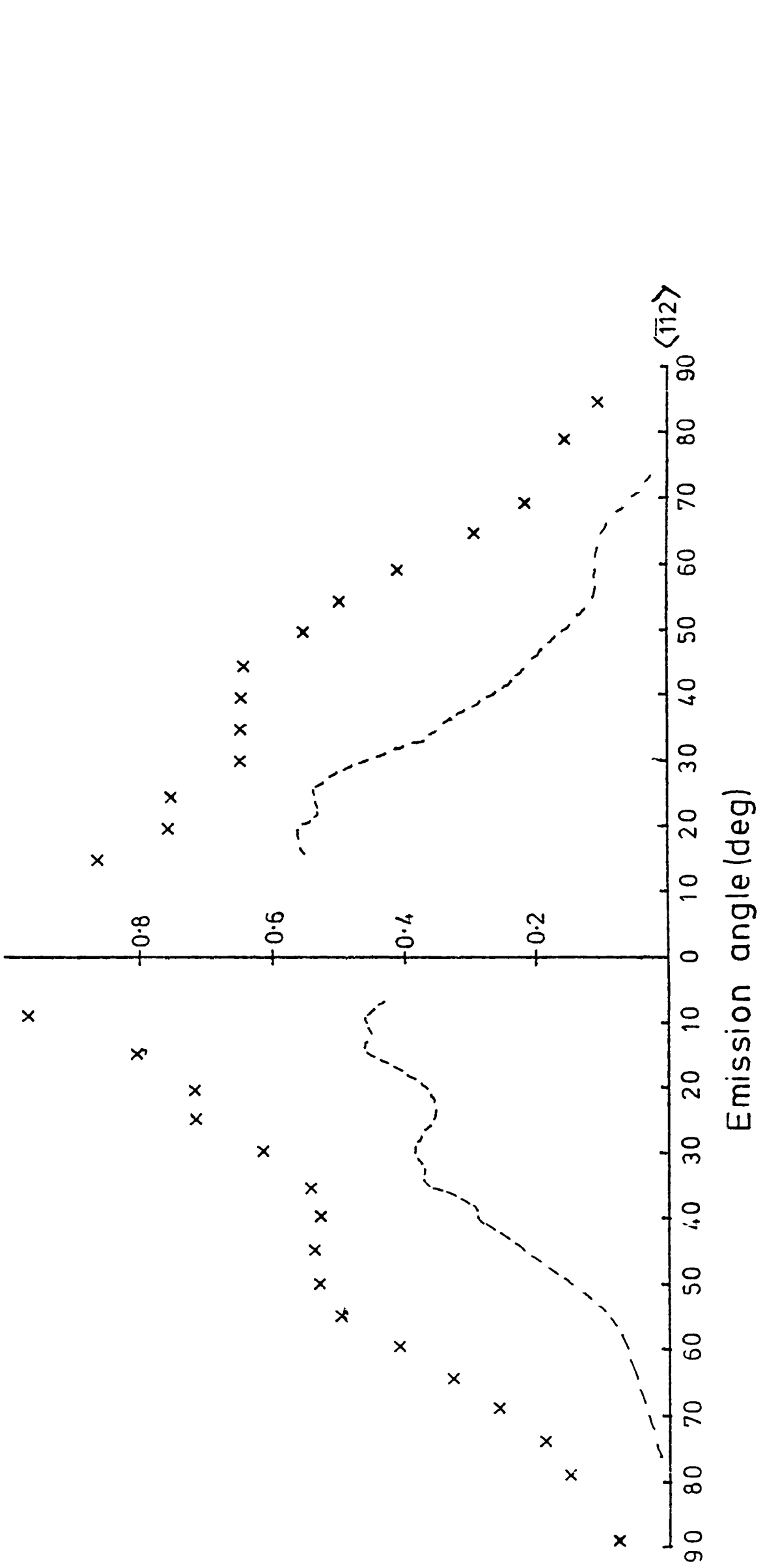


Fig.4.7 Angular distributions of silicon $L_{2,3}VV$ signal(×) and elastic peak(---) from silicon(111) surface in $\langle\bar{1}\bar{1}2\rangle$ azimuth. E_p=170eV, θ_p=0°

peak at 170eV is shown in figure 4.7.

4.4.4. Discussion and conclusion

These results show quite clearly that the measured angular distributions in Auger emission can be changed by varying the primary beam energy and angle. Another example of this type of effect was shown for a 12eV "Auger like" peak of unknown origin by Rusch and Ellis (1975) who examined the angular profile of this peak from arsenic (0001) at primary energies of 400 and 1000eV. They did not however comment on this result or try to explain its significance. Recently Place and Prutton (1979) have observed a similar effect for their results from MgO and NiO but mechanical problems prevented them investigating the effect properly.

To answer the question posed in the last section as to whether the reconstructed surface layer in silicon (111) (7x7) produces an angular profile different from that of the bulk it is important to ensure that the results shown in figures 4.6 and 4.7 are not due to some instrumental effect. It seems almost inevitable that the bulk plasmon loss appearing in the data taken using a primary energy of 130eV will interfere with the Auger peak at 92eV since the two features are very close and of similar size. For this reason more attention will be focussed on the data recorded at a primary energy of 170eV. It has already been shown that the angular distributions of the plasmon loss features are of the same form as the elastic angular distribution although the "contrast" in the distribution decreases as the energy loss increases. It would therefore be expected that any contribution to the measured Auger angular profile due to interference between the plasmon loss signal and the Auger signal would be related to the form of the elastic angular distribution. The comparison between the Auger angular profile and the angular profile of elastic peak in figure 4.7 shows no such correlation which would indicate that this change in Auger profile is a genuine effect.

This result shows that at least part of the reason for the lack of angular structure in the silicon $L_{2,3}VV$ Auger angular profiles from the silicon (111) (7x7) surface is that the top layers produce angular profiles slightly different from those in the bulk and hence the two profiles tend to cancel out. This proposal is at least partly borne out by Best (1976) who suggests that the large differences observed in secondary electron spectra from the silicon (111) (7x7) and (1x1) are due to incoherent scattering in the reconstructed layer. Conversely Shih et.al. (1976) comment that the LEED spectra from the two surfaces are very similar.

It is also relevant to consider here the effect of ordered adlayers on the angular distributions of the Auger emission from the substrate. For the case of oxygen on copper (100) $(\sqrt{2}x\sqrt{2})R\ 45^{\circ}$-O (White et.al. (1978), Noonan et.al. (1977)) the only effect of the overlayer was to weaken the angular structure of the substrate emission. In the case of sulphur on Nickel (001)-C (2x2) -S (Allié et.al. (1976)) only small variations in the polar plot of the Nickel $M_{2,3}VV$ signal were observed but the azimuthal profiles were drastically changed. The Fe O(100) / Fe(100) surface (Matsudaira et.al. (1974)) produced an Iron $M_{2,3}VV$ angular distribution very similar to that obtained from clean iron surface but with slightly more structure, however in this case the surface is not just a simple ordered,one atom thick overlayer. Thus it appears that the presence of an overlayer with a structure different to that of the bulk will at least reduce the angular variations in the substrate Auger angular distribution if not alter them in a more drastic way. Therefore the presence of the reconstructed overlayer on the silicon (111) surface will tend to produce smooth Auger angular profiles both as a result of the overlayer, taken by itself, producing an angular distribution different to that of the bulk and also because the overlayer is likely to smooth out the substrate angular distributions in a way similar to that observed for overlayers of foreign atom.

From these results it appears very unlikely that unique structural

information could be obtained by matching theoretical calculations to expiments for surfaces of this type. This of course does not rule out this possibility if the signal originates in an overlayer of foreign atoms on a substrate. Nevertheless it is vital to be aware of these angular effects from the point of view of quantitative analysis.

4.5.1. The Copper (111) surface

4.5.2. Introduction

The single crystal copper surfaces have received considerable experimental and theoretical attention (McDonnel et.al. (1975), Noonan et.al. (1976), Zehner et.al. (1976), White et.al. (1978), Zehner et.al. (1977), Aberdam et. al. (1978) and (1976), Davis and Kaplan (1976), Lindsay and Kinniburgh (1977)) and there is now general agreement (Aberdam et.al. (1978), Lindsay and Kinniburgh (1977)) that the wavefunction describing the emitted Auger electron is dominated by $l_a = 3$ terms for the $M_{2,3}VV$ signal although the agreement of theory with experiment still leaves room for improvement.

It is well known that the copper $M_{2,3}VV$ signal is a doublet ascribed by Chung and Jenkins (1971) as being due to the energy difference in the M_2 and M_3 core levels. Unfortunately most of the experimental work done on the angular distributions of this signal has been able to resolve these peaks and consequently three experiments in fact measure the angular distributions of a composite peak. Madden et.al. (1978) consider that the $M_{2,3}VV$ peak is made up of two identical peaks M_2VV and M_3VV that are simply shifted in energy relative to one another. If this were so then the angular variations of M_2VV M_3VV or $M_{2,3}VV$ would be expected to be the same and hence being able to resolve the peaks is unimportant. However recent calculations by McGuire (1977) have shown that the lower energy peak is M_3-$M_{4,5}M_{45}(^1G)$ and the higher energy peak is a superposition of M_2-$M_{4,5}M_{4,5}(^1G)$ and M_3-$M_{4,5}M_{4,5}(^3F)$. It is therefore possible that the values of l_a used to describe the Auger wavefunction in the

high and low energy components of this peak may be different and that the angular distribution of the high and low energy peaks may differ from one another. This and other possibilities will be investigated in the next sections.

4.5.3. Experimental

The 99·999% pure copper single crystal rod was oriented to within 1^{o} of the (111) face using the standard Laue method. The goniometer used was specially designed to be transferred to an acid saw where a slice of crystal was cut off using nitric acid fed onto stainless steel cutting wires. Still in the same goniometer the crystal rod was transferred to an acid polishing wheel based on a discarded slitting saw. The front face of the single crystal rod was then polished using a mixture of 200 parts orthophosphoric, 200 parts glacial acetic, 200 parts conc. hydrochloric, 15 parts of saturated solution of cupric chloride in HCl. fed slowly onto a thick denim pad attached to the polishing wheel. Finally a disc about 0·5mm thick was cut from the end of the rod and a 5·5mm diameter disc was cut out using a spark machine. This disc was then electropolished in a mixture of 30% orthophosphoric and 70% distilled H_2O, and after washing in distilled H_2O followed by ultrasonic cleaning in isopropanol, it was mounted in the U.H.V. system.

In situ cleaning was done by a sequence of Argon ion bombardment at 500eV and annealing at $\sim 450^{o}C$. This produced a clean well ordered surface giving high peak to background ratios in the LEED pattern at 150eV (typically $\sim$8:1).

The crystal was orientated in the U.H.V. system using the same method described for the silicon (111) surface and as an example figure 4.8 shows the elastic peak variation at 1500eV in the $\langle 01\bar{1} \rangle$ azimuth exhibiting the symmetrical angular distribution expected. As before an azimuthal variation of $\pm$ $1·5^{o}$ produced a very noticeable assymmetry in the pattern showing that the $\langle 01\bar{1} \rangle$ azimuth is located to within $\pm$ $1·5^{o}$.

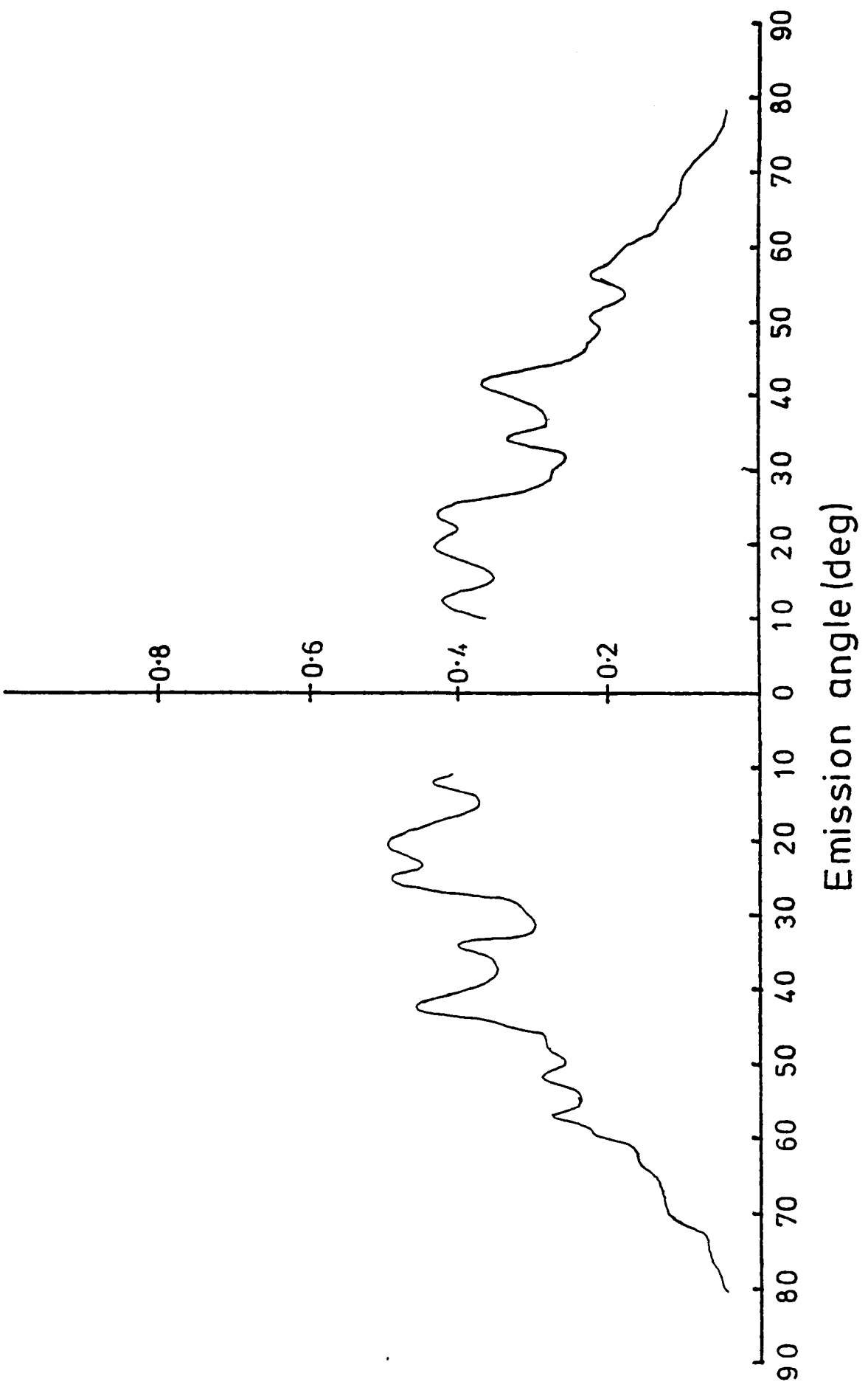


Fig.4.8 Angular variation of elastic peak at 1500eV from copper(111) surface in $\langle 01\bar{1} \rangle$ azimuth, $\theta_p = 0^\circ$

4.5.4. Angular profiles of the Copper M_1VV and $M_{2,3}VV$ signals

All the data presented here was collected using 0.4Vr.m.s. modulation on the specimen which allows the doublet structure in the $M_{2,3}VV$ signal to be clearly seen. Figure 4.9 shows the copper $M_{2,3}VV$ signal recorded in the $\langle 11\bar{2} \rangle$ azimuth at angles of emission of 0° and -15°. In all the angular profiles presented here the $M_{2,3}VV$ peak was taken to be proportional to A minus C for comparison with results published elsewhere. A minus B was taken as proportional to M_3VV and D minus C was taken as proportional to M_2VV. The data shown in figure 4.9 shows quite clearly that the line shape is not constant with angle of emission and therefore each component in the $M_{2,3}VV$ signal was plotted seperately as a function of emission angle. Data was collected in the $\langle 01\bar{1} \rangle$ and $\langle 11\bar{2} \rangle$ azimuths and the results are shown in the next set of figures as follows. Figure 4.10 shows the M_1VV and $M_{2,3}VV$ signals in the $\langle 01\bar{1} \rangle$ azimuth, the $M_{2,3}VV$ profile is very similar to that recorded by McDonnel et.al. (1975). Figure 4.11 shows the M_2VV and M_3VV profiles recorded in the same azimuth and the first thing to notice is that the M_2VV and M_3VV profiles are very different from each other and also different from the $M_{2,3}VV$ profile in figure 4.10. Figures 4.12, 4.13 and 4.14 show the $M_{2,3}VV$, M_2VV and M_3VV profiles respectively in the $\langle 11\bar{2} \rangle$ azimuth, the gun was moved to $\pm 30^\circ$ in the $\langle 11\bar{2} \rangle$ azimuth to allow collection of data from all emission angles. Again all three angular profiles are quite different although it is often possible to identify features in the $M_{2,3}VV$ profile as being due to the M_2VV or M_3VV signals alone.

4.5.5.(a) Discussion

These results how for the first time that each component in the copper $M_{2,3}VV$ signal exhibits its own characteristic angular distribution. The slight difference ($\sim 4\%$) in energy between the two peaks is not enough to cause such drastic changes in the angular distributions and it must therefore be concluded that the initial states of the emitted Auger electrons are responsible. This

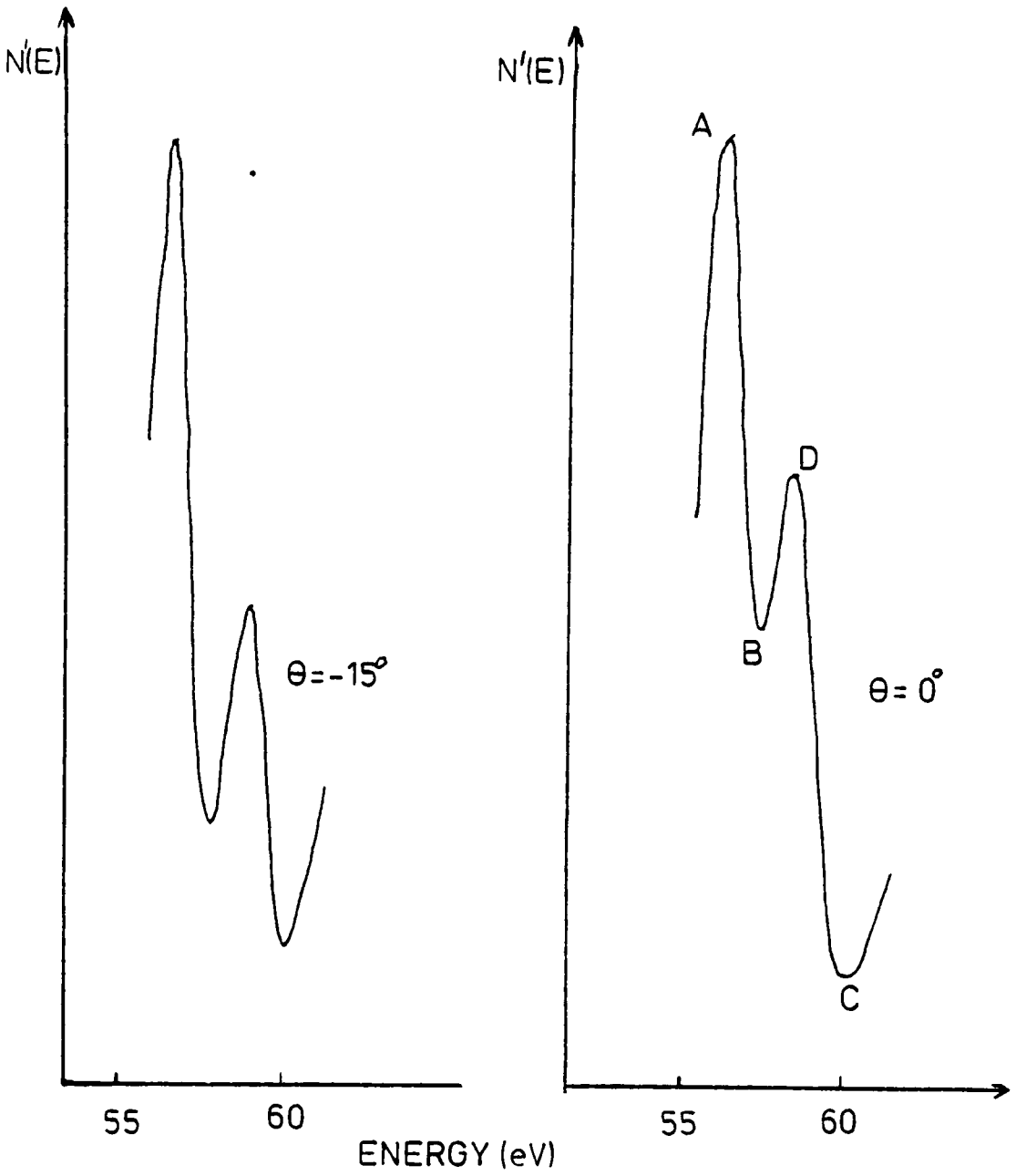
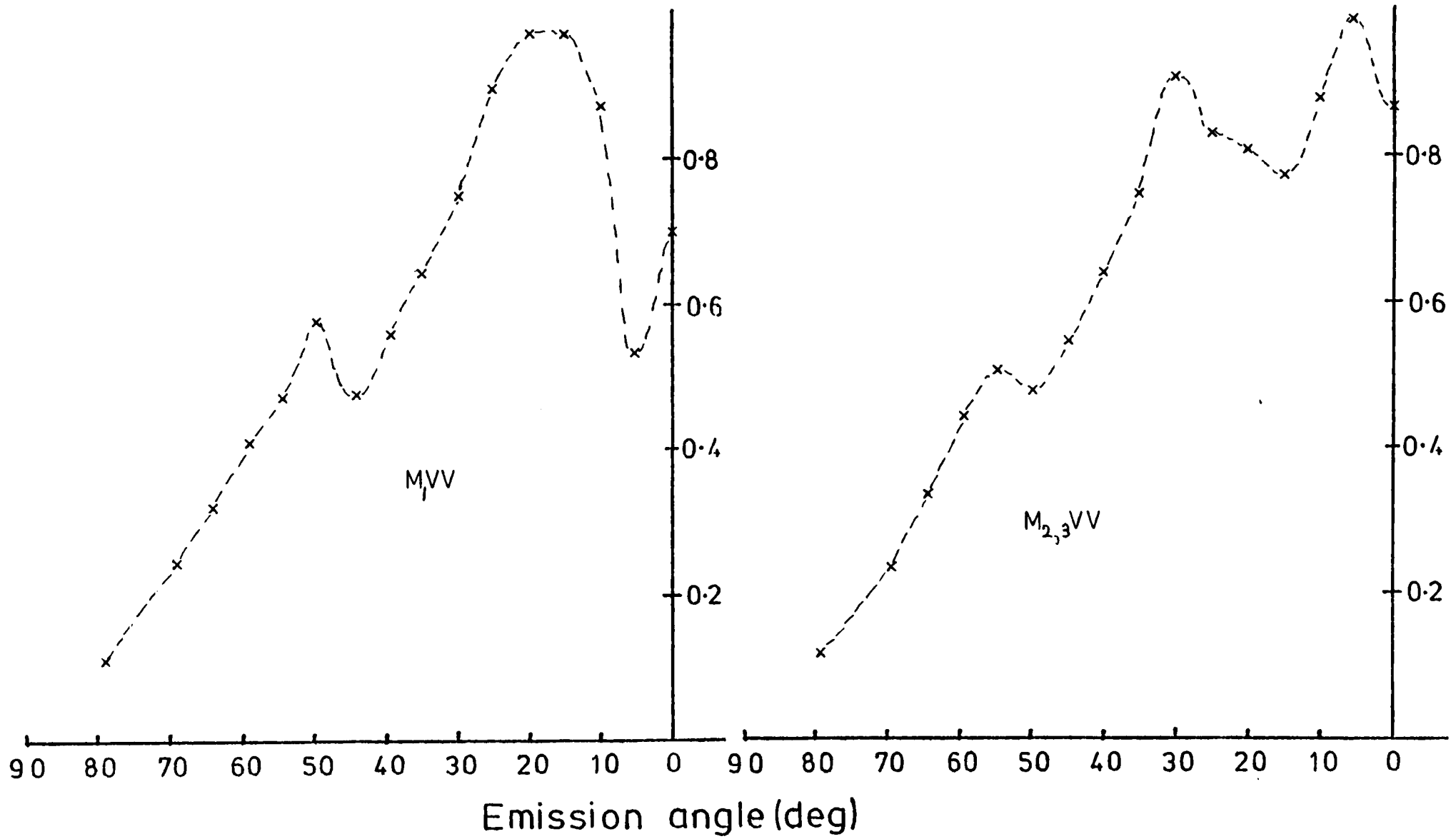


Fig.4.9 Copper $M_{2,3}VV$ line shapes at two angles of emission from copper(111) surface in $\langle 11\bar{2} \rangle$ azimuth

$E_p = 1500eV, \theta_p = 30^\circ$

Fig.4.10 Angular distributions of copper M_1VV and $M_{2,3}VV$ signals from copper(111) surface in $\langle 01\bar{1} \rangle$ azimuth, E_p=1500eV, θ_p=30°



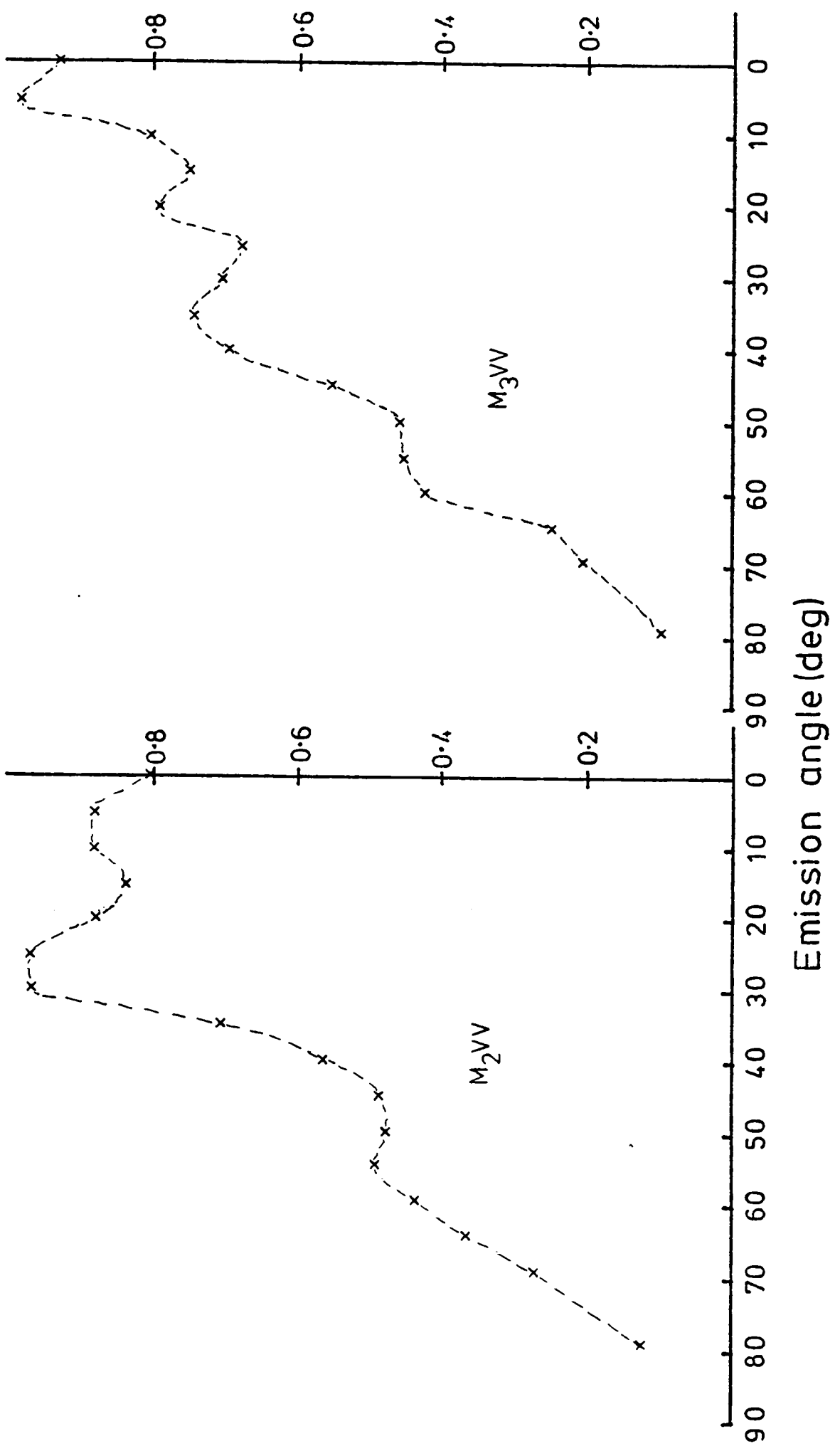


Fig.4.11 Angular distributions of copper M_2VV and M_3VV signals from copper(111) surface in $\langle 01\bar{1} \rangle$ azimuth, E_p=1500eV, θ_p=30°

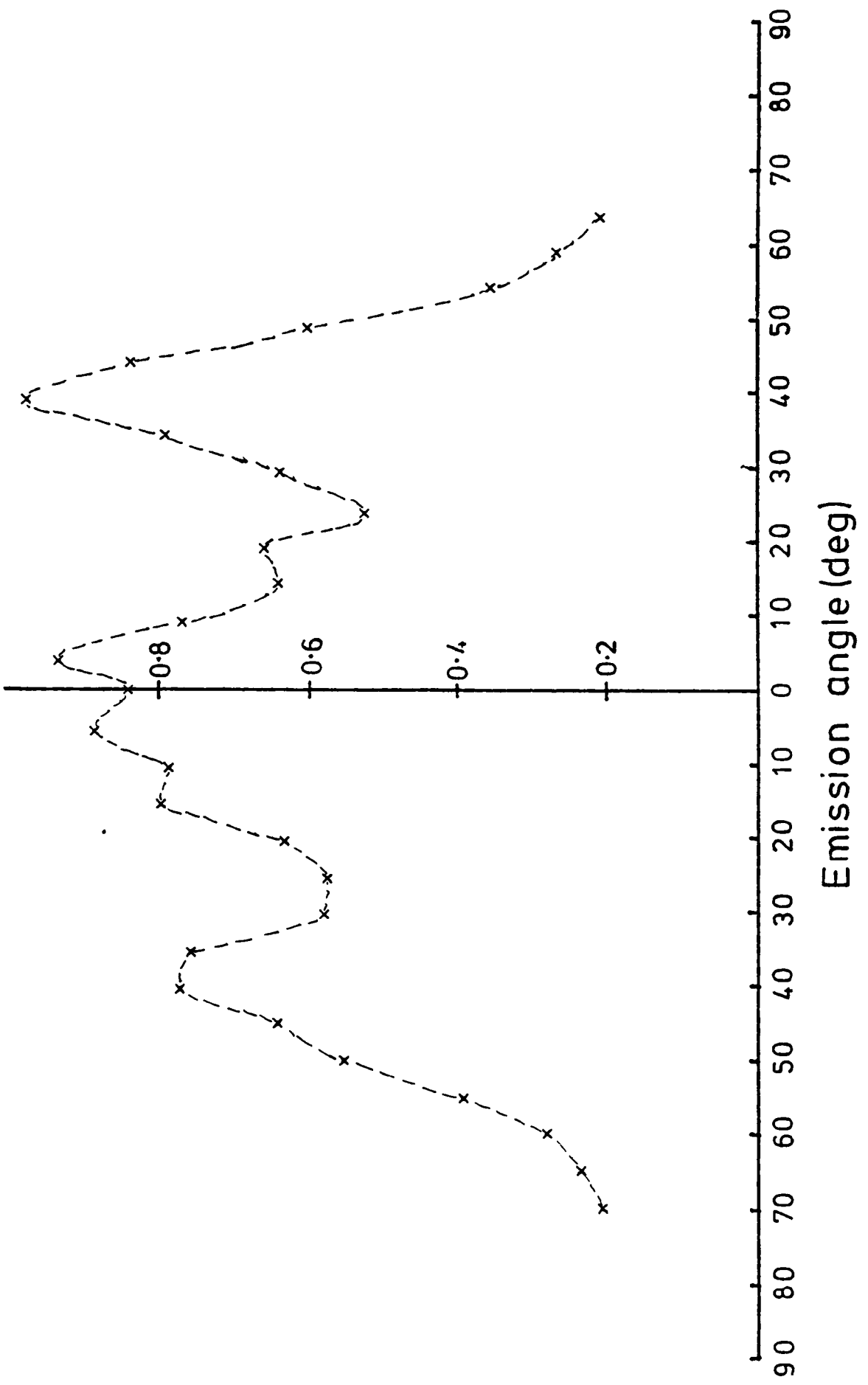


Fig.4.12 Angular distribution of copper $M_{2,3}VV$ signal from copper(111) surface in $\langle 11\bar{2} \rangle$ azimuth

E_p=1500eV, θ_p=±30°

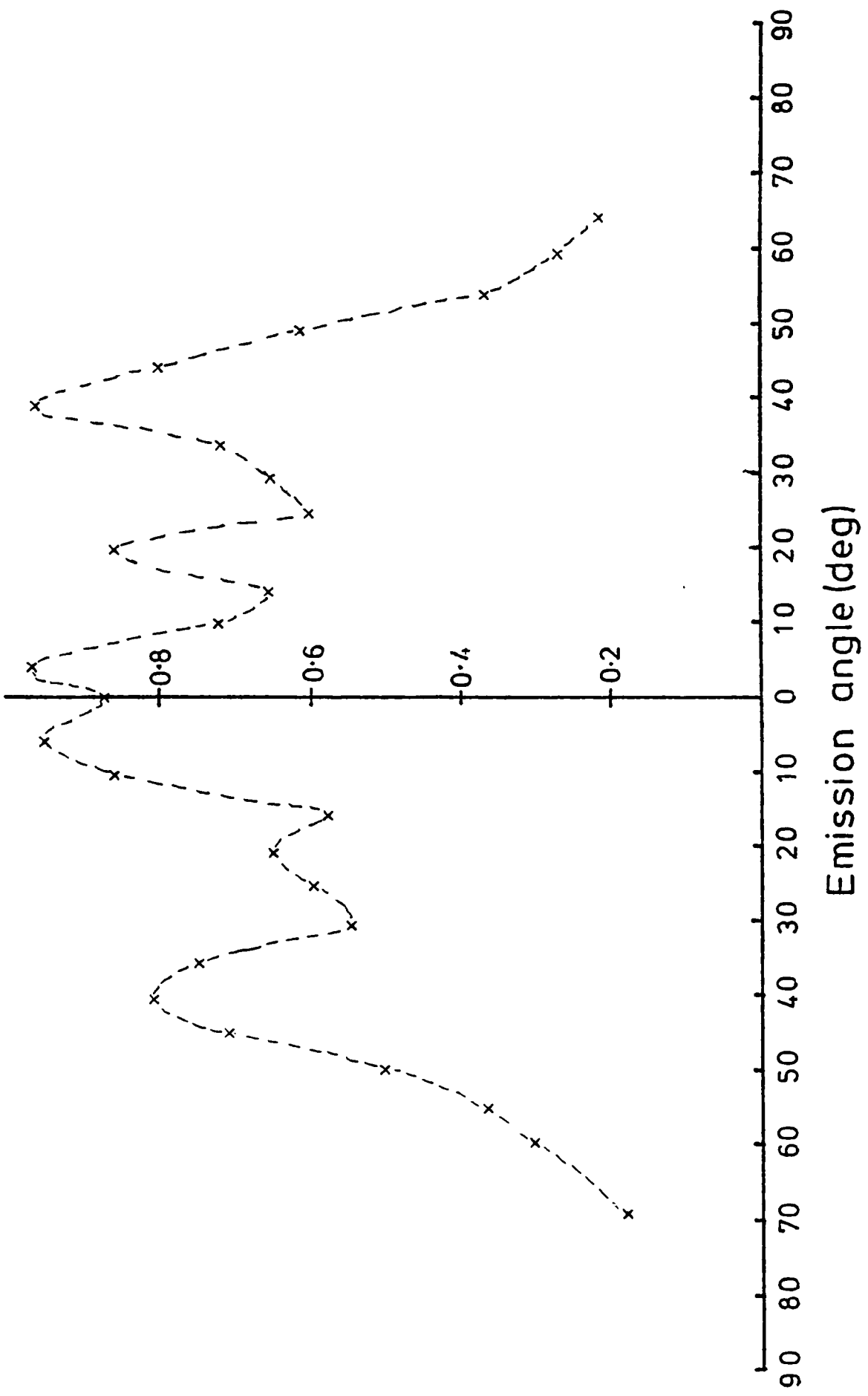


Fig.4.13 Angular distribution of copper M_2VV signal from copper(111) surface in $\langle 11\bar{2} \rangle$ azimuth, E_p=1500eV, θ_p=±30°

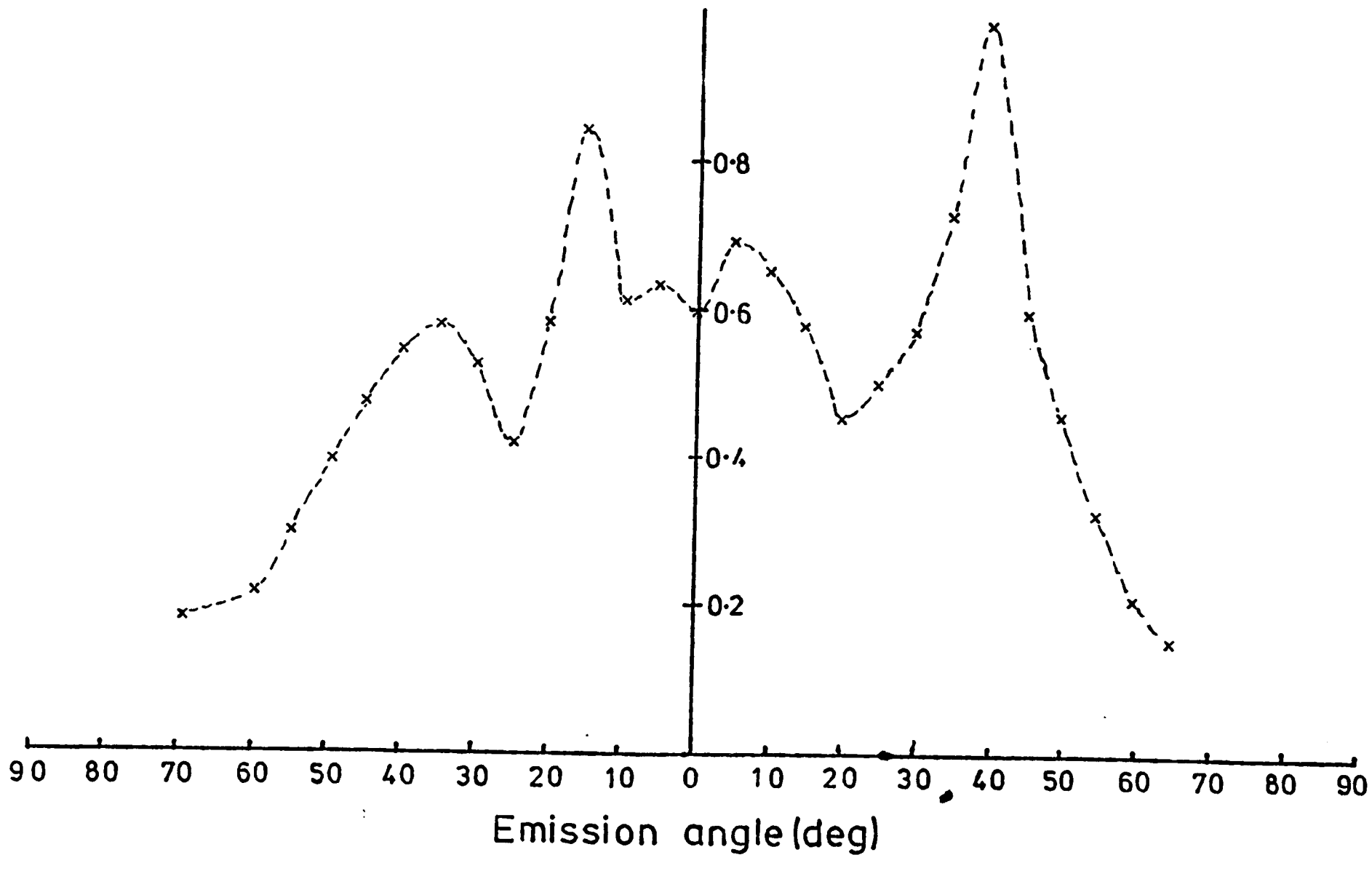


Fig.4.14 Angular distribution of copper M_3VV signal from copper(111) surface in $\langle 11\bar{2} \rangle$ azimuth, E_p=1500eV, θ_p=±30°

of course means that any theoretical model (e.g. Aberdam et.al. (1978)) that uses only one type of wavefunction to describe the initial state of the $M_{2,3}VV$ copper Auger electrons cannot hope to succeed in describing the experimental angular distributions. However it may be the case that either of the M_2VV or M_3VV peaks is associated with only one type of source wavefunction. Aberdam et.al. (1976, 1978) have calculated the angular profile of the copper $M_{2,3}VV$ signal for Copper (111) in the $\langle 11\bar{2} \rangle$ azimuth using source wavefunctions described by l_a, $m_{l_a} = 0, 0$ and l_a, $m_{l_a} = 2, 0$ (Aberdam et.al. (1976)) and $l_a = 3$ (Aberdam et.al. (1978)). The angular profile calculated with $l_a = 3$ is in fact obtained by calculating angular profiles for each possible value of m_{l_a} and then averaging over them all to give a composite profile independent of m_{l_a}. The best agreement between any of these calculated profiles and the experimental profiles is to be found between the $l_a = 3$ theoretical profile and the M_2VV experimental profile and this is illustrated in figure 4.15. There is virtually no agreement between the theoretical profiles with l_a, $m_{l_a} = 0, 0$ or l_a, $m_{l_a} = 2, 0$, and any experimental profile. From this comparison it can be seen that the $l_a = 3$ source wavefunction is an important factor in describing the M_2VV angular profile. The agreement however is far from perfect and there still remains the problem of finding a suitable source wavefunction to describe the M_3VV angular profile. Assuming the theoretical models are basically sound, the work of Lindsay and Kinniburgh (1977) discussed in 4.2.2. should indicate which other values of l_a are important in describing the copper $M_{2,3}VV$ signal. Their results, quoted in tables 1 and 2, show that $l_a = 3$ Auger electrons account for, 78% of the $M_{2,3}VV$ peak when theory is compared to experiment for the copper (100) surface and 57% of the $M_{2,3}VV$ peak for the copper (110) surface. The $l_a = 3$ Auger electrons were found to dominate in all the comparisons of theory with experiment made by Lindsay and Kinniburgh (1977). Unfortunately no other values of l_a were found to contribute in a consistent way to the $M_{2,3}VV$ angular profiles and in table 2 it can be seen that $l_a = 2$ Auger electrons, which should be forbidden because of

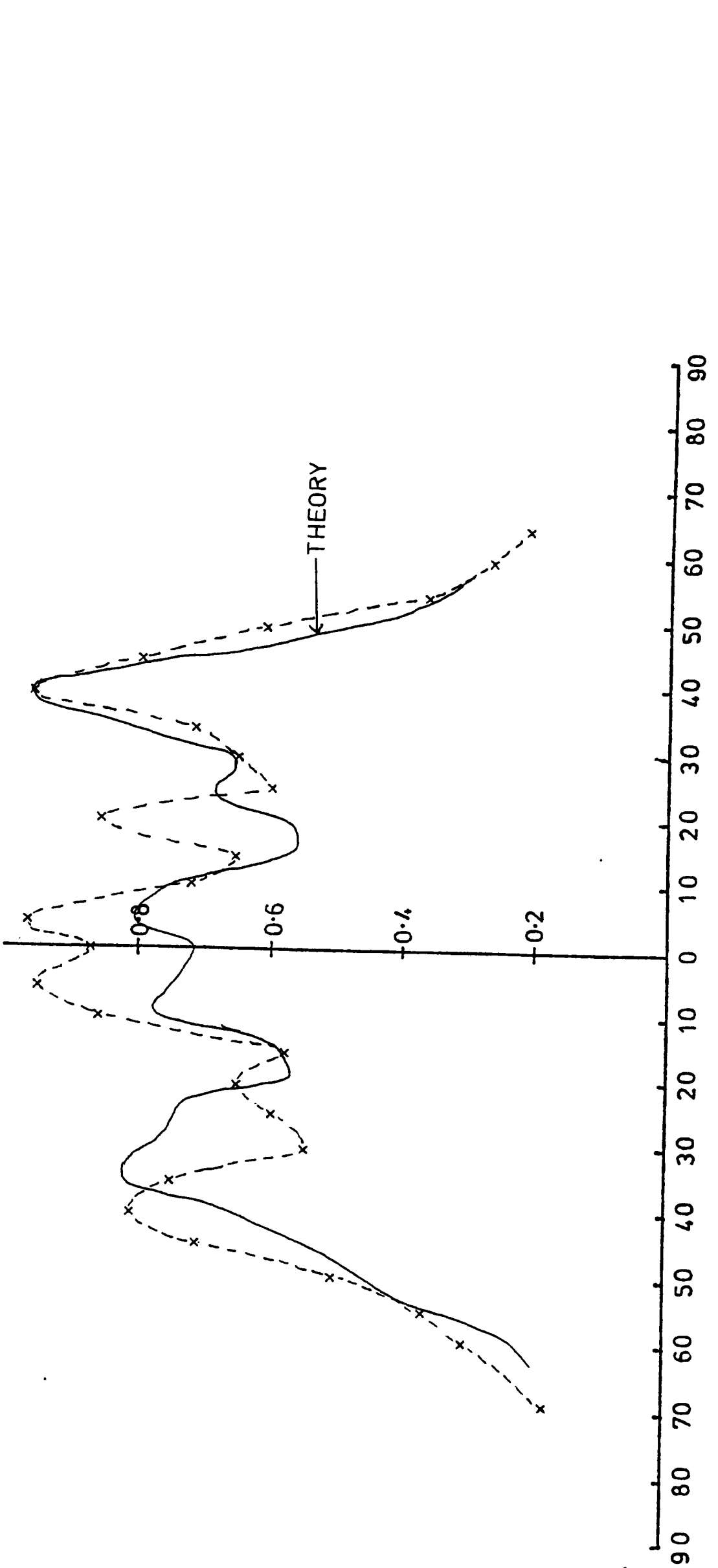


Fig.4.15 Comparison of theory due to Aberdam et.al. (1978) using $l_a=3$ source wavefunction, with experimental angular distribution of copper M_2VV signal from copper (111) surface in $\langle 11\bar{2} \rangle$ azimuth.

selection rules and parity conservation, contribute 25% of the weight to the overall $M_{2,3}VV$ signal. Thus no indication of other important values of l_a can be obtained in this way. Another way of finding important values of l_a is to calculate the relevant transition rates and this will now be discussed.

4.5.5.(b) Transition Rates

Aberdam et.al. (1978) justified their choice of $l_a = 3$ on the basis of transition rates calculated by Asaad (1963) using matrix element, calculated in j-j coupling, according to McGuire (1971). Although these calculations apply strictly only to free atoms, the fact that the solid state copper Auger spectra are atomic like (Antonides et.al. (1977)) indicates that these transition rates should still be reasonable. On this basis Aberdam et.al. (1977) showed that $l_a = 3$ Auger electrons account for 98% of either the M_2VV or M_3VV signal (assuming their nickel and copper results are similar). This then, gives no indication of what value of l_a, might be appropriate to describe the M_3VV peak and in fact it says that the values of l_a should be the same for both peaks. In view of the importance of this result in trying to understand the initial states of the copper $M_{2,3}VV$ Auger electrons the calculations of Aberdam et.al. (1978) were examined in detail and a number of errors were found.

In table 3 (Aberdam et.al. (1978)) for the ss configuration they say $D(1) = E(1) = 0{\cdot}49$. These are in fact the values of McGuire's (1971) matrix elements $D(1,1)$ which are related to $D(1)$ by an equation of the type (McGuire (1971))

$$D(\lambda) = \frac{\sqrt{4\pi}}{2\lambda+1} \; D(\lambda, l_a)$$

and therefore the correct value of $D(1)$ should be $0{\cdot}579$. The quoted transition probability for the pp configuration with $l_a = 1$ reads

$$\frac{5}{10}\,(D(2)+E(2))^2 + \frac{9}{5}\,(D(2)-E(2))^2$$

This should in fact read

$$\frac{9}{5}\,(D(2)-E(2))^2 + \frac{7}{5}\,\tau^2(D(2)+E(2))^2$$

where $\tau = 1$ or $-\frac{1}{2}$ (see Asaad (1963) for details)

These errors appear in the evaluation of transition rates for aluminium but they do cast doubt on the validity of the calculations performed for copper where only the results were quoted.

Aberdam et.al. (1978) must also have had problems finding suitable matrix elements, in the tables of McGuire (1971), for the $M_{2,3}\,M_{4,5}\,M_{4,5}$ transition since no Super Coster-Kronig matrix elements involving an $M_{2,3}$ core hole are tabulated therein. It appears that Aberdam et.al. (1978) have used $L_{2,3}MM$ matrix elements assuming that the angular momentum quantum number of the core hole is the important parameter. A comparison of Super Coster-Kronig matrix elements for the $M_{2,3}MM$ transition in McGuire (1977) with matrix elements for the $L_{2,3}MM$ transitions (McGuire (1971)) show that there are major differences between them and therefore the approach of Aberdam et.al. (1978) appears to be invalid due to the use of inappropriate data.

It will now be shown how the dominant values of l_a can be predicted using the data in McGuire (1977) where the transition rates and matrix elements are specifically evaluated for the $M_{2,3}\,M_{4,5}\,M_{4,5}$ transition. In the absence of configuration interaction (shown to be small by McGuire (1977)) the transition rate (cf equation 2 McGuire (1977)) is given by

$$\frac{76}{45}\,R_1(1122)^2 + \frac{552}{1715}\,R_3(1122)^2 - \frac{24}{35}\,R_1(1122)\,R_3(1122) + \frac{28}{15}\,R_1(1322)^2$$

$$+ \frac{64}{245}\,R_3(1322)^2 - \frac{16}{35}\,R_1(1322)\,R_3(1322) + \frac{100}{343}\,R_3(1522)^2$$

Where R_k (a b c d) is the general Slater integral, Chattarji (1976). The terms a b c d refer to the l values of, the core hole, the emitted Auger electron, and the two final holes in the atom. Using the values of R_k (a b c d) given in table 7 of McGuire (1977) for the $3p - 3d^2$ configuration the transition rates associated with each value of l_a are :-

Table 3

l_a	transition rate
1	4·79
3	124
5	0·02

transition rate in units of

4×10^{12} sec^{-1}

This agrees with the results of Aberdam et.al. (1978) showing that 96% of the copper $M_{2,3}VV$ peak is accounted for by Auger electrons with l_a=3.

Thus the evidence concerning the composition of the copper $M_{2,3}VV$ peak can be summarised as follows. According to both transition rate calculations at least 96% of the $M_{2,3}VV$ transition involves $l_a = 3$ Auger electrons. The results of Lindsay and Kinniburgh (1977) indicate that $\sim$65% of the peak involves $l_a = 3$ Auger electrons but no consistent contribution from other values of l_a could be found. Finally the two different angular distributions of the M_2VV and M_3VV peaks show that two types of initial state are involved. This last result could be explained by saying that different values of l_a are associated with each peak but this would be inconsistent with the transition rate calculations. Since the results of Lindsay and Kinniburgh (1977) give no indication what the other values of l_a might be, it would be worthwhile considering another explanation which could reconcile all the above observations.

The calculations of Aberdam et.al. (1978) and Lindsay and Kinniburgh (1977) both assume that only the value of l_a is important in determining the form of the angular profiles and they therefore calculate an angular profile for each of the $(2l_a + 1)$ possible values of m_{l_a} and add them together to produce one angular profile characteristic of l_a. Aberdam et.al. (1978) justify this procedure by saying that their experimental data are averaged over the 4·5V peak to peak modulation voltage used and therefore neglecting the contribution of m_{l_a} and hence band structure effects is justified. This justification ceases to be valid for the experiments performed here because the modulation voltage used was only 0·6V peak to peak, eight times smaller

than that used by Aberdam et.al. (1978).

Lindsay and Kinniburgh (1977) justify this same assumption on the basis of work by Cleff and Mehlhorn (1974(a)), who showed that the anisotropy in Auger emission resulting from the initial ionisation of atoms in the gas phase was less than 6%. Due to the rotational symmetry of their experiment, where the electron beam used to ionise the atoms defines the quantization axis, only variations in Auger current as a function of angle θ between the direction of Auger emission and the incident electron beam could be detected. This experimental arrangement effectively averages the emission anisotropies over the azimuthal angle ϕ that may be detected if the rotational symmetry was broken by some external field. This averaging over ϕ is reflected in the theoretical treatment of Cleff and Mehlhorn (1974(b)) where they sum incoherently over the magnetic quantum numbers to ensure that the rotational symmetry of the system is observed. The situation for an atom located in a crystal is very different from that in the gas phase where the symmetry of the system is not defined by one axis of rotation but by the many symmetry axes associated with the crystal. It therefore seems likely that removing the rotational symmetry in the experiment of Cleff and Mehlhorn (1974(a)) could produce emission anisotropies greater than 6%, and thus averaging over m_{l_a} for the case of an atom in a crystal lattice would not be a good approximation.

The rejection of these assumptions now allows a different explanation of the experimental profiles to be given. The two different initial states, implied by the different angular distributions of the M_2VV and M_3VV signals, could both be associated with the same value of $l_a = 3$, but with different values of m_{l_a}. This would be consistent with the transition rate calculations and also with the dominance of $l_a = 3$ terms already found by Aberdam et.al. (1978) and it may also explain why the same combination of l_a values could not explain all the experimental results studied by Lindsay and Kinniburgh (1977)

4.5.5.(c) The $M_{2,3}VV$ signal in copper

The different angular distributions observed for the M_2VV and M_3VV signals of course implies that the line shape of the copper $M_{2,3}VV$ signal is a function of emission angle which can give important information about the nature of the transition. Madden et.al. (1978) have studied the $M_{2,3}VV$ line shape in detail and they conclude that the peak is simply a superposition of two identical peaks of the type M_2VV and M_3VV seperated by the spin-orbit splitting of the M_2 and M_3 holes. They were however unable to explain the difference in the theoretical and experimental intensity ratio of the M_3VV to M_2VV peaks found to be respectively 2:1 and 1·3:1. The data in figure 4.a shows that the intensity ratio is a function of angle with the ratios being 2:1 at $\theta_e = -15^\circ$ and 1:1 at $\theta_e = 0^\circ$. These ratios are obtained from data in the derivation mode so the values may not be directly comparable to those of Madden et.al. (1978) but the difference in the two ratios is certainly significant.

Thus it appears that the conclusion arrived at by Madden et.al. (1978) saying that two identical M_2VV type peaks superpose to give the $M_{2,3}VV$ peak is wrong, which lends support to the model of McGuire (1977) (see § 4.5.2) which associates different spectral terms with each peak of the $M_{2,3}VV$ doublet.

4.5.6. Conclusions

The detailed lineshape of the copper $M_{2,3}VV$ transition has been examined as a function of emission angle for the first time. The results show that each peak in the doublet exhibits its own characteristic angular profile which must indicate that the initial state associated with each peak is different. An explanation is proposed whereby different values of m_{l_a} are associated with the different initial states.

Unfortunately this explanation would complicate an already difficult theoretical task still further by demanding a knowledge of the correct values of, not only l_a, but also m_{l_a}.

4.6. Summary

In this chapter the angular profiles of the silicon $L_{2,3}VV$ signal from the silicon (111) 7x7 surface and the angular profiles of the copper $M_{2,3}VV$ signal from the copper (111) surface have been studied.

The emission angular distributions of the silicon $L_{2,3}VV$ signal were shown to be dependent on the incident beam conditions and the results were interpreted to mean that the top few layers of the crystal produce angular distributions different to those of the sub-surface layers. This mechanism was also thought to be partly responsible for the rather structureless angular profiles usually observed.

In marked contrast, the angular distributions of the copper $M_{2,3}VV$ signal were shown to contain a large amount of structure and the line shape itself was shown to be a function of emission angle. Different values of m_{l_a} were thought to be associated with the two different initial state implied by these results.

The results from the silicon may be peculiar to reconstructed surfaces but the results from the copper surface will probably apply, to a greater or lesser extent, to all transition metal surfaces and perhaps to all materials producing quasi-atomic Auger spectra. A detailed explanation of the results from copper demands an extremely detailed knowledge of the emission process in solids, which is currently not available, and hence there seems to be no readily exploitable way of obtaining crystallographic information from such angular profiles.

Chapter 5.

Angular Distributions of High Energy Auger Electrons from Clean Single Crystal Surfaces

		page
5.1	Introduction	80
5.2.1	The Silicon KLL Angular Distributions	81
5.2.2	Experimental	81
5.2.3	Results	82
5.2.4	Discussion	83
5.3.1	The Copper LVV Angular Distributions	86
5.3.2	Introduction	86
5.3.3	Experimental	86
5.3.4	Results	87
5.3.5	Angular Momenta of the Emitted Auger Electrons	88
5.3.6	Discussion	90
5.4.	Final State Effects and Kikuchi Correlation	93
5.5	Summary	96

5.1. Introduction

In the previous chapter the discussion was confined to low energy Auger emission and it was shown that the initial state of the emitted electron can profoundly affect the emission angular distribution. As these initial state effects are not well understood much work still remains to be done before any crystallographic information can be obtained from angular profile obtained at low energies.

In this chapter the high energy Auger transition ($\sim$1000eV) will be investigated with a view to understanding the relative contributions of the initial and final state to the emission angular distribution. Very little work has been done in this area especially regarding the initial state contribution to the overall angular distribution. The angular distribution of the sodium KLL(^{1}D) (990eV), the copper $L_3\ M_{4,5}\ M_{4,5}$ (920eV) and the silver $M_{4,5}VV$ (355eV), $M_{4,5}\ N_{2,3}V$ (303eV) and $M_{4,5}\ N_1\ V$ (265eV) Auger electrons have been measured (Siegbahn et.al. (1970), Zehner et.al. (1977), Matsudaira and Onchi (1978)) from the NaCl (100), Cu (100) and Ag (100) surfaces respectively. The data from the Ag (100) surface is the most significant from the point of view of initial state effects since all the peaks measured exhibited exactly the same angular distributions, indicating that either the initial state wavefunctions for the three transitions are the same or that the initial state wavefunction does not influence the angular distribution. Similar conclusions can be drawn from the work on NaCl (100) by Siegbahn et.al. (1970) who showed that the angular profile of the Sodium 2s photoelectron emission at 1190eV was virtually identical to the sodium KLL($^1D_2$) Auger emission at 990eV. Even the sodium 1s photoelectron angular distribution at 414eV was very similar to the angular distributions of the other two emissions at $\sim$1KeV. In a similar way the chlorine $2p_{3/2}$ photoelectrons at 1288eV and 1055eV produced very similar angular distributions to the chlorine 3p photoelectron angular distribution at 1249eV. All of this evidence seems to suggest that the high energy

(~1KeV) electron angular distributions are relatively insensitive to initial state effects. However recent work by Chang (1977) on the silicon KLL transition at ~1600eV from silicon (111) seems to suggest that the various members of the KLL series do not all exhibit the same angular profiles indicating a possible influence of the initial state on the emission angular distributions. To try to understand these effects, the angular distributions of various members of the silicon KLL series and copper LVV series have been measured from silicon (111) and copper (111). In the case of the copper LVV results, calculations have been performed to see if certain values of l_a can be associated with particular peaks in the series.

In all the results from the (100) surfaces of NaCl, Cu and Ag, peaks in the emission angular profiles have appeared close to the ⟨110⟩ direction and certain other crystallographic directions although the other directions have not always been the same ones. These correlations have also been observed for the results from Si (111) and Cu (111) and the results have been compared with the elastic angular distributions corresponding to the back reflection Kikuchi patterns.

5.2.1. The Silicon KLL Angular distributions

5.2.2. Experimental

The silicon (111) specimen was prepared and oriented in the UHV chamber using the methods described previously. In situ cleaning was done by heating the specimen to ~1200°C for ~10 mins. and this usually reduces the carbon signal to less than $\sim \frac{1}{80}$ the peak to peak height of the silicon LVV signal. The high energy limit of the minature electron gun used in the goniometer was 2·4KeV and consequently the signal strength of the silicon KLL series at 1600eV was rather low and time constants of 10 seconds had to be used in the lock-in amplifier. To further improve the signal to noise by increasing the time constant was found to be impractical since small variations in the beam current (~1%) were found to occur in times comparable with the long scan times

(750 seconds) necessary. Attempts were made to regulate the beam current by controlling the emission current from the gun cathode (the circuit is shown in appendix A). Although the cathode emission current was controlled to much better than 1% the overall beam current could still vary by $\sim 1\%$ presumably due to changes induced in the electron trajectories by changes in the wehnelt bias, which in turn changes the fraction of the emitted electrons transmitted through the aperture in the first anode of the gun. Due to the nature of the power supplies used it was impossible to measure the actual beam current and hence no direct beam current control was possible.

5.2.3. Results

A typical derivative spectrum of the silicon KLL series is shown in figure 5.1. The peak assignments are taken from Chattarji (1976), the unlabelled peaks are due to energy losses associated with the strongest peaks in the spectrum. According to Chang (1977) the relative amplitudes of the energy loss peak at 1600eV and the $KL_1L_2(^1P)$ peak at 1560eV reverse on rotating from 0^o to 5^o in his apparatus. It should be noted here that the silicon (111) specimen used by Chang had $\sim 10A^o$ of oxide present but that the peaks referred to originate from elemental silicon in the substrate. To try and find the origin of Chang's observation the angular distributions of the silicon KL_2L_3 (^1D) (1620eV) peak, the energy loss peak at 1600eV and the $KL_1L_2(^1P)$ (1560eV) peak were measured in the $\langle 11\bar{2} \rangle$ azimuth. Figure 5.2 shows the angular distribution of the loss peak at 1600eV and the main $KL_2L_3(^1D)$ (1620eV) peak. Within the rather broad limits set by the poor signal to noise ratio the angular distributions are similar except for a peak at $\sim 55^o$ in the 1600eV signal. This is very difficult to explain since an energy loss peak involving only plasmon excitation should exhibit an almost identical angular distribution to that of the no loss peak. The large variation in intensity of $KL_2L_3(^1D)$ peaks with emission angle is consistent with Chang's observation for that peak. Figure 5.3 shows the angular distribution of the $KL_1L_2(^1P)$ (1560eV) peak

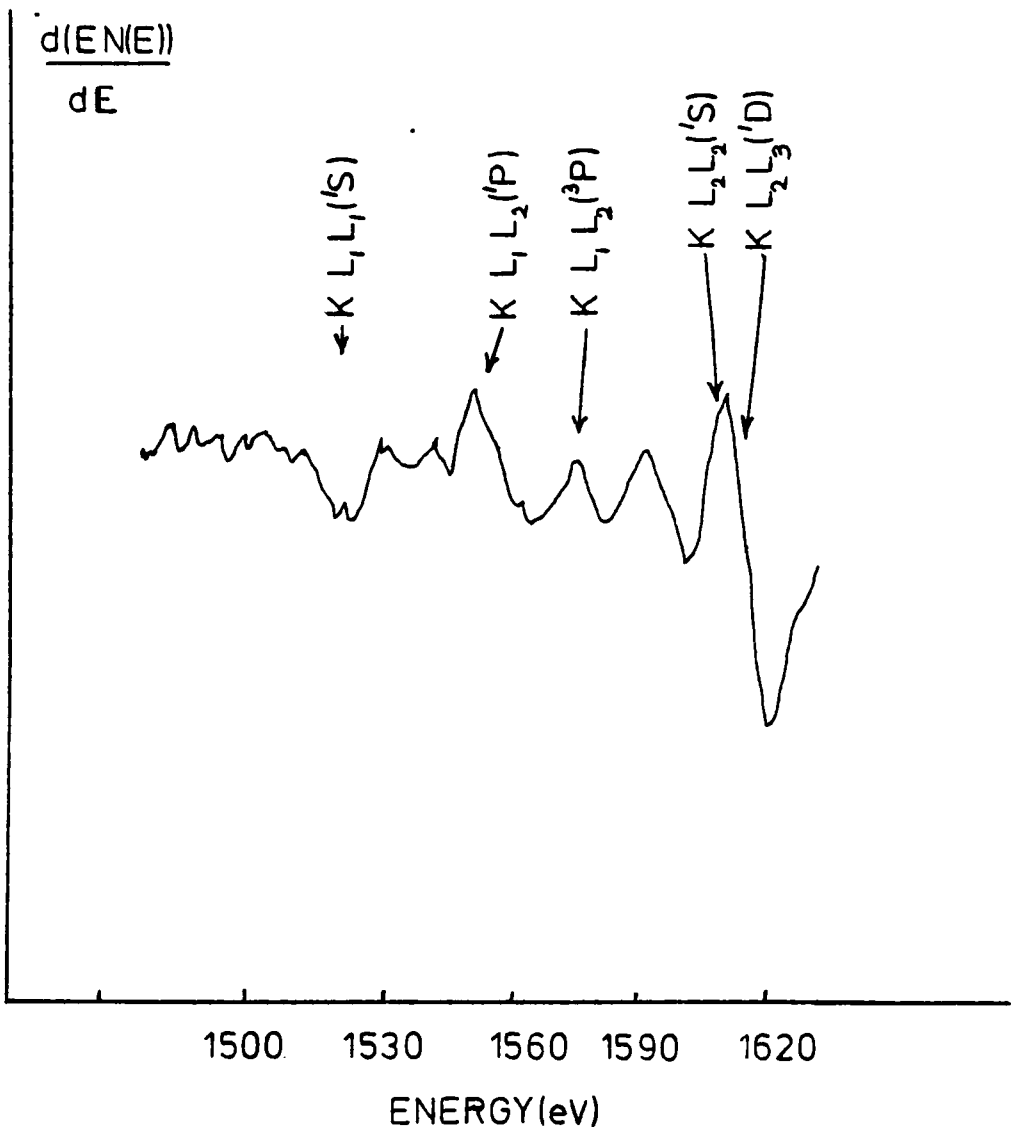


Fig.5.1 Derivative spectrum of Silicon KLL transition from silicon(111) surface in $\langle 11\bar{2} \rangle$ azimuth.

E_p=2400eV, θ_p=0°, θ_e=15°

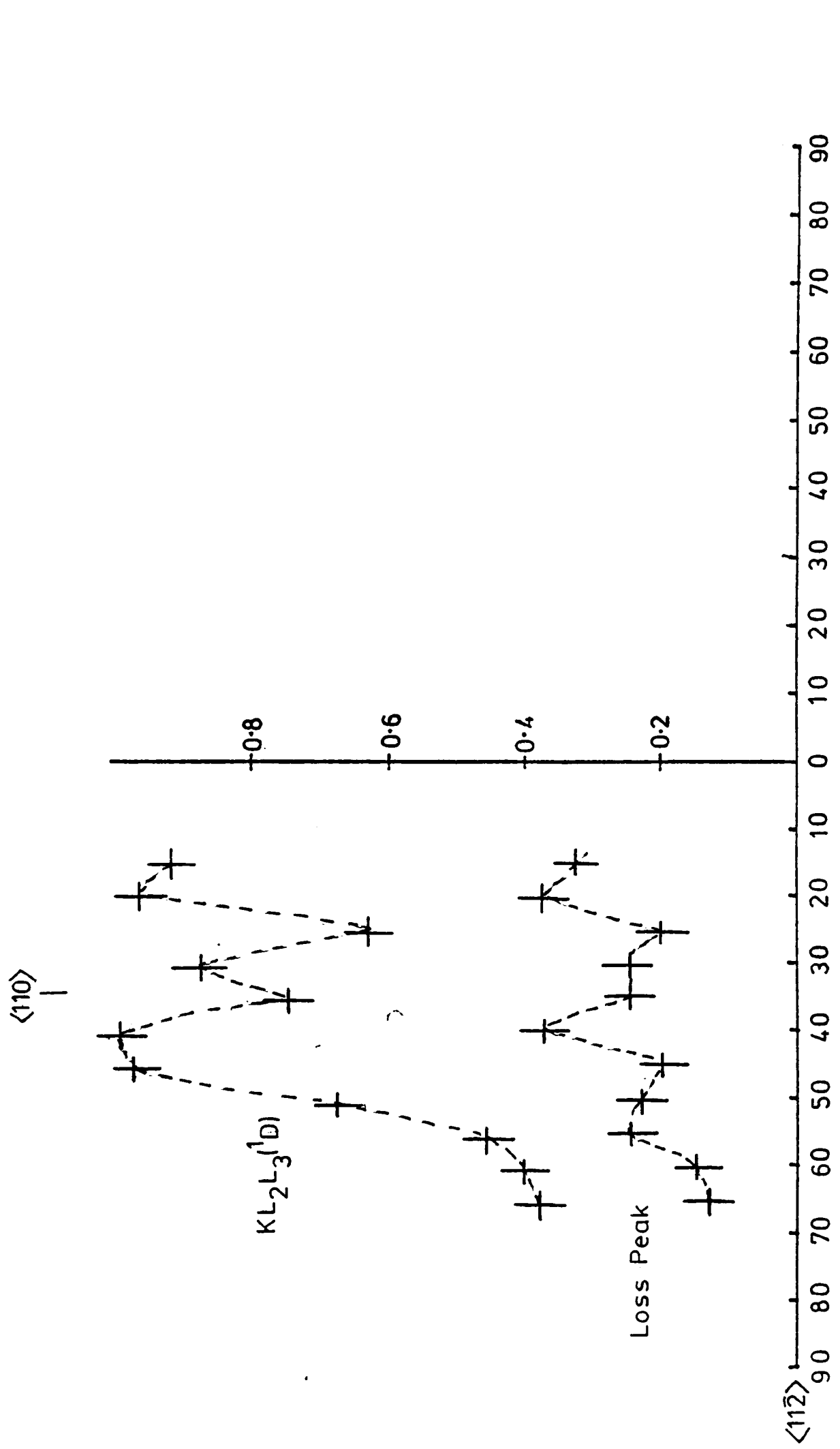


Fig.5.2 Angular distribution of $KL_2L_3(^1D)$ signal and plasmon loss signal from the silicon(111) surface in the ⟨11$\bar{2}$⟩ azimuth, E_p=2400eV, $\theta_p = 24^o$

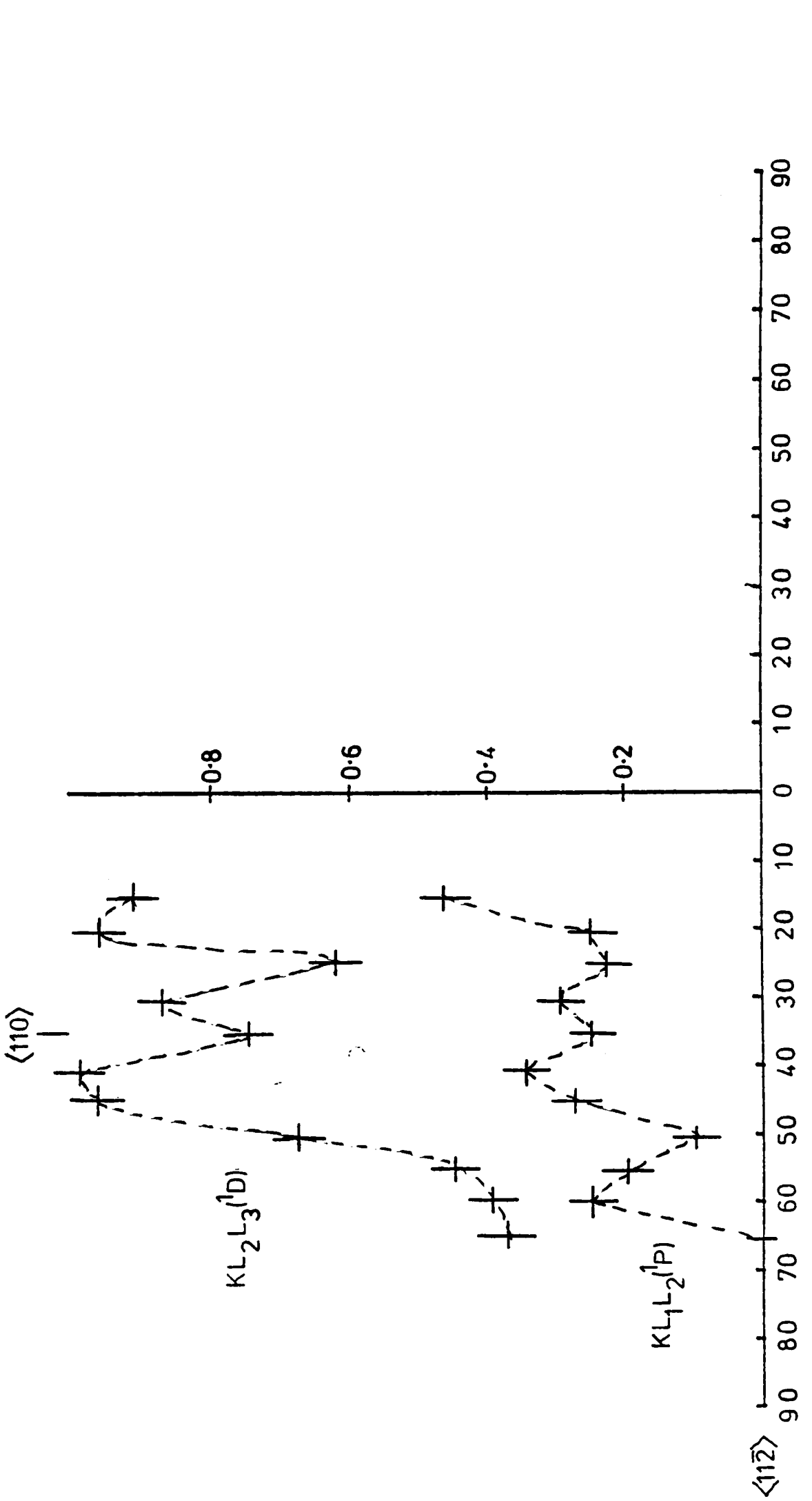


Fig.5.3 Angular distributions of $KL_2L_3(^1D)$ and $KL_1L_2(^1P)$ signals from the silicon(111) surface in the ⟨11$\bar{2}$⟩ azimuth, E_p=2400eV, θ_p=24°

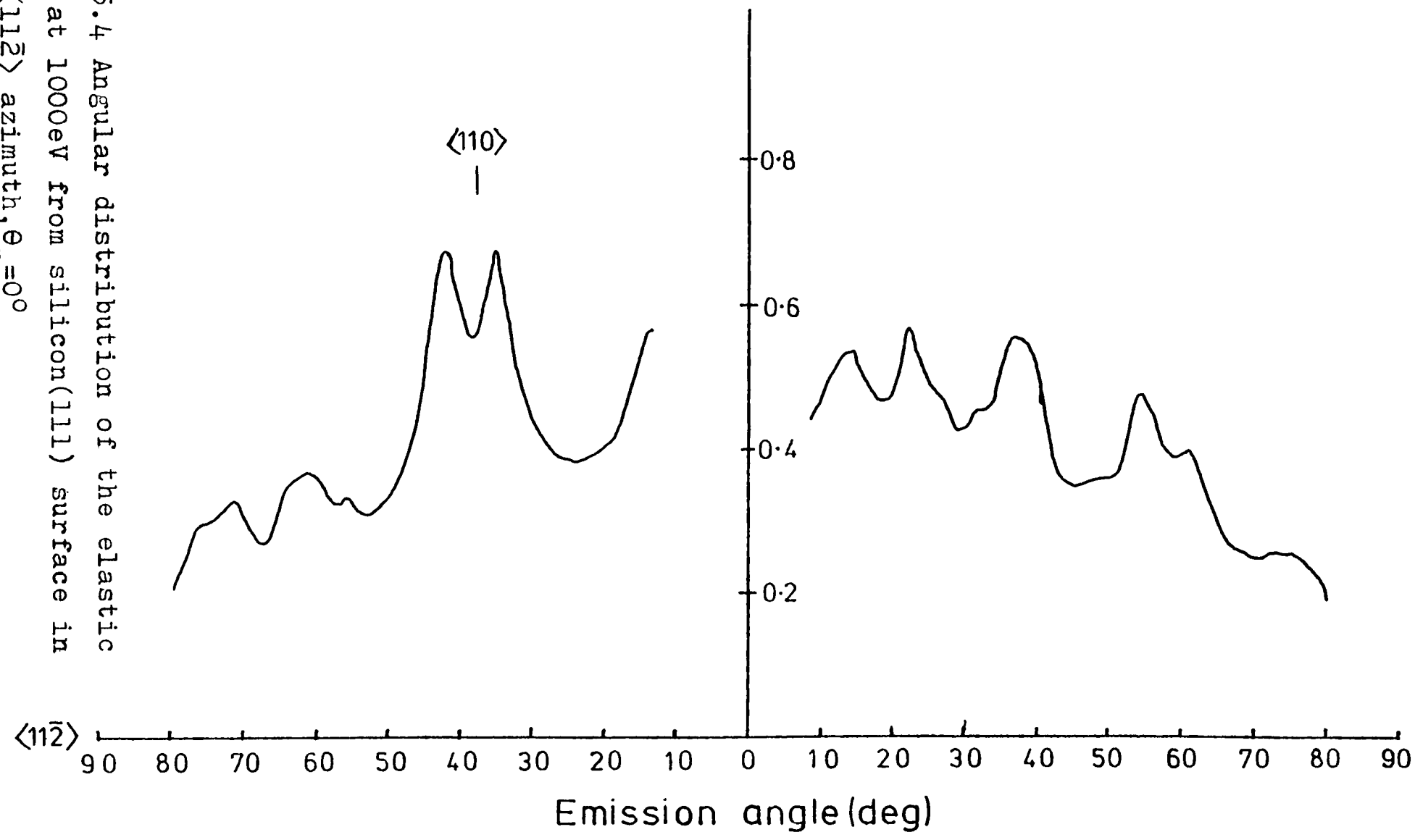
again compared with the main $KL_2L_3(^1D)$ (1620eV) peak. The two angular profiles are similar except for the peak at $\sim 60^\circ$ in the $KL_1L_2(^1P)$ profile. The reversal in relative intensities between the 1600eV loss peak at the $KL_1L_2(^1P)$ peak observed by Chang (1977) does not appear to occur in this data although there is a change in intensity ratios between either of the low energy peaks, the $KL_1L_2(^1P)$ or the loss peak, and the main $KL_2L_3(^1D)$ peak at 50° - 60°.

The two main peaks in the $KL_2L_3(^1D)$ angular distribution lie on either side of the $\langle 110 \rangle$ direction at $\sim 35^\circ$ from the (111) surface normal. This is very similar to the Kikuchi pattern at 1000eV and in figure 5.4 the angular distribution of the elastic peak at 1000eV corresponding to the Kikuchi pattern is shown for the $\langle 11\bar{2} \rangle$ azimuth.

5.2.4. Discussion

There is obviously a very marked difference in the amount of angular structure present in the angular profiles of the silicon KLL (1600eV) peaks as compared to the LVV (92eV) peak. This is different from the observations of Matsudaira and Onchi (1978) where the intensity variations of the high and low energy peaks in silver (100) were of similar magnitude but shifted in angular position. It was proposed in the previous chapter that part of the reason for the smooth angular profile of the silicon LVV signal was the reconstructed overlayer producing an angular profile different from that of the sub-surface layers which tends to average out structure in the total angular distribution. Since this mechanism is due to the crystallography of the surface it might be expected that a similar overlayer would occur for the high energy angular distributions. However this type of effect would be much less marked for the high energy transitions since the inelastic mean free paths of the 1600eV KLL electrons are about four times those of the 92eV LVV electrons and therefore the contribution of the surface layer to the overall angular distributions is only $\sim 10\%$ as opposed to $\sim 40\%$ for the LVV peak. This implies that the high

Fig.5.4 Angular distribution of the elastic peak at 1000eV from silicon(111) surface in the $\langle 11\bar{2} \rangle$ azimuth, $\theta_p = 0^\circ$



energy Auger angular distributions are fairly insensitive to the surface layer itself unless the signal originates in a surface atom.

Before trying to extract any information from these results, consider what sort of behaviour can be expected on the basis of the peak assignments and also what can be learnt from Chang's(1977) results. The three most prominent peaks in the silicon KLL series are the $KL_2L_3(^1D)$ / $KL_2L_2(^1S)$ at 1620eV (the stroke indicating that the two are experimentally unresolved), the plasmon loss peak associated with the 1620eV peak appearing at 1600eV and the $KL_1L_2(^1P)$ at 1560eV. It is well known that plasmon creation changes the energy but not significantly the direction of an electron (e.g. Ferrel (1956)) and therefore the 1620eV and 1600eV peaks should exhibit the same angular structure. This has been experimentally verified in the case of the elastic and plasmon loss angular distributions associated with the Kikuchi pattern in silicon (111) This is the case in Chang's (1977) results to within ~8% in terms of the peak ratios of the 1620eV and 1600eV signals. Chang (1977) comments that the relative intensity changes are large since the relative amplitudes of the $KL_1L_2(^1P)$ (1560eV) peak and the loss peak at 1600eV reverse on going from an angle of 0° to 5° in his apparatus. However it seems more sensible to compare the peak ratios of the main peak at 1620eV to the 1560eV peak, rather than involve a loss peak, and the ratio of these two peaks changes from 4·6 : 1 at 0° to 2·4 : 1 at 5°. This result can indicate one of two things. Either the angular distributions of the two signals are totally different, or the shape of the angular distributions are the same but the magnitude of the signal variations are different. It is important to distinguish between these two possibilities since totally different angular distributions for the two signals would imply that the initial state plays a major part in determining the form of the angular distribution.

The strong similarity observed in figure 5.3 between the angular distributions of the $KL_2L_3(^1D)$ and $KL_1L_2(^1P)$ peaks show that the shapes of the two

angular distributions are the same with the exception of the peak $\sim 60^{\circ}$ in the lower curve. These results do not, however, exhibit such large changes in the ratio of the two peaks as observed by Chang (1977) and hence it is difficult to understand the origin of Chang's results. The discrepancy in figure 5.3 at $\sim 60^{\circ}$ further confuses the issue but as this discrepancy also appears in figure 5.2, when the angular profiles should be the same for the reasons mentioned earlier, it is thought that the lack of a peak at $\sim 60^{\circ}$ in the main $KL_2L_3(^1D)$ peak is probably an artifact, perhaps due to the beam current instabilities already discussed.

The differences in experimental method between this work and Chang's (1977) work will now be considered to see if any explanations for these contradictory results can be found. Chang's experiments were performed by simply rotating the silicon (111) specimen, with 10Å of amorphous oxide present, in front of a CMA with a co-axial electron gun. Work to be presented in chapter 6 will show that varying the incident beam direction can alter the overall Auger signal due to diffraction of the incoming electrons. In Chang's (1977) work the incident beam direction changes on rotating the sample and hence the overall Auger yield will change due to changes in the ionisation rate of the K-shell. This however does not provide a mechanism for changing the ratios of various signals in the K-series. This leaves the 10Å oxide layer as the only other fundamental difference between the experiments. According to Thomas (1974) the silicon KLL peaks are all shifted by 3eV in the oxide and hence the peaks examined by Chang (1977) must all originate in the elemental silicon substrate so that the only effect the oxide should have on Chang's results is to uniformly attenuate all the substrate signals. Again no explanation of the experimental differences can be found. Further experiments on the KLL series were attempted but extreme difficulty associated with operating the miniature electron gun at $\sim 2{\cdot}4$KeV prevented the collection of reliable data and hence some of the problems raised have remained unresolved.

Further discussion of the final state diffraction effects will be postponed until the results from Cu (111) have been presented and analysed in terms of initial state effects on the overall angular distributions.

5.3.1. The Copper LVV Angular Distributions

5.3.2. Introduction

In this section the angular distributions of the three main peaks in the copper L_3VV series have been measured. Calculations, to determine the value of l_a discribing the initial state emitted Auger electrons in the three peaks, were then performed to see what effect, if any, l_a has in determining the shape of the emission angular distributions. Studies at high energy resolution show that each of the three peaks can be further subdivided into their various spectral terms and the possibility that different spectral terms in the $L_3M_{4,5}M_{4,5}$ peak produce different angular distributions has been investigated by measuring the detailed line shape at various emission angles. Finally the correlations between the Auger angular distributions and the Kikuchi patterns will be examined to try and understand the diffraction processes involved.

5.3.3. Experimental

The copper (111) surface was prepared and orientated in the UHV chamber using the methods described earlier. In-situ cleaning was done by a sequence of ion bombardment and annealing. The copper LVV derivative spectra were recorded using a primary beam energy of 2KeV with a modulation of 2·5vrms applied to the specimen. The various spectral terms in the $L_3M_{4,5}M_{4,5}$ line were examined in the EN(E) mode by using a 2keV primary energy and applying a 4 volt square wave to the Wehnelt cylinder, thus chopping the incident beam current. These methods provided satisfactory signal to noise ratios and it was not necessary to resort to the signal averaging techniques of Zehner et.al.

(1977) in their study of the same transition. The electron gun was always set at an angle of 30° to the surface normal in the plane defined by the emission angles. To obtain sepctra from all emission angles in the Cu (111) $\langle 11\bar{2} \rangle$ azimuth the electron gun was moved to the opposite side of the surface normal from that in which data was being collected. The results were then normalised at an emission angle of 0°. In the symmetric $\langle 01\bar{1} \rangle$ azimuth this problem did not arise since spectra were only recorded on one side of the surface normal.

5.3.4. Results

A typical copper LVV stectrum is shown in figure 5.5. and the peaks are labelled according to Andrews and Weightman (1979). The peak shapes agree well with the spectrum by Palmberg (1972). The angular profile of the three main peaks, denoted in figures 5.5 as ; $L_3M_{2,3}M_{2,3}$ (776eV) $L_3M_{2,3}M_{4,5}$ (840eV) and $L_3M_{4,5}M_{4,5}$ (920eV), in the $\langle 01\bar{1} \rangle$ azimuth are shown in figures 5.6 and 5.7. The intensities are taken to be proportional to the peak to peak height in the derivative spectrum and in the case of the doublet $L_3M_{2,3}M_{4,5}$ peak the maximum peak to peak height associated with the higher energy minimum is taken as a measure of intensity. This is justified since the line shapes did not change with emission angle. All the signals have been normalised to equal 1 at the most intense point ~5° from the surface normal. It can be seen that all the angular profiles are the same within the experimental error and in particular the angular variations are of equal magnitude, The prominent $\langle 120 \rangle$ direction can be associated with the peak at ~40°. Similar angular distributions from the three main peaks in the $\langle 11\bar{2} \rangle$ azimuth are shown in figure 5.8 and in this case the relative magnitude of the peaks are plotted in their correct relation. The main crystallographicdirections associated with the peaks in the emission angular distribution are indicated on the diagram. The similarities between the Auger angular profiles and the back scattered Kikuchi pattern can be seen in figure 5.9 where the elastic signal at 2KeV is plotted

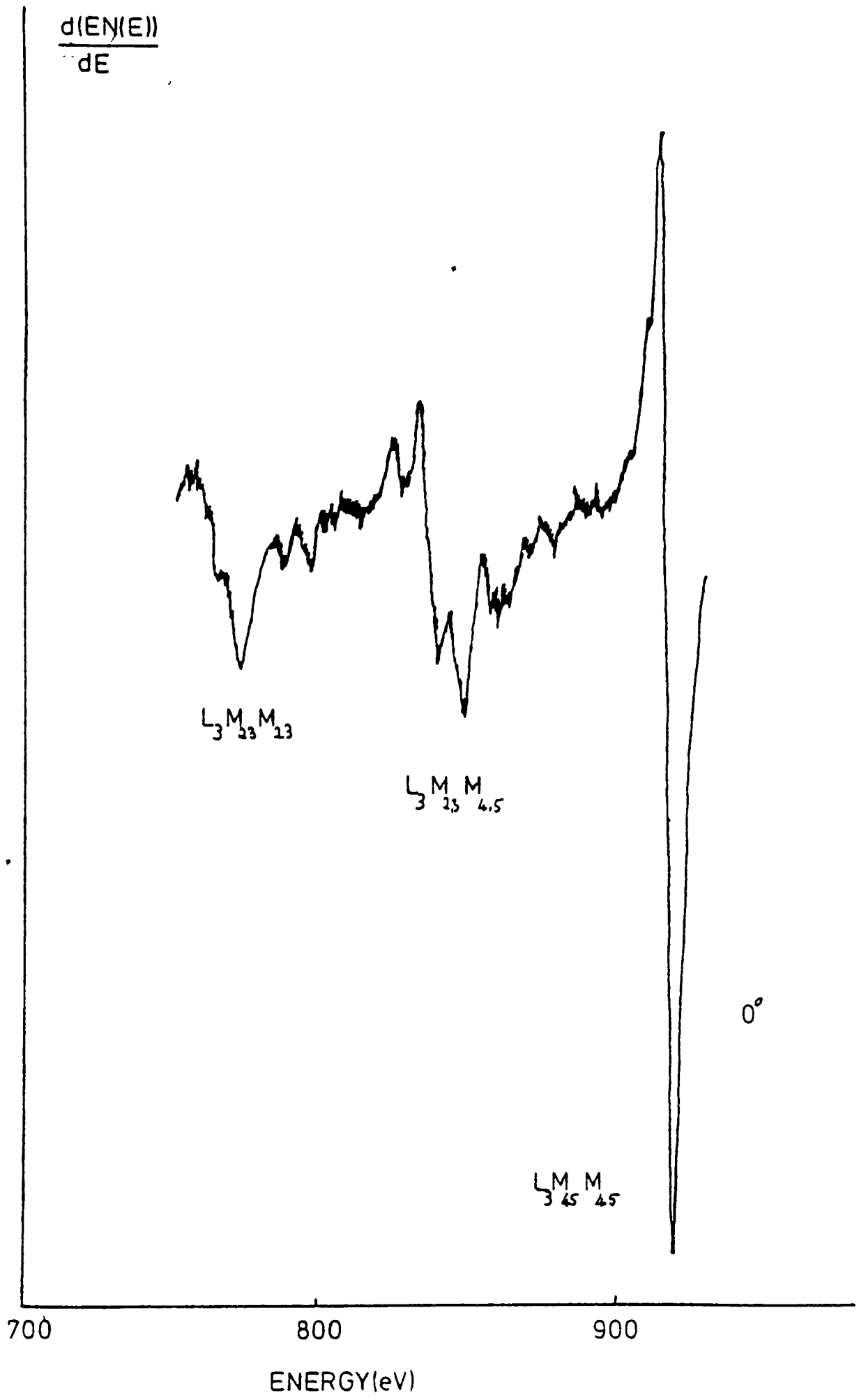


Fig.5.5 Copper LVV spectrum, E_p=2000eV, θ_p=30°, θ_e=0°

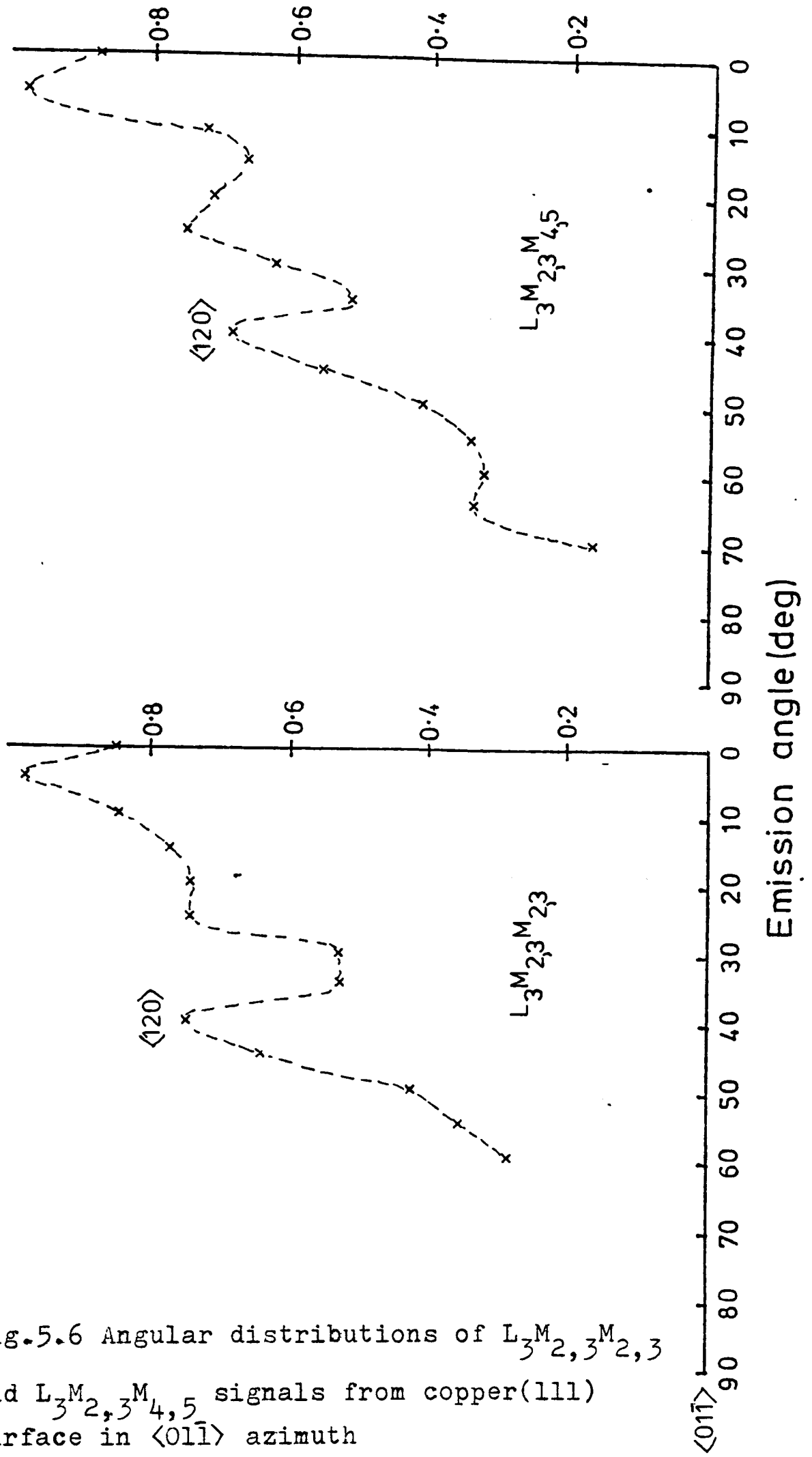


Fig.5.6 Angular distributions of $L_3M_{2,3}M_{2,3}$ and $L_3M_{2,3}M_{4,5}$ signals from copper(111) surface in ⟨011̄⟩ azimuth

E_p=2000eV, θ_p=30°

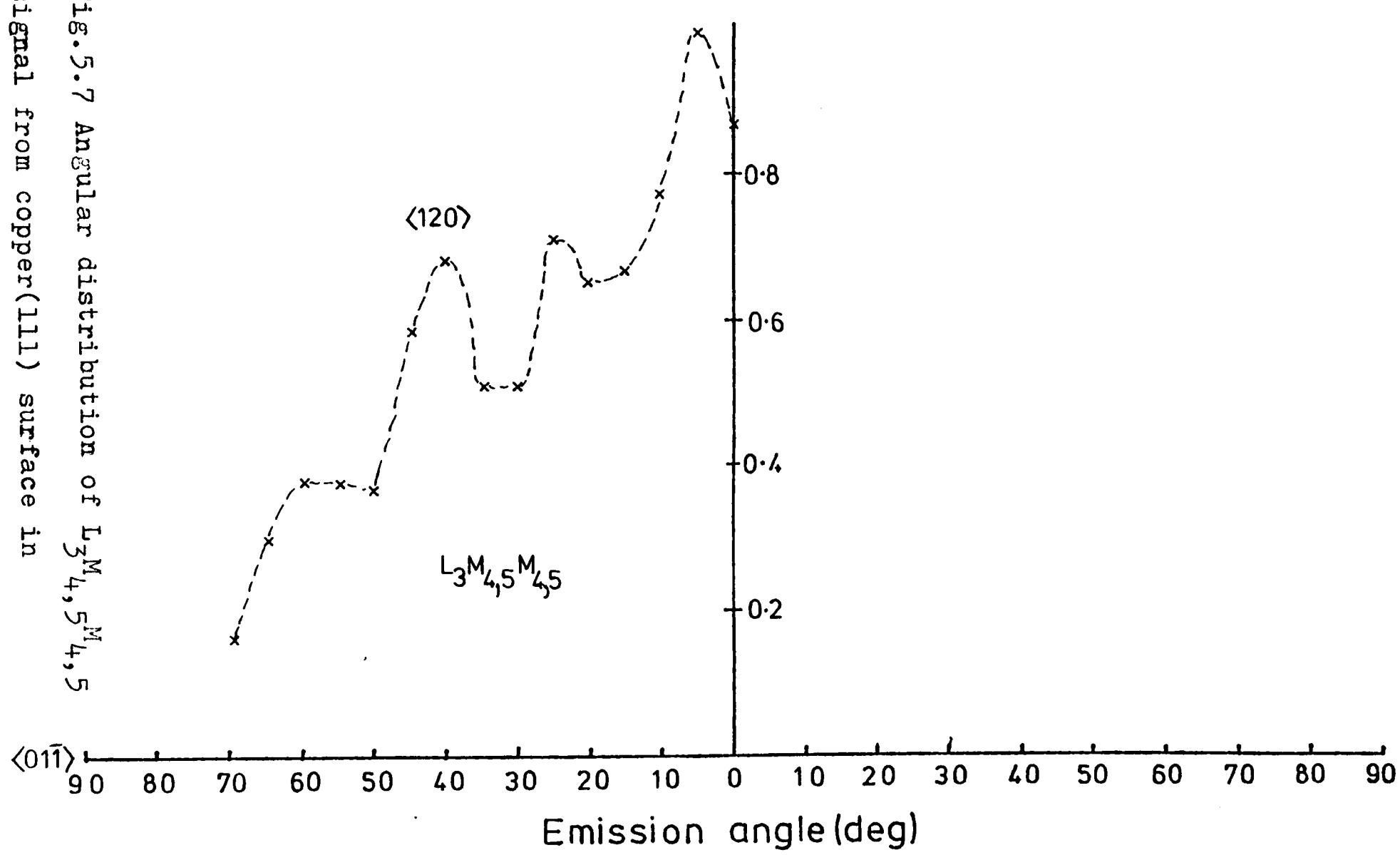


Fig.5.7 Angular distribution of $L_3M_{4,5}M_{4,5}$ signal from copper(111) surface in ⟨011̄⟩ azimuth, E_p=2000eV, θ_p=30°

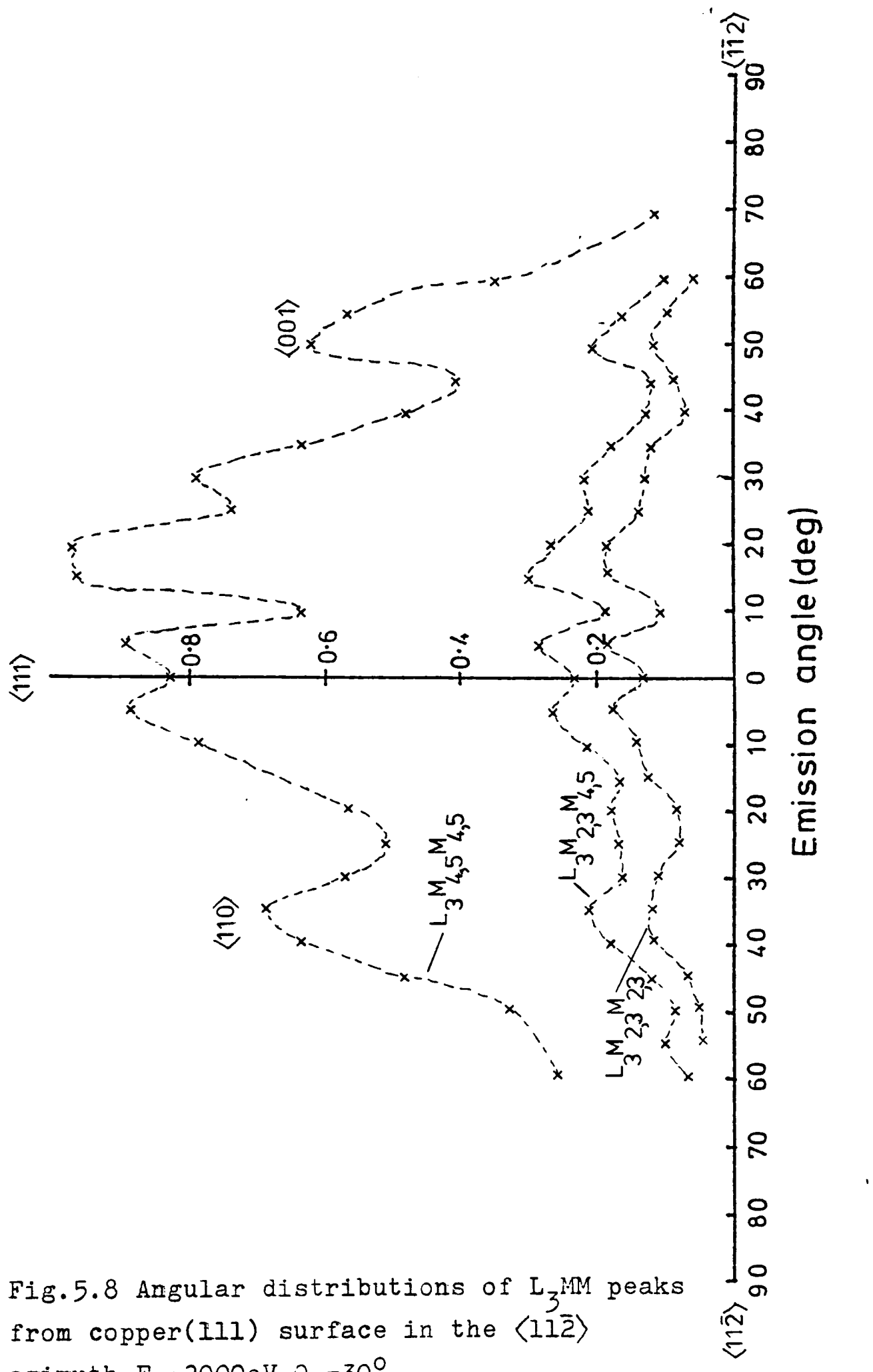


Fig.5.8 Angular distributions of L_3MM peaks from copper(111) surface in the ⟨11$\bar{2}$⟩ azimuth, E_p=2000eV, θ_p=30°

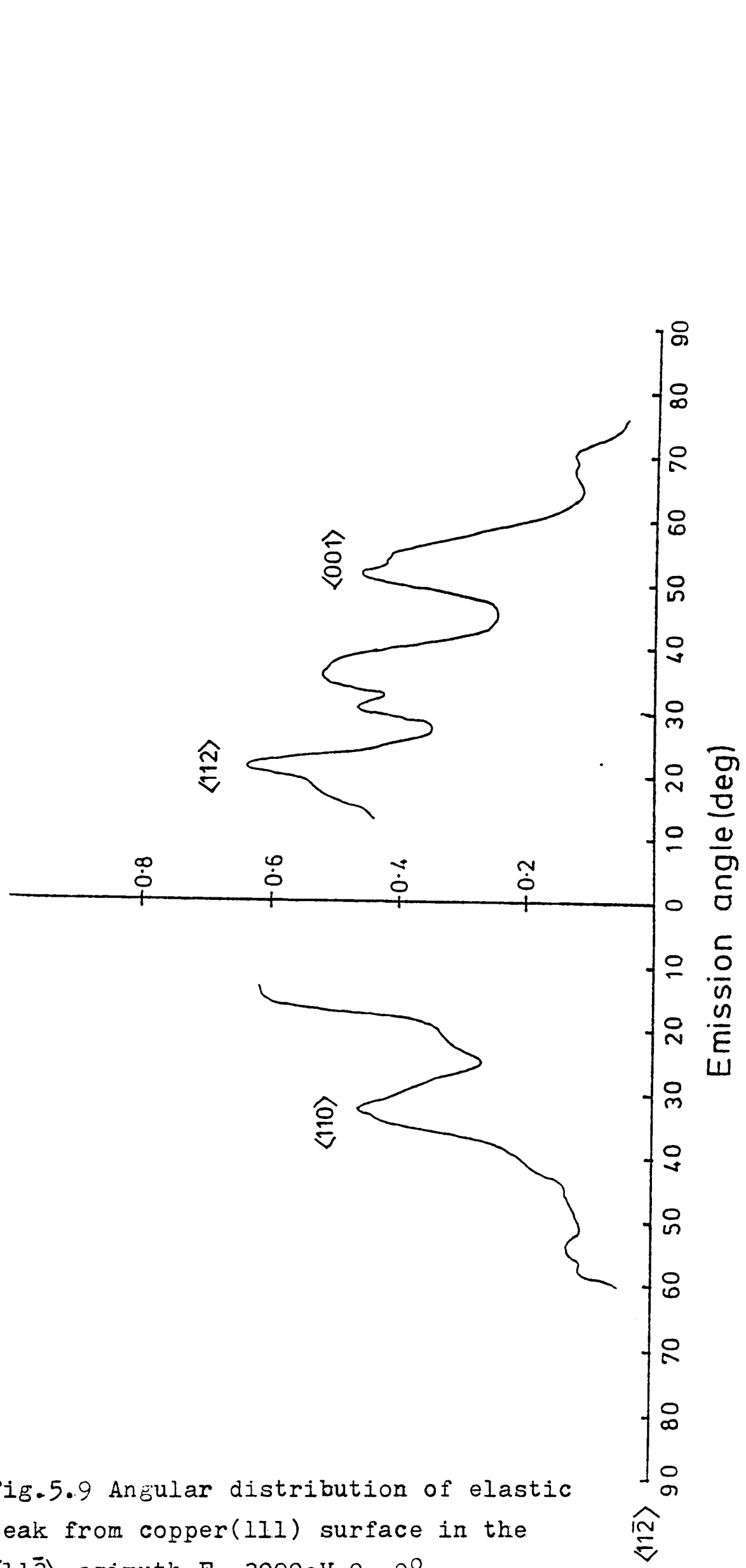


Fig.5.9 Angular distribution of elastic peak from copper(111) surface in the ⟨11$\bar{2}$⟩ azimuth, E_p=2000eV, θ_p=0°

as a function of emission angle. The most obvious similarities occur near the ⟨110⟩ and ⟨001⟩ directions.

These results show quite clearly the similarities in the angular distributions of the three main LVV peaks. High resolution spectra of the $L_3M_{4,5}M_{4,5}$ signal (Kowalczyk 1973) show that many spectral terms combine to give the overall line shape and the possibility exists of each term having its own angular distribution. This was examined by measuring the $L_3M_{4,5}M_{4,5}$ and $L_2M_{4,5}M_{4,5}$ lines in the EN(E) mode at various emission angles in the $\langle\overline{112}\rangle$ azimuth. The results are shown in figure 5.10 for two particular emission angles and it can be seen that the line shape is invariant within the experimental error.

These results are in marked contrast to the copper $M_{2,3}VV$ angular distributions where each member of the doublet exhibited its own characteristic angular profile.

5.3.5. Angular Momenta of the Emitted Auger Electrons

As with the results from the Ag(100) surface (Matsudaira and Onchi,1978) these results from copper (111) indicate either that the initial states of the Auger electrons in all three peaks are the same or that the angular distributions are insensitive to the initial state. The values of l_a associated with the emitted electrons in the three copper LVV peaks will now be calculated.

The transition probabilities, calculated in extreme j-j coupling, can be found in Asaad (1963). The three main lines examined were $L_3M_{2,3}M_{2,3}$(776eV), $L_3M_{2,3}M_{4,5}$(840eV) and $L_3M_{4,5}M_{4,5}$. In Asaad's notation $L_2=\bar{p}$, $L_3=p$, $M_2=\bar{p}$, $M_3=p$, $M_4=\bar{d}$, and $M_5=d$. Only one of the calculations will be shown in full since they are long and rather uninformative and only the results for the rest will be given. Consider the $L_3M_{2,3}M_{4,5}$ transition rate. Transition probabilities are given in terms of direct and exchange matrix elements $D(\lambda)$, and $E(\lambda)$ for all the following final state possibilities :- M_2,M_4 (l_a=0,2,4); M_2M_5 (l_a=0,2,4);

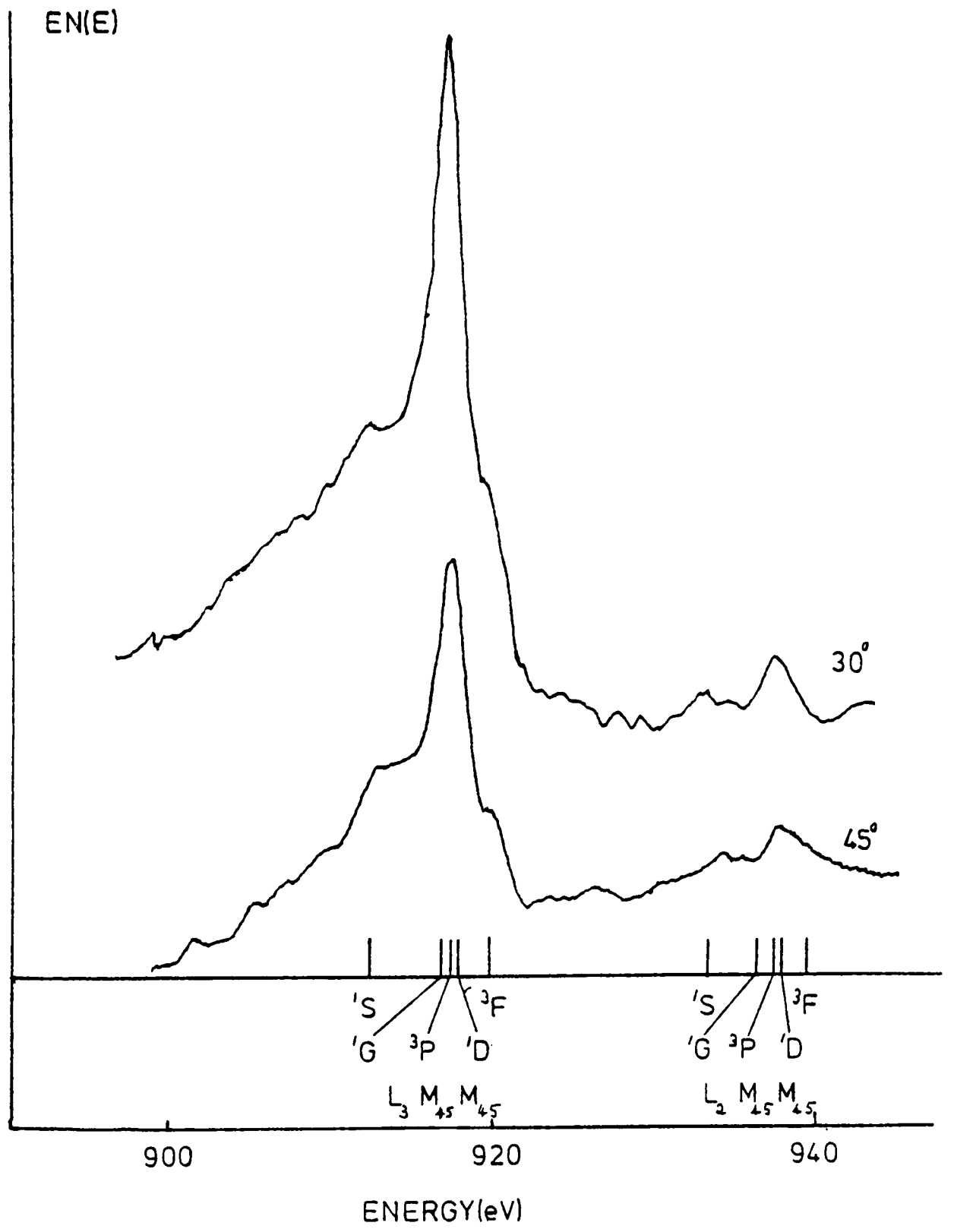


Fig.5.10 Detailed line shapes of $L_3M_{4,5}M_{4,5}$ and $L_2M_{4,5}M_{4,5}$ peaks at two angles of emission from copper(111) surface in $\langle\bar{1}\bar{1}2\rangle$ azimuth, E_p=2000eV, $\theta_p=30^\circ$

M_3, M_4 (l_a=0,2,4). A typical example for the M_2, M_4 (l_a=2) is given by

$$\frac{24}{140}\left(D(2)-E(3)\right)^2 + \frac{1}{5}\left(D(2)-E(1)\right)^2 + \frac{3}{20}\left(D(2)+3E(3)\right)^2 \text{ ---}$$

$$+ \frac{1}{15}\left(3D(2)-E(1)\right)^2 \qquad \text{---------} \quad (1)$$

Values for $D(\lambda)$ can be calculated from M^{c}Guire's (1971) tabulation of $D(\lambda, l_2)$ using the relation

$$D(\lambda) = \frac{\sqrt{4\pi}}{(2\lambda+1)} D(\lambda, l_a) \qquad \text{---------} \quad (2)$$

$l_2 = l_a$ in the notation used here. The values of D(2), E(3), E(1) for $l_a = 2$ are found to be; 0·55, 0·43, 2·16 and the transition rate for the $L_3M_2M_4(l_a=2)$ transition is 2·16 and similarly for $L_3M_2M_4(l_a=0)$ and $L_3M_2M_4(l_a=4)$ where the transition rates are 0·39 and 6·08 respectively. Tabulating all these results leads to :-

Table 5.1

configuration	l_a	transition rate
M_2M_4	4	6·08
$(\overline{pd})$	2	2·16
	0	0·39
M_2M_5	4	2·81
$(\overline{pd})$	2	19·05
	0	1·02
M_3M_4	4	5·92
$(\overline{pd})$	2	24·63
	0	0·7
M_3M_5	4	6·59
(pd)	2	41·44
	0	3·08

Since the various configurations are not experimentally seperable their contributions are simply added together for each value of l_a to find the total

transition rate into the appropriate l_a channel giving :-

Table 5.2

l_a	total transition rate
0	5·16
2	87·28
4	21·4

Cu $L_3M_{2,3}M_{4,5}$

Thus for the copper $L_3M_{2,3}M_{4,5}$ transition the main value of l_a for the emitted Auger electron is l_a=2. Similarly for the Cu $L_3M_{2,3}M_{2,3}$ transition

Table 5.3

l_a	total transition rate
1	91·51
3	2·45

and the Cu $L_3M_{4,5}M_{4,5}$ transition

Table 5.4

l_a	total transition rate
1	11·06
3	100·46
5	2·87

Therefore the dominant values of l_a associated with the transitions $L_3M_{2,3}M_{2,3}$ (776eV), $L_3M_{2,3}M_{4,5}$ (840eV) and $L_3M_{4,5}M_{4,5}$ (920eV) are simply 1, 2 and 3. These results are not expected to be exact since they strictly apply to an isolated atom and they are also calculated in extreme j-j coupling but the general trends should be correct.

5.3.6. Discussion

The correlation of l_a=1,2 and 3 with the $L_3M_{2,3}M_{2,3}$, $L_3M_{2,3}M_{4,5}$ and $L_3M_{4,5}M_{4,5}$ Auger electrons makes it clear that the reason behind the similarities

of the three angular distributions is the insensitivity of the overall diffraction process to the value of l_a describing the emitted electron, rather than the same value of l_a being associated with each peak. This is certainly not what would be expected on the basis of the theories outlined in the previous chapter (e.g. Aberdam et.al. (1978)) where the value of l_a was shown to play a major part in determining the shape of the emission angular distribution even when the results are averaged over all possible values of m_{l_a}. Unfortunately these theories, based on LEED formalisms, cannot be directly applied above energies of $\sim$250eV since the intra-layer scattering part of the calculation starts to consume excessive amounts of computer time.

As yet no attempts have been made to describe theoretically the high energy Auger angular distributions but Lindsay and Pendry (1978) have studied theoretically the angular distributions of photoemitted electrons in the energy range 390eV to 1413eV and most of the ideas should be applicable to Auger emission as well. As mentioned above, the main problem lies in the intra-layer scattering part of the calculation and this was overcome by using the chain method of Pendry and Gard (1975). In this method the layer is split up into a set of parallel chains of atoms and an outgoing cylindrical wave is calculated that includes all multiple scattering between atoms in the chain. In a similar way the wavefield emitted from the layer is evaluated that includes all multiple scattering between chains. The calculation then proceeds, in exactly the same way as the method for low energy, by assembling the layers together to form the crystal and evaluating the multiple scattering between layers to find the total emitted wavefield. The method has been applied to calculate azimuthal angular profiles from the copper (100) surface for $2S_{\frac{1}{2}}$ (390eV), $2P_{\frac{3}{2}}$ (556eV) photoelectrons (Lindsay and Pendry (1978)) and 3p (1413eV), $2S_{\frac{1}{2}}$ (390eV) photoelectrons (Lindsay et.al. (1979)). As before the l value of the emitted electron is evaluated, and for the $2S_{\frac{1}{2}}$ electrons l = 1, and for the 3p electrons l = 0 was found to dominate (for 3p electrons the selection

rule $l = L \pm 1$ allow $l = 0,2$, where L refers to the core level). The angular distributions of all three peaks studied were found to be very different from one another. Unfortunately no indication was given about how sensitive the angular distributions were to the choice of l although the assignment of a particular value to it must imply that the authors considered it important. The very marked differences in the angular distributions calculated for the $2S_{\frac{1}{2}}$ (390eV) and $2P_{\frac{3}{2}}$ (556eV) photoelectrons, where the l values must be respectively 1 and 0 or 2, also suggests that l is important since the energy difference of $\sim 30\%$ is roughly comparible to the 25% energy difference for the silver peaks at 265eV and 355eV whose angular profiles were shown to be almost identical by Matsudaira and Onchi (1978). This comparison with the silver results only serves to illustrate that final state scattering effects alone would not produce drastically different angular distributions in these energy ranges. It therefore appears that this theoretical approach also predicts a marked dependence of emission angular distributions on the value of l describing the emitted electron. This is not surprising since the only difference, in the approach of Lindsay and Pendry (1978) to that of Aberdam et.al. (1978) at lower energies, occurs in the evaluation of the intra-layer scattering.

It now appears that the results from the copper L_3VV angular distributions contradict either theoretical model, in that l_a does not influence the emission angular distributions. This however, does not necessarily imply that the photoemitted electron angular distributions are insensitive to l since no direct experimental evidence of this exists. The only experiment relevant in this context is that of Siegbahn et.al. (1970) where the angular distributions of the Na 2S (1190eV) photoelectrons and Na KLL ($^1D_2$) 990eV Auger electrons were shown to be virtually identical which strongly suggests that photoemitted electron angular distributions are insensitive to l. The energy above which initial state effects cease to be important must lie in the range $100 \sim 265$eV but no better estimate can be given on the basis of

these experiments.

This insensitivity of emission angular distributions, at higher electron energies $\sim$ 1KeV, to initial state effects may well prove of considerable practical value since it removes the nead to calculate the initial state of the emitted electron which in the case of Auger emission is very much an unsolved problem in the solid state environment.

5.4. Final State Effects and Kikuchi correlation

In the previous section it was shown that the emission angular distributions of electrons emitted in the 1KeV region are insensitive to the wavefunction describing the emitted electron. The contribution of the final state scattering to the overall angular distribution will now be considered.

The only theories specifically developed for use in this energy region are those already mentioned by Lindsay and Pendry (1978) and Lindsay et.al. (1979). Due to computational difficulties associated with electrons travelling at large angles to the axes of the "chains" the theory is only viable at angles of emission $\geqslant 50^{o}$ from the surface normal and hence most of the data collected here, as a function of polar angle, could not be analysed using this theory. Therefore another approach must be adopted.

De Wames and Hall (1968) and Howie (1966) have studied electron emission from single crystals in the 50 - 200 KeV region using the dynamical theory of electron diffraction developed for electron microscopy (Hirsch et.al. (1965)). Solving the problem by considering the emission of a spherical wave from a lattice site is in fact rather difficult therefore De Wames and Hall (1968) approached the problem in a different way by the use of the reciprocity principle (Laue (1935)). This states that the intensity at a point A due to a source at point B is equal to the intensity at point B due to the same source at point A. This means that the intensity at a large distance from the crystal due to the source at the lattice site is equal to the intensity at the lattice site due to a spherical source at a large distance

from the crystal. Since the source is a large distance from the crystal, the incoming wave can be approximated by a plane wave and the problem to be solved becomes one of calculating the intensity at a lattice site due to a plane wave incident on the crystal. The type of profile predicted by De Wames and Hall (1968) will be illustrated with reference to the peak observed close to the ⟨001⟩ direction for the copper L_3VV signal shown in figure 5.8. The reciprocal lattice construction relevant to the azimuth in question is shown in figure 5.11. Using a three beam formulation of the problem, which in this case would be the $\overline{220}$, 000 and 220 beams, they showed that a peak should occur central on the ⟨001⟩ direction with minima close to the Bragg angles. This is illustrated schematically in figure 5.11. This of course is an example of planar channeling where only the systematic reflections are considered and the situation would be more complex if non-systematic reflection were strongly excited.

This type of profile is exactly the same as that observed in back reflections Kikuchi patterns at ~1KeV (e.g. Mosser et.al. (1976)) with defect lines bounding the excess bands. This is perhaps not surprising since Kikuchi patterns can be thought of as arising from electron emission from "internal sources" created by inelastic scattering due to phonon creation. This analogy cannot be taken too far since the sources associated with phonon scattering are probably not well described by the spherical source used by De Wames and Hall (1968) to describe the true electron emission.

Nevertheless the position of the Kikuchi lines and the minima associated with the electron emission can still be plotted in the same way and the most prominent lines are shown in figure 5.12 for the Cu (111) surface at an energy of 1KeV. Comparing this with the results in figures 5.8. and 5.9 it can be seen that the peaks in the Auger or elastic angular profiles close to the ⟨110⟩ and ⟨001⟩ direction are associated with the 002 and 220 bands. In both these directions the only effect that the energy difference between the

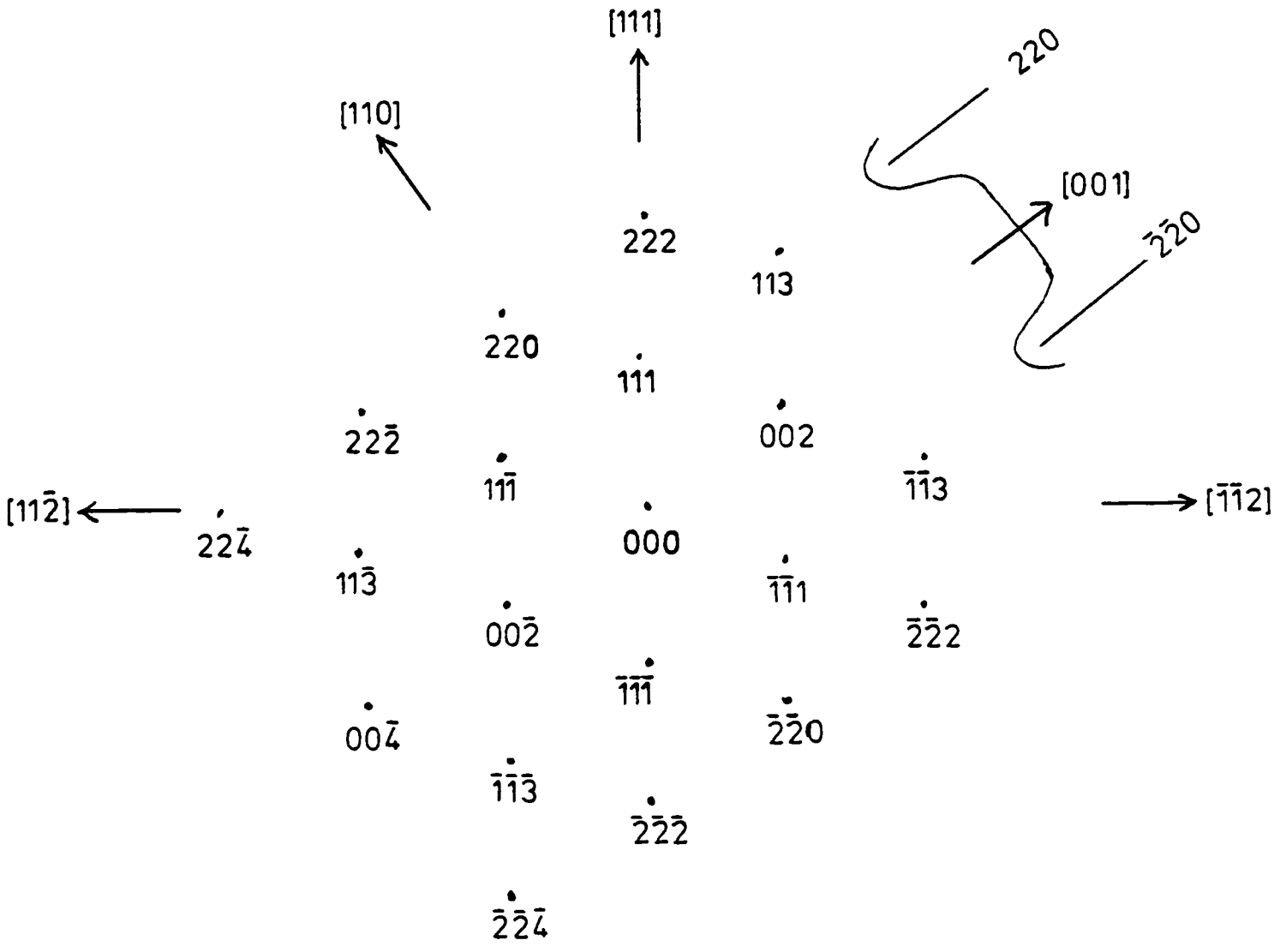
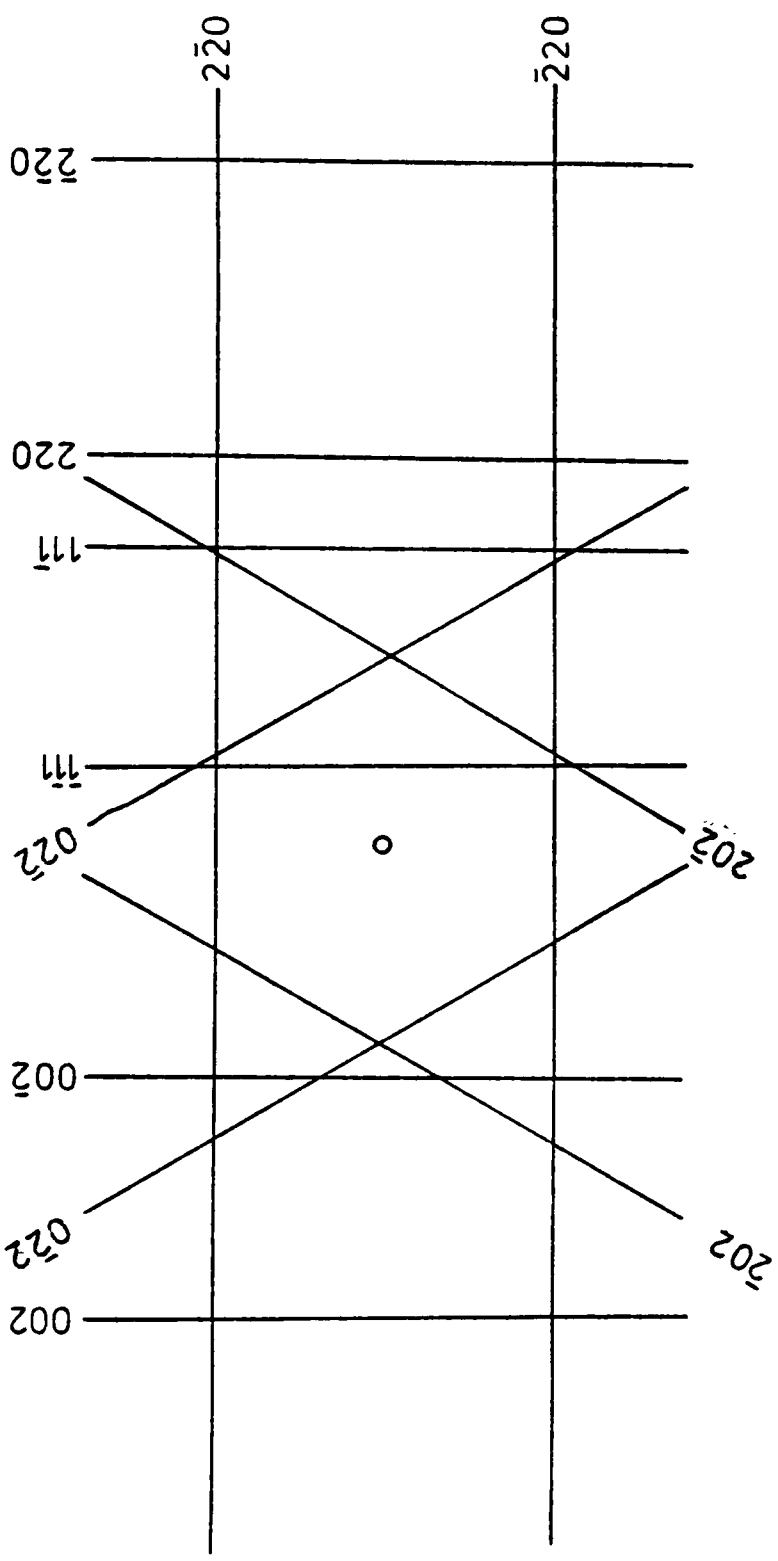


Fig.5.11 Reciprocal lattice construction for copper(111) in $\langle \bar{1}\bar{1}2 \rangle$ azimuth



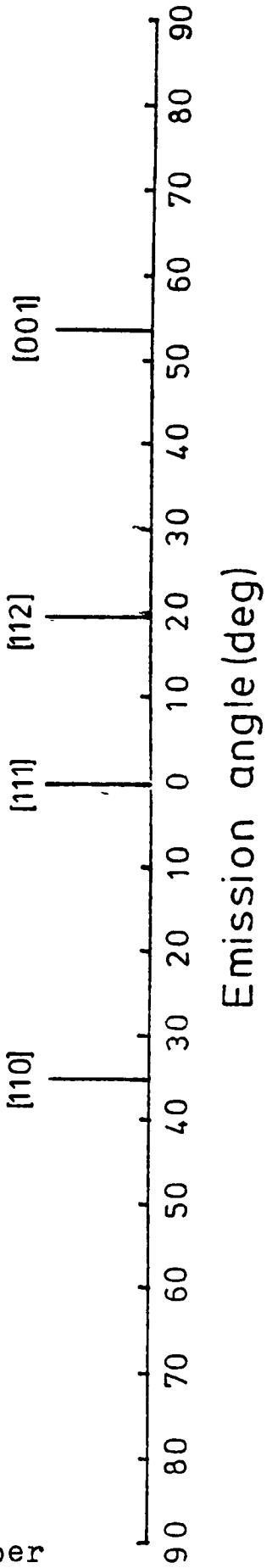


Fig.5.12 Prominent Kikuchi lines for copper (111) surface in $\langle\bar{1}\bar{1}2\rangle$ azimuth at an energy of 1000eV

Auger and elastic electrons will have is to change the width of the Auger peaks. From the data present in figures 5.8 and 5.9 it is not possible to associate any other peaks in the angular profiles with particular bands nor for that matter with crystallographic directions but more data from different azimuths would probably allow the identification of more bands. This can be seen in figure 2.18 chapter 2 where a photograph of the Kikuchi pattern allows the identification of the 220, 202 and 022 bands. It can be seen from figure 5.8 that the angular structure in regions where many defect lines cross can be quite complex due to non systematic reflection making large contributions to the angular profile. In this situation the direct association of peaks in the emission angular distribution with crystallographic directions, as attempted by Zehner et.al. (1977) and Matsudaira et.al. (1978), could lead to ambiguities and indeed peaks at $\sim 20^{\circ}$ in the ⟨001⟩ azimuth for Cu (001) and Ag (001) have been assigned ⟨201⟩ and ⟨301⟩ by Zehner and Matsudaira respectively. It therefore appears that many of the features in high energy Auger angular distributions can be understood on the basis of electron channeling models originally developed for much higher energies.

These models were shown by Tomlinson and Howie (1968) to be capable of predicting the behaviour of electron emission from atoms occupying interstitial sites. This effect can be best understood using the reciprocity relation again. The intensity at a lattice site, due to a plane wave directed along say the ⟨001⟩ direction of figure 5.8, will be high and correspondingly the intensity between site will be low. In terms of two beam dyramical theory (Hirsch et.al. (1965)) this would amount to type 2 waves, which have maximum amplitudes on atomic sites, being strongly excited. Thus what appears as a peak in the emission angular distributions for atoms on a latiice site will appear as a dip for atoms lying between the planes in question. This then provides a very straightforward way of detecting the presence of interstitial atoms, and by examining the emission behaviour along different directions it

should be possible to determine the position of the atom with respect to different sets of planes. Therefore in the context of figure 5.8 a dip in the angular distribution along the ⟨001⟩ direction would indicate an atom sitting between the (110) planes and a dip along the ⟨110⟩ direction would indicate an atom sitting between the (001) planes. In the case of an atom occupying a surface site these arguments may not be directly applicable, in such a simple form, but it still seems probable that electron angular distributions in this energy range will be more readily understood that at lower energies where initial state effects are very important.

5.5. Summary

In this chapter it has been shown that the angular distributions of Auger electrons in the ~1KeV region can be qualitatively understood on the basis of electron channeling and that the initial state contribution to the overall angular distribution is negligible. Simple ways of recognising interstitial atoms have been proposed and it seems much more probable that surface crystallographic information can be obtained from Auger angular distributions in this energy range than at lower energies where the major effort has, to date, been concentrated.

Chapter 6.

Effects of the Incident Beam Direction on Auger Electron Emission

		Page
6.1	Introduction	97
6.2	Theory for Non-Crystalline Substrate	98
6.3	Experimental	102
6.4	Results and Discussion	103
6.5.1	Variations in Auger Yield as a function of Primary Beam Direction from Single Crystals	104
6.5.2	Theory	104
6.6	Results from the Silicon (111) Surfaces	106
6.7	Results from the Copper (111) Surface	108
6.8	Discussion	109
6.9	Summary	114

6.1. Introduction

In the previous chapters the main emphasis has been placed on understanding the variations in Auger current as a function of emission angle, at fixed angles of incidence. It is the purpose of this chapter to investigate the variation in Auger current as a function of the incident beam angle at fixed angles of emission. The discussion will first of all concentrate on non-crystalline surfaces and then the more complex case of single crystal surfaces will be considered.

The effect of the angle of incidence on the Auger currents from clean polycrystalline surfaces and surfaces with small amounts of adsorbate present have already been examined by Harris (1969) and Matsudaira and Onchi (1978). Their results, which show that the Auger current increases with increasing beam angle, were interpreted on the basis of a simple model that assumes an exponential decay in the rate of ionisation with depth. From the point of view of performing quantitative analysis, the worst thing that can happen is that the relative strengths of the signals from the substrate and adsorbate change with the angle of incidence. Harris (1969) found no such effect but the results of Matsudaira and Onchi (1978) show that the primary beam angle dependencies of the overlayer signals and signals from a clean surface were slightly different. Unfortunately they did not record substrate and overlayer signals from the same specimen but their results do seem to suggest that the relative signal strengths may change with incident beam angle. This type of effect has been studied on a well characterised surface with a continuous overlayer present and the results are analysed using a simple model.

The variation in Auger current as a function of primary beam direction, from single crystal surfaces, has been investigated experimentally by Rusch et.al. (1973), Allié et.al. (1974) and Baines et.al. (1975) from Silicon (111), Aluminium (001) and Aluminium (111). In all cases the results were obtained for the low energy Silicon and Aluminium LVV transitions at 92eV and 63·5eV.

The results were able to establish a marked correlation between the back reflected Kikuchi pattern and the variation in Auger yield as a function of the primary beam direction. The only theoretical work directly applicable to this problem is that of Andersen and Howie (1975) based on the dynamical theory of electron diffraction (Hirsch et.al. 1975). Their results showed that the variations in Auger current with angle of incidence, due to primary and backscattered electrons, exhibited very similar structure but were of different magnitude. A further, more puzzling conclusion from this theory (Baines et.al. (1975)) is that a significant amount of the signal must come from depths greater than 10Å if the magnitude of the angular structure is to be understood.

This conclusion has been investigated by recording the variations in high and low energy Auger signals as a function of the primary beam direction and the results are discussed in terms of the "Bragg modulation region" proposed by Andersen and Howie (1975). A mechanism is also proposed to explain the larger than expected changes in the Auger yield as a functionof the incident beam direction. Finally the correlations observed between the various emission angular distributions and these results are discussed in terms of the reciprocity principle.

6.2. Theory for Non-Crystalline Substrate

The simplest case to consider when deriving a formula to describe the variations in Auger current as a function of the primary beam direction is that already described in chapter 1 for the case of an adsorbed monolayer on a substrate. The total Auger current, from the monolayer, leaving the surface is given by (equation (9) chapter 1)

$$I_a = I_p \sigma(E_p)\ F(\theta_p).r.N\ (1-\omega) \qquad \text{------ (1)}$$

In this particular case I_a will always be directly proportional to the collected Auger current, regardless of the analyser geometry, because the

escape probability is equal for all electrons created in the overlayer. The backscattering factor r for this case can be written as (Vrakking and Meyer (1973))

$$r = 1 + \frac{1}{I_p\, \sigma(E_p) \sec\theta_p} \int_{E_c}^{E_p} \int_{\theta} I(E,\theta)\, \sigma(E) \sec\theta \, dE \, d\theta \qquad \text{---- (2)}$$

This is simply the ratio of the number of ionisations that actually occur in the overlayer over the number that would occur in the absence of backscattering. Thus, it can be seen that the variation in the emitted Auger current as a function of θ_p is proportional to $r(E_p,\theta_p) \sec\theta_p$ (assuming $F(\theta_p) = \sec\theta_p$)

To calculate the variation in Auger current as a function of θp from a clean specimen it is necessary to use a model similar to that already mentioned in § 3.2. On the basis of these models the Auger current at depth z in the specimen can be written (c.f equation (1) chapter 3)

$$i_a(z) = \int_{E_c}^{E_p} \int_{\theta} I(E,\theta,z)\, \sigma(E)\, N(1-\omega)\, F(\theta) \sin\theta \, d\theta \, dE \qquad \text{---- (3)}$$

where the terms have the usual meanings defined in § 1.6.1 and in particular $I(E,\theta,z)$ refers to the total current in layer dz at depth z in the specimen. From this it can be seen that the current collected at angle θ_e from the surface normal $i_a(\theta_e)$ due to the whole specimen can be written

$$i_a(\theta_e) = \int_{E_c}^{E_p} \int_{\theta} \int_{z=0}^{\infty} I(E,\theta,z)\, \sigma(E)\, F(\theta)\, N(1-\omega) \exp\left(-\frac{z}{\lambda_a \cos\theta_e}\right) \text{---}$$

$$\text{---} \sin\theta \, d\theta \, dE \, dz \, \frac{\Delta\Omega}{4\pi} \qquad \text{---- (4)}$$

As before it is desirable to express equation (4) in terms of primary beam effects times a backscattering factor r. In the case of a clean specimen the definition of r given in equation (2) is no longer of any use because it is necessary to consider, not only the rate of ionisation at a depth z in the specimen but also the escape probability for the Auger electrons created at this depth. Consequently, Jablonski (1979) has suggested that the back-

scattering factor should be defined as

$$r(E_p,\theta_p,\theta_e) = \frac{i_a(\theta_e)}{i_a^1(\theta_e)}$$

where $i_a(\theta_e)$ is the Auger current actually detected by the analyser and $i_a^1(\theta_e)$ is the current that would be detected in the absence of all back-scattering and energy loss. In this way the Auger current $i_a(\theta_e)$ recorded by the analyser is given by

$$i_a(\theta_e,\theta_p) = r(E_p,\theta_p,\theta_e) \int_0^\infty I_p(E_p,\theta_p)\,\sigma(E_p)\,\sec\theta_p\,N(1-\omega) \;---\; \exp\left(-\frac{z}{\lambda_a\cos\theta_e}\right) dz\,\frac{\Delta\Omega}{4\pi} \qquad ---- \quad (5)$$

Assuming $\theta_e = 0$ (as will be the case in the experimental work) the variation in Auger current as a function of θ_p is proportional to

$$r\,(E_p,\theta_p)\,\sec\theta_p$$

Jablonski (1979) has calculated $r(E_p,\theta_p)$ as a function of θ_p for a number of elements and his results show that $r(E_p,\theta_p)$ varies by less than 10% for $\theta_p \leqslant 60^o$ and is usually in the range $1{\cdot}0 \leqslant r \leqslant 1{\cdot}4$. The treatments of Matsudaira and Onchi (1978) and Harris (1969) both neglect the possible effects of $r(E_p,\theta_p)$ and therefore predict that the Auger yield is proportional to only $\sec\theta_p$. Had they included the effects of $r(E_p,\theta_p)$, the departure of their experimental results from $\sec\theta_p$ at high angles of incidence could have been properly explained, since $r(E_p,\theta_p)$ tends to 0 at high angles.

Consider now what happens when an overlayer of thickness n is present, as illustrated in figure 3.9. The Auger current from the overlayer $i_a^o(\theta_p)$ can be evaluated by integrating equation (5) over the range 0 to n and in a similar way the Auger current from the substrate $i_a^s(\theta_p)$ can be evaluated. These calculations simply show that

$$i_a^o \;\alpha\; r_o(E_p,\theta_p)\,\sec\theta_p$$

$$i_a^s \;\alpha\; r_s(E_p,\theta_p)\,\sec\theta_p$$

where $r_o(E_p,\theta_p)$ - backscattering factor relevant to overlayer

and $r_s(E_p,\theta_p)$ - backscattering factor relevant to substrate

Unfortunately this predicts that the ratio of the overlayer to substrate Auger currents is proportional to $\frac{r_o(E_p,\theta_p)}{r_s(E_p,\theta_p)}$ and, in the absence of detailed calculations of r, no predictions can be made about possible changes in signal ratio as a function of θ_p. It is therefore necessary to make a simpler approximation to describe $I(E,\theta,z)$ in equation (4). Following Matsudaira and Onchi (1978) and putting

$$I(E,\theta,z) = I_p^o \exp\left(-\frac{n}{\lambda_p \cos\theta_p}\right)$$

with λ_p = inelastic mean free path of primary electrons

allows the evaluation of the overlayer Auger current $i_a^o(\theta_p)$, emitted along the surface normal, by integrating equation (4) from 0 to n and therefore

$$i_a^o(\theta_p) = I_p\,\sigma(E_p)\sec\theta_p\, N\,(1-\omega)\,\frac{\lambda_p\,\lambda_a^o}{\lambda_a^o + \lambda_p\cos\theta_p} \;---$$

$$---\left[1-\exp\left(-\left(\frac{1}{\lambda_p\cos\theta_p}+\frac{1}{\lambda_a^o}\right)n\right)\right]\frac{\Delta\Omega}{4\pi} \quad ---- \quad (6)$$

λ_a^o - inelastic mean free path of overlayer Auger electrons.

The Auger current from the substrate $i_a^s(\theta_p)$ is found by integrating equation (4) from 0 to ∞ with the origin defined at the substrate / overlayer interface. $I(E,\theta,z)$ is replaced by $I_p \exp(-\frac{n}{\lambda_p\cos\theta_p})\exp(-\frac{z}{\lambda_p\cos\theta_p})$ and the probability of the Auger electron escaping from depth z is given by $\exp\left(-\frac{z+n}{\lambda_a^s}\right)$. Therefore $i_a^s(\theta_p)$ is given by

$$I_p\,\sigma(E_p)\sec\theta p\, N(1-\omega)\frac{\lambda_p\,\lambda_a^s}{\lambda_a^s+\lambda_p\cos\theta_p}\;\exp\left(-\left(\frac{1}{\lambda_p\cos\theta_p}+\frac{1}{\lambda_a^s}\right)n\right) \quad --- \quad (7)$$

λ_a^s - inelastic mean free path of substrate Auger electrons.

It is now possible to obtain an expression for $\frac{i_a^o(\theta_p)}{i_a^s(\theta_p)}$ given by

$$\frac{(\lambda_a^o+\lambda_p)(\lambda_a^s+\lambda_p\cos\theta_p)\left(1-\exp\left(-\frac{n}{\lambda_p}\left(\frac{\lambda_a^o+\lambda_p\cos\theta_p}{\lambda_a^o\cos\theta_p}\right)\right)\right)}{(\lambda_a^s+\lambda_p)(\lambda_a^o+\lambda_p\cos\theta_p)\left(1-\exp\left(-\frac{n}{\lambda_p}\left(\frac{\lambda_a^o+\lambda_p}{\lambda_a^o}\right)\right)\right)\exp\left(-\frac{n}{\lambda_p}\left(\frac{1-\cos\theta_p}{\cos\theta_p}\right)\right)} \quad --(8)$$

Providing $\lambda_a^o \simeq \lambda_a^s$ and $\lambda_p \gg \lambda_a$ this reduces to

$$\exp\frac{n}{\lambda_p}\left(\frac{1-\cos\theta_p}{\cos\theta_p}\right) \quad ---- \quad (9)$$

(these expressions have been normalised to equal 1 at $\theta_p = 0^o$).

The usefullness of these approximations will be discussed after presenting the experimental results.

6.3. Experimental

The experimental results were obtained from the oxidised silicon (111) surface, whose preparation has already been described in § 3.8.2. The variation in Auger current as a function of incident beam angle is measured in the following way. The goniometer is set at a fixed position relative to the CHA so that θ_e is held constant (in this case at 15^o). The angle of incidence is then varied by engaging the T bar labelled C in figure 2.14. The actual angle can be obtained by knowing that one complete turn of the worm gear changes θ_p by 6^o. Individual spectra are then recorded at each desired angle of incidence.

Just before performing these experiments the electron gun was inadvertantly knocked off axis and this unfortunately caused the electron beam to hit the specimen holder at $\theta_p \geqslant 50^o$. This could be detected by the presence of molybdenum peaks in the Auger spectrum. This means that the actual Auger currents are unreliable and therefore only the ratios of the various peaks involved will be presented. The peak ratios should not be affected since the

beam hitting the holder will only change the magnitude of primary beam current incident on the specimen.

6.4. Results and Discussion

Figure 6.1 shows the changes in the relative sizes of the elemental silicon peak at 92eV and the chemically shifted silicon peak in SiO_2 at 76eV. This illustrates vividly how sensitive the relative peak heights are to the angle of incidence. The ratios of the 76eV peak to the 92eV peak at various angles of incidence have been plotted in figure 6.2 and plotted above these are the ratios of the 510eV oxygen peak to the 92eV silicon peak. It can be seen in both cases that the overlayer signals are being accentuated at large angles of incidence. Both theoretical curves are plotted from equation 9 with $\frac{n}{\lambda_p} = 0{\cdot}5$ and the values are simply scaled to match experiment at $\theta_p = 0$. In the case of the 92eV and 76eV silicon peaks the approximation of $\lambda_a^o = \lambda_a^s$ made in deriving equation (9) will be almost exact whereas in the case of the 510eV oxygen peak and the 92eV silicon peak $\lambda_a^o \simeq 3\lambda_a^s$ (Seah and Dench (1978)). Theoretical curves based on equation (8) with $\lambda_a^o = 3\lambda_a^s$ do not produce any better agreement with experiment and equation (9) was used in preference. Similar attempts were made to obtain better fits by putting $\lambda_p = 4\lambda_a$ in equation (8) but again no better agreement with experiment was found.

An estimate of the overlayer thickness n can be obtained from this data. Taking $\lambda_p = 20\text{Å}$ (Seah and Dench (1978)) shows that $n = 10\text{Å}$ for the theoretical curves drawn in figure 6.2. Fitting the theoretical curves to the ratios at 60^o and 70^o gives values of $n = 5\text{Å}$ and 14Å respectively so that $n = 10 \pm 5\text{Å}$. This is in complete agreement with the estimates of film thickness made in chapter 3 on the basis of the emission angular distributions.

Thus it has been shown that the presence of overlayers can be detected by observing the changes in signal ratios as a function of incident beam angle. This provides a useful alternative to the methods based on emission angular

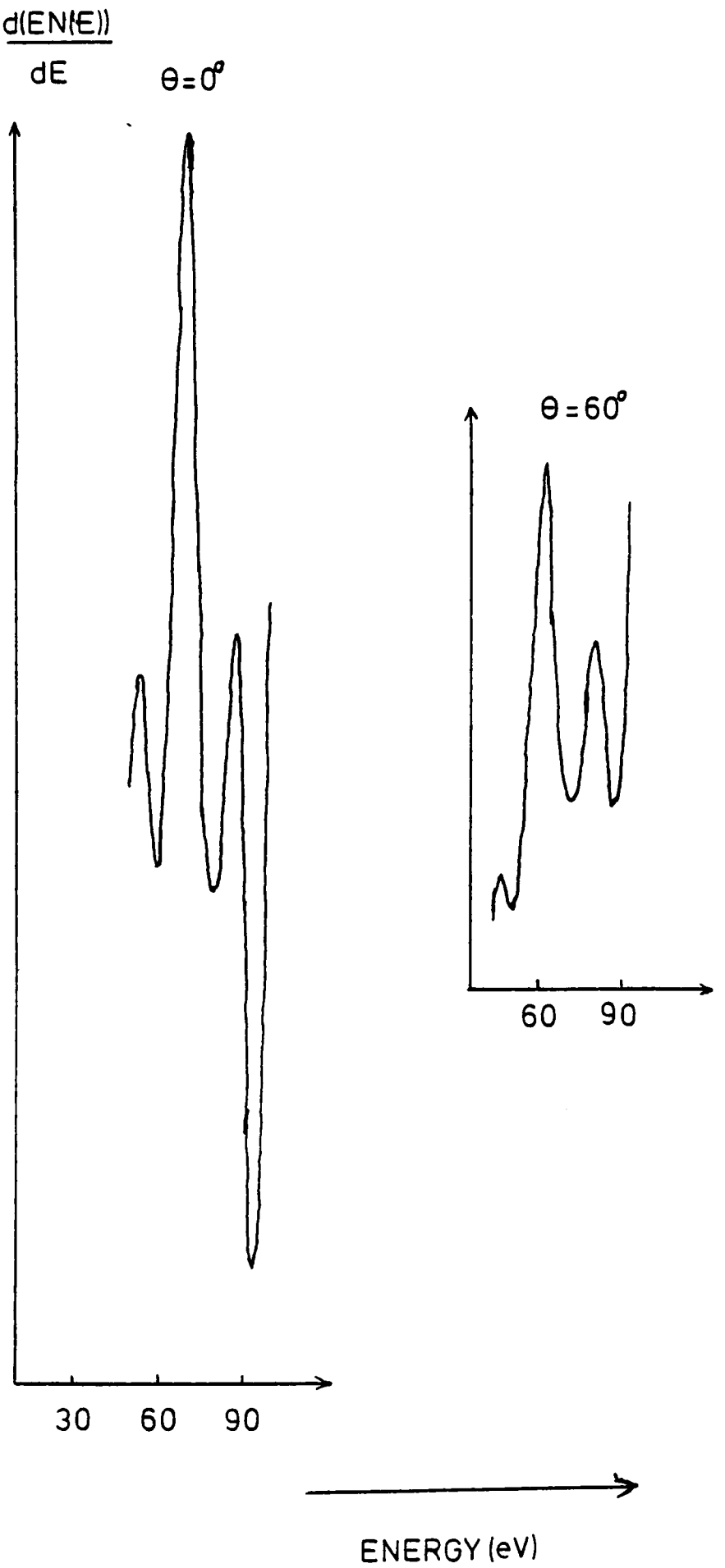


Fig.6.1 The change in ratio of the elemental silicon peak at 92eV and the chemically shifted silicon peak at 76eV.

E_p=1000eV, θ_e=15°

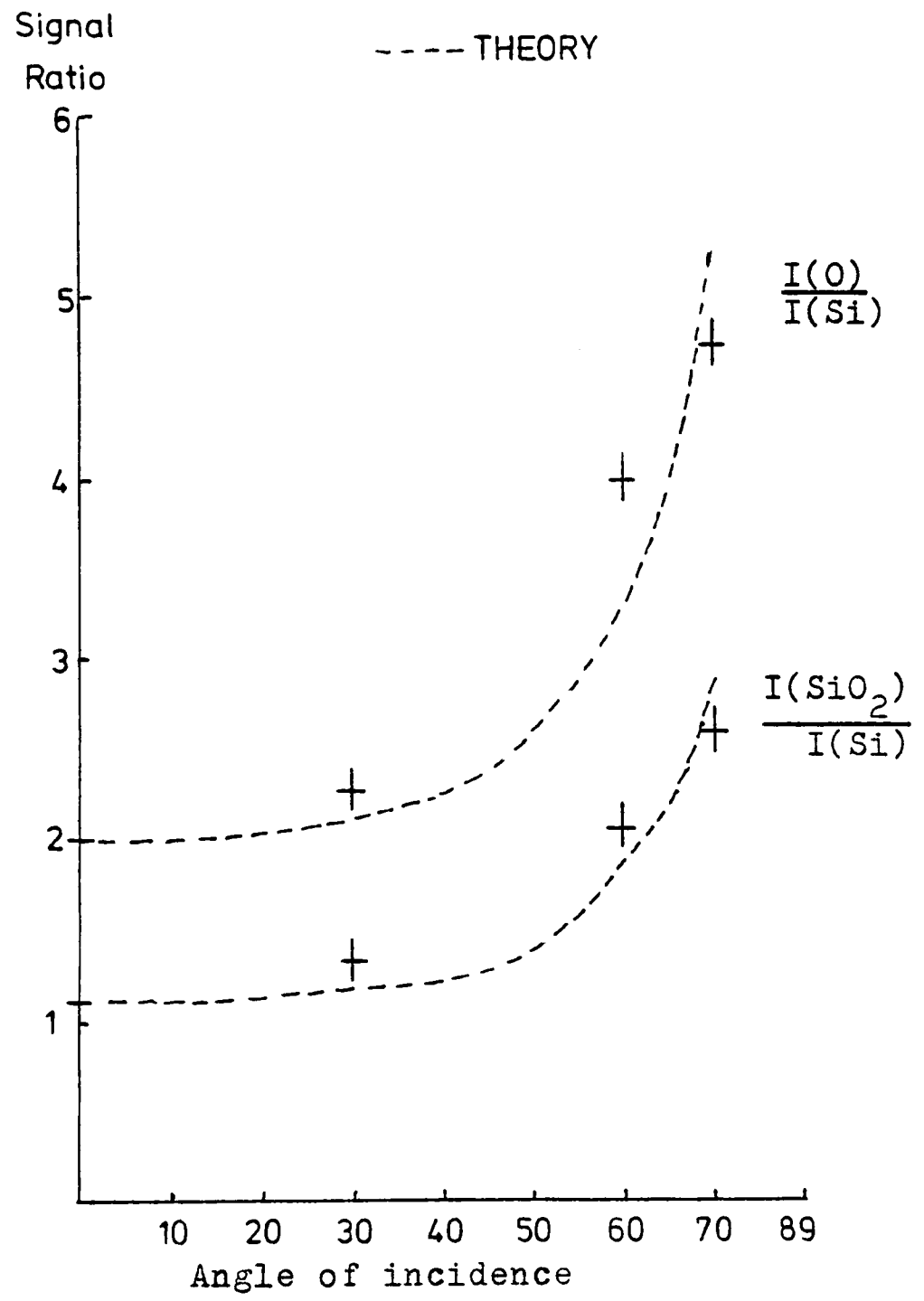


Fig.6.2 The variation in the ratios of the overlayer to substrate Auger signals as a function of the incident beam direction from oxidised silicon, E_p=1000eV, θ_e=15°

distributions discussed in chapter 3 and may well be more widely applicable on Auger systems that already have normal incidence and glancing incidence electron guns. It can be seen from the theory that this method relies on the attenuation of the primary beam, so that even though the primary beam attenuation does not affect the emission angular distributions at $\frac{E_P}{E_c} \geqslant 2{\cdot}5$ (table 3.2) it certainly does affect the ratio of substrate to overlayer Auger signals even at $\frac{E_p}{E_c} = 10$. Vrakking and Meyer (1973) have also shown the importance of primary beam attenuation by varying the primary beam energies and observing the changing signal ratios.

6.5.1. Variations in Auger Yield as a Function of Primary Beam Direction from Single Crystals

6.5.2. Theory

It was shown in the previous section that a complete description of the changes in emitted Auger current, as a function of primary beam direction, from a clean specimen demands a complete calculation of the changing rate and depth distribution of the ionisations. This in turn demands a complete description of the primary and backscattered electron distributions from E_c to E_p.

Calculations with this degree of generality have not yet been performed for single crystal specimens and it is therefore necessary to make some approximations to gain at least a qualitative understanding of the processes involved. A first approximation would be to consider only the contribution of the elastic wavefield to the ionisation rate and this was perhaps first done by Hirsch et.al. (1962) for the case of X-ray production in thin foils. Although the energy regime is different the basic problem is still the same, that of calculating the rate of ionisation as a function of primary beam direction. They showed on the basis of two beam theory that the X-ray production (and hence the rate of ionisation) would go from a maximum at one side of the exact Bragg position to a minimum at the other side. This is very

similar to the behaviour predicted by De Wames and Hall (1968) for the case of electron emission, and indeed it should be recalled that De Wames and Hall invoked the reciprocity principle to relate the emission angular profile, that they wished to obtain, to the change in electron intensity at a lattice site as a function of incident beam direction. Therefore the type of profile predicted by De Wames and Hall (1968), that is illustrated in figure 5.11, can apply equally well to the emission angular profile or to the change in the intensity of the elastic wavefield at the lattice site as a function of the incident beam direction.

Taub and Stern (1968) and Taub et.al. (1969) have used this type of approach to explain their results on secondary emission from tungsten single crystals using energies in the kilovolt region. They essentially say that when a type 2 wave is excited close to the Bragg position the high absorption associated with this wave tends to localise the electron wavefield close to the surface thus increasing the probability of creating secondaries in the surface region. Again this was based on two beam theory and empirical factors had to be used to describe the strengths of the various reflection involved to obtain agreement with experiment.

The only treatments describing the changes in Auger yield, as a function of primary beam direction, that include the effects of backscattered electrons are those of Andersen and Howie (1975) and Baines et.al. (1975). Their treatments, based on many beam dynamical theory, includes the effects of both zero loss and first plasmon loss backscattered electrons. Most of the calculations in fact refer to variations in the elastic and first plasmon loss backscattered intensities as a function of primary beam direction. The variation in the Auger yield is estimated by adding the contribution of the primary wavefield to that of the backscattered electrons such that

$$i_a(\theta_p,\phi_p) \propto \sigma(\bar{E}p)\left[\sec\theta_p I_o(\theta_p,\phi_p) + \gamma(\theta_p,\phi_p) I_B(\theta_p,\phi_p)\right] \quad \text{---- (1)}$$

$I_B(\theta_p,\phi_p)$ - represents the contribution of the backscattered electrons

$I_o(\theta_p,\phi_p)$ - represents the contribution of the primary wavefield

$\gamma(\theta_p,\phi_p)$ - relates the efficiency of the backscattered electrons to that of the primary electrons at Auger production.

$\gamma(\theta_p,\phi_p)$ was estimated to be 1 and $I_B(\theta_p,\phi_p)$ was estimated, from experimental observations, to be $\frac{1}{10}$ the primary beam current. The contribution of $I_o(\theta_p,\phi_p)$ to the Auger production was estimated by assuming that the angular variation in the zero loss backscattered signal would be the same as the Auger variation providing a suitably short inelastic mean free path was used to describe the backscattered electrons. These calculations showed that the variations in the Auger yield, as a function of incident beam direction, due to the primary wavefield and the backscattered electrons exhibited the same angular structure but were of rather different magnitude. This type of approach represents a considerable improvement over the methods described earlier, based on two beam theory, which are only likely to be of use where few Bragg reflections are strongly excited. Considerable doubts do however remain about the relative contributions of the primary wavefield and the backscattered electrons to the total Auger signal. Indeed the calculations do seem to imply (Baines et.al. (1975)) that a significant amount of the Auger signal must come from depths in excess of 10Å to explain the amount of angular structure observed.

6.6. Results from the Silicon (111) Surface

The preparation of this surface has already been described in § 3.8.2 and the method of measuring the Auger signal as a function of the incident beam direction was described in § 6.3. The lower part of figure 6.3 shows the variation in the silicon LVV signal as a function of primary beam angle. It can be seen that the overall variation is close to sec θp but that superimposed on this is extra structure due to the diffraction of the incident electrons. The spectra were all recorded in the E N(E) form and the intensity was taken as proportional to the height of the peak, referred to as A minus B

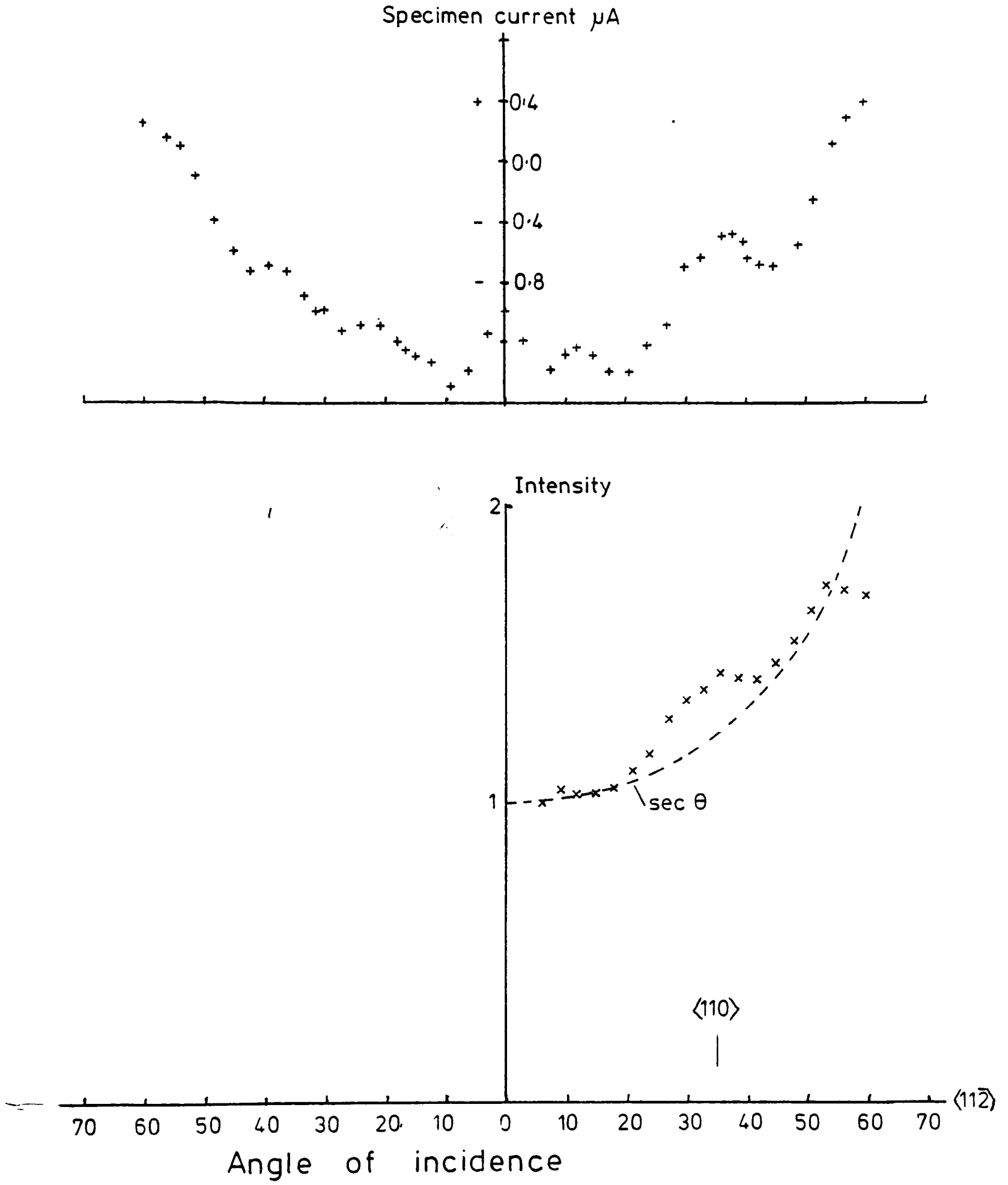


Fig.6.3 The variation in the silicon LVV peak and the specimen current as a function of incident beam angle from the silicon(111) surface, E_p=1000eV, θ_e=15°

in figure 3.4. Also on figure 6.3, is the variation of the specimen current as a function of incident beam angle. From this it can be seen that as θ_p increases the electron current entering the specimen decreases until at $\sim 55^\circ$ there is in fact a net electron current leaving the specimen. There is an obvious correlation between the specimen current and the Auger yield and in particular there are rather prominent peaks in both diagrams close to the ⟨110⟩ direction. For the purposes of future comparison the "contrast" in the angular variations will always refer to the maximum along the ⟨110⟩ direction, and the minimum between the ⟨110⟩ and ⟨111⟩ direction at $\sim 20^\circ$, the actual contrast being defined as $\frac{Imax - Imin}{Imax + Imin}$. In this way the contrast in the silicon LVV signal is 16%, although in this instance, the sec θ_p dependence rather distorts this figure. Correcting for the sec θ_p background produces a figure of $\sim 7\%$ for this peak.

These results are rather similar to those obtained by Rusch et.al. (1973), from the same surface, except that the Auger signals measured here are recorded at a fixed, well defined emission angle. The results of Rusch et.al. (1973) were recorded by simply rotating the specimen in front of a standard LEED/RPA analyser and therefore the collection solid angle changes at the same time as the incident beam angle.

This means that their measurements of the silicon LVV Auger signal do not exhibit the sec θ_p dependence of these results, since at high values of θ_p their collection solid angle is considerably reduced. The emission angular distribution of the elastic peak at 1000eV was also examined as a function of incident beam angle. Figure 6.4 shows these results for two angles of incidence, 0° and 36°. Again there is a large peak close to the ⟨110⟩ direction and the relationship between this and the peak in the Auger yield with the incident beam along the same direction can be qualitatively understood on the basis of the reciprocity principle. There is also a rather more exact example of reciprocity working in figure 6.4. In the top curve labelled with $\theta_p = 36^\circ$

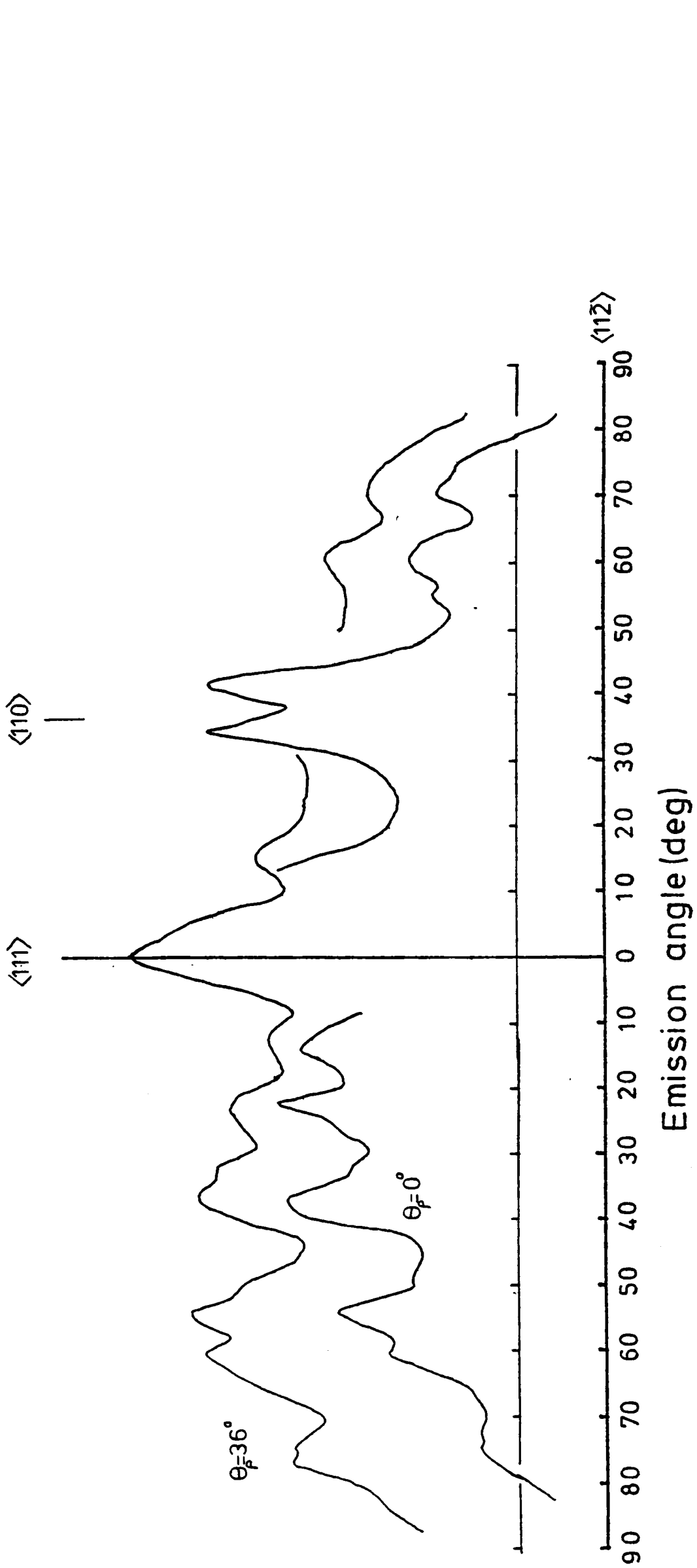


Fig.6.4 The emission angular distributions of the elastic peak from the silicon(111) surface at two angles of incidence, E_p=1000eV

the primary beam is exactly on the position of the innermost peak of the pair close to the ⟨110⟩ direction and similarly in the bottom curve the primary beam lies exactly along the ⟨111⟩ direction. Application of the reciprocity principle to this situation implies that the intensity at $\theta_e = 0^\circ$ in the top curve due to the incident beam at $\theta_p = 36^\circ$ should be the same the intensity at $\theta_e = 36^\circ$ in the bottom curve due to the incident beam at $\theta_p = 0^\circ$. This can be verified from the figure.

6.7. Results from the Copper (111) Surface

The preparation of the copper (111) surface has already been described in § 4.5.3. All the Auger spectra were collected in the differential mode, and the method described in § 6.3 was used to record the signal as a function of incident beam direction. The variations of the copper $M_{2,3}VV$, M_2VV and M_3VV peaks as a function of incident beam direction are shown in figure 6.5. It will be recalled that the $M_{2,3}VV$ signal is a doublet (see figure 4.9) with M_2VV referring to the high energy part and M_3VV to the low energy part. The three peaks all exhibit the same variation with incident beam angle showing that the copper $M_{2,3}VV$ line shape is not affected by the incident beam angle, as it was by the emission angle (§ 4.5.4). This is what would be expected since the primary beam conditions should affect only the distribution and rate of the initial ionisation but not the spectral character of the peak. The contrast in this signal, as defined earlier, is ~11%, slightly larger than the corrected figure for the silicon LVV peak. The background in this case is much flatter than the sec θ found for the silicon LVV data.

Figure 6.6 shows the variation of the copper $L_3M_{4,5}M_{4,5}$ (920eV), $L_3M_{2,3}M_{4,5}$ (840eV) and $L_3M_{2,3}M_{2,3}$ (776eV) peaks as a function of incident beam direction. The three peaks all vary in the same way and the general form is the same as for the $M_{2,3}VV$ data shown in figure 6.5. The contrast in this data is however ~26%, much larger than the contrast in the $M_{2,3}VV$ signal. Finally

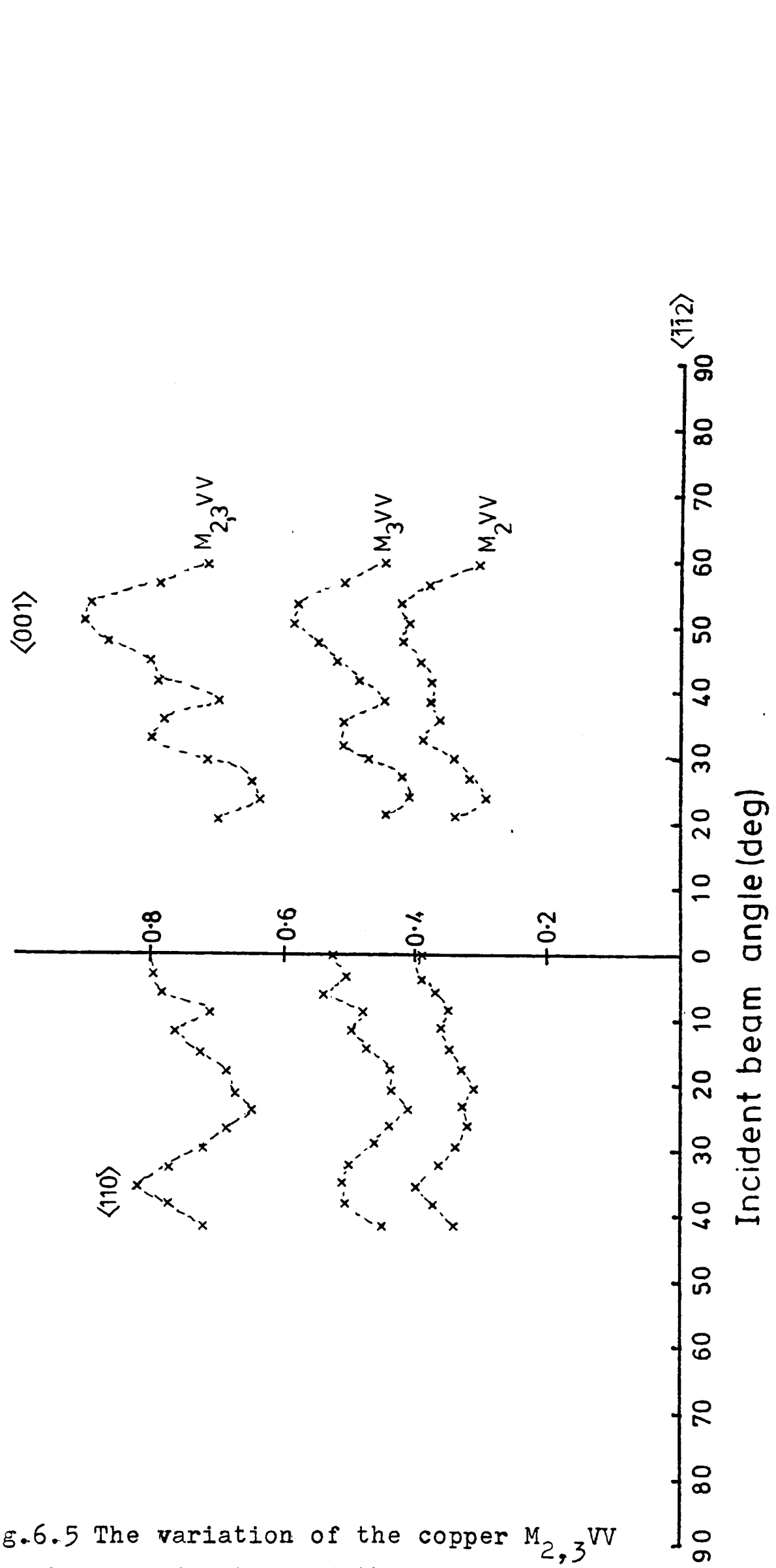


Fig.6.5 The variation of the copper $M_{2,3}VV$ signals as a function of the primary beam direction from the copper(111) surface

E_p=1500eV, θ_e=15°

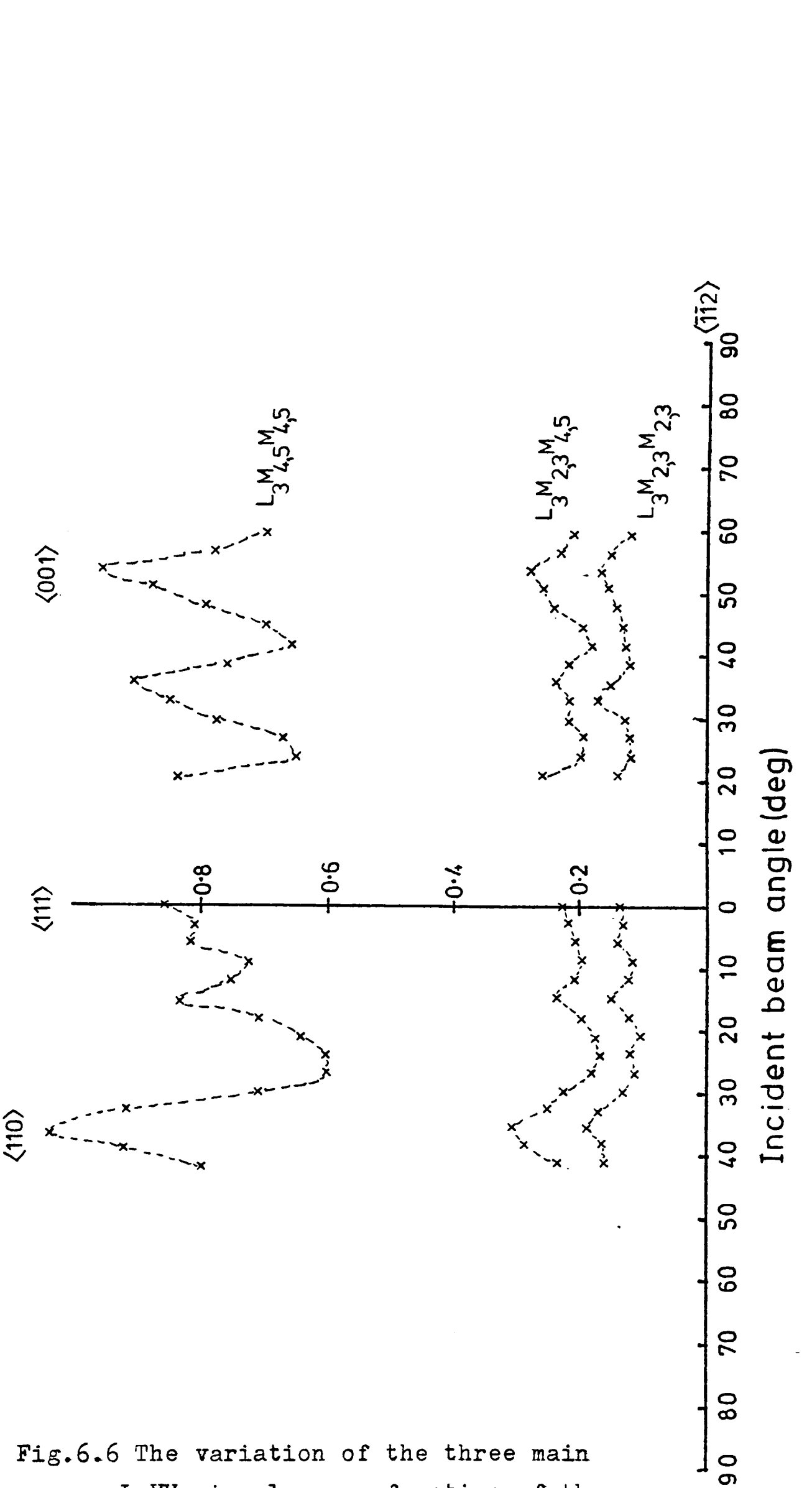


Fig.6.6 The variation of the three main copper L_3VV signals as a function of the primary beam direction from the copper(111) surface, E_p=1500eV, θ_e=15°

figures 6.7 and 6.8 show respectively, the variation in the specimen current as a function of the primary beam direction and the variation in the elastic peak as a function of emission angle. Again the similarities between these figures and figures 6.5 and 6.6 can be qualitatively understood on the basis of the reciprocity principle. It is also interesting to note the similarity between the emission angular distribution of the L_3VV signals (figure 5.8) and the variations in the L_3VV signals (figure 6.6) due to changes in the incident beam direction. This relationship certainly does not hold for the $M_{2,3}VV$ signals where the emission angular distributions are totally different from the changes in yield as a function of primary beam direction.

6.8. Discussion

These results show that there is a very marked correlation between the elastically backscattered electron angular distributions (figures 6.4 and 6.8) and the variations in the measured Auger current as a function of the primary beam direction (figures 6.3, 6.5 and 6.6). This agrees with the results of Allié et.al. (1974) and Rusch et.al. (1973). These correlations can be qualitatively explained on the basis of the reciprocity principle in the following way.

The simplest way to describe the origins of the Kikuchi patterns is to consider the electrons as originating from spherical sources centred on lattice sites. It therefore follows from the reciprocity principle that electrons of the same energy, directed into the crystal along directions, which show high intensity in the Kikuchi pattern, will have high intensities at the lattice sites. This in turn will lead to a high rate of ionisation at the lattice sites and therefore an enhanced Auger yield. This argument ignores the contribution of the inelastically scattered electrons and also the very small escape depth of the Auger electrons, which means that not all the Auger electrons created will leave the crystal.

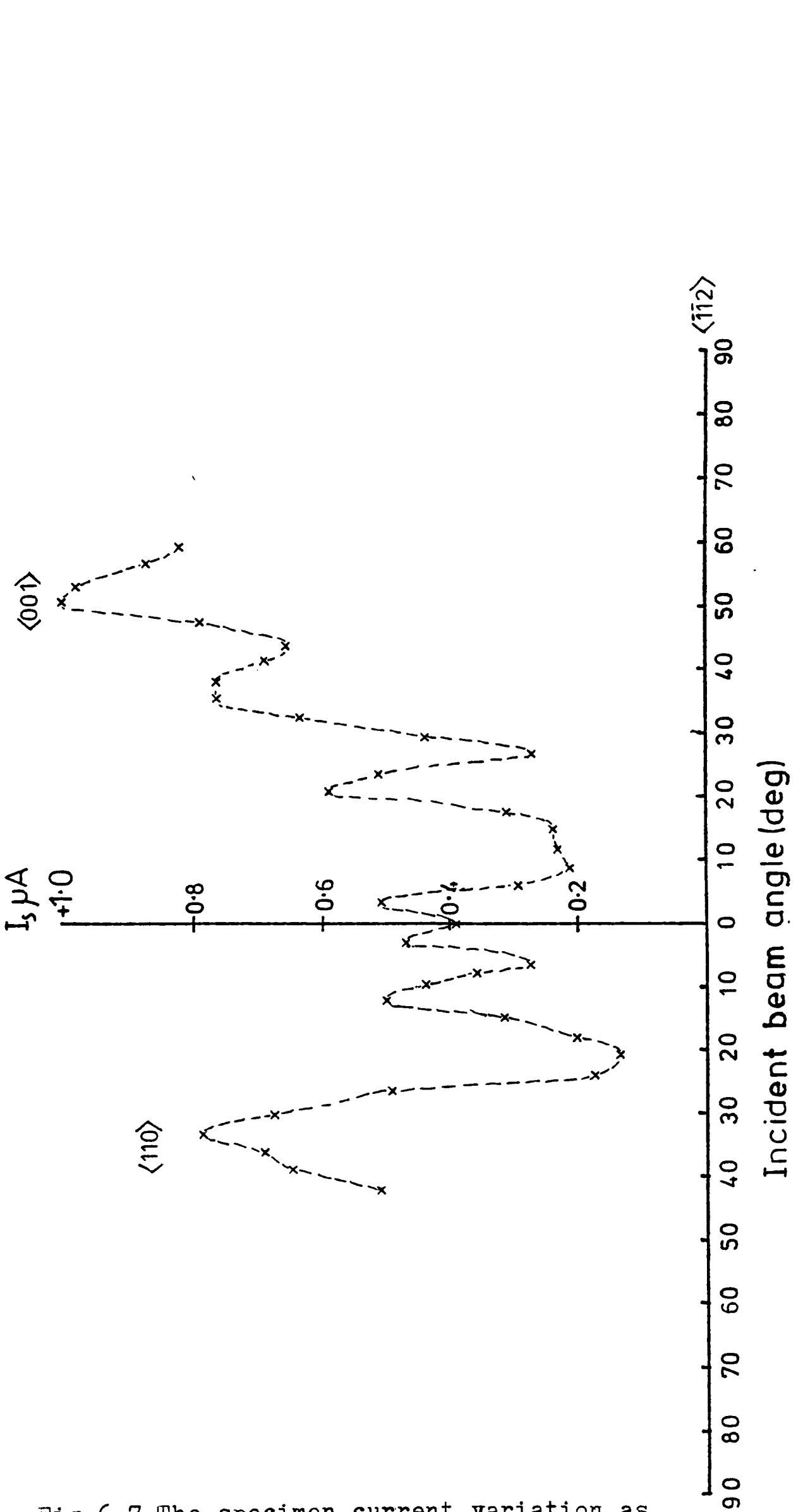


Fig.6.7 The specimen current variation as a function of the incident beam direction from the copper(111) surface, E_p=1500eV

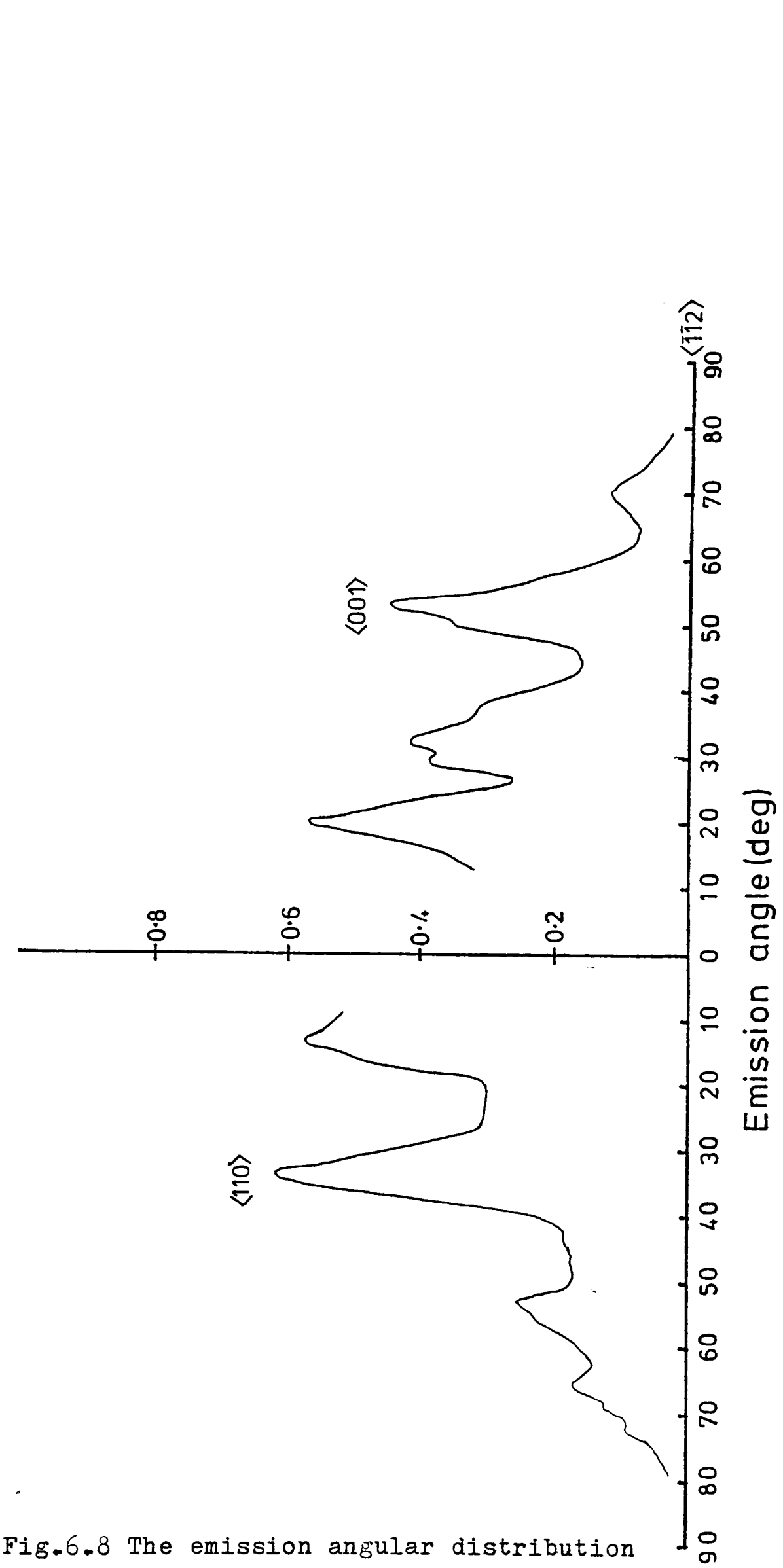


Fig.6.8 The emission angular distribution of the elastic peak from the copper(111) surface, E_p=1500eV, θ_p=15°

The variation in the specimen current as a function of primary beam direction (figures 6.3 and 6.7) also showed a correlation with the elastically backscattered electron angular distributions (figures 6.4 and 6.8) and to an even greater extent with the Auger yields as a function of θ_p. The variation in the specimen current from the silicon (111) surface shown in figure 6.3 agrees with the results of Rusch et.al. (1973). It should also be noted that the specimen current measured from the copper (111) surface is always positive, whereas the specimen current from the silicon (111) surface only becomes positive at large angles of incidence. This implies that the total backscattered and secondary electron signal is higher for the copper specimen and this is consistent with the results of Smith and Gallon (1974) where it was shown that the backscattering factor increases with z, the atomic number, If it is assumed that the probability of creating backscattered and secondary electrons is proportional to the intensity of the incident wavefield at a lattice site, then the same argument already used to explain the correlation between the Auger yield as a function of θ_p, and the Kikuchi pattern, can be used to explain the correlation between the specimen current variation as a function of θ_p and the Kikuchi pattern.

The final correlation worth noting is between the emission angular distributions of the high energy Auger electron, shown in figures 5.2 and 5.3 for silicon (111) and figure 5.8 for copper (111), and the variations in Auger yields as a function of θ_p. The same arguments as before, based on the reciprocity principle, give a qualitative explanation of this correlation. Therefore it appears that the construction shown in figure 5.11, originally intended to describe the emission angular distributions of the high energy Auger electrons, can also be used, with the aid of the reciprocity principle, to describe the variations in many diverse backscattered electron signals as a function of θ_p. Although these arguments give a qualitative understanding of the variations in the different backscattered signals as a function of θ_p they cannot, for instance, explain why the variations of the copper L_3VV signals are larger

than those of the copper $M_{2,3}VV$ signals (figures 6.6 and 6.5).

This effect can be more readily understood from the work of Andersen and Howie (1975) and Baines et.al. (1975). According to this theory primary wavefield modulation starts to build up at depths greater than $\sim 0.1\,\xi_g \cos\theta_p$, where ξ_g is the extinction distance of dynamical theory. ξ_g for low order reflections in copper at 1500eV can be estimated from the data of Hirsch et.al. (1965) to be ~ 40 to $50\mathring{A}$. Thus at normal incidence the primary wavefield modulation starts to become significant at depths greater than $\sim 4\mathring{A}$ and is fully developed at $\sim 8\mathring{A}$. The inelastic mean free paths of the copper $M_{2,3}VV$ and L_3VV Auger electrons can be estimated from Seah and Dench (1978) to be $\sim 4\mathring{A}$ and $\sim 12\mathring{A}$ respectively. This means that the L_3VV Auger electrons can escape from depths where the primary wavefield modulation is fully developed, whereas the majority of the $M_{2,3}VV$ electrons originate at depths where the primary wavefield modulation is less well developed. Thus the experimental observations, that the contrast ($\sim 25\%$) in the copper L_3VV signal is greater than the contrast ($\sim 14\%$) in the copper $M_{2,3}VV$ signal, can be explained on the basis of a "Bragg modulation region" starting at $\sim 8\mathring{A}$ below the surface, as described by Andersen and Howie (1975).

If the primary wavefield modulation is not developed within the escape depth of the copper $M_{2,3}VV$ Auger electron, then this implies that the variations in Auger yield as a function of θ_p must be due to the backscattered electrons. An estimate of the magnitude of this effect can be made in the following way. The Auger current can be written as (Andersen and Howie (1975))

$$i_a(\theta_p,\phi_p) \propto \sigma(E_p)\left[\sec\theta_p I_o(\theta_p,\phi_p) + (\theta_p,\phi_p) I_B(\theta_p,\phi_p)\right] \quad \text{---- (2)}$$

where the terms are defined in § 6.5.2.

If no angular structure is introduced by the primary wavefield $I_o(\theta_p,\phi_p)$, then, assuming $(\theta_p,\phi_p) = 1$, all the angular structure must be due to variations in $I_B(\theta_p,\phi_p)$. An upper limit on the angular variation of $I_B(\theta_p,\phi_p)$ is

given by the contrast in the backscattered elastic signal, and the magnitude of $I_B(\theta_p,\phi_p)$ can be estimated from the data of Allié et.al. (1974) and Rusch et.al. (1973) to be less than 0·14 I_p. Thus from the experimental data of Baines et.al. (1974), where the contrast in the backscattered elastic signal was 38%, the maximum contrast expected in the Auger signal would be 0·14x38% = 5%. Their experimental contrast in the Auger signal was 9·5%, almost twice that expected. In a similar way the results of Allié et.al. (1974) show that the contrast in the backscattered elastic signal is ~38% and therefore the predicted contrast in the Auger signal would again be ~5%. Their experimental results showed a contrast of 8% in the Auger signal. In both these sets of data the aluminium $L_{2,3}VV$ signal at 67eV was studied which, like the copper $M_{2,3}VV$ signal, will originate in the top ~4Å of the crystal.

Similar estimates of the contrast in $I_B(\theta_p,\phi_p)$ can be obtained from the data in figures 6.4 and 6.8. These figures in fact show the emission angular distributions of the elastic signal from the silicon (111) surface with θ_p=0° and 36° and from the copper (111) surface with θ_p=0°. The reciprocity principle can be applied exactly to this data to find the variation in the backscattered electron signal at normal emission, as a function of the angle of incidence, since the intensity measured at a particular value of θ_e, with the primary beam at normal incidence, will be exactly the same as the intensity measured at normal emission with the primary beam set with $\theta_p = 0_e$. This relation is illustrated quite clearly in figure 6.4 where it can be seen that the intensity measured at θ_e = 36° with θ_p = 0° is exactly the same as the intensity measured at θ_e = 0° with θ_p = 36°. Thus the contrast in the backscattered elastic signal at θ_e = 0°, from the silicon (111) surface is 33% and from the copper (111) surface is 33%. In the same way as before this predicts a contrast in the Auger signal from the silicon (111) surface and the copper (111) surface of ~5%. The experimentally observed values are 7% for the silicon $L_{2,3}VV$ signal and 14% for the copper $M_{2,3}VV$ signal. Using a similar argument Rusch et.al. (1973) predicted that the contrast in the Auger

signal from a carbon overlayer would be 5% whereas the observed value was 11%. In summary it appears that the contrast in the angular variations of the Auger signals, as a function of θ_p, are larger than the contrast predicted on the basis of the work by Anderson and Howie (1975). This problem has already been mentioned by Baines et.al. (1975), and they are forced to conclude that, even in the case of low energy Auger electrons, a large amount of the signal must come from depths of more than 10Å below the surface. Since this does not seem a very likely explanation it seems worth examining the backscattered electron contribution in a little more detail.

Applying the reciprocity principle to the data of figure 6.4 showed that the variation in the backscattered electron intensity at $\theta_e = 0$, as a function of θ_p, would be represented by the same curve with the angular readings referring, not to emission angle, but to the incident beam angle θ_p. Allié et.al. (1974) have measured the elastic backscattered electron intensity as a function of ϕ_p, using an R.P.A. system with a collection solid angle of 2π steradian. This data exhibited a contrast of ~39%. They also measured the corresponding emission angular distribution with $\theta_p = 0^\circ$ and the contrast in this signal was 18%. Applying the reciprocity principle to this data, in the same way as was done for the data of figure 6.4, shows that the elastic backscattered intensity measured at $\theta_e = 0^\circ$ would also exhibit a contrast of 18%. This seems to indicate that the elastic backscattered electrons travelling close to grazing emission angles exhibit larger changes as a function of θ_p than electrons that have been scattered through larger angles. This same effect can also be seen in the data of figure 6.4 where it can be seen that the difference between the two curves recorded at $\theta_p = 0^\circ$ and 36° increase with increasing emission angle. This effect can be explained because the Debye - Waller factor $\exp(-2\alpha \sin^2 \theta_s / \lambda^2)$, will be less for electrons scattered through smaller angles θ_s close to grazing emission angles. This means that the wavefield associated with these electrons will be of a more coherent nature and will exhibit larger variations as θ_p is changed, than the wavefield associated with large angle

scattering. This argument may go some way to explaining why the backscattered current $I_B(\theta_p,\phi_p)$ can cause such large variations in the Auger yield since the electrons travelling at grazing angles to the surface, which will also be the most efficient at producing Auger electrons, also exhibit the largest intensity changes as θ_p (or ϕ_p) is varied.

A further point worth considering is the value of the backscattering factor relevant to the primary energies used in these experiments. Smith and Gallon (1974) have shown that the backscattering factor r for silicon (z = 14) is $\sim$1·5, this should also be close for aluminium (z = 13), and for copper (z = 29) r would be expected to be slightly larger. This implies either that γ in equation (2) is equal to 2 or 3 or that the value of I_B measured outside the surface underestimates the backscattered current in the top 4Å of the crystal. It therefore appears that there are grounds for believing that the backscattered electrons produce almost 30% of the overall Auger signal and that the most effective part of this current, travelling at large angles θ from the surface normal, also exhibits the largest intensity changes as a function of θ_p. These mechanisms provide an alternative way of understanding the relatively large variations in Auger yield that are observed, to that of Baines et.al. (1975), that requires a large amount of the Auger signal to come from depths of 10Å or greater.

6.9. Summary

Large changes in the relative strengths of substrate to overlayer Auger signals have been shown to occur as the primary beam direction is changed. These results were explained on the basis of a simple model that includes the effects of primary beam attenuation and an estimate of the overlayer thickness was obtained.

The variations in the Auger signal and various other signals have been measured as a function of incident beam direction from single crystal surfaces.

It was shown that the correlations observed between these results and the emission angular distributions of the Auger and elastic signals at ~1KeV, could be qualitatively explained on the basis of the reciprocity principle. By examining the variations in the copper L_3VV and $M_{2,3}VV$ signals as a function of incident beam direction, it was possible to test one of the conclusions of Andersen and Howie (1975) concerning the "Bragg modulation region" and the results support the model. Finally, a mechanism has been suggested that explains the relatively large changes observed in the Auger yield, that does not require an excessively large escape depth for low energy Auger electrons.

Chapter 7

An Investigation of the Growth Form of Thin Metallic Films using Angle Resolved Auger Spectroscopy

		page
7.1	Introduction	116
7.2	Preparation and Calibration of Equipment	117
7.3	Theory	120
7.4	Experimental Method	123
7.5	Results	124
7.5.1	The Iron/Copper System	124
7.5.2	The Copper/Gold System	130
7.5.3	The Iron/Tin System	134
7.6	Discussion and Summary	138

7.1. Introduction

The work to be described in this chapter has been performed with two interrelated aims in mind. The first is the accurate determination of inelastic mean free paths and the second concerns the growth forms of evaporated metal films.

The most common way of determining inelastic mean free paths (imfp's) is to measure the variation in intensity of Auger or photoemitted electrons as known quantities of material are deposited on a substrate. An accurate imfp determination therefore requires an accurate calibration of the amount of condensate present and a suitable theoretical model to relate the measured intensities to the imfp. Although this seems a fairly straightforward type of experiment, the compilation of Seah and Dench (1978) shows that the scatter of experimental points often extends over an order of magnitude, indicating the need for more accurate experimental procedures.

Many methods, including LEED (Palmberg and Rhodin (1968)(a)) and ellipsometry (Meyer and Vrakking (1972)), have been used to measure the amount of condensate material present but perhaps the most accurate method, described by Seah (1972), is to use a well calibrated quartz crystal oscillator. This forms the basis of the method used here and the preparation and calibration of the quartz crystal will be described in section (7.2).

The second part of the problem is to describe theoretically the variation in the Auger signal as a function of condensate thickness. At its simplest the Auger current from the substrate, i_n^s, emitted along the surface normal can be written as (Seah (1972))

$$i_n^s = i_o^s \exp\left(-\frac{n}{\lambda_s^o}\right) \qquad \text{-----} \quad (1)$$

i_o^s - Auger current from clean surface

n - overlayer thickness in monolayers

λ_s^o - imfp of substrate Auger electrons in overlayer

This model assumes that the condensate atoms are deposited in uniform layers and that the rate of Auger production in the substrate is not affected by the overlayer. This is of course only one of the many ways in which thin films can grow (e.g. Chopra (1969)) and each mode of growth will cause the Auger signals to change in a different way as a function of film thickness. It is therefore of great importance to be able to detect the departure from a layer growth mode to avoid the erroneous application of equation (1) to the experimental data. For the case of Copper deposited onto Silver, Seah (1972) observed that the 60eV and 935eV Copper Auger electrons both behaved in exactly the same way as a function of overlayer thickness. Since the imfp's of the high and low energy electrons would be expected to be different, Seah (1972) concluded that copper islands were forming on the surface. In materials where two such sets of Auger transitions are not available, or where both sets were not measured, this method of island detection would fail and other methods would have to be found.

It was shown both theoretically and experimentally in chapter 3 that the presence of islands or uniform overlayers could be detected by measuring the emission angular distributions of the substrate and overlayer Auger electrons. The rest of this chapter will go on to show how this technique has been used to determine the growth forms of various metal on metal systems where the amount of condensate present has been quantitatively determined using the quartz crystal oscillator. The necessary modifications to the apparatus will be described in the next section.

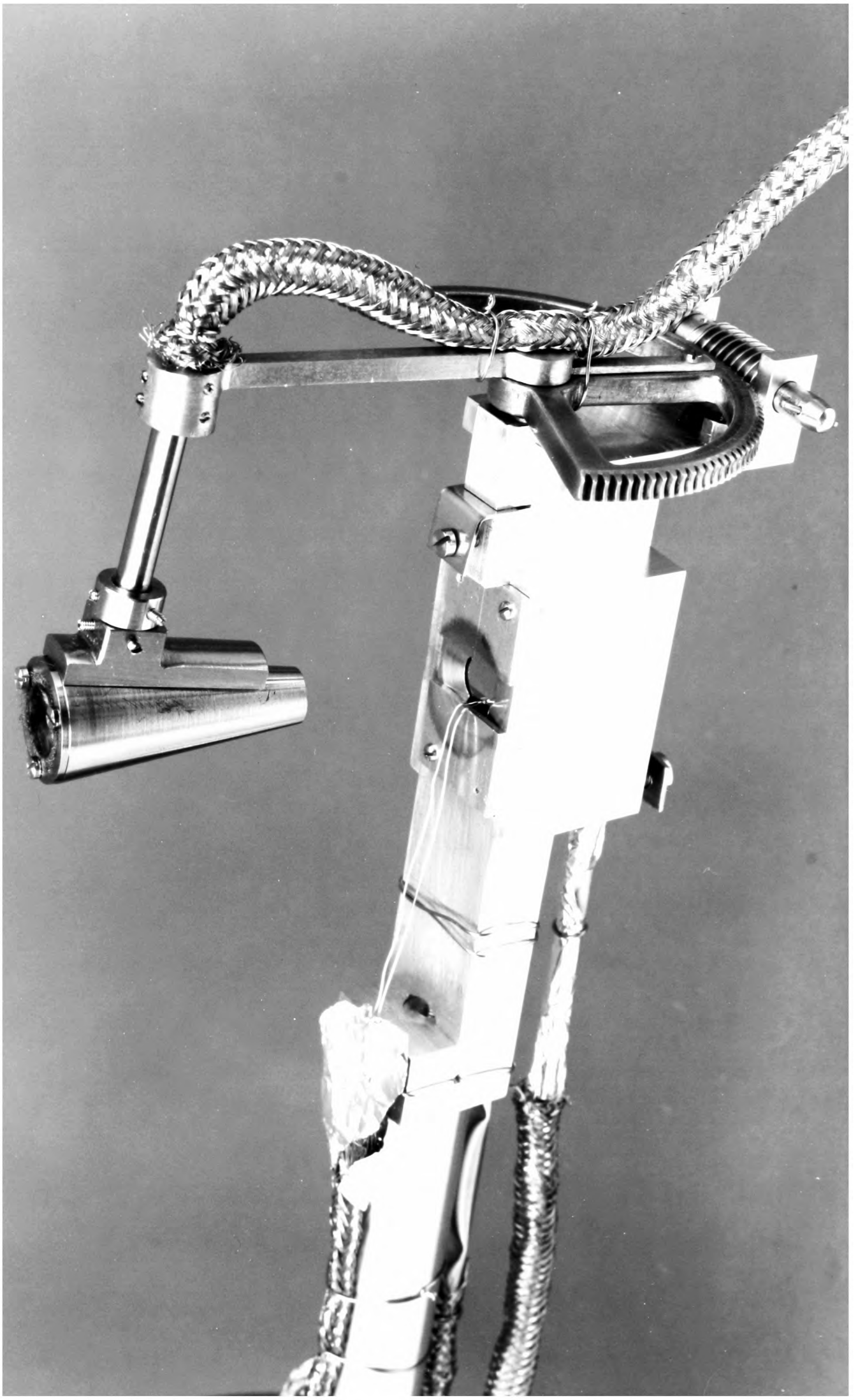
7.2. Preparation and Calibration of Equipment

The usual method of using a quartz crystall oscillator is to position the quartz crystal as close as possible to the substrate being studied as possible. Great care must therefore be taken to ensure that the flux of particles incident on the substrate and quartz crystal are identical otherwise systematic errors can arise. It must also be assumed that the sticking

probabilites of the two surfaces are equal for all the conditions of temperature etc. used in the experiments. These problems have been eliminated in the experiments that follow by using the quartz crystal as the substrate ensuring that any mass changes observed apply exactly to the substrate being studied. Unfortunately the quartz crystals normally used in commerical thin film monitors have a rather rough surface finish, which makes them unsuitable for the angle resolved experiments envisaged. An optically smooth surface finish was obtained by polishing a standard 6MHz AT cut crystal, using "Syton". Gold electrons about 1000Å thick were then evaporated onto the crystal in the usual way. The amount of polishing required did not significantly effect the resonant frequency of the crystal and any small difference could be corrected by using a slightly thicker than normal electrode.

The crystals used were 13·7mm in diameter which prevented them being used in the specimen goniometer described in chapter 2. It was therefore necessary to design and build a new goniometer to accept the larger crystals. Since only polycrystalline specimens were to be examined it was unnecessary to incorporate the azimuthal rotations of the original goniometer and a rather simpler design was possible. The completed goniometer is shown in figure 7.1. The takeoff angle is adjusted by rotating the whole goniometer and the incident beam angle is adjusted in the same way as before, by rotating the worm gear. As before a fluorescent screen was used in place of the quartz crystal to ensure the beam did not change position on the specimen, as the incident beam direction was varied. The quartz crystal is held in place in the goniometer by two stainless steel wires which also make the electrical connections to the front and rear electrons on the crystal. These wires, which carry the 6MHz signal to the crystal, are led out to the electrical feedthroughs in a UHV compatible screened cable made with fibre glass sleeving and copper braid. Finally the specimen can be heated by a tungsten filament placed behind the crystal and the surface temperature of the crystal can be measured using the

Fig.7.1 The goniometer



thermocouple (Pt - Pt 13% Rh) held in contact with the front face of the crystal. Having mounted the crystal in this way the calibration of the Edwards FTM2 quartz crystal oscillator was performed as follows.

An Aluminium film about 1000Å thick was evaporated onto a polished glass slide and the quartz crystal to ensure that the sticking probabilities of both surfaces would be equal. The FTM2 unit was set onto its "1K - 3K" range and the density control was set to 1g/cc for maximum sensitivity. The glass slide, with part of its surface covered by a razor edge, was then placed beside the crystal and an Aluminium film was deposited which gave a reading of 2660 $\pm$ 15 Å on the 3K scale. The film thickness was then determined by measuring the step height created by the razor edge using a multiple beam interferometer. The film thickness can be calculated knowing the spacing of the interference fringes S, the size of the kink caused by the surface step k, and the wavelength λ of the light being used (in this case 5890Å). The film thickness t is given by (Tolansky (1960)) $t = \frac{\lambda}{2} \times \frac{k}{S}$

and for $k = 23 \pm 1$mm and $S = 53 \pm 1$mm. the film thickness is

$$t = 1278 \pm 89 \text{Å}$$

Thus full scale deflection on the 3K scale corresponds to 1441Å $\pm$ 100Å and on the 300 scale, full scale deflection is 144 $\pm$ 10Å. This calibration can be used for other metals providing the film densities are known, thus taking the film density of aluminium as $\rho = 2{\cdot}60$ g/cc (Clapham et.al. (1969)) and that of copper as 8·10 g/cc (Wolter (1965)) implies that full scale deflection on the 300 scale corresponds to 48 $\pm$ 3Å of copper.

Since it is clearly advantageous to study the effects of different condensates without exposing the substrate to atmosphere, a five port evaporator was built. Each port could be rotated to face the substrate in turn allowing any sequence of evaporations to be performed. Since only monolayer quantities of evaporant were required very fine tungsten and molybdenum wires only 0·125mm in diameter were used, keeping the powers required to evaporate material to a minimum (typically 5 watts or less). The condensate material was always

evaporated at normal incidence by rotating the gun well away from normal incidence and rotating the whole goniometer to face the appropriate port of the evaporator. After outgassing the sources the chamber vacuum always remained at $\sim 8 \times 10^{-10}$ torr or less during evaporations. Before presenting the results obtained with this apparatus a short discussion of the relevant theory will now be given.

7.3. Theory

In this section, the changes expected in the substrate and overlayer Auger signals, as a function of condensate quantity, will be discussed on the basis of simple layer growth and island growth models. The theory describing the Auger emission angular distributions, already discussed in § 3.5 for uniform layers, will be extended to cover the case of island growth and the case where a concentration gradient exists between substrate and overlayer.

As mentioned earlier, if it is assumed that the presence of an overlayer does not affect the rate of Auger production in the substrate, then the substrate Auger current i_n^s emitted along the surface normal, in the presence of a uniform overlayer n monolayers thick, can be written

$$i_n^s = i_o^s \exp\left(-\frac{n}{\lambda_s^o}\right) \qquad \text{------} \quad (2)$$

where i_o^s - Auger current from clean surface

λ_s^o - imfp of substrate Auger electrons in overlayer.

In a similar way (Seah (1972)) the overlayer Auger current i_n^o emitted along the surface normal can be written

$$i_n^o = i_\infty^o \left(1-\exp\left(-\frac{n}{\lambda_o^o}\right)\right) \qquad \text{----} \quad (3)$$

where i_∞^o - current from bulk condensate

λ_o^o - imfp of overlayer Auger electrons in overlayer

As discussed by Seah (1972), this theory should give good agreement with experiment for thin overlayers since this would not be expected to alter the backscattering factor in a significant way. If however the overlayer is in

the form of discrete islands the following model would be more appropriate.

In this model it is assumed that :-

a) The number of nuclei per unit area (N) remains fixed

b) The islands are of a fixed rectangular shape of height t, covering a surface area of w^2. The shape of the island is simply defined by the ratio of $\frac{t}{w} = x$. The unit of length used is the monolayer thickness.

It can then be shown that the fraction of the surface area occupied by islands is given by $F = Nw^2$. This can be expressed in terms of n, the equivalent monolayer thickness, by equating the volumes of N islands per unit area to the volume of a monolayer of atoms per unit area such that $Ntw^2 = n$ and since $x = \frac{t}{w}$, F can be written as

$$F = \left(N \frac{n^2}{x^2}\right)^{\frac{1}{3}} \qquad \text{---- (4)}$$

Therefore on the basis of this model the substrate Auger signal i_n^s is given by

$$i_n^s = i_o^s \left((1 - F) + F \exp\left(- \frac{t}{\lambda_s^o}\right)\right) \qquad \text{---- (5)}$$

and the overlayer signal i_n^o is given by

$$i_n^o = i_\infty^o \; F \left(1 - \exp\left(- \frac{t}{\lambda_o^o}\right)\right) \qquad \text{---- (6)}$$

It is now necessary to express t as a function of n, x and N. It can easily be shown that $t = \left(\frac{nx^2}{N}\right)^{\frac{1}{3}}$ and equation (5) becomes

$$i_n^s = i_o^s \left[\left(1 - \left(\frac{Nn^2}{x^2}\right)^{\frac{1}{3}}\right) + \left(\frac{Nn^2}{x^2}\right)^{\frac{1}{3}} \exp\left(- \left(\frac{nx^2}{N}\right)^{\frac{1}{3}} \cdot \frac{1}{\lambda_s^o}\right)\right] \qquad \text{---- (7)}$$

and equation (6) becomes

$$i_n^o = i_\infty^o \left(\frac{Nn^2}{x^2}\right)^{\frac{1}{3}} \left(1 - \exp\left(- \left(\frac{nx^2}{N}\right)^{\frac{1}{3}} \cdot \frac{1}{\lambda_o^o}\right)\right) \qquad \text{---- (8)}$$

Typical values of N lie in the range 10^{-3} to 10^{-5} (Chopra (1969)) and for low energy Auger electrons $\lambda \simeq 2$ monolayers (Seah and Dench (1978)). Figure 7.2 shows the behaviour of the substrate and overlayer Auger signals

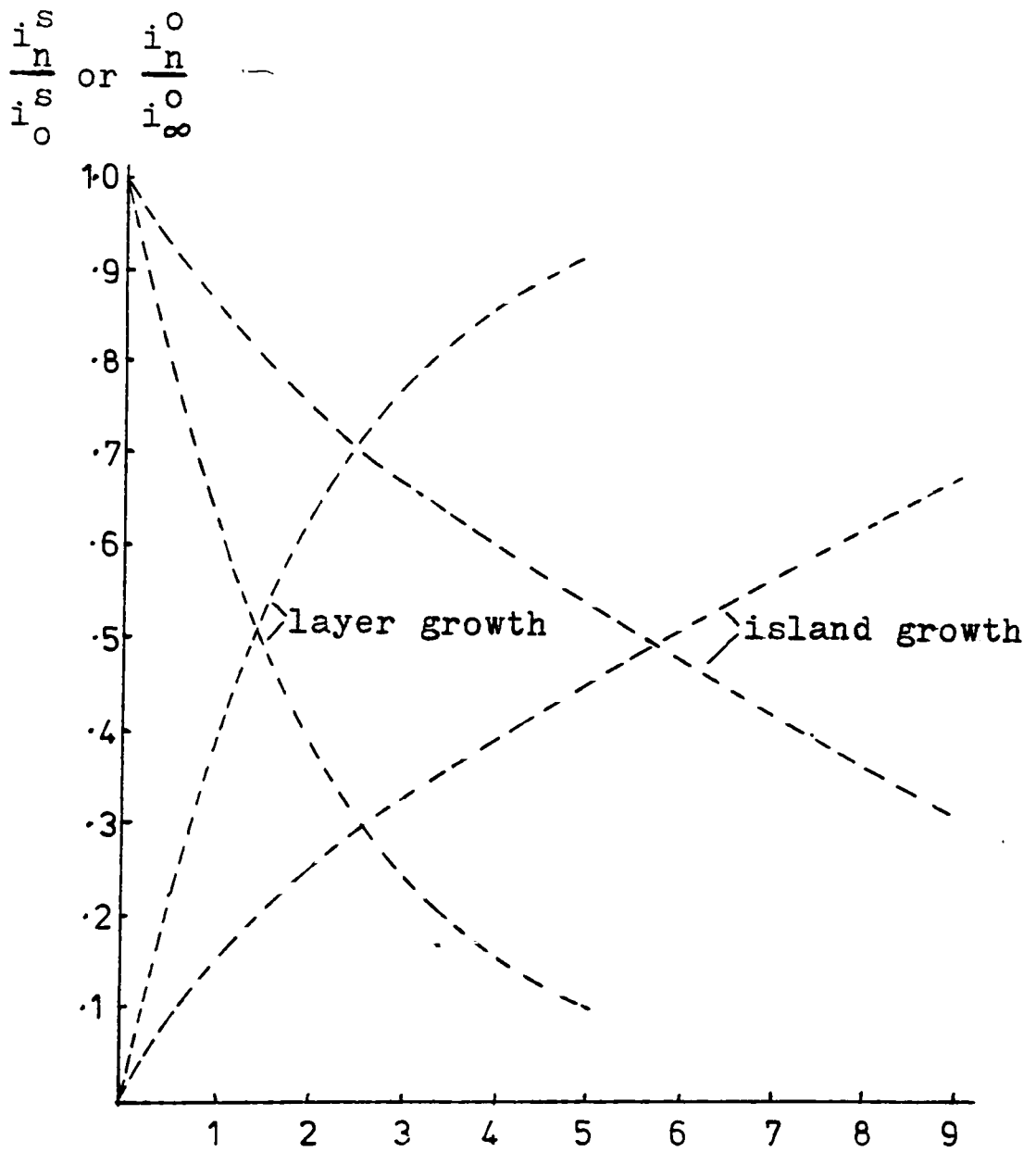


Fig.7.2 Monolayers of condensate

Theoretical predictions for the variation in substrate and overlayer Auger signals as a function of condensate quantity with λ =2monolayers and $N=10^{-3}$, $x=0.5$

predicted on the basis of equations (7) and (8) with $\lambda_s^o = \lambda_o^o = 2$ monolayers, $x = 0{\cdot}5$ and $N = 10^{-3}$. Also shown for comparison is the behaviour predicted on the basis of the layer growth model (equations (2) and (3)) with $\lambda_s^o = \lambda_o^o =$ 2 monolayers. Thus it can be seen that the Auger signals behave in a quite different way depending on the growth mode of the film. It is therefore extremely important to be able to determine the growth mode of the film before attempting to extract values of λ from data of this type.

The substrate and overlayer Auger angular distributions expected from a surface with islands t monolayers thick, covering a certain fraction F, of the surface area, can be derived from equations (9) and (11) of chapter 3. The substrate Auger angular distribution is simply a superposition of the angular distributions from the clean parts of surface, and from the covered parts of the surface, and equation (9) of chapter 3 becomes

$$\frac{i_a^s(\theta)}{i_a^s(0)} = \cos\theta\left[(1-F) + F\exp\left(-\frac{t}{\lambda_s^o}(\sec\theta - 1)\right)\right] \quad \text{-----} \quad (9)$$

The overlayer angular distributions from islands t monolayers thick are exactly the same as the overlayer angular distributions from a uniform layer t monolayers thick and equation (11) of chapter 3 is therefore valid for either system.

Consider now what happens where the concentration of condensate atoms per unit depth $n_c(z)$ is given by $n_c(0)\exp(-\frac{z}{g})$. The Auger angular distribution expected on the basis of this type of model has already been considered in § 3.2 and the result is

$$\frac{i_g^c(\theta)}{i_g^c(0)} = \frac{1 + \frac{g}{\lambda_c}\cos\theta}{\frac{g}{\lambda_c} + \cos\theta} \quad \text{-----} \quad (10)$$

λ_c = imfp of condensate Auger electrons.

The substrate Auger angular distribution $\frac{i_g^s(\theta)}{i_g^s(0)}$ can be evaluated as follows. The total concentration of sites per unit depth is taken to be n_t

and therefore $n_c(0)\exp(-\frac{z}{g}) + n_s(z) = n_t$ where $n_s(z)$ is the concentration of substrate atoms per unit depth.

Taking $n_c(o) = Cn_t$, $n_s(z)$ becomes

$$n_s(z) = n_t\,(1 - C\exp(-\tfrac{z}{g})) \qquad \text{-----} \quad (11)$$

and since $i_a^s(z)$, the substrate Auger current at depth z is proportional to $n_s(z)$

$$i_g^s(\theta) \propto n_t \int_0^\infty (1-C\exp(-\tfrac{z}{g}))\exp\left(-\frac{z}{\lambda_s\cos\theta}\right) dz\,\frac{\Delta\Omega}{4\pi} \qquad \text{-----} \quad (12)$$

and therefore

$$\frac{i_g^s(\theta)}{i_g^s(0)} = \cos\theta\left(\frac{\cos\theta + \frac{g}{\lambda_s}(1-C)}{\cos\theta + \frac{g}{\lambda_s}}\right)\left(\frac{1 + \frac{g}{\lambda_s}}{1 + \frac{g}{\lambda_s}(1-C)}\right) \qquad \text{----} \quad (13)$$

taking C = 1 this becomes

$$\cos^2\theta\left(\frac{1 + \frac{g}{\lambda_s}}{\cos\theta + \frac{g}{\lambda_s}}\right) \qquad \text{-----} \quad (14)$$

It should be noted that taking C = 1 implies only that $n_s(z) = 0$ in the layer dz at the surface, it should not be taken to mean that the top monolayer is pure condensate.

7.4. Experimental Method

Before presenting the experimental results a brief description will be given of the experimental proceedures used to obtain the plots of Auger signal versus condensate quantity. The evaporator filaments were charged with beads of 5N pure gold, copper, tin and iron, and the evaporations were carried out at rates of a few monolayers per minute. After the condensation of a known quantity of material the goniometer was rotated into a horizontal position such that the angle of emission was 15°. To avoid having to move the miniature electron gun back to normal incidence after each evaporation an auxiliary electron gun was used. This was mounted in such a way that the angle of incidence was 50° when the goniometer was in the horizontal position.

To check that thermally induced changes in the crystal frequency did not cause false readings, the output of the Edwards FTM2 film thickness monitor was always plotted on a chart recorder for a few minutes before and after the evaporation. In this way thermal effects could be detected as changes in the FTM2 readings after the evaporator had been switched off.

7.5. Results

In this section the experimental results will be presented and analysed to try and determine the growth modes of the films and the inelastic mean free paths of the Auger electrons involved. Three different systems have been studied, Cu/Au, Fe/Cu and Fe/Sn. In each system A/B, condensation experiments have been performed for A on B and B on A. According to the criteria of Bauer and Poppa (1972), based on the surface energies of the substrate and condensate materials, island growth should occur for either B on A or A on B, unless the surface energies are equal.

7.5.1. The Iron/Copper System

Figure 7.3 shows the variation in the copper (920eV) and iron (703eV) signals as a function of copper condensate quantity in monolayers. The data were recorded in the derivative mode using a 1·5 V r.m.s. modulation on the substrate and the peak to peak heights of the signals were taken as proportional to the Auger currents and the copper monolayer thickness was taken to be 2·56Å (the atomic diameter). Small amounts of oxygen, with a signal strength about $\frac{1}{4}$ that of the iron (703eV) peaks, were always present on the iron films and could not be removed, even by evaporating a few hundred angstroms of iron. Both signals have been normalised such that $i_o^s = 1$ and $i_\infty^o = 1$ and the relative scaling factor K for the overlayer signal relative to the substrate signal is 1·36. Thus at 5 monolayers of copper for instance, the signal ratio of the copper to iron signals from the diagram is 1·4. The actual signal ratio is given by K x 1·4 = 1·9.

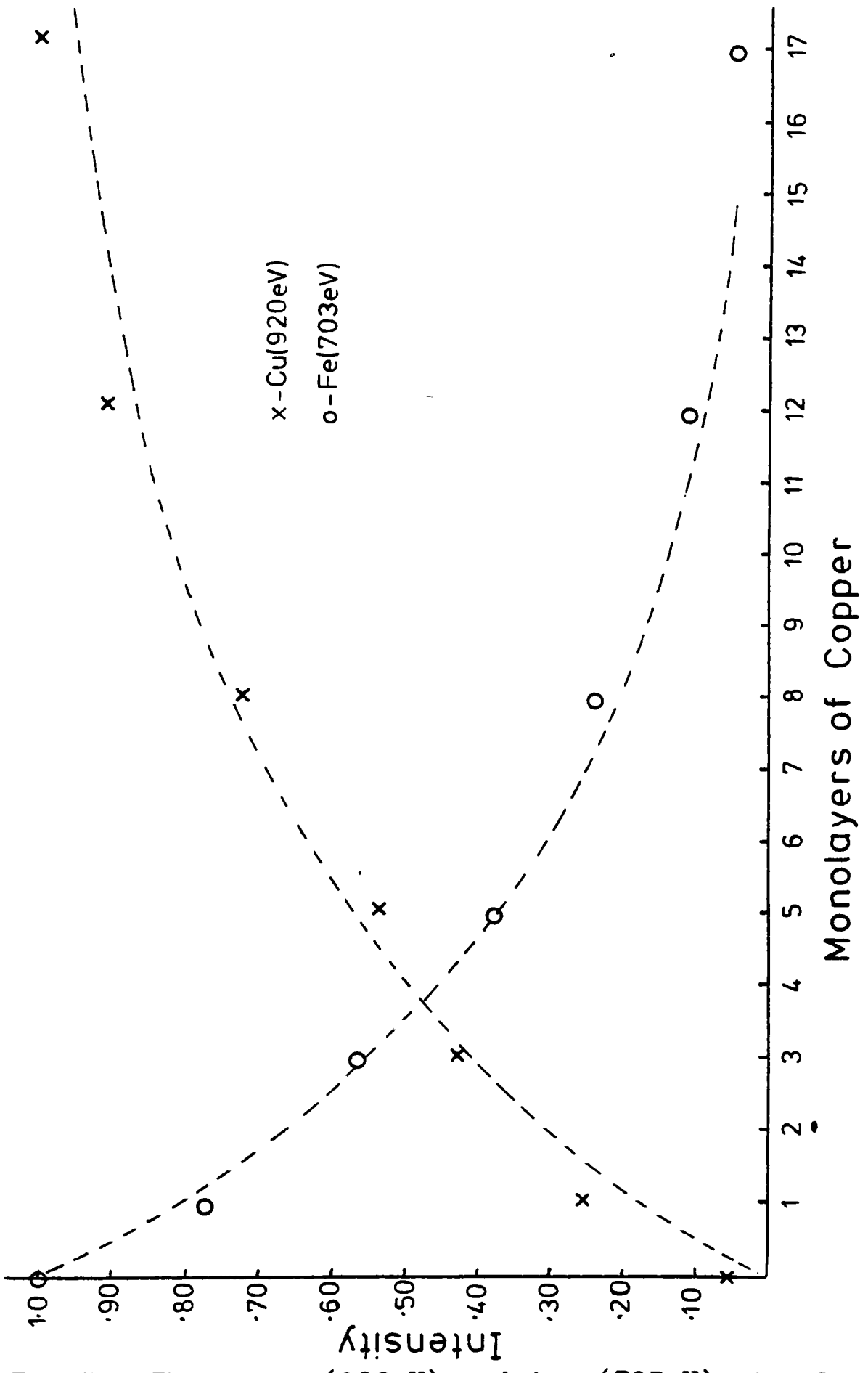


Fig.7.3 The copper(920eV) and iron(703eV) signals as a function of copper condensate quantity. K=1.36, E_p=2.5keV

This value of $K = 1{\cdot}36 = \frac{i(Cu(920eV)\ signal\ from\ bulk\ copper}{i(Fe(703eV)\ signal\ from\ bulk\ iron}$ is slightly larger than the value of 1·04 obtained from the data of Palmberg et.al. (1972). The dotted curve passing through the copper points is given by equation (3) with $\lambda_o^o = 6$ monolayers and the curve passing through the iron points is given by equation (2) with $\lambda_s^o = 5$ monolayers.

Figure 7.4 shows the variation in the copper (60eV) and iron (47eV) signals as a function of copper coverage in monolayers. The data were recorded in the derivative mode using a modulation of 0·5 V r.m.s. on the substrate and the peak to peak heights of the signals were taken as proportional to the Auger currents. The value of $K = 1{\cdot}1$ is again slightly larger than the value of $\frac{i_\infty^o}{i_o^s} = 0{\cdot}83$ obtained from Palmberg et.al. (1972). The curve passing through the copper points is given by equation (3) with $\lambda_o^o = 6$ monolayers and the curve passing through the iron points is given by equation (2) with $\lambda_s^o = 1{\cdot}9$ monolayers. Thus it can be seen that the low and high energy copper signals behave in exactly the same way as a function of copper coverage. Similar behaviour to this has been observed by Seah (1972) for copper condensed onto silver and it was interpreted to mean that copper forms thick islands on the silver substrate. An examination of the emission angular distributions of the substrate and overlayer Auger electrons should help to clarify this point.

Figure 7.5 shows the emission angular distributions of the copper (60eV) and iron (47eV) signals with two monolayers equivalent of copper present. The outer dotted curve is the Auger angular distribution that would be expected on the basis of equation (11) of chapter 3 for an overlayer of thickness $n = 2{\cdot}1\,\lambda_o^o$. Assuming that $\lambda_o^o \simeq 2$ monolayers this implies that islands of copper about 4 monolayers thick cover approximately half the iron surface. The substrate Auger angular distribution for this situation can be estimated from equation (9) with $F = 0{\cdot}45$ and $n = 2{\cdot}1\,\lambda_s^o$ and this is shown as the middle curve. The bottom curve is what would be expected, on the basis of equation (9) of chapter 3, for the substrate Auger angular distribution in the presence

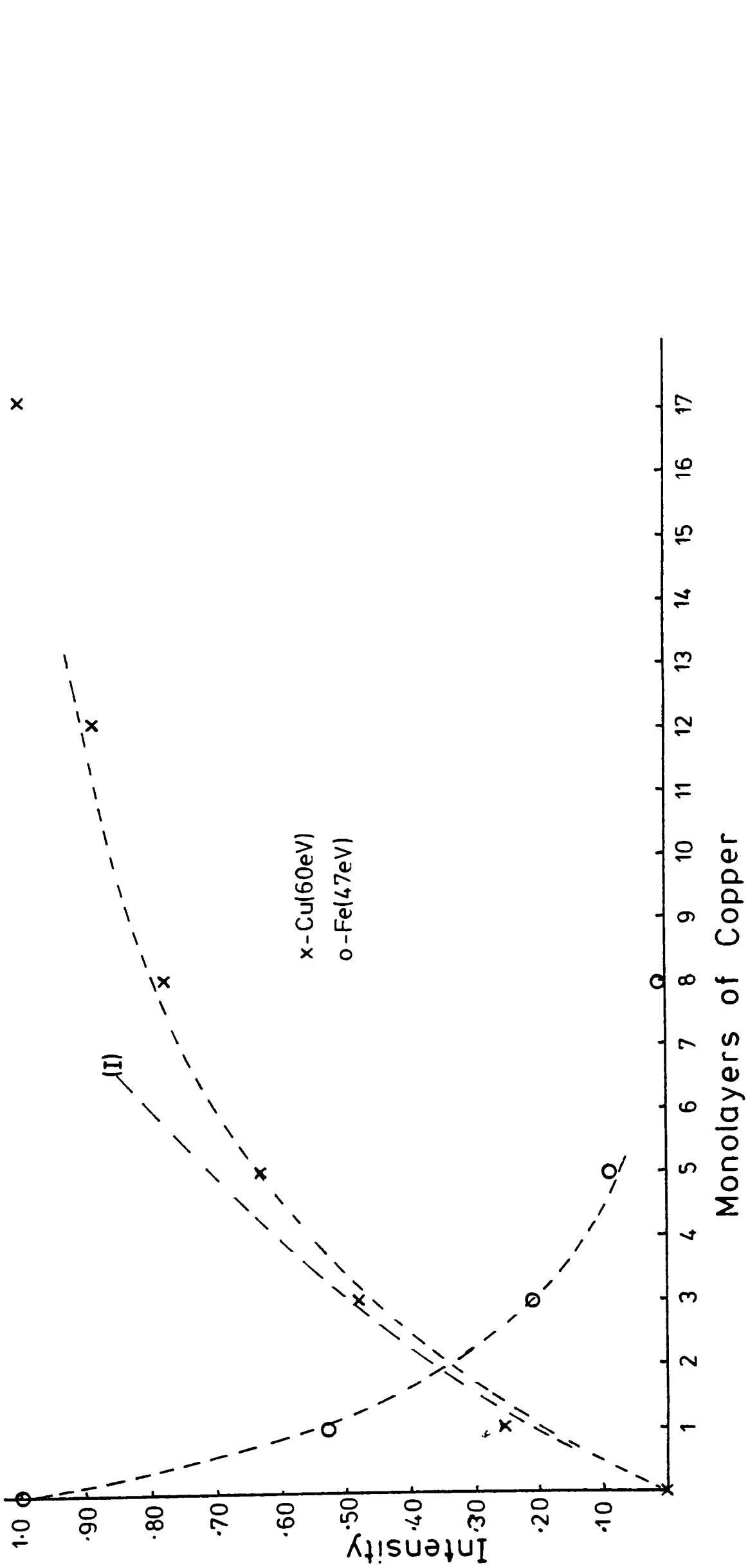


Fig.7.4 The copper(60eV) and iron(47eV) signals as a function of copper condensate quantity. K=1.1, E_p=2.5keV

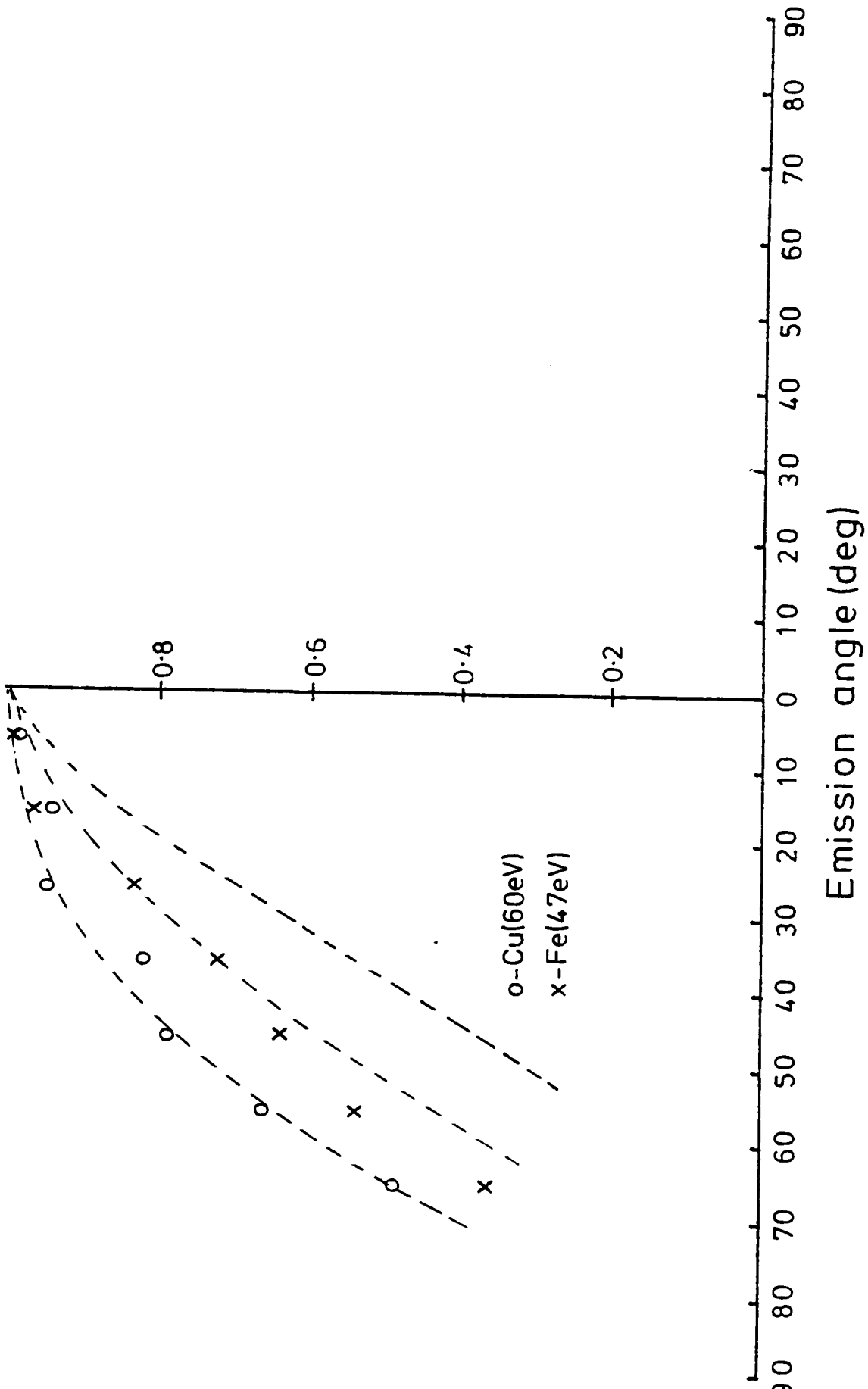


Fig.7.5 The angular distributions of the copper(60eV) and iron(47eV) signals from iron with 2 monolayers of copper present. E_p=2keV, θ_p=30°

of a uniform overlayer of thickness n = 2·1 λ_s^o. This data then seems to suggest that the copper is present in islands about 4 monolayers thick covering about half the iron surface.

If this island growth hypothesis is correct then it should be possible to predict the form of the condensation curves in figure 7.4 on the basis of the island growth model discussed in section 7.3. If λ_o^o for the copper (60eV) electrons is taken as 2 monolayers and the value of N is taken as 10^{-3} (Chopra (1969)) then the fractional coverage F is equal to 0·40 for two monolayers equivalent of copper, if x = 0·25. The prediction of equation (8) based on an island growth model with these values is shown as curve (I) in figure 7.4. Although this model gives reasonable agreement with the copper signals in figure 7.4 it would give very poor agreement with the iron signals.

It therefore appears that the data presented in figures 7.3, 7.4 and 7.5 cannot all be understood on the basis of either a layer growth or an island growth model. Before discussing some other possible ways of explaining these apparently contradictory observations the experimental results for iron condensed onto copper will be presented.

Figure 7.6 shows the variations in the iron (47eV) and copper (60eV) signals as a function of iron condensate thickness. The calibration for the iron was done by taking the density ρ = 7·87 g/cc and the monolayer thickness equal to 2·46Å. A modulation voltage of 0·5V r.m.s. was used to obtain the spectra in differential form and the usual peak to peak heights of the signals were used as a measure of the Auger current. The value of $\frac{i_\infty^o}{i_o^s}$ = 0·8 is smaller than the value of 1·2 obtained from the data of Palmberg et.al. (1972). The decrease in the copper signal and the increase in the iron signal are both almost linear which means that no single exponential curve can be made to fit the data. The dotted curves shown are predicted on the basis of equations (7) and (8) with N = 10^{-2}, x = 0·25 and $\lambda_o^o = \lambda_s^o$ = 2 monolayers. Although these curves fit the data reasonably well, the value of N is higher than usually

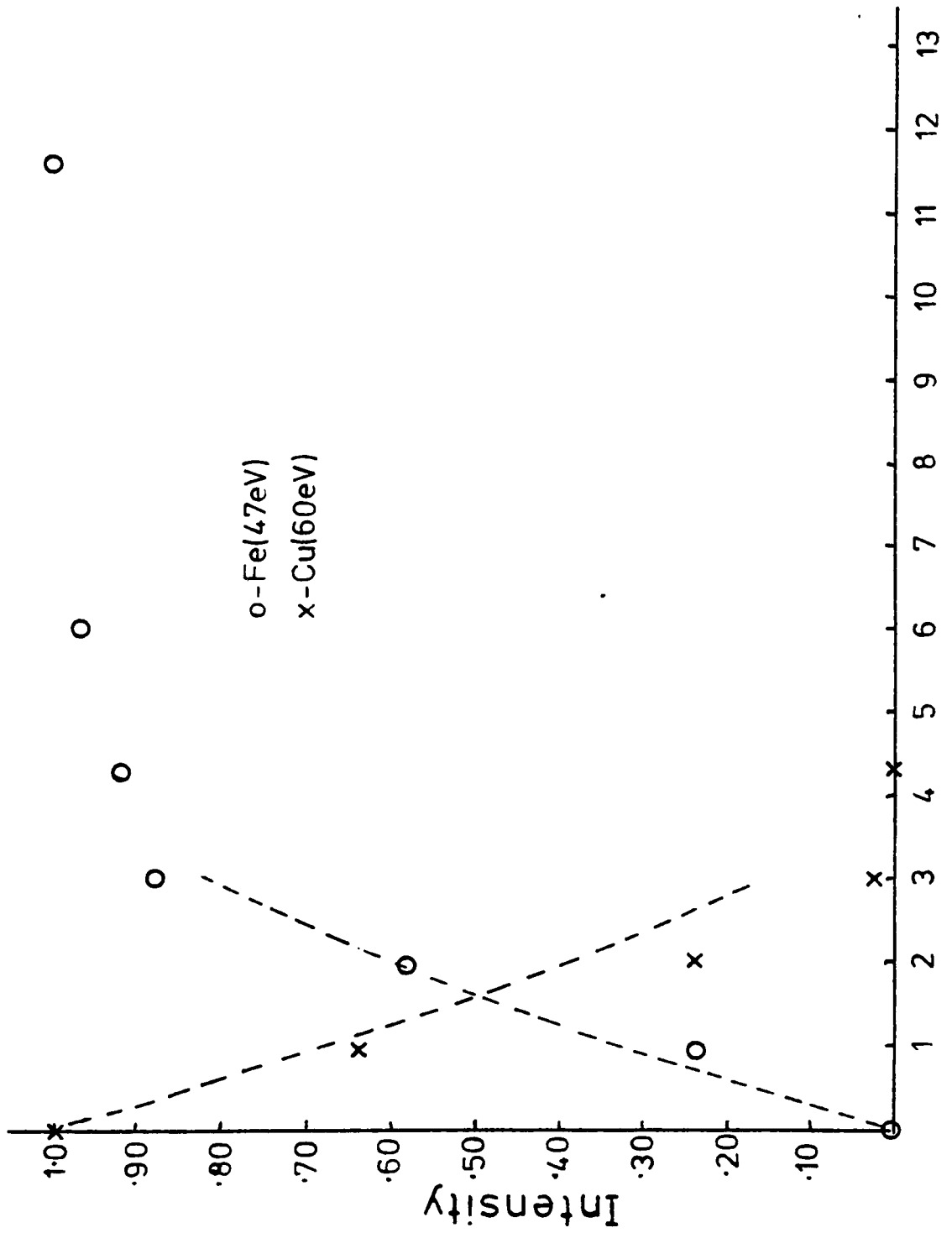


Fig.7.6 The iron(47eV) and copper(60eV) signals as a function of iron condensate quantity. $K=0.9$, $E_p=2.5$keV

observed (Chopra (1969)). A similar fit to the data can also be obtained with $N = 10^{-3}$, $x = 0{\cdot}125$ and $\lambda_o^o = \lambda_s^o = 2$ so this type of analysis does not provide unique values of N, x or λ .

Figure 7.7 shows the variation of the iron (703eV) and copper (920eV) signals as a function of iron condensate thickness. A modulation voltage of 1·5V r.m.s. was used to obtain the differential spectra. The value of $\frac{i_\infty^o}{i_o^s} = 0{\cdot}82$ compares quite well with the value of 0·96 obtained from the data of Palmberg et.al. (1972). The theoretical curves shown are obtained from equations (2) and (3) with $\lambda_s^o = 5$ monolayers and $\lambda_o^o = 4$ monolayers. Again the behaviour of the low energy Auger signals, shown in figure 7.6, seems to suggest a departure from a layer growth mechanism whereas the behaviour of the high energy Auger signals (figure 7.7) is adequately described on the basis of a layer growth model. To try and understand this, the angular distributions of the iron (47eV) and copper (60eV) signals were measured from the copper surface in the presence of 1·3 monolayers (figure 7.8) and 2·4 monolayers (figure 7.9) of iron.

In both cases the angular distributions of the iron (47eV) signals were fitted closely by curves predicted on the basis of equation (11) in chapter 3 with n, the overlayer thickness equal to 2·1 λ_o^o. Assuming $\lambda_o^o \simeq 2$ monolayers implies that the fractional coverage (F) of the copper surface in the presence of 1·3 monolayers of iron is 0·3. The bottom curve of figure 7.8 is predicted on the basis of equation (9) with $F = 0{\cdot}3$ and $n = 2{\cdot}1\ \lambda_s^o$. This produces very poor agreement with experiment and similar attempts to describe the copper (60eV) substrate signal in figure 7.9 on the basis of equation (9) met with even less success.

As with the results obtained from the condensation of copper on iron, these results for iron condensed onto copper cannot be understood on the basis of either the layer growth model or the island growth model. It therefore seems that some other growth mechanism must be invoked to explain these results.

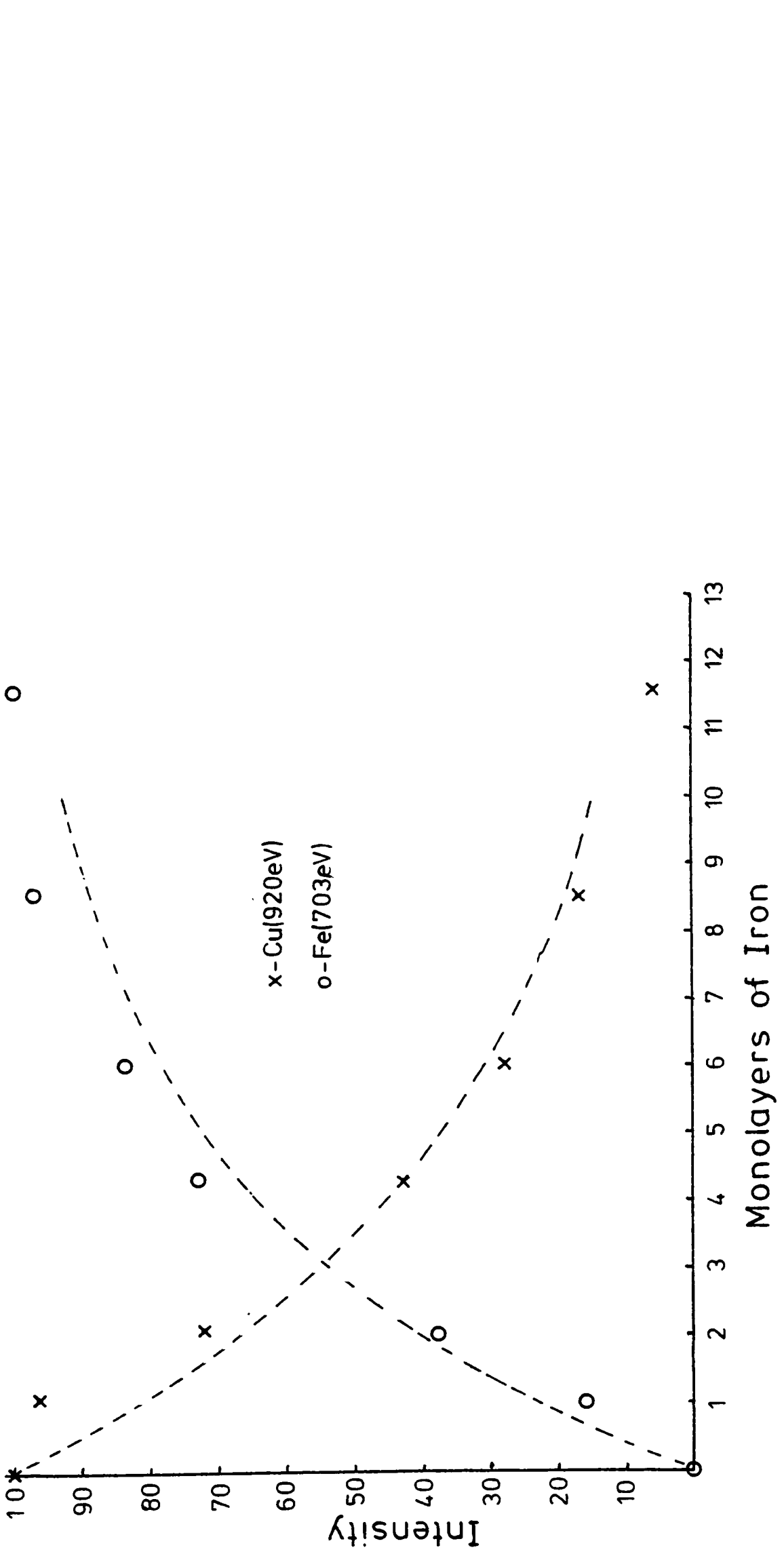


Fig.7.7 The iron(703eV) and copper(920eV) signals as a function of iron condensate quantity. $K=0.8$, $E_p=2.5$keV

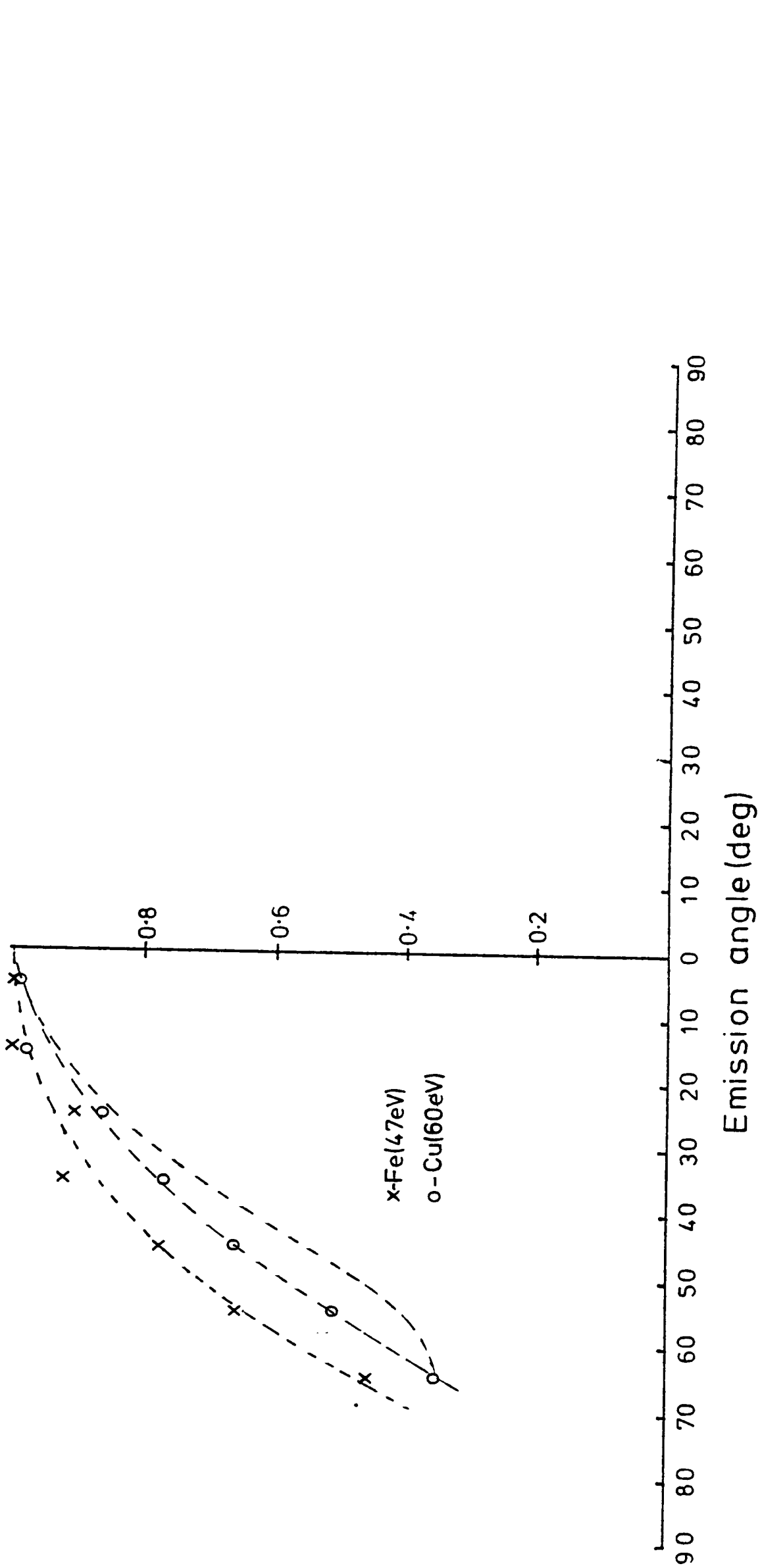


Fig.7.8 The angular distributions of the iron(47eV) and copper(60eV) signals from copper with 1.3 monolayers of iron present. E_p=2keV, θ_p=30°

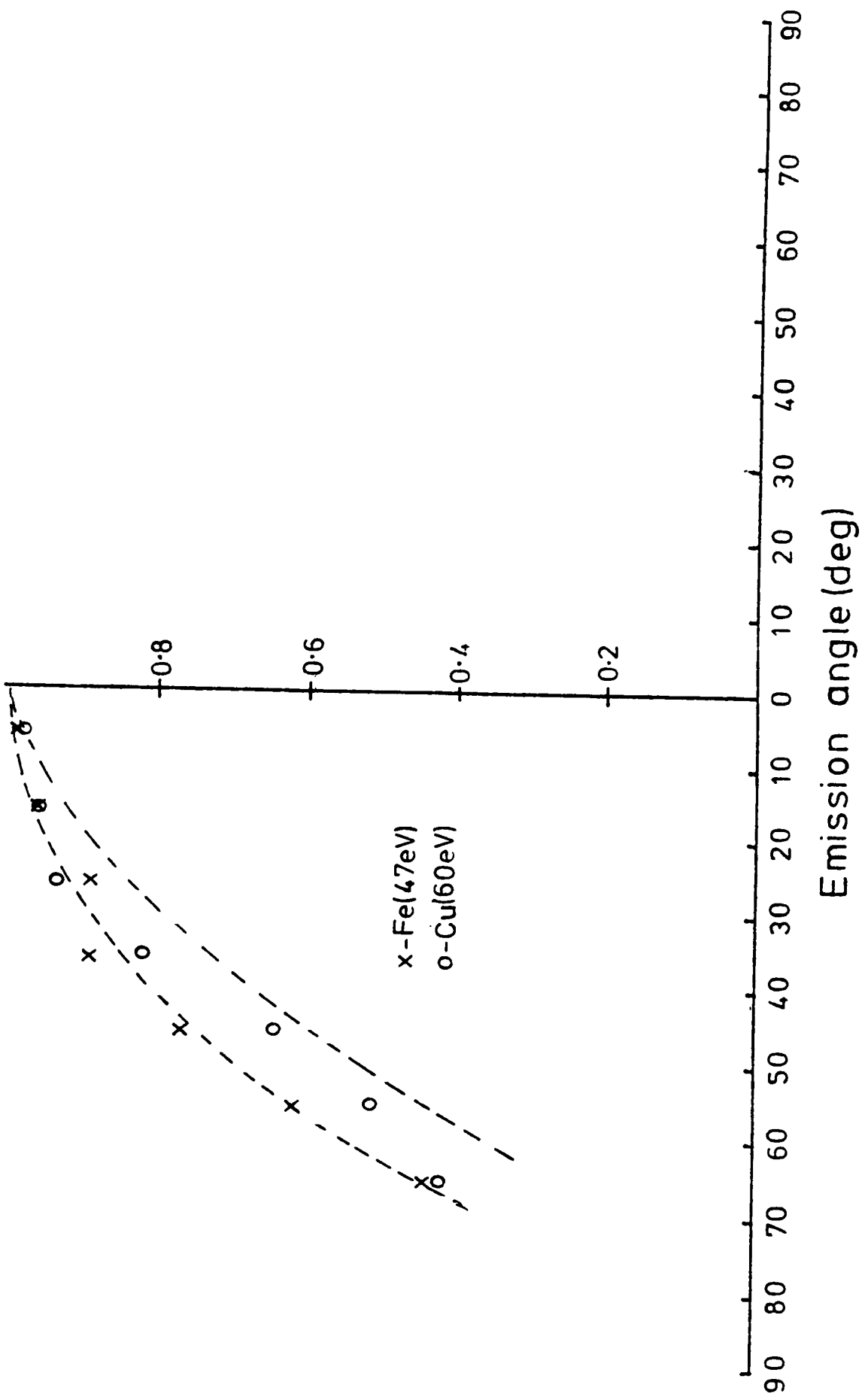


Fig.7.9 The angular distributions of the iron(47eV) and copper(60eV) signals from copper with 2.4 monolayers of iron present. E_p=2keV, θ_p=30°

A growth form that has not been considered is the so called Stranski-Krastanov mechanism (e.g. Bauer & Poppa (1972)) where an initial uniform layer about one monolayer thick forms and then the rest of the condensate grows in island form on top of this initial layer. If this mechanism were operating for the case of iron deposited onto copper then the angular distributions of the copper and iron signals shown in figure 7.8 would have been characteristic of a thin uniform layer, which they are clearly not. A similar argument holds for the angular distributions of the copper and iron Auger signals shown in figure 7.5 for iron in the presence of two monolayers equivalent of copper. In this case the argument is less clear cut, but having deposited one of the two copper layers as a uniform monolayer, it is impossible for the other copper monolayer equivalent to distribute itself in such a way as to give the observed overlayer angular distribution, that is characteristic of 4 monolayers of copper. Therefore there seems to be little evidence to support this type of growth model.

Having rejected a layer growth model, an island growth model and the Stranski - Krastanov model leaves only one other possible way of explaining these results, that of diffusion of the condensate atoms into the substrate.

Consider first the effect on the Auger angular distributions. Equation (10) describing the condensate Auger angular distribution and equation (14) describing the substrate Auger angular distributions, with C = 1, are both plotted in figure 7.10 with $g = \lambda_s = \lambda_c$. Also shown for comparison in figure 7.10 are the substrate and condensate Auger angular distributions that would be expected if the same number of condensate atoms formed an even layer of thickness n = g, and where $n = \lambda_s^o = \lambda_o^o$. The angular distributions of the condensate Auger electrons do not differ greatly between the two models but the angular distributions of the substrate Auger electrons are noticeably different with the diffusion model producing a substrate Auger angular distribution much closer to $\cos\theta$. It therefore seems that this diffusion model

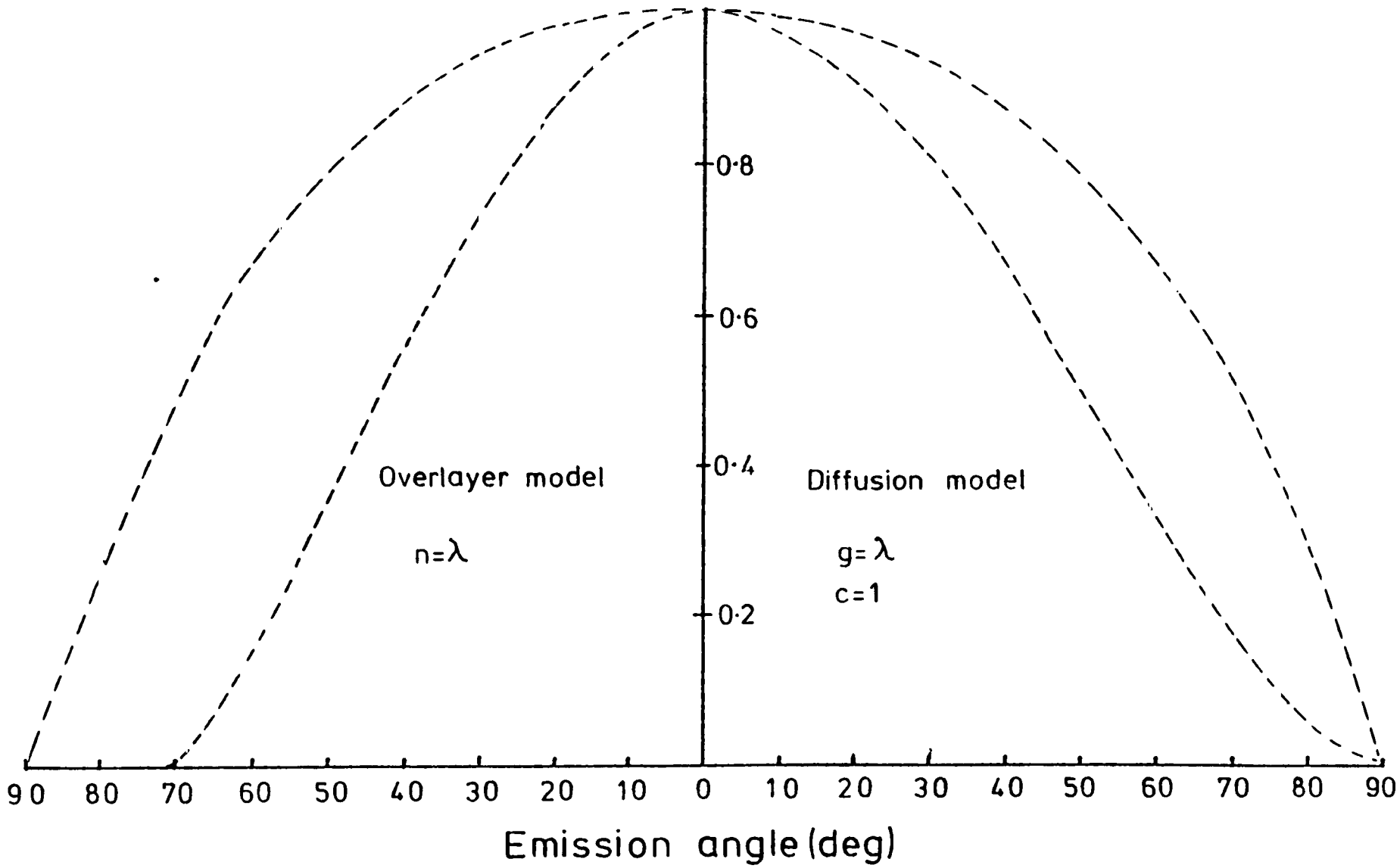


Fig.7.10 Theoretical angular distributions predicted on the basis of an overlayer and a diffusion model

would produce better agreement with the experimental angular distributions shown in figures 7.5, 7.8 and 7.9 than the overlayer model. However the agreement between experiment and theory is still not perfect. The agreement between theory and experiment can be substantially improved by adjusting C and the middle curve in figure 7.8 is obtained from equation (13) with C=0.65 and $g = \lambda_s$. (The upper curve in figure 7.8 is indistinguishable from that given by equation (10) with $g = \lambda_c$). This value of C is also perfectly reasonable since this would correspond to $\sim \frac{\lambda}{2}$ equivalent monolayers of condensate present. The lower curve in figure 7.9 is also given by equation (13) with $C = 1$ and $g = \lambda_s$ and similar use of equations (10) and (13) could be made to fit the data of figure 7.5 since the angular distributions are very similar to those in figure 7.8 and 7.9. Thus it appears that this diffusion model can be used to explain all the angular distributions observed so far. The overlayer angular distribution determines the value of g that must be used and the value of C can be adjusted to fit equation (13) to the substrate angular distribution.

It is rather more difficult to understand how this model will affect the changes in Auger signal as a function of condensate quantity. Providing g is much less than the imfp's of the high energy iron (703eV) and copper (920eV) Auger electrons then these signals will still behave in a very similar way to that expected on the basis of a layer growth model or an island growth model, because the interface region is small compared to the probed depth. Thus the results shown in figures 7.3 and 7.7 for the high energy copper and iron Auger electrons can be explained on either the layer growth or the diffusion model. In the case of the low energy iron (47eV) and copper (60eV) Auger electrons g is more likely to be close to the imfp's of the Auger electrons and the strength of the signals will depend critically on the depth distribution of the species involved. The observation that the copper (60eV) and (920eV) Auger signals behave in the same way (figures 7.3 and 7.4) as a function of copper condensate quantity can be explained on the basis of a diffusion

model providing the depth distribution of the copper atoms remains constant during the deposition. Similarly a change in the depth distribution of the condensate atoms as a function of condensate quantity would lead to the low and high Auger signals behaving in a different way, as observed in figures 7.6 and 7.7.

According to this interpretation of the results there is interdiffusion at the copper/iron interface to a depth of 2 or 3 monolayers for iron deposited onto copper or copper deposited onto iron. The diffusion depths cannot be much greater than this otherwise the values of $\frac{i_\infty^o}{i_s^o}$ would have disagreed with the values predicted on the basis of the work by Palmberg et.al. (1972). The only difference in growth form between the two systems is that for copper on iron, the depth distribution of copper atoms remains constant during the deposition, whereas for iron on copper the depth distribution of iron atoms changes as a function of condensate quantity. Apart from the interdiffusion at the interface the growth form seems to essentially layer by layer as indicated by the goodness of fit between experiment and theory in figures 7.3 and 7.7. Finally the values of λ obtained are :- for 47eV electrons in Cu, $\lambda \leqslant 1{\cdot}9$ monolayers of Cu for 60eV electrons in Fe, $\lambda \leqslant 2$ monolayers of Fe, for 920eV electrons in Fe, $\lambda \leqslant 5$ monolayers of Fe and for 703eV electrons in Cu, $\lambda \leqslant$ 5 monolayers of Cu. It is difficult to put a lower limit on these values because of doubts about the exact growth mechanism of the film.

7.5.2. The Copper/Gold System

The copper (60eV) and gold (69eV) Auger signals were recorded in the derivative mode by applying a 0·5V r.m.s. modulation to the specimen and the peak to peak heights were assumed to be proportional to the Auger current. One of the first things to be noticed for either gold deposited onto copper or copper deposited onto gold was that the condensate Auger signal decayed rapidly under the electron beam. A beam energy of 1KeV and a beam current of 1μA caused the condensate Auger signals to fall to $\sim\frac{1}{e}$ of their initial

value in about 40 minutes. This decay of the condensate Auger signal was localised within the irradiated area since defocussing the incident beam caused the condensate Auger to return to almost its initial value. The second observation to be made about the condensate Auger signals was that, having been reduced in size under the electron beam, they would return to a value midway between their initial and final values if the electron beam was left off overnight. This second observation is of some importance since it shows that there must be a significant mobility of the surface atoms even at room temperature. The sensitivity of the surface composition to the electron beam meant that, between experiments, the beam had to be switched off using the Wehnelt cylinder. This unfortunately seemed to disturb the emission stability of the electron gun and only the signal ratios were found to be reliable.

Figure 7.11 shows the change in the ratios of the copper (60eV) to the gold (69eV) Auger signals as a function of copper condensate quantity. To minimise the amount of beam induced diffusion the irradiation times were kept to less than 30 seconds when recording the signal ratios. The dotted curve is derived on the basis of the layer growth model where the ratio of the over-layer signal to the substrate signal $\frac{i_n^o}{i_n^s}$ is found by dividing equation (3) by equation (2) to give:-

$$\frac{i_n^o}{i_n^s} = \frac{i_\infty^o}{i_o^s}\left(\exp\left(\frac{n}{\lambda}\right) - 1\right) \qquad \text{-----} \quad (15)$$

where λ_s^o is assumed equal to λ_o^o.

The dotted curve in figure 7.11 is derived from equation (15) with $\lambda = 1{\cdot}7$ monolayers and $\frac{i_\infty^o}{i_o^s} = 0{\cdot}5 = \frac{i\ (\text{bulk copper})}{i\ (\text{bulk gold})}$. An estimate of $\frac{i\ (\text{bulk copper})}{i\ (\text{bulk gold})}$ can be obtained from the standard spectra recorded by Palmberg et.al. (1972) and it is found to be 0·67, in reasonable agreement with the value obtained here.

Due to the sensitivity of the surface composition to the electron beam it was not possible to record the Auger angular distributions in the usual way

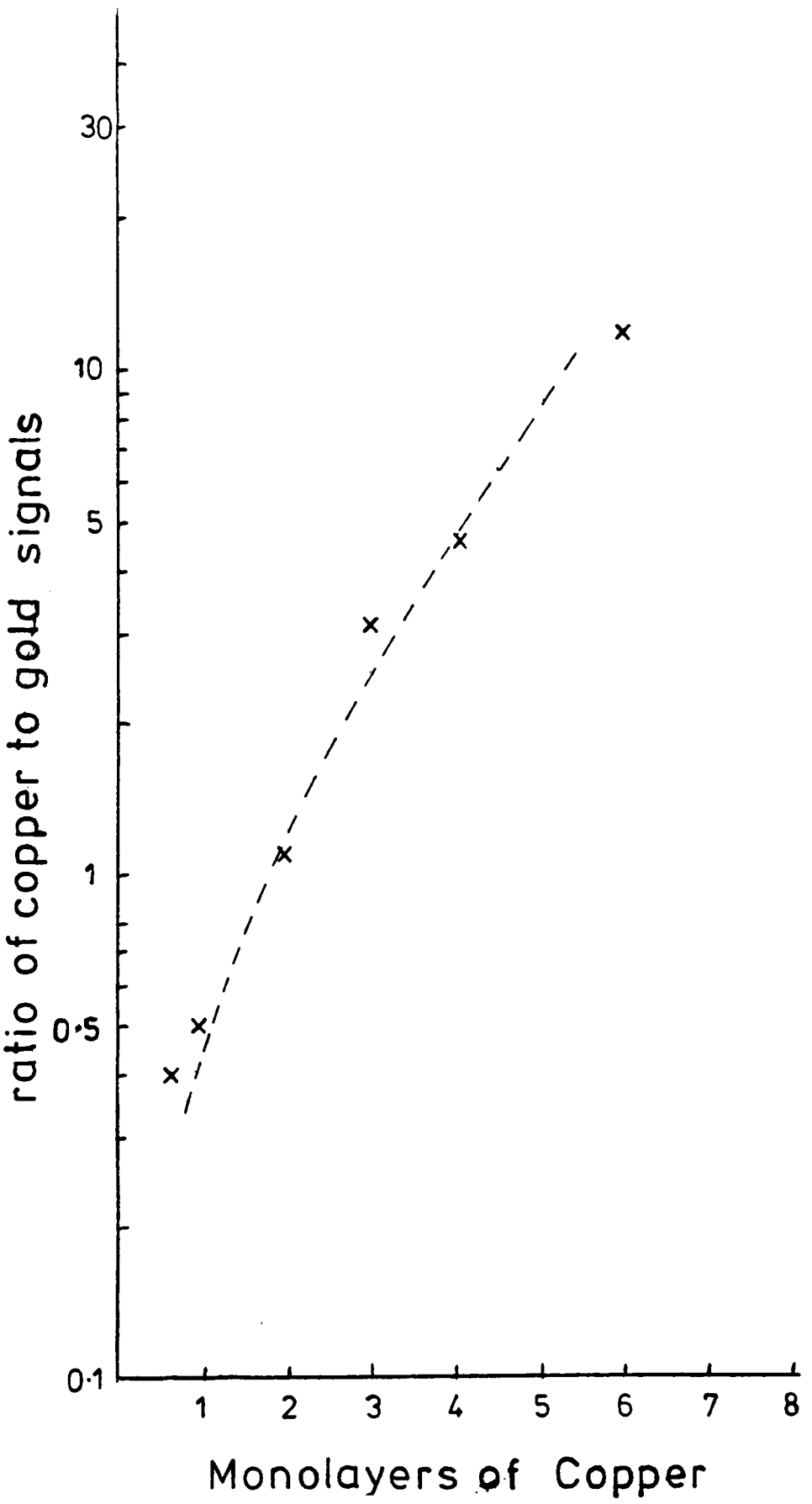


Fig.7.11 The ratio of the copper(60eV) to the gold(69eV) signals as a function of copper condensate quantity. E_p=1keV

and only the signal ratios at a few angles of emission were measured. Immediately after the deposition of 3 monolayers of copper the ratio of the copper (60eV) to the gold (69eV) signal was 3·6 at 5° from normal emission and 4·6 at 75° from normal emission. In the presence of a uniform overlayer 3 monolayers thick, and where $\lambda_o^o = \lambda_s^o = 1{\cdot}7$ monolayers, the overlayer to substrate ratio, predicted using equations (9) and (11) in § 3.5, would go from 1 at 50° to ~50 at 70°, so this system is clearly not an example of layer by layer growth. The experimental results can be understood on the basis of the diffusion model where the concentration of copper atoms is proportional to $\exp\left(-\frac{z}{2\lambda}\right)$. An island growth model could also explain the results but the islands would have to be ~12 monolayers thick covering less than 25% of the surface. This growth model would clearly disagree with the results of figure 7.11 and it must be concluded that appreciable diffusion has occurred at the interface and that the copper is evenly distributed over the gold surface.

Figure 7.12 shows the change in the ratio of the gold (69eV) signal to the copper (60eV) signal as a function of gold condensate quantity. The calibration for gold assumed that $\rho = 18{\cdot}9 g/cc$ and the monolayer thickness was taken to be $2{\cdot}88\text{Å}$ and as before the irradiation times were kept to a minimum. The dotted curve is given by equation (15) with $\lambda = 2$ monolayers and $\frac{i_\infty^o}{i_o^s} = 0{\cdot}2 = \frac{i\ (\text{bulk gold})}{i\ (\text{bulk copper})}$. This clearly gives a very poor description of the overall signal behaviour and attempts to fit the data on the basis of an island growth model also failed. The value of $\frac{i\ (\text{bulk gold})}{i\ (\text{bulk copper})} = 0{\cdot}2$ is also very different from the value of 1·5 expected on the basis of the work by Palmberg et.al. (1972), or the value of 2 used to explain the data in figure 7.11. Since copper is likely (Smith and Gallon (1973)) to have a smaller backscattering factor than gold this relatively low gold Auger signal is at least partly explained, but these experimental results would imply that the backscattering factor for copper is a factor of seven or more less than that for gold. Since this is very unlikely these results suggest that the gold

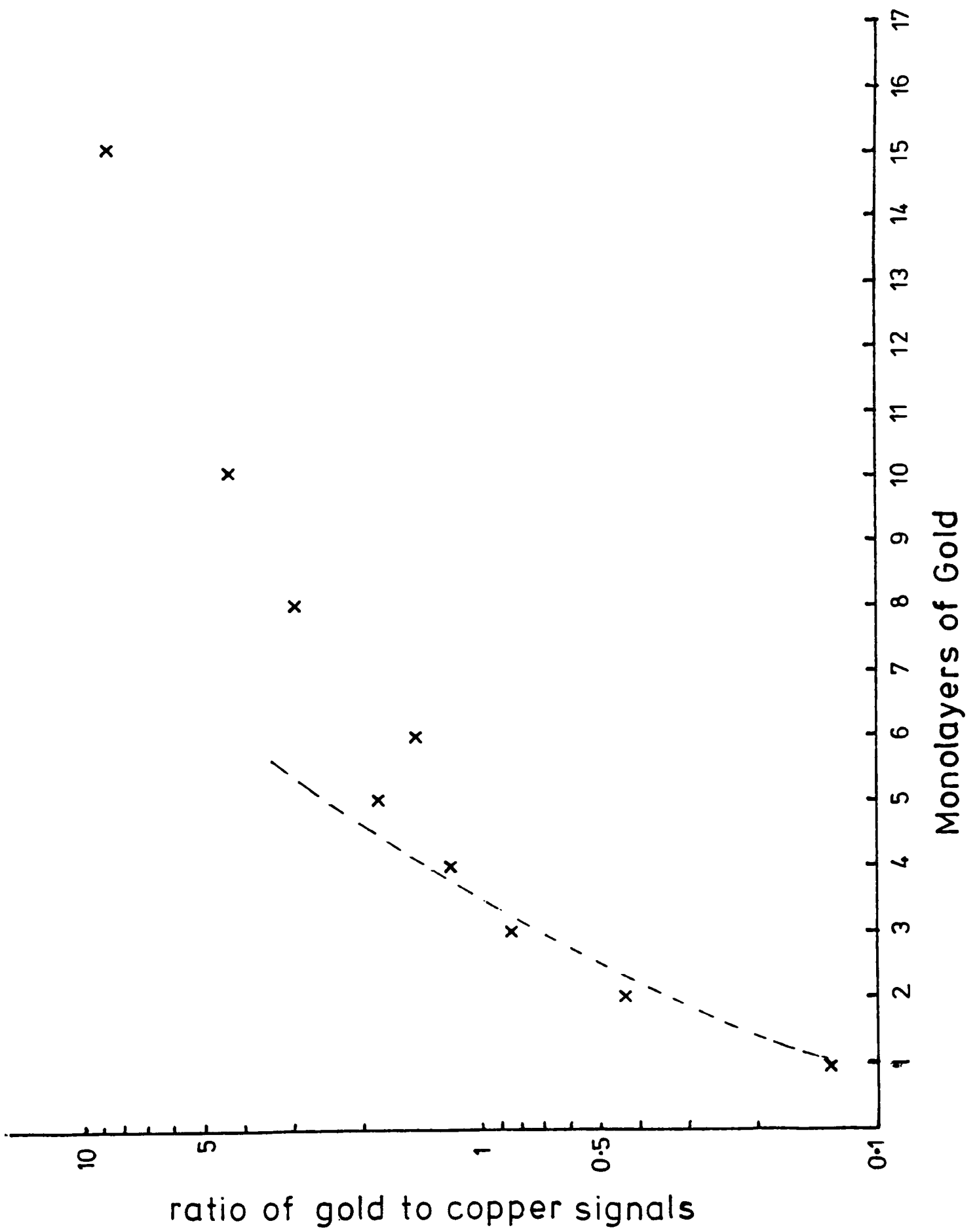


Fig.7.12 The ratio of the gold(69eV) to the copper(60eV) signals as a function of gold condensate quantity. E_p=1keV

atoms are diffusing into the copper to depths greater than the escape depths of the Auger electrons or forming very large islands on the copper surface.

Unfortunately the sensitivity of the surface composition to the electron beam prevented the measurement of complete substrate and overlayer Auger angular distributions and as before only signal ratios at a few angles of emission were recorded. In the presence of 5 monolayers equivalent of gold, the ratio of the gold (69eV) to the copper (60eV) Auger signals increased by 20% on changing the emission angle from 5° to 45° from the surface normal. In the presence of a uniform monolayer the ratio would have more than doubled so this can be ruled out. If it is assumed, as before, that the substrate Auger angular distribution is proportional to $\cos\theta$, then a depth distribution of gold atoms proportional to $\exp(-\frac{z}{\lambda})$ would explain the observed change in signal ratio. This behaviour could also be interpreted on the basis of gold islands of appropriate thickness but this seems unlikely for the following reasons. If it is assumed that the seven fold decrease in the size of the gold signal is due to island formation and the consequent decrease in the surface area of the gold, then it can be shown that rectangular islands of at least 35 monolayers thickness would be required to reduce even the surface area of the top of the islands by this amount. Islands of this thickness would produce overlayer Auger angular distributions proportional to $\cos\theta$ and hence virtually no change in substrate to overlayer signal ratio as a function of emission angle would be expected. It also seems improbable that the layer growth model would produce the level of agreement with experiment shown in figure 7.12 if this were the case.

Unfortunately the conclusion regarding the growth form of gold on copper are rather tentative. For coverages of less than ~ 5 monolayers equivalent of gold it seems that appreciable diffusion of gold into copper must occur with gold being evenly distributed on the surface. Above this coverage the data can be interpreted to indicate either island formation or diffusion of gold into copper. The situation for gold onto copper is more comprehensible

and it seems that copper diffuses 2 or 3 monolayers into the gold and that the copper is evenly distributed over the surface. The values of λ obtained from this data are:- for ~60eV electrons, λ = 1·7 monolayers of Cu or 2 monolayers of Au. The doubts about the growth form makes the accuracy of these results difficult to determine.

7.5.3. <u>The Iron/Tin System</u>

The iron (703eV) and Tin (430eV) signals were recorded in the differential mode by applying a 1·5V r.m.s. modulation to the specimen and the peak to peak height were assumed proportional to the Auger current. Figure 7.13 shows the variations in the Tin (430eV) and Iron (703eV) Auger signals as a function of Tin condensate quantity. The calibration of the oscillator for Tin assumes that ρ = 7·3g/cc and the monolayer thickness was taken to be 2·8Å. As before there was always some oxygen found on the iron surface with a signal strength of ~$\frac{1}{4}$ that of the iron (703eV) peak. The height of the tin (430eV) peaks shown in figure 7.13(a) are plotted in their correct relationship to the heights of the iron (703eV) peaks. This avoids the problems of normalising the tin signal at large coverages

The dotted curve passing close to the iron points in figure 7.13(a) is given by equation (2) with λ_s^o = 4 monolayers and the dotted curve passing through the tin points is given by equation (3) with i_∞^o = 2·47 and λ_o^o = 4 monolayers. Similarly the upper dotted curve in figure 7.13(b) is given by dividing equation (3) by equation (2) with $\frac{i_\infty^o}{i_o^s}$ = 2·47 = $\frac{i\ (\text{bulk tin})}{i\ (\text{bulk iron})}$ and $\lambda_o^o = \lambda_s^o$ = 4 monolayers. The ratio for $\frac{i\ (\text{bulk tin})}{i\ (\text{bulk iron})}$ expected from the work of Palmberg et.al. (1972) is 2·60, in reasonable agreement with the value obtained here. This data then seems to be in reasonable agreement with the theory derived on the basis of a layer growth model. There is however a difference between the data of figure 7.13(b) and a similar plot obtained by Seah (1973), where he found a pronounced change in slope at ~1 monolayer equivalent of tin. Figure 7.14 shows a continuation of the type of data shown

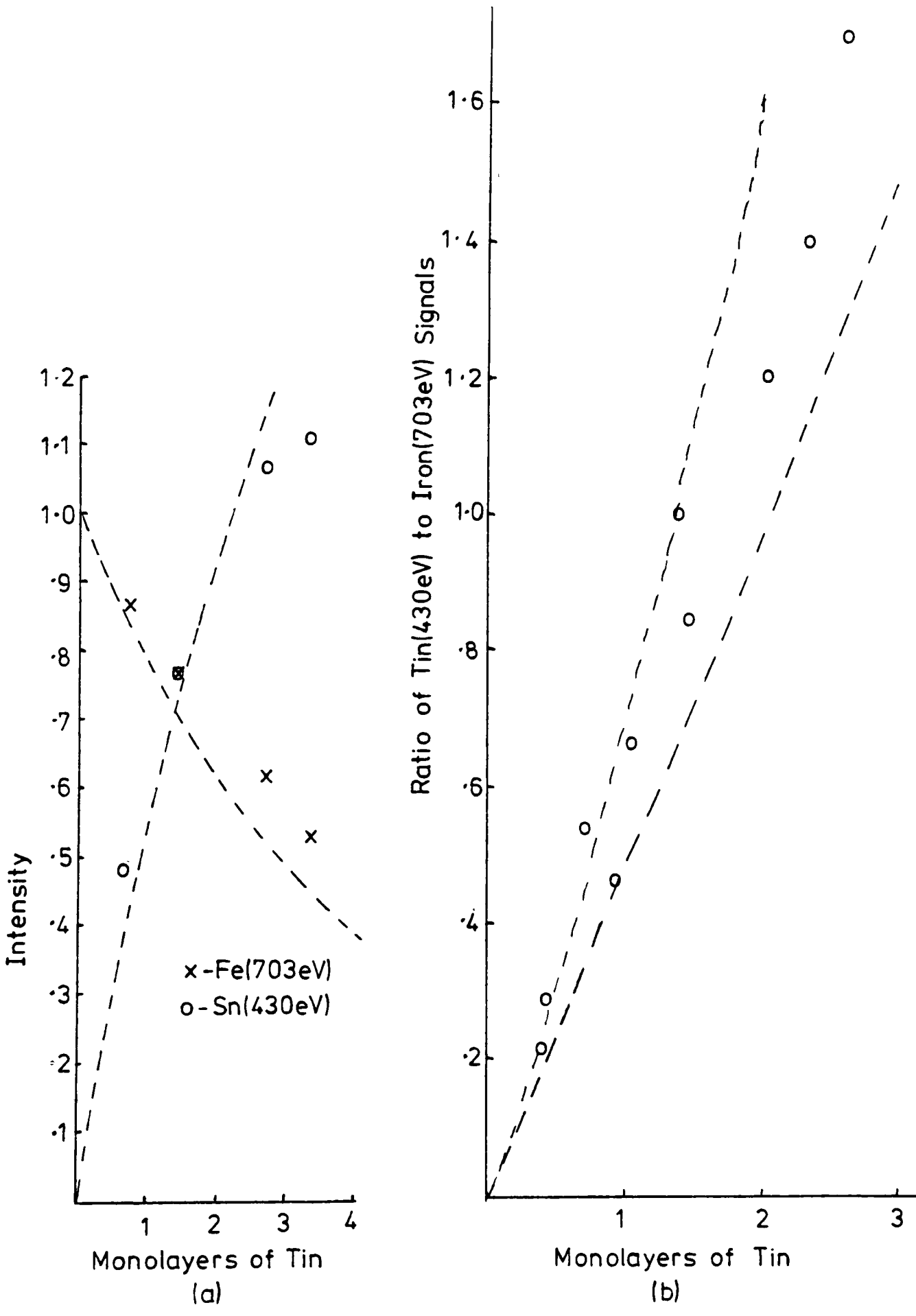


Fig 7.13 The iron(703eV) and tin(430eV) signals as a function of tin condensate quantity. E_p=2.5keV

Fig.7.14 The ratio of the tin(430eV) to the iron(703eV) signals as a function of tin condensate quantity, E_p=2.5keV

in figure 7.13(b), to a coverage of 18 monolayers equivalent of tin. The dotted curve is again given by dividing equation (3) by equation (2) with $\lambda_s^o = \lambda_o^o = 4$ monolayers and $\frac{i_\infty^o}{i_o^s} = 2{\cdot}47$. It can be seen that there is a major divergence between the theoretical curve and the experimental points at coverages greater than about 2 monolayers of tin. This divergence may have a similar origin to the change of slope observed by Seah (1973)(b). Thus for coverages of less than ~ 2 monolayers of tin the behaviour of the signal can be described reasonably well on the basis of a layer grwoth model, whereas above this, the signal ratios appear to change in a linear manner as a function of tin coverage. A better fit to the data, shown as the lower curve in figure 7.14, above coverages of ~ 2 monolayers, is given by dividing equation (8) by equation (7) and letting $N = 10^{-3}$, $x = 0{\cdot}5$, $\lambda_o^o = \lambda_s^o = 4$ monolayers and as before $\frac{i_\infty^o}{i_o^s} = 2{\cdot}47$. The angular distributions of the tin (430eV) and iron (703eV) signals will now be examined to see if such a transition from a layer growth to an island growth mode is likely.

Figure 7.15 shows the angular distributions of the tin (430eV) and iron (703eV) Auger signals in the presence of 0·46 monolayers of tin. The upper dotted curve is given by equation (11) of chapter 3, that describes the angular distribution from an overlayer, with n the overlayer thickness equal to $1{\cdot}1\,\lambda_o^o$ which in this case implies islands ~ 4 monolayers thick. The inner curve is given by $\cos\theta$ which would be indistinguishable from the curve predicted by equation (9) in the presence of islands 4 monolayers thick, which also implies $F = 0{\cdot}1$. Figure 7.16 shows the same Auger angular distributions in the presence of 0·94 monolayers of tin. The dotted curves are the same as those shown in figure 7.15, again the $\cos\theta$ curve would be indistinguishable from the curve predicted by equation (9) with F this time equal to $\sim 0{\cdot}2$. Thus both these angular distributions can be understood on the basis of islands ~ 4 monolayers thick growing on the surface.

This type of island growth would clearly affect the Auger signals from

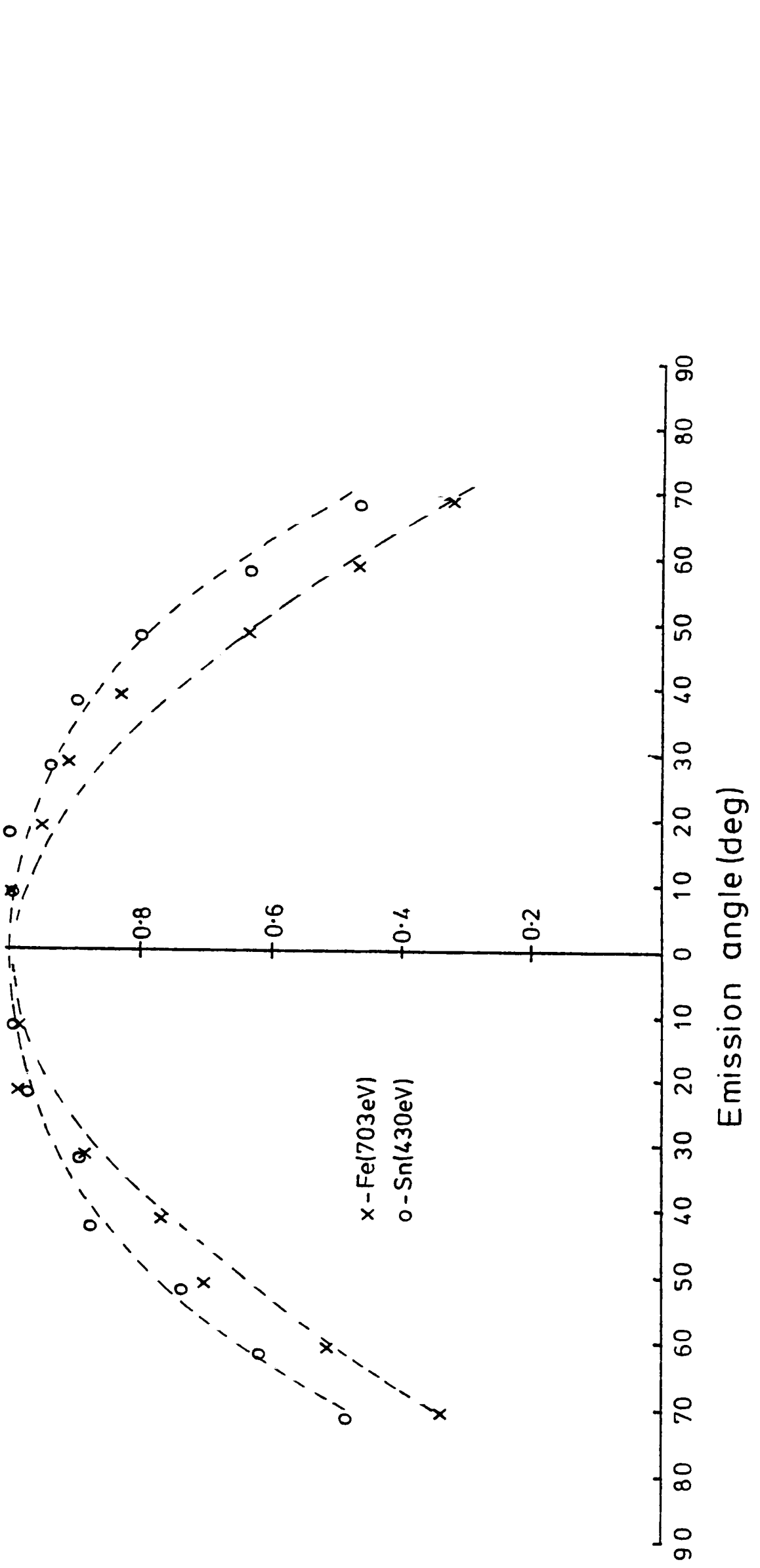


Fig.7.15 The angular distributions of the tin(430eV) and iron(703eV) signals from iron with 0.46 monolayers of tin present. E_p=2keV, $\theta_p = \pm 30^\circ$

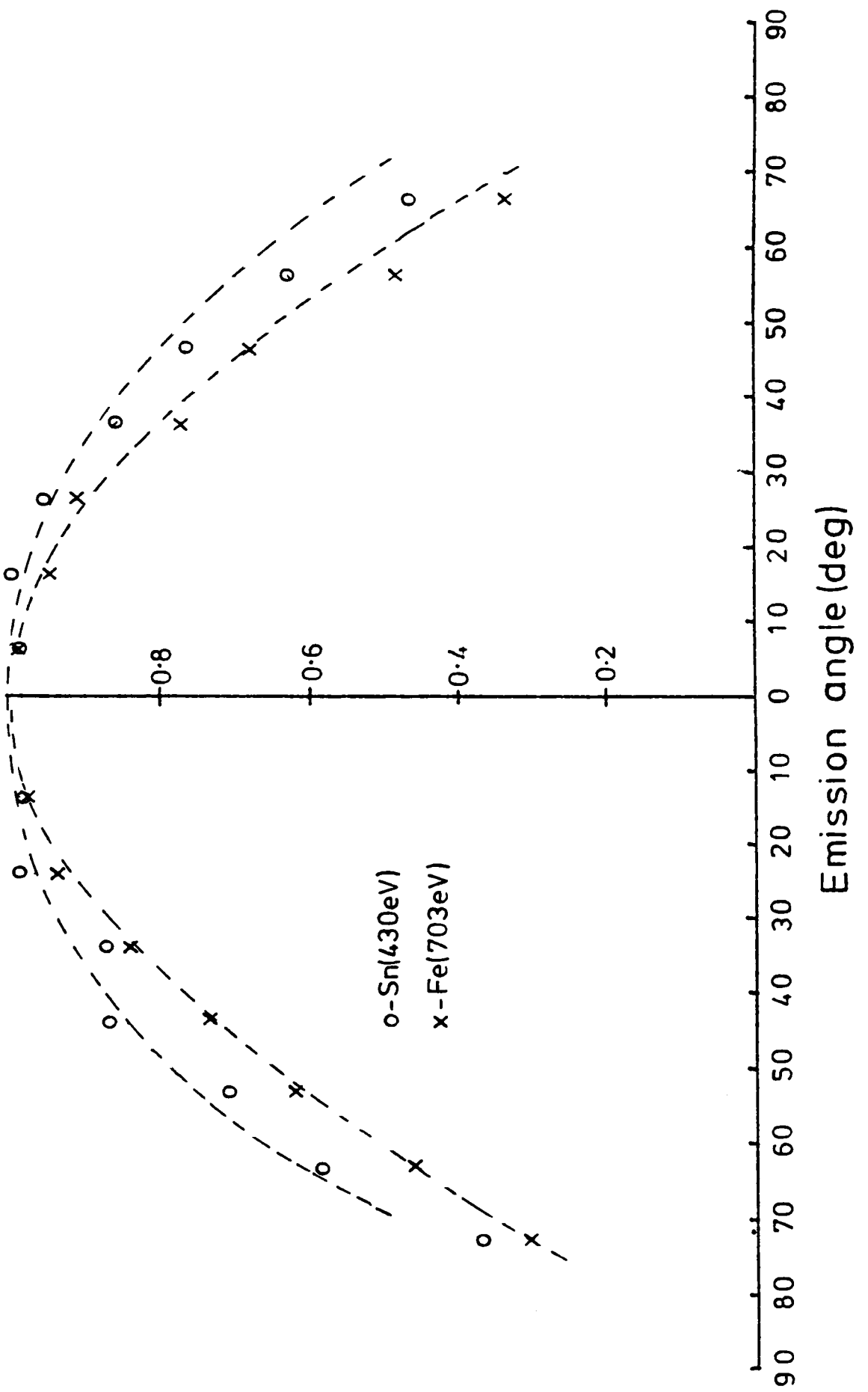


Fig.7.16 The angular distributions of the tin(430eV) and iron(703eV) signals from iron with 0.94 monolayers of tin present. E_p=2keV, θ_p=$\pm$30°

the substrate and overlayer. A fractional coverage F = 0·25 in the presence of one monolayer of tin, would be predicted on the basis of the island growth model discussed earlier with $N = 10^{-3}$ and $x = 0{\cdot}25$. The lower dotted curve in figure 7.13(b) is obtained from this island growth model by dividing equation (8) by equation (7) with $\lambda_o^o = \lambda_s^o = 4$ monolayers and $\frac{i_\infty^o}{i_o^s} = 2{\cdot}47$. Thus for tin coverages of less than 3 monolayers equivalent this island growth model gives agreement with experiment similar to that found using the layer growth model, but beyond this coverage the agreement rapidly deteriorates until at 8 monolayers equivalent of tin, the signal ratio predicted using this island growth model is 16·5 compared to the measured value of 4·2. It therefore seems that some form of island growth mechanism would explain both the angular distribution measurements shown in figures 7.15 and 7.16 and the changes in signal ratios as a function of condensate quantity shown in figure 7.13(b). However it also probable that a model which allows tin to diffuse a small distance ($\lesssim 4$ monolayers) into the iron would give just as good agreement with experiment.

To try and understand what sort of change in the growth form occurs with larger amounts of tin present, the angular distributions of the tin (430eV) and iron (703eV) Auger signals were measured in the presence of 10·5 monolayers of tin and the data is shown in figure 7.17. The upper dotted curve is given by equation (11) of chapter 3 with the overlayer thickness $n = 1{\cdot}6\ \lambda_o^o$ and the lower curve is simply $\cos\theta$. This $\cos\theta$ angular distribution of the iron Auger signal shows quite clearly that the tin is not present in a uniform layer 10·5 monolayers thick. The angular distribution of the tin Auger peak would seem to indicate that an overlayer of tin about 6·4 monolayers thick is present. This clearly disagrees with the known fact that 10·5 monolayers equivalent of tin is present and in any case the substrate angular distribution must indicate the presence of either thick islands or that diffusion of the tin into the iron has occurred. The relatively low value of the tin signal with 10·5 monolayers of tin present on iron, and these angular distributions, indicate quite

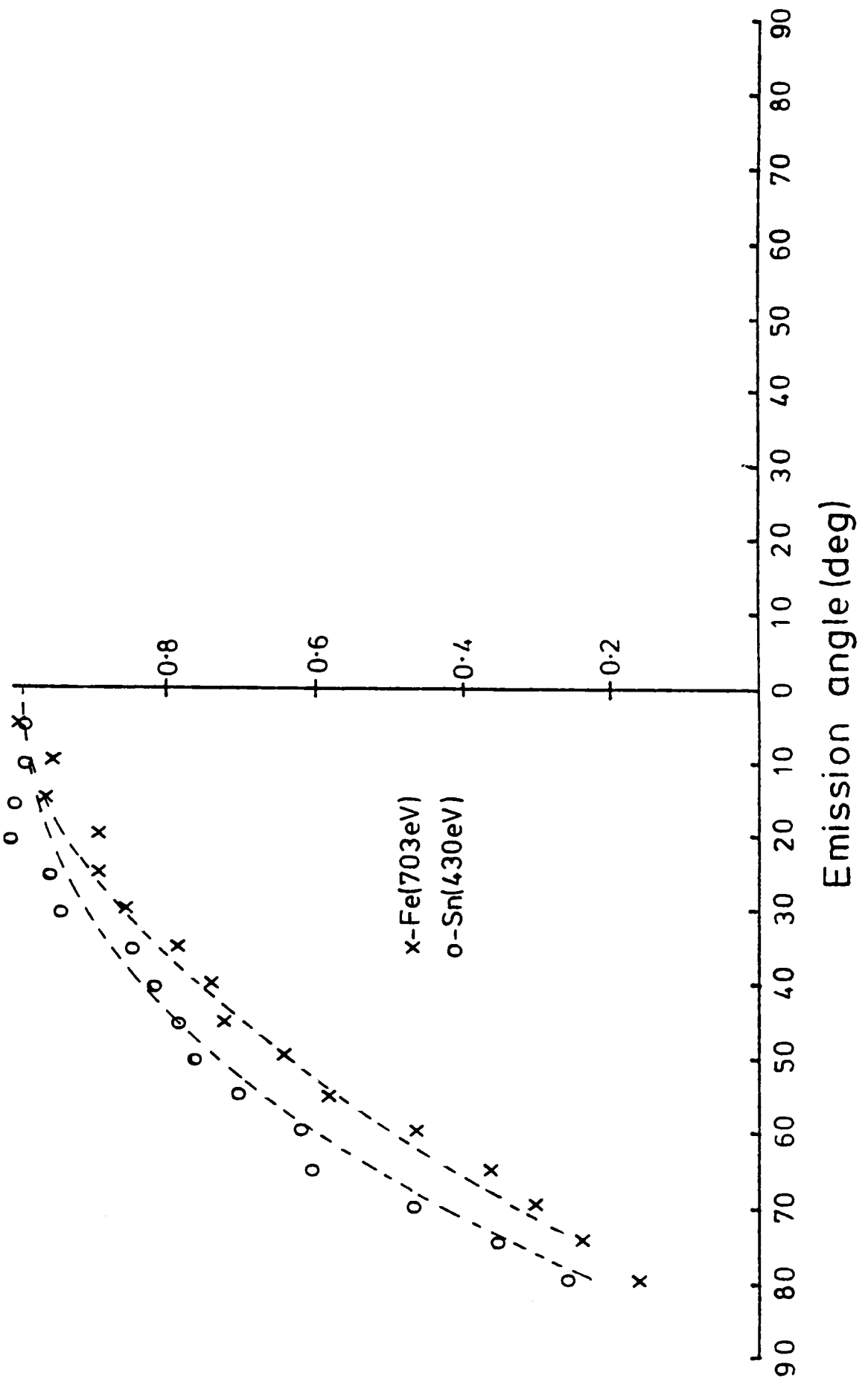


Fig.7.17 The angular distributions of the tin(430eV) and iron(703eV) signals from iron with 10.5 monolayers of tin present. E_p=2keV, θ_p=30°

clearly that appreciable interdiffusion of tin and iron has occurred during the deposition process.

In the case where less than ~3 monolayers of tin are present on the surface the signal strength of the tin signal indicates that very little tin has diffused beyond the escape depth of the Auger electrons. The angular distributions with 0·46 and 0·94 layers of tin present suggests either island growth or that a small amount of tin has diffused into the iron. The rate of change of the signal ratios as a function of tin coverage would be compatible with either the layer growth or island growth model suggested. For tin coverages of more than ~3 monolayers equivalent a different island growth model has to be used to explain the change in the signal ratios as a function tin coverage. The shape of the Auger angular distributions and the low strength of the tin Auger signal after 10·5 monolayers equivalent of tin has been deposited, seems to suggest that appreciable amounts of tin has diffused to a depth greater than the Auger escape depth and such diffusion could also explain the changes in the Auger signal ratios as a function of tin coverage. Figure 7.18 shows that the tin and iron Auger angular distributions in the presence of 0·94 monolayers of tin can also be understood on the basis of a diffusion model (equation (10) and (13)) with $g = \lambda_c = \lambda_s$ and $C = 0{\cdot}25$. This value of C is exactly as expected if $\frac{\lambda}{4}$ (ie. one monolayer) of atoms distribute themsleves with a concentration gradient proportional to $\exp(-\frac{z}{g})$ where $g = \lambda_c$.

In the early stages of the condensation of tin onto iron it is difficult to distinguish between an island growth model or a diffusion model but in any case layer by layer growth is ruled out. In the later stages considerable diffusion must have taken place as indicated by the low strength of the tin signal and the angular distributions shown in figure 7.17. The value of λ obtained for both 703eV and 430eV electrons is 4 monolayers of tin.

The condensation of tin onto iron exhibited very extreme behaviour with the iron signal rising by only 15% of its bulk value after the condensation

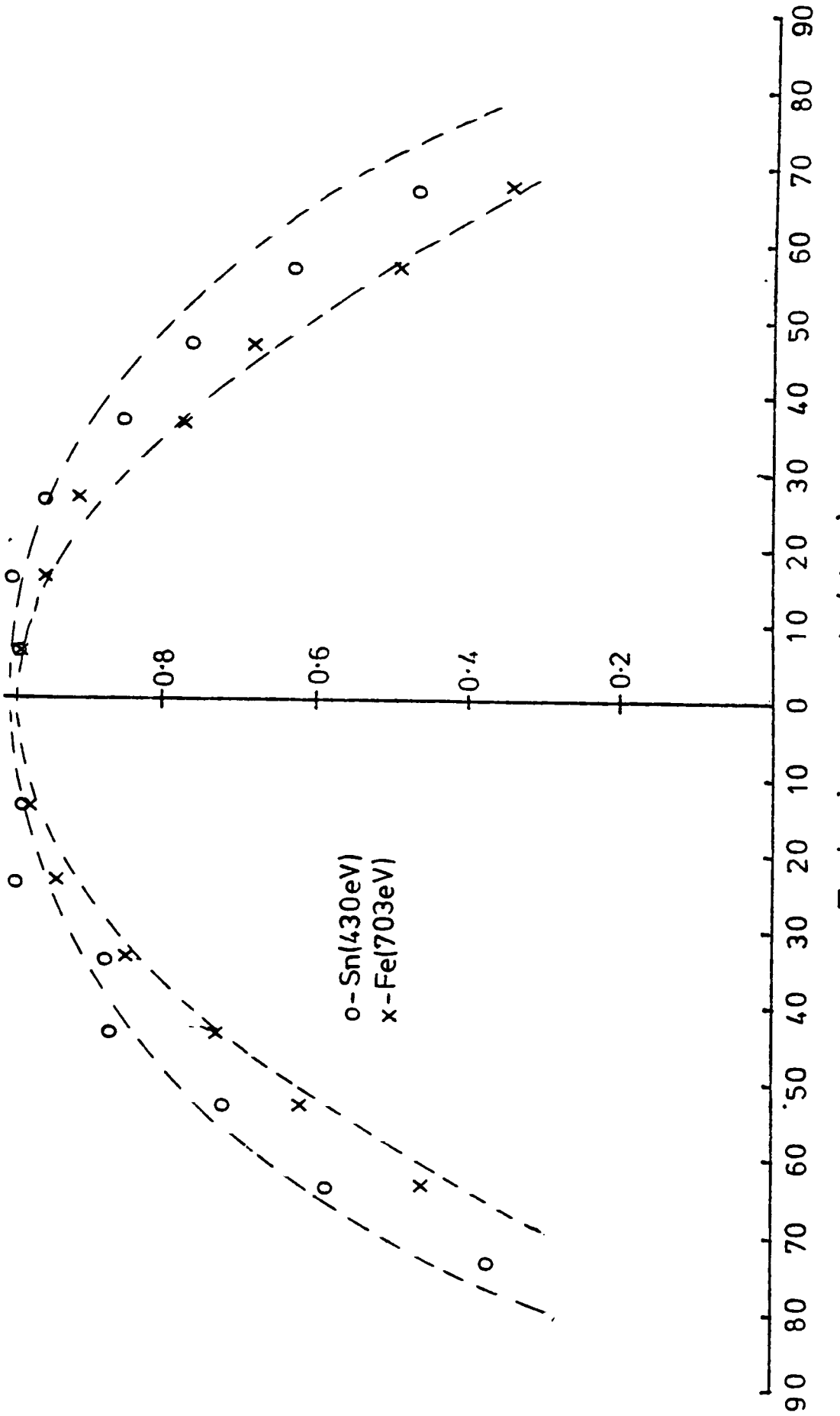


Fig.7.18 The angular distributions of the tin(430eV) and iron(703eV) signals from iron with 0.46 monolayers of tin present.The theoretical curves are derived from the diffusion model.E_p=2keV,$\theta_p=\pm 30^o$

of 7 monolayers of iron and the tin signal dropped by only 20% after the same deposition. The ratios of the iron (703eV) and tin (430eV) signals were constant with emission angle indicating either the formation of thick islands or a uniform distribution of both materials within the Auger escape depth. The tin Auger signal was found to persist even after the deposition of up to 400 monolayers of iron which seems to indicate that the tin was diffusing to the iron surface during the deposition process.

7.6. Discussion and Summary

In all the systems studied here the experimental resulst can be interpreted on the basis of varying amounts of diffusion at the substrate/overlayer interface although in some cases, such as iron with small amounts of tin present, it is not possible to rule out the possibility of island formation. In the cases where the plots of Auger signals as a function of condensate quantity are fitted by the layer growth model, it seems that the overlayer must build up in a uniform fashion, otherwise the substrate signal would persist longer than expected. Conversely when the layer growth model does not fit this type of data it must indicate either the onset of island growth, as in the gold on copper case, or perhaps enhanced diffusion as in the case of tin or iron.

It is however rather difficult to accept the idea of diffusion of these metals since the bulk diffusion coefficients to indicate that the diffusion at room temperature should be negligible. Even in the most favourable case studied, the Cu/Au system, the diffusion distance for copper in gold at 500K should be less than 1$\mathring{A}$ in 3 minutes. This rate of diffusion is in fact fairly close to that observed for copper in gold under the electron beam which may indicate quite severe specimen heating. It should however be noted that the thermocouple mounted at the edge of the specimen did not register temperature rises more than a few degrees, and that the copper diffusion was well localised in the area under the electron beam indicating a very localised heating effect.

Specimen heating due to the electron beam does not however explain the diffusion in the other systems since their surface compositions remained constant while being irradiated. It therefore appears that any diffusion must occur during the deposition process.

Evidence for this type of effect, based on reflection electron diffraction, has also been discussed by Pashley (1965). For the case of copper deposited onto gold he concluded that a surface alloy of ~50 - 50 composition was first of all formed, and then further deposition led to the formation of copper nuclei. This effect was explained by saying that the kinetic energy of the copper atoms arriving at the surface was sufficient to allow the copper to diffuse into the gold. Similar effects were also observed for platinum deposited onto silver (Pashley (1965)) and for copper deposited onto silver (Newman and Pashley (1955)). It is interesting to note that in these systems the solubilities of, either platinum or copper, in silver are very low at room temperature and Pashley (1965) concludes that highly supersaturated alloys form in the surface layers because condensate atoms can penetrate the surface layers due to their kinetic energy and then become "frozen in" as they lose energy. Palmberg and Rhodin (1968) have shown, on the basis of LEED studies, that surface alloys are formed during the deposition of gold onto copper. By performing the evaporation at - 50°C they were able to show that the alloy would form at about room temperature showing that it is not necessary, in this system, to have "hot"incident atoms before alloy formation occurs. Their attempts to form a Cu - Au alloy by evaporating copper onto gold failed although they do note that the copper stabilises the Au (100) (1x1) structure.

Jesser and Matthews (1967) have studied the growth of iron deposited onto copper in the T.E.M. (Transmission Electron Microscope). The conclude that pseudomorphic growth occurs for the first 20Å or so of iron deposited, because no change was observed in either the diffraction patterns or the micrographs. They discount diffusion of the iron into the copper as an explanation, because of the low solubility of iron in copper and the low diffusion

coefficient at room temperature. The results presented here suggest that iron does diffuse into copper and Pashley (1965) has shown that the solid solubilities and bulk diffusion coefficients do not give a good indication of whether diffusion will occur or not. It therefore seems that the results of Jesser and Matthews (1967) could also be interpreted to indicate diffusion at the copper/iron interface.

According to the evidence presented here, tin either diffuses into the iron or forms islands at low coverage. This disagrees with the conclusion of Seah (1973), where he considers that the presence of tin plasmon loss peaks in the iron Auger spectrum indicates that the iron Auger electrons have travelled through a uniform tin layer. Since his observations were made in the presence of 10·5 monolayers of tin it does seem possible that, even on the basis of the diffusion model discussed earlier, the high concentration of tin in the surface region could modify the plasmon loss structure association with the iron Auger electrons leading to the above conclusions.

Chapter 8

Summary and Conclusions

This thesis has described the design and application of a novel instrument to the study of angle resolved Auger spectroscopy from various crystalline and non crystalline surfaces. The angular distributions from non-crystalline surfaces can be interpreted on the basis of quite simple theoretical models to give information about the depth concentrations of the emitting atoms and also about the thickness and continuity of thin surface films. This type of information can be very difficult to obtain by other methods and a knowledge of the depth distributions of the emitting atoms is a prerequisite for quantitative Auger analysis.

Despite the large amount of theoretical effort that has been directed towards understanding the angular distributions of low energy Auger electrons emitted from single crystal surfaces many unsolved problems, involving primarily the initial state of the Auger electron, still prevent the technique being used for surface structure determination. Results presented in chapter 4 suggest that it is necessary to specify not only the value of l describing the Auger wavefunction but also the value of m_l. This unfortunately would complicate the theory still further, making the short term prospects of obtaining surface structures, using this method, rather poor.

In marked contrast to this, the results of chapter 5 show that the high energy Auger angular distributions from single crystal surfaces are totally insensitive to the initial state of the Auger electron. This combined with the fact that the dynamical theory of electron diffraction can already give a qualitative understanding of the emission angular distributions, seems to indicate that much better prospects exist of obtaining surface structural information from the high energy Auger angular distributions.

Appendix A

This section describes in detail the various pieces of electronics that were built within the laboratory.

A.1 Helmholtz Coil Supply and Chart Recorder Control

A.2 The C.H.A. Control Box

A.3 The C.H.A. Head Box

A.4 The LEED Gun Control

A.5 The Auger Gun Control

A.6 The R.P.A. Head Box

A.7 The Programmer

A.8 The Modulator Box

A.9 Phase Shift and Attenuation Network

A.10 AC to DC Convertor

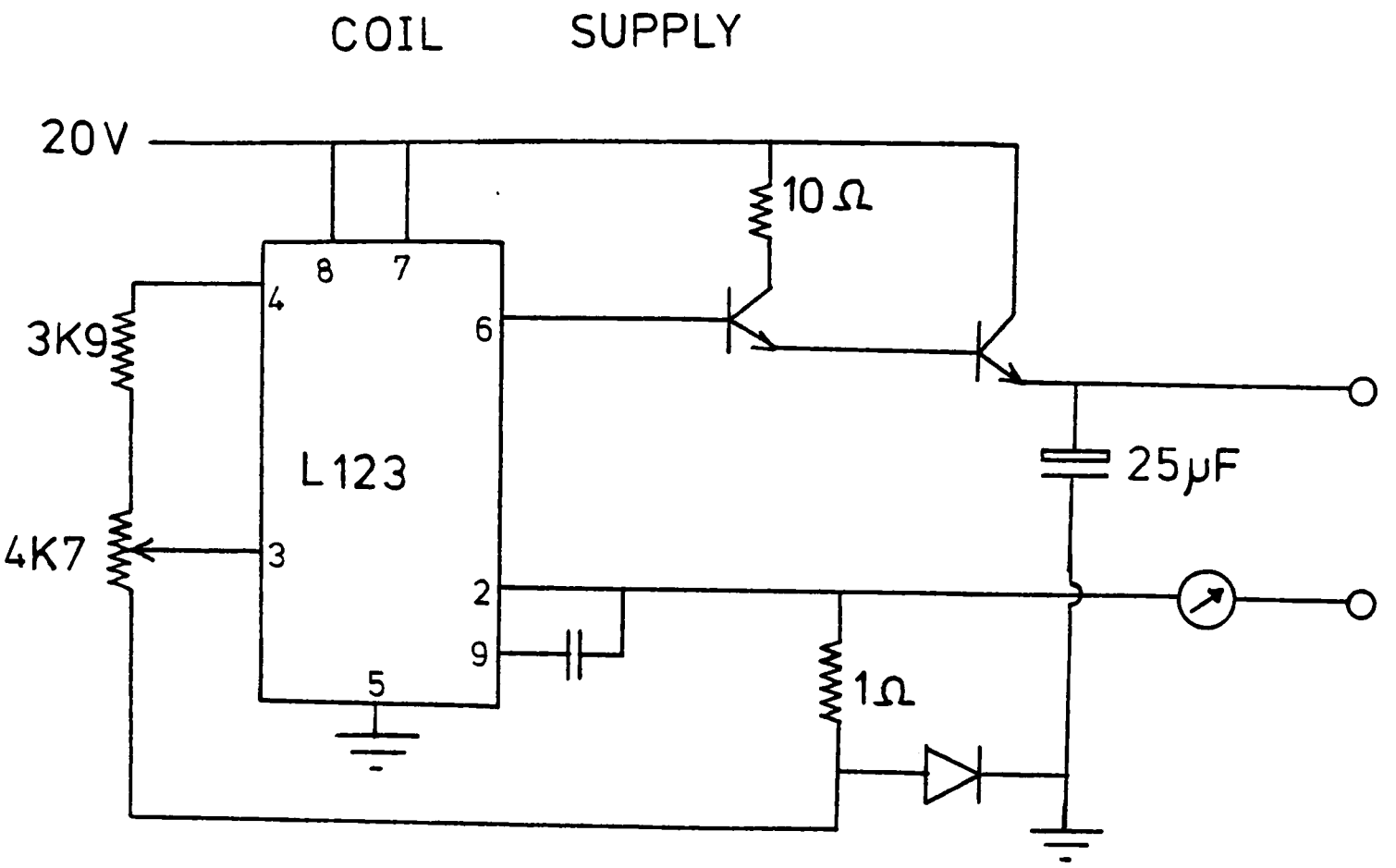
A.11 The Analyser Box

A.12 Output Filter

Figure A.1 Helmholtz Coil Supply and Chart Recorder Control

There are three identical coil supplies, housed in the same unit, to control each of the three orthogonal pairs of Helmholtz coils. The 20V lines come from a discarded, computer style, high current power supply.

The chart recorder control is used to automatically plot signals as a function of emission angle by attaching the 10K W/W potentiometer to the rotary feedthrough controlling the goniometer.



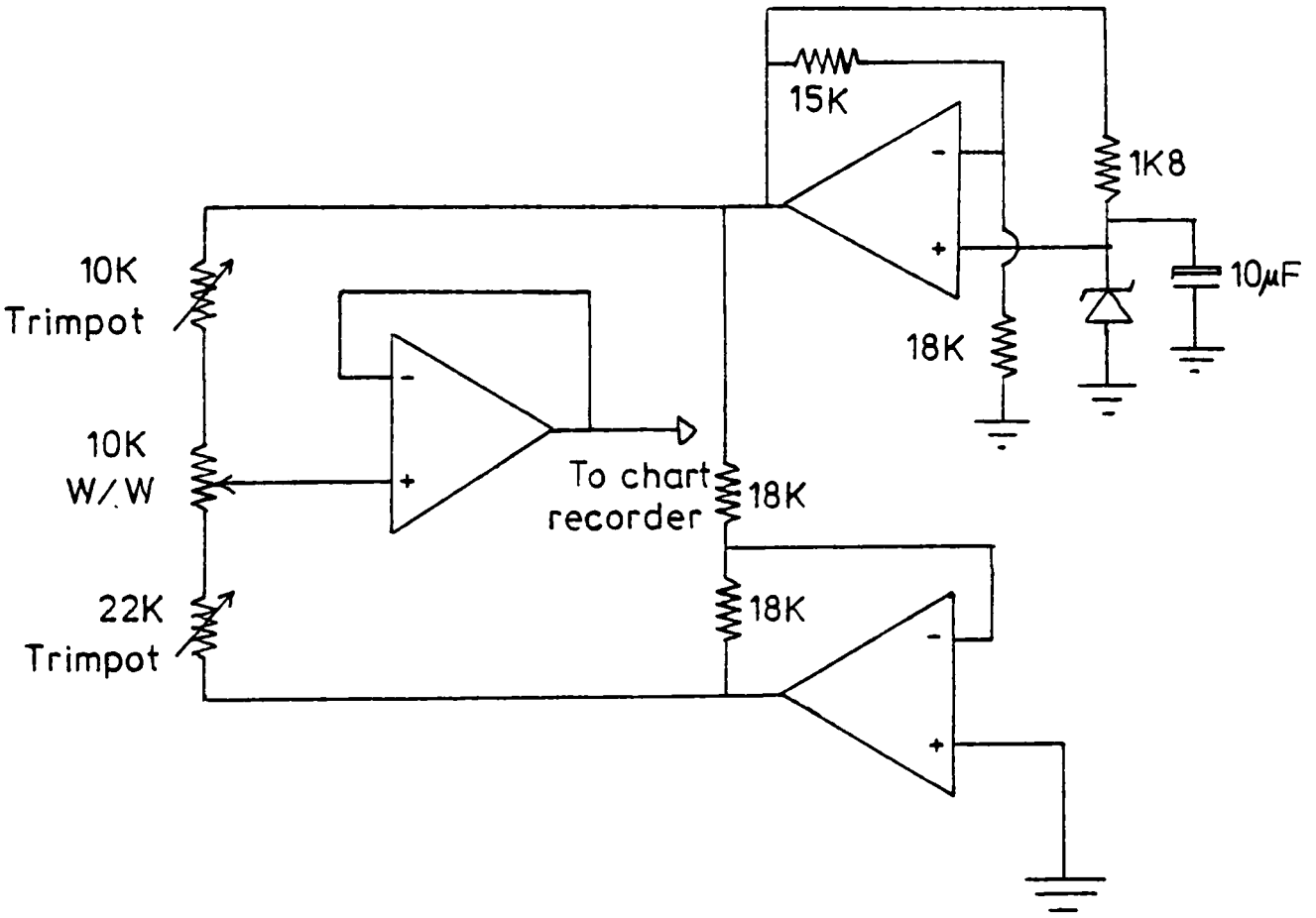


CHART RECORDER CONTROL

Figure A.2 The C.H.A. Control Box

This shows the resistor chains used to obtain the potentials for the C.H.A. The KEPCO BHK 2000 supply provides the voltage input labelled (1) and the HEWLETT-PACKARD 6516 supply provides the electron multiplier accelerating voltage at the inputs labelled (2) and (3)

CHA CONTROL BOX

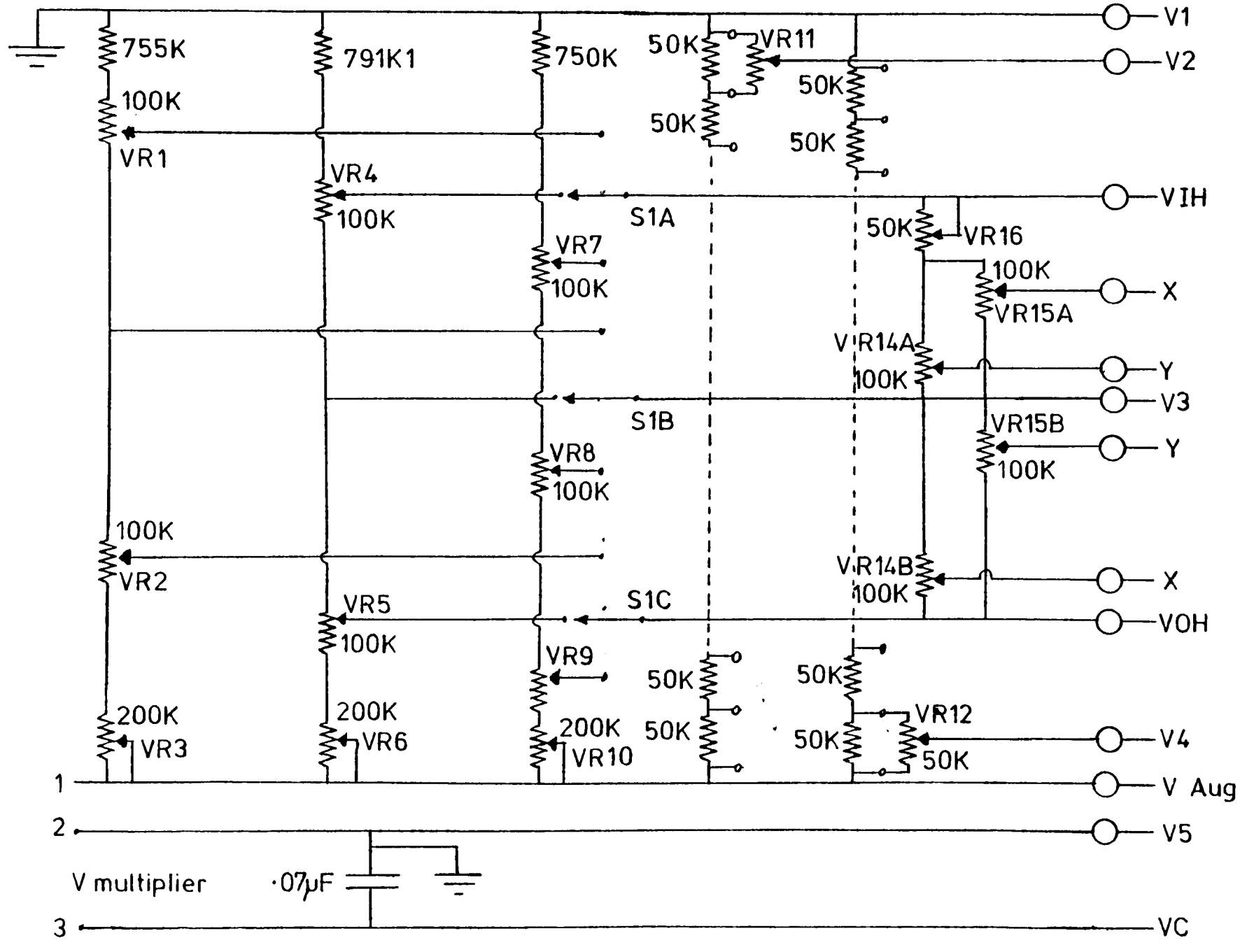


Figure A.3 The C.H.A. Head Box

The FET MOPA is configured as a current to voltage convertor, with a conversion ratio of 10^6, to amplify the electron multiplier output current collected at V_c. The voltage V_6 applied to the first dynode of the electron multiplier can be adjusted from 0V to + 200V when using the C.H.A. at low pass energies. The output from the current to voltage converter, which is floating at 2·5KV, is fed into the ANALOG 272J isolation amplifier to obtain a suitable signal referenced to ground.

CHA HEAD BOX

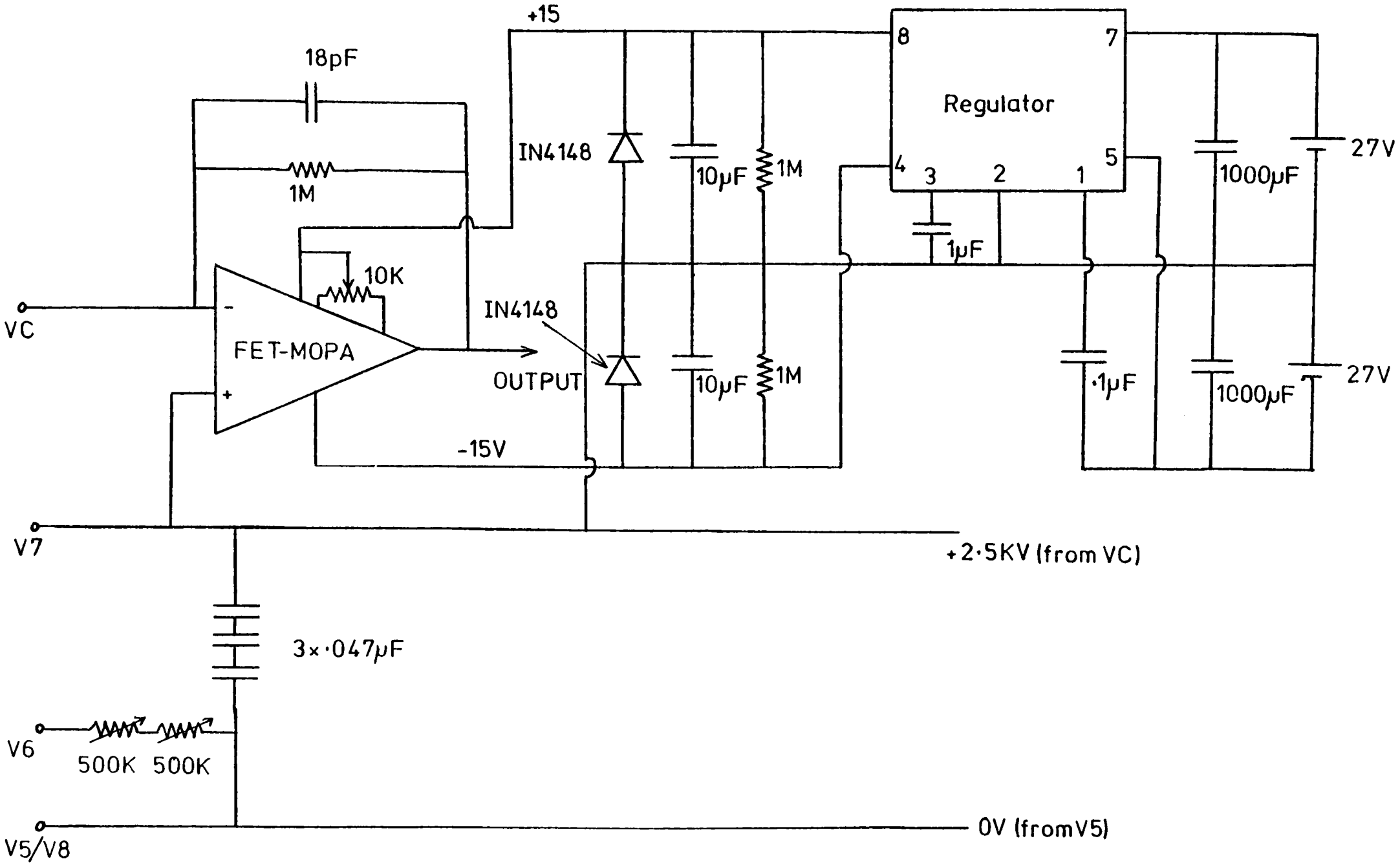

+15
18pF
1M
IN4148
10µF
1M
Regulator
8
7
4
3
2
1
5
1µF
1000µF
27V
10K
VC
FET-MOPA
IN4148
OUTPUT
10µF
1M
·1µF
1000µF
27V
-15V
V7
+2·5KV (from VC)
3×·047µF
V6
500K
500K
V5/V8
0V (fromV5)

Figure A.4 The LEED Gun Control

The accelerating voltage applied to point (1) is supplied by the J & P NM 120 supply and the FLUKE 412B AF supply is connected to point (2) to provide the lens potentials. The filament supple, the KSM KTI 10/10A, is connected to pins A and D. The other connections are as follows :-

BA15

A - To + on KSM

B - To filament + on gun

C - To filament - on gun

D - To - on KSM

F - Filament shield

J - To A4

L - To E1

M - To A1

P - To A2

S - To A3

PAINTON

1 - Local Program out

4 - -12V D.C.

5 - +12V D.C.

6 - Ground

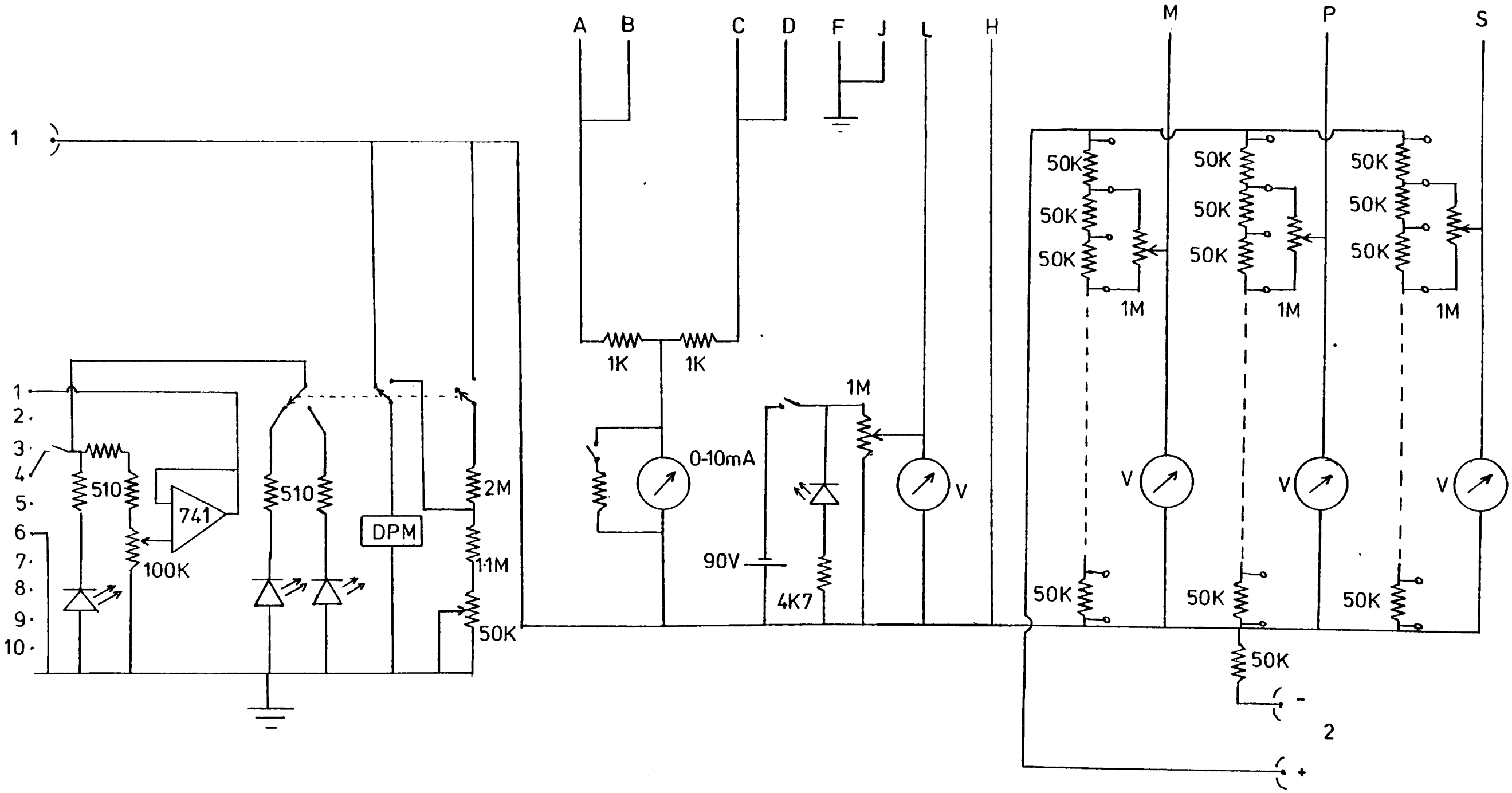

A
B
C
D
F
J
L
H
M
P
S
1
1K
1K
0-10mA
1M
90V
4K7
V
50K
50K
50K
1M
50K
50K
50K
1M
50K
50K
50K
1M
50K
50K
50K
50K
1
2
3
4
5
6
7
8
9
10
510
741
100K
510
DPM
2M
1·1M
50K
-
2
+

Figure A.5 The Auger Gun Control

The accelerating potential applied to pin (3) is derived from the FLUKE 423A sepply. The focussing potential, derived from the FLUKE 412B AF supply is applied between E-BNC pins (1) and (2). The filament supply the KSM KTI 10/10A, is connected to pins A & D. The other connections are as follows :-

BA 15	PAINTON
A - To + on KSM	1 - Local program out
B - To filament - on gun	4 - -12V D.C.
C - To filament + on gun	5 - -12V D.C.
D - To - on KSM	6 - Ground
BNC - To DVM box	7 - X1 to gun
F - To Wehnelt	8 - X2 to gun
H - To A2 on gun	9 - Y1 to gun
	10 - Y2 to gun

The DVM box is not shown since the circuit used is the same as in the LEED gun control.

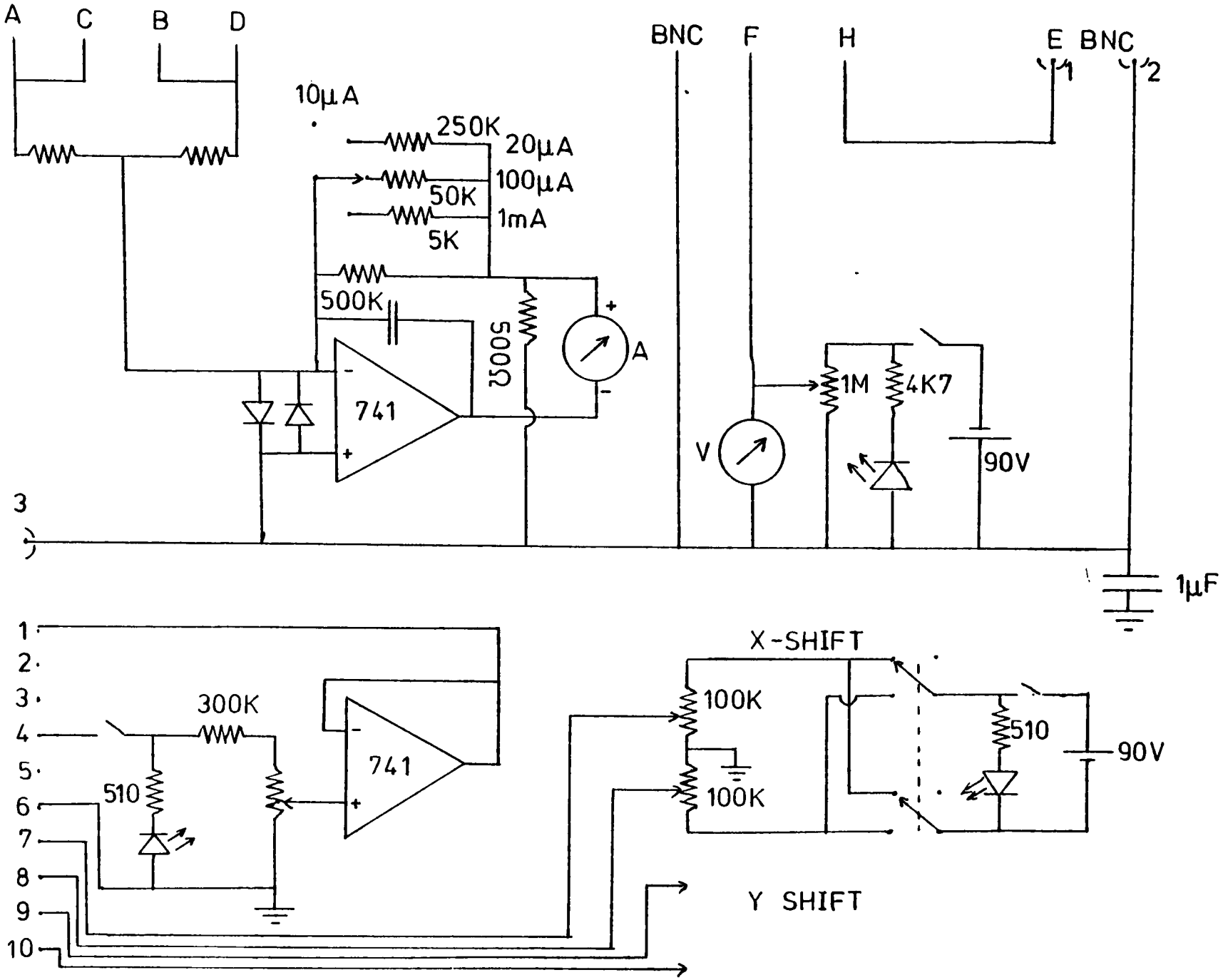

A
C
B
D
10µA
250K
20µA
100µA
50K
1mA
5K
500K
500Ω
741
A
BNC
F
H
E
BNC
1
2
1M
4K7
V
90V
3
1µF
1
2
3
4
5
6
7
8
9
10
300K
510
741
X-SHIFT
100K
100K
510
90V
Y SHIFT

Figure A.6 The R.P.A. Head Box

This circuit is only connected when the LEED/R.P.A. unit is operated in the Analysing mode. (see figure 2.5). The "signal in" comes from the collector. The first stage is a tuned transimpedance amplifier, the second stage a 50Hz notch filter, the third stage a tuned amplifier and the fourth is a unity gain subtractor. The capacitively induced signal is nulled out by applying a signal of suitable phase and amplitude to the "compensation in" terminal on the subtractor. It should be noted that this unit must be switched on before the 180V bias is applied to the collector, otherwise the voltage spike will destroy the AD 40 K amplifier.

TUNED AMPLIFIER AND SUBTRACTOR

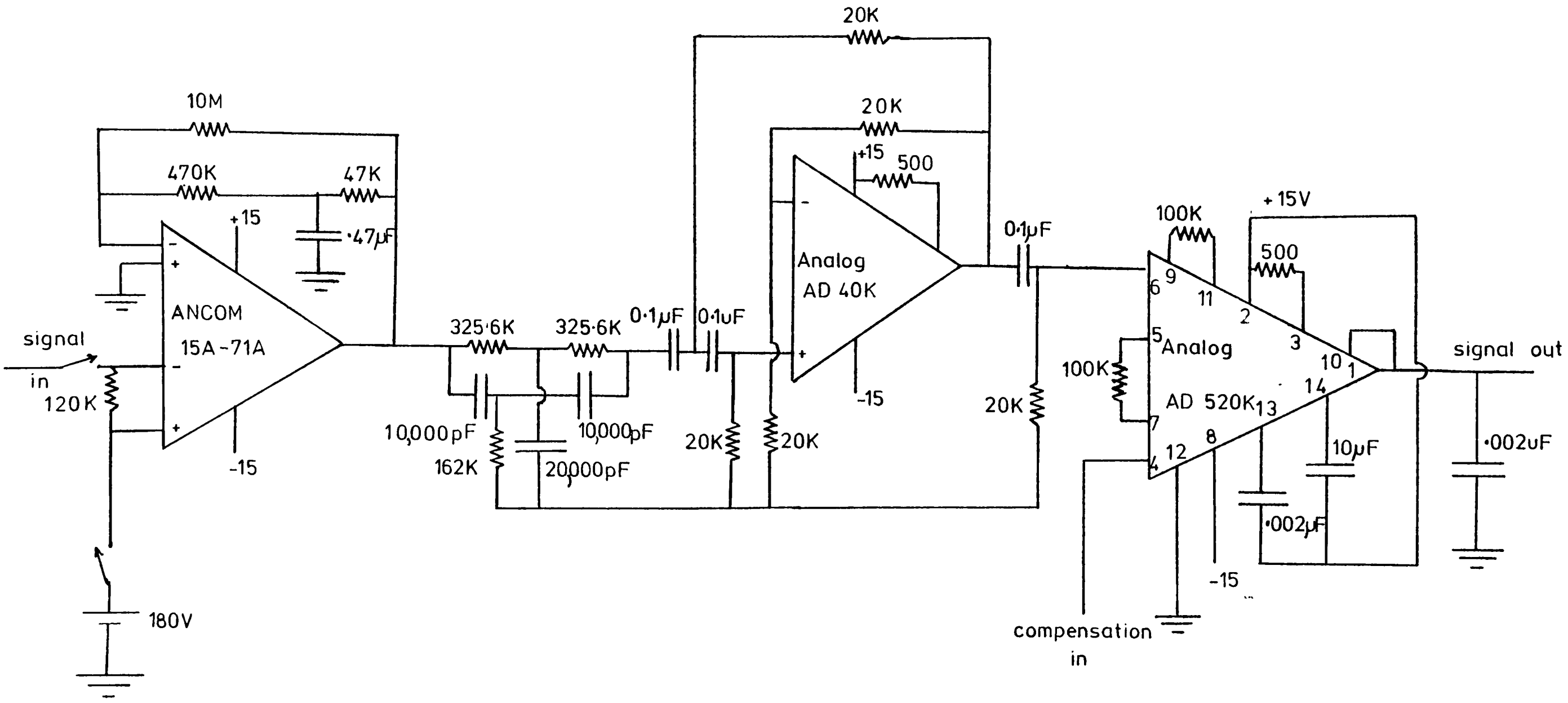
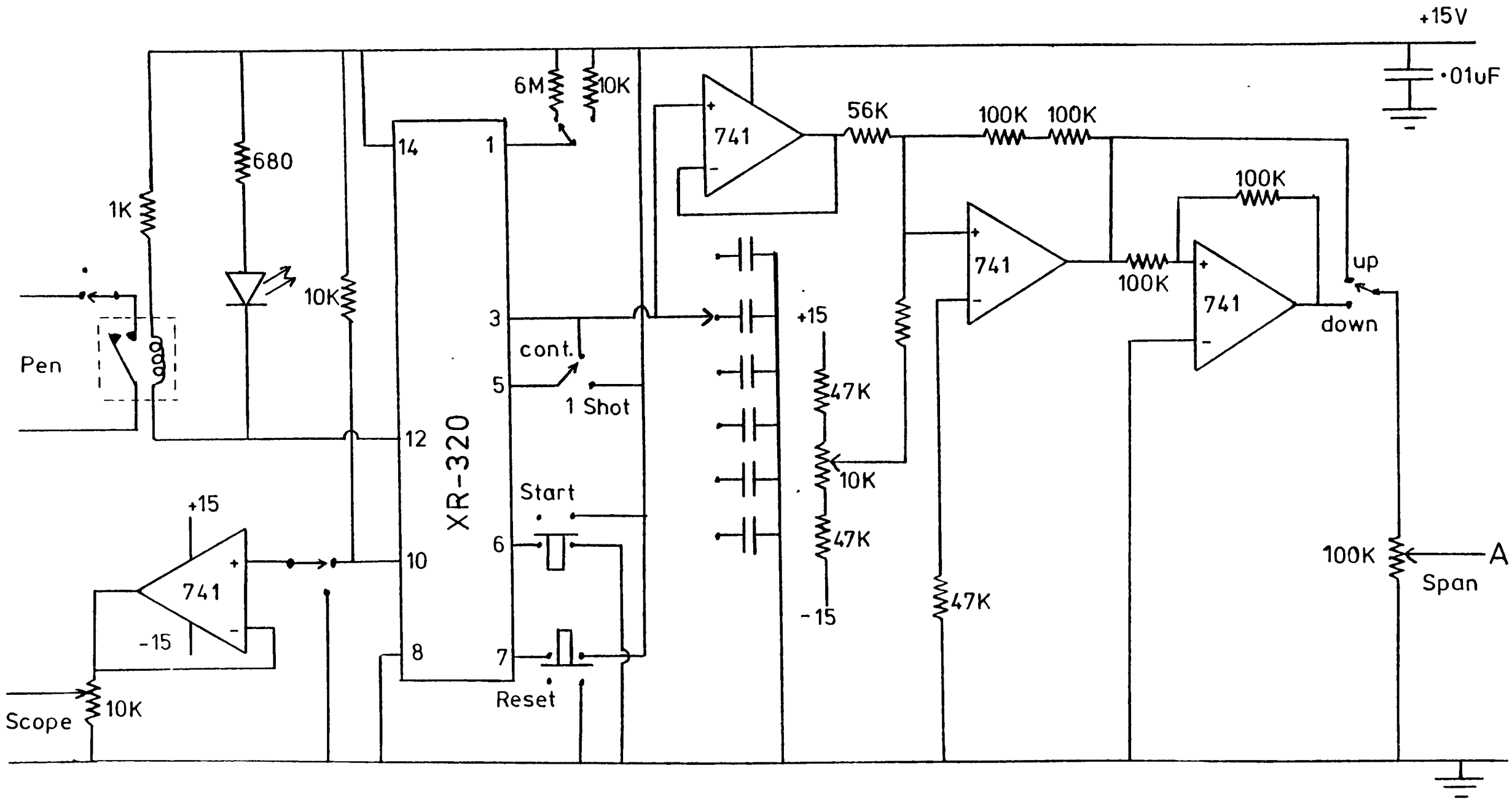


Figure A7 (A & B) The Programmer

This unit provides ramp voltages in the "1 shot" mode or saw-tooth waveforms in the "continuous" mode. The unit is normallly used to scan the analysing energy of the R.P.A. or C.H.A. by controlling the appropriate programmable power supply (the J & P NM 231 or KEPCO BHK 2000). It can also be used to programme the energies of the Auger or LEED guns by controlling the FLUKE 423A or J & P NM 120 supplies.

PROGRAMMER (A)



PROGRAMMER (B)

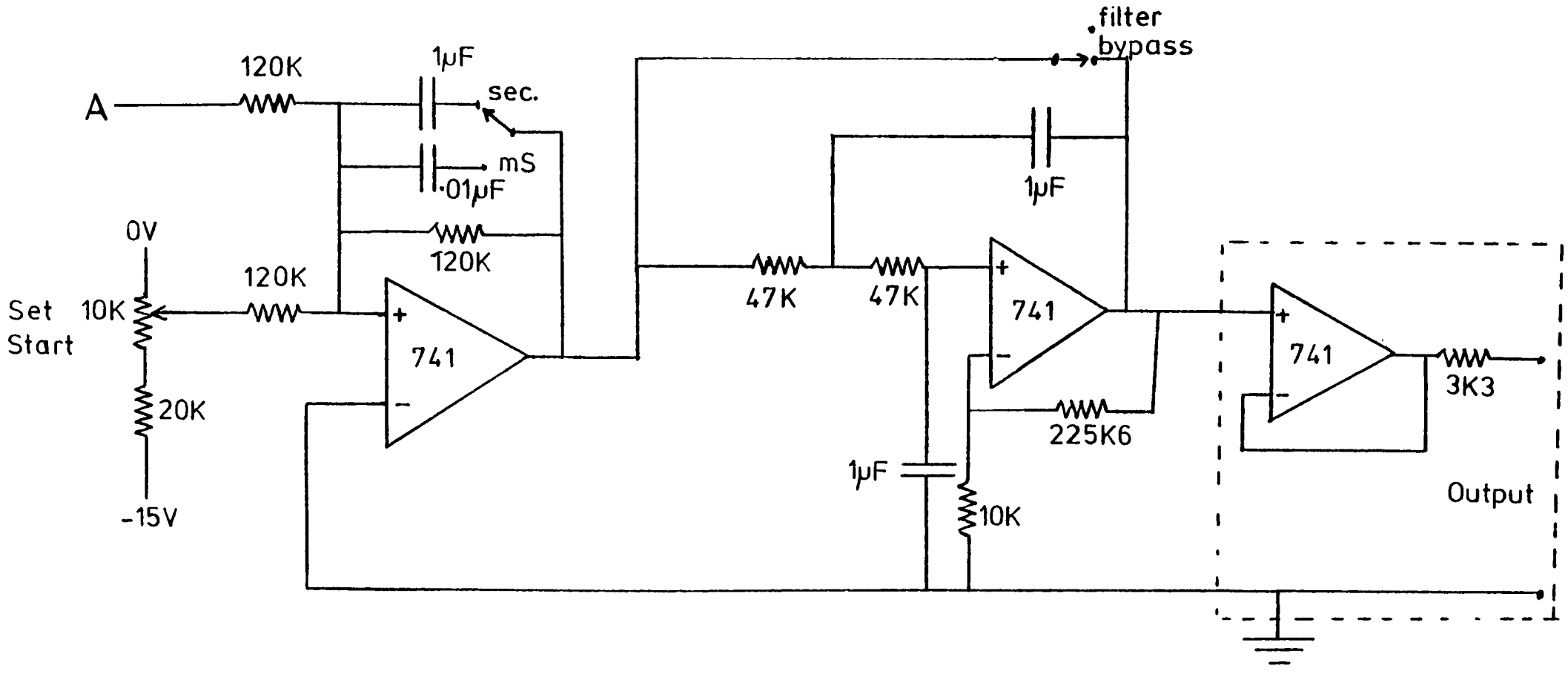


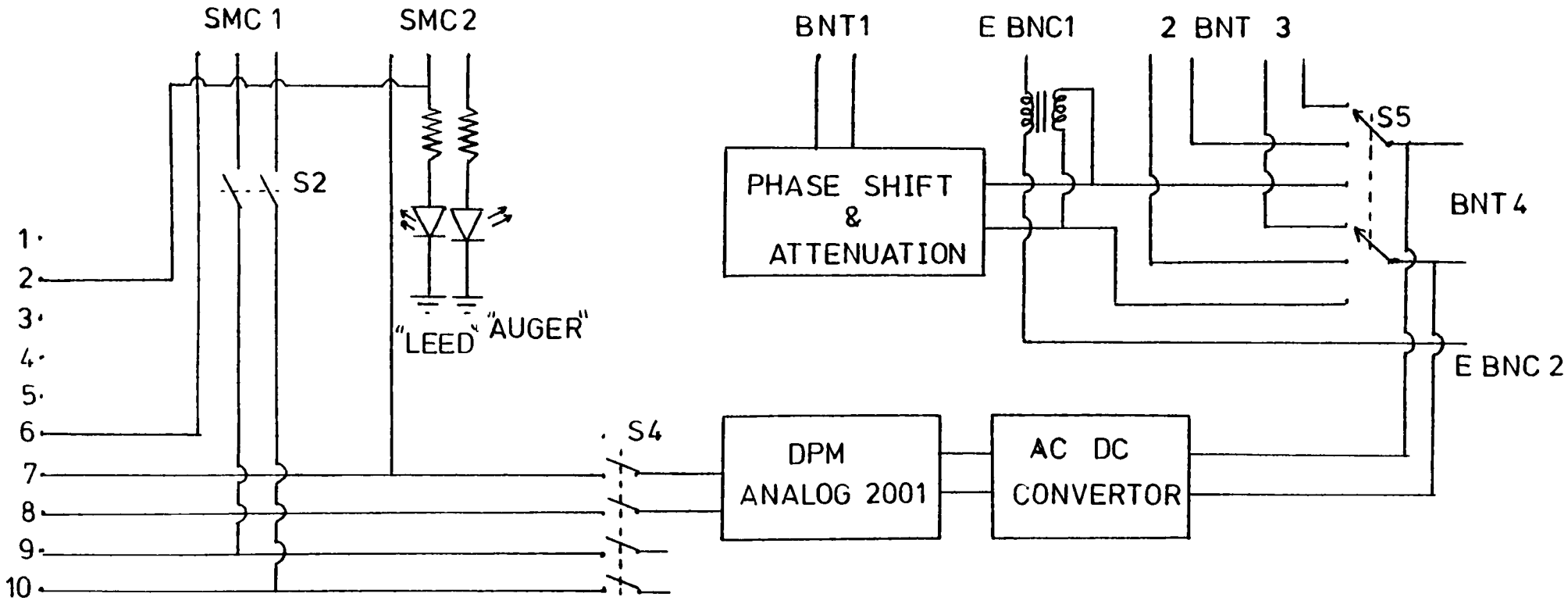
Figure A.8 The Modulator Box

This unit provides facilities for superimposing the modulation voltage, onto the analysing ramp for the R.P.A. or onto the specimen for use with the C.H.A. It also provides the compensation signal for the R.P.A. Head Unit. The connections are as follows:-

PAINTON

2 - LEED tell-tale out	SMC-1 - Power to R.P.A. Head Box
4 - -12V D.C.	SCM-2 - To LEED/Auger switch on Head Box
5 - +12V D.C.	E BNC-2 - Ramp in
6 - Ground	E-BNC-1 - Modulated Ramp Out
7 - +5V D.C.	BNT-1 - Compensation Out
8 - -5V D.C.	BNT-2 - Modulation to Target
9 - +15V D.C.	BNT-3 - Modulation Auxiliary
10 - -15V D.C.	BNT-4 - Modulation in

Figures A.9, A.10 show the Phase Shift and Attenuation Network, and the A.C. to D.C. Convertor respectively.


SMC 1
SMC 2
S2
1
2
3
4
5
6
7
8
9
10
"LEED"
"AUGER"
S4
BNT1
E BNC1
2 BNT 3
S5
BNT 4
PHASE SHIFT
&
ATTENUATION
E BNC 2
DPM
ANALOG 2001
AC DC
CONVERTOR

PHASE SHIFT AND ATTENUATION NETWORK

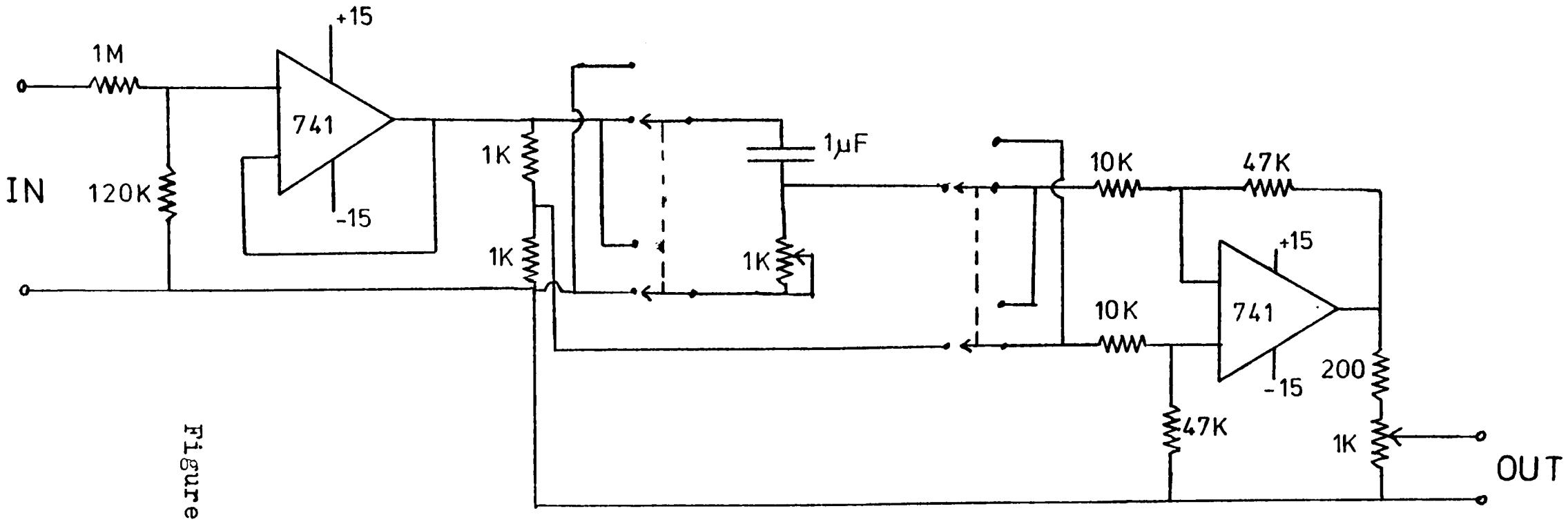


Figure A.9

AC-DC CONVERTOR

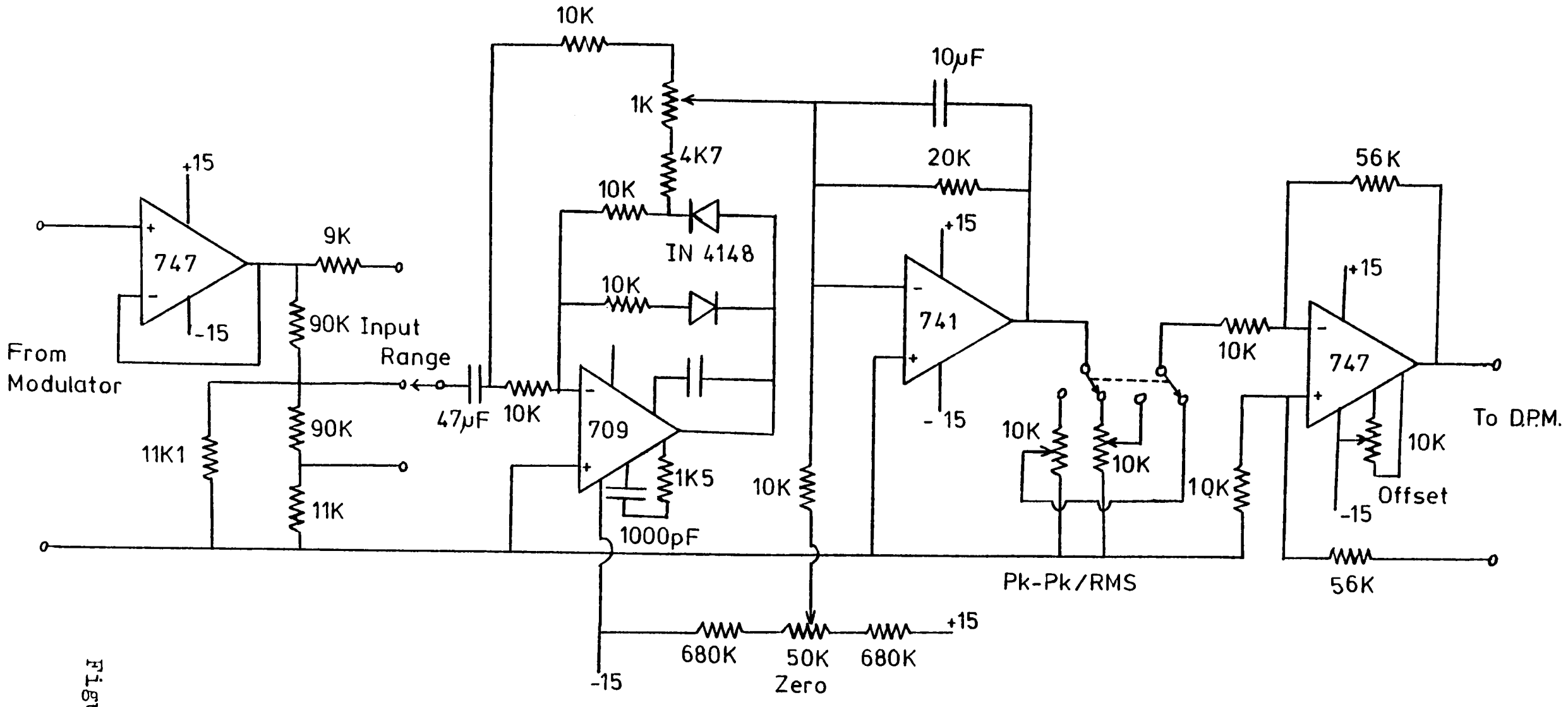


Figure A.10

Figure A.11 The Analyser Box

This unit measures the analysing energy of the R.P.A. or C.H.A. and provides the supressor potential to grids G3/3A when running in the LEED mode.

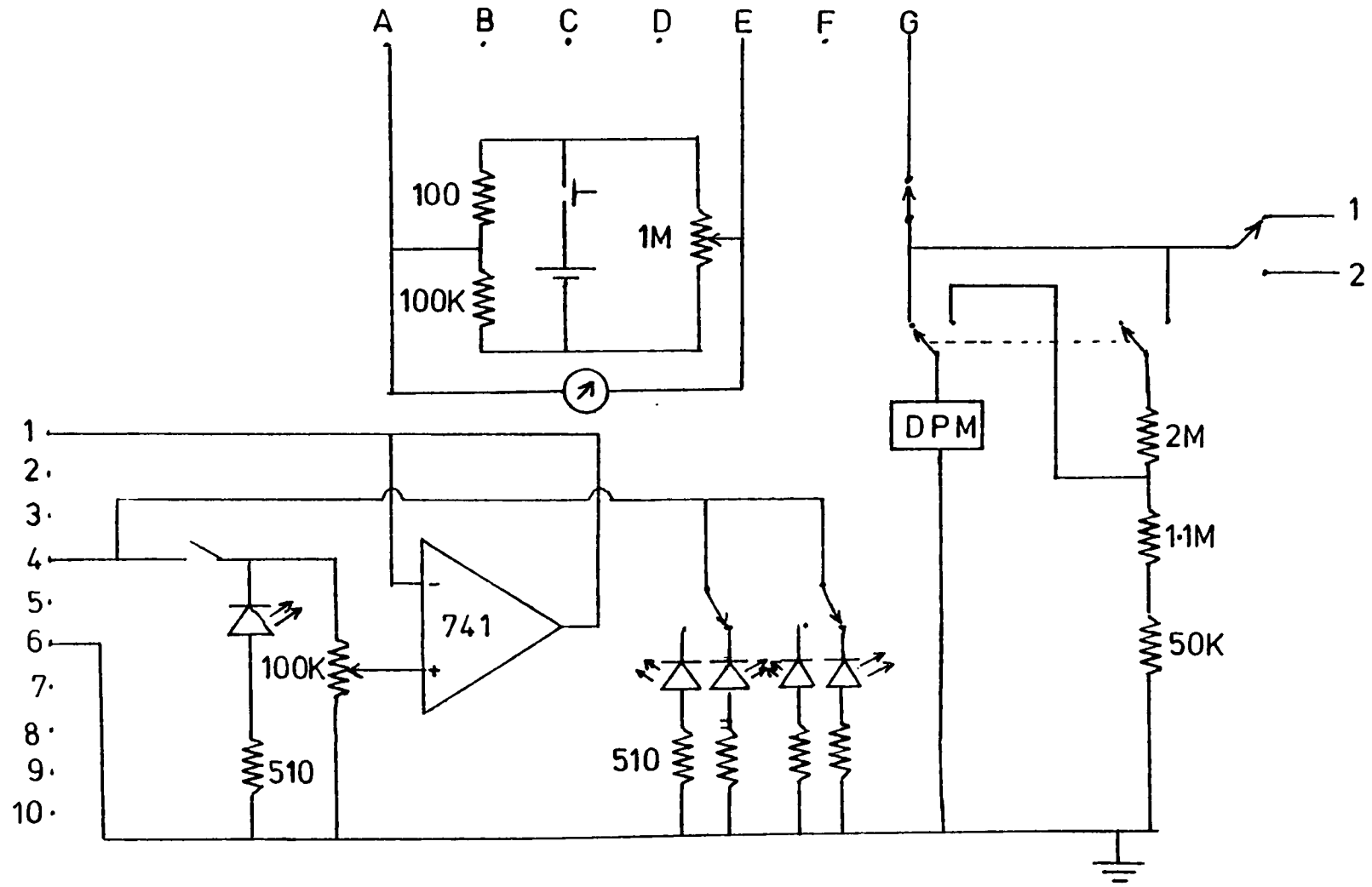
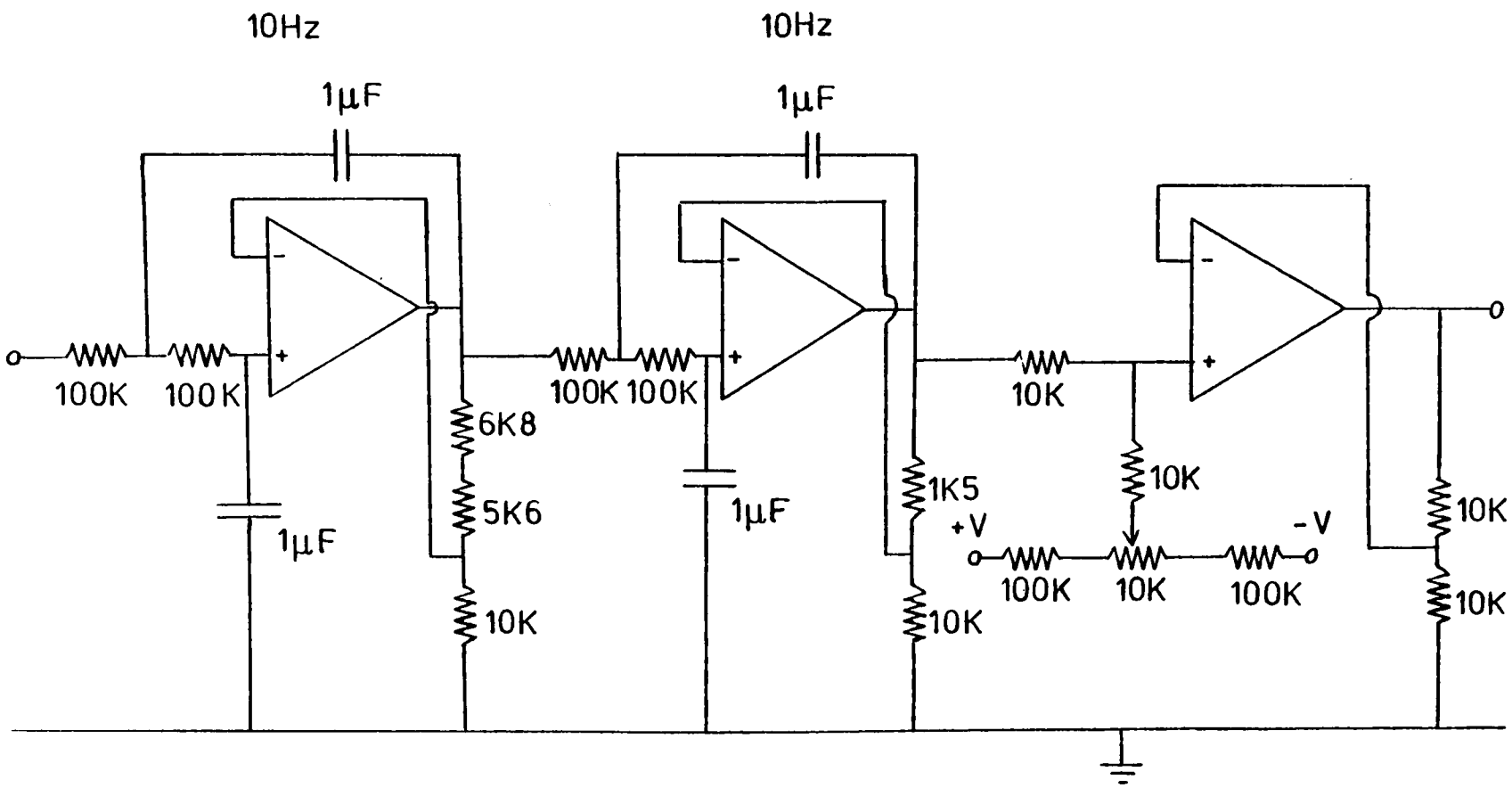

A
B
C
D
E
F
G
100
100K
1M
1
2
DPM
2M
1·1M
50K
741
100K
510
510
1
2
3
4
5
6
7
8
9
10

Figure A.12 Output Filter

This is a second order low pass filter with $_{o} = 10H_{z}$ used when the lock in amplifier is not being used.


10Hz
1μF
10Hz
1μF
100K
100K
6K8
5K6
10K
1μF
100K
100K
1μF
1K5
10K
+V
100K
10K
-V
100K
10K
10K
10K

References.

1) Arnott, D.R. and Haneman, D. (1974)
Surface Sci., 45, 128

2) Asaad, W.N. (1963)
Nucl. Phys., 44, 415

3) Auger, P. (1925)
Compt, Rend., 180, 65

4) Auger, P. (1926)
Ann. Phys. (Paris), 6, 183

5) Aberdam, D., Baudoing, R., Blanc, E., and Gaubert, C. (1976)
Surface Sci., 57, 306

6) Aberdam, D., Baudoing, R., Blanc, E., and Gaubert, C. (1978)
Surface Sci., 71, 279

7) Allié, G., Blanc, E. and Dufayard, D. (1976)
Surface Sci., 57, 293

8) Allié, G., Blanc, E., Dufayard, D. and Stern, R.M. (1974)
Surface Sci., 46, 188

9) Amelio, G.F. (1970)
Surface Sci., 22, 301

10) Andersen, S.K., and Howie, A. (1975)
Surface Sci., 50, 197

11) Andrews, P.T., and Weightman, P. (1979)
J. Electron Spectrosc., 15, 133

12) Antonides, E., Janse, E.C., and Sawatzky, G.A. (1977)
Phys. Rev. B, 15, 4596

13) Baines, M., Howie, A. and Andersen, S.K. (1975)
Surface Sci., 53, 546

14) Bassett, P.J., Gallon, T.E. and Prutton, M. (1972)
J. Phys. E., 5, 1008

15) Bassett, P.J. (1974)
J. Phys. E., 7, 461

16) Bauer, E. and Poppa, H. (1972)
Thin Solid Films, 12, 167

17) Bean, J.C., Becker, G.E., Petroff, P.M. and Seidel, T.E. (1977)
J. Appl. Phys., 48 (3), 907

18) Best, P.E. (1976)
Phys. Rev. B, 14 (2), 606

19) Bishop, H.E. and Rivière, J.C. (1969(a))
Surface Sci., 17, 446

20) Bishop, H.E. and Rivière, J.C. (1969(b))
J. Appl. Phys., 40, 1740

21) Browning, R., Bassett, P.J., El. Gomati, M.M. and Prutton, M. (1977)
Proc. R. Soc. Lond., A357, 213

22) Chang, C.C. (1970)
Surface Sci., 23, 283

23) Chang, C.C. (1977)
Applied Physics Letters, 31, 304

24) Chattarji, D. (1976)
The Theory of Auger Transitions, Academic Press, London

25) Chopra, K.L. (1969)
Thin Film Phenomena, McGraw Hill, New York.

26) Chung, M.F. and Jenkins, L.H. (1970)
Surface Sci., 22, 479

27) Clapham, P.B., Downs, M.J. and Raine, K.W. (1969)
Thin Solid Films, 4, R39

28) Cleff, B. and Mehlhorn, W. (1974(a))
J. Phys. B, 7, 593

29) Cleff, B. and Mehlhorn, W. (1974(b))
J. Phys. B, 7, 605

30) Davis, H.L. and Kaplan, T. (1976)
Solid State Comman, 19, 595

31) Domeij, B. (1965)
Nucl. Instr. Methods, 38, 207

32) Ellis, W.P. (1974)
Surface Sci., 41, 125

33) Fathers, D.J. and Rez, P. (1979)
Scanning Electron Microscopy Symposium, SEM Inc., Washington.

34) Feibelman, P.J., McGuire, E.J. and Pandey, K.C. (1976)
Phys. Rev. Letters, 36, 1154

35) Feibelman, P.J. and McGuire, E.J. (1977)
Phys. Rev. B, 15, 3575

36) Feibelman, P.J. and McGuire, E.J. (1978)
Phys. Rev. B, 17, 690

37) Ferrel, R.A. (1956)
Phys. Rev., 101, 554

38) Fiermans, L. and Vennik, J.J. (1977)
Advances in Electronics and Electron Physics 43, 139

39) Frank, F.C. and van der Merwe, J.H. (1949)
Proc. Roy. Soc., London, 189A, 216

40) Gerlach, R.L., Houston, J.E. and Park, R.L. (1970)
Appl. Phys. Letters, 16, 179

41) Gryzinski, M. (1959)
Phys. Rev., 115, 374

42) Gryzinski, M. (1965)
Phys. Rev., 138A, 305

43) Haas, J.W., Grant, J.T. and Dooley, E.J. (1972)
J. Appl. Phys., 43, 1853

44) Harris, L.A. (1968)
J. Appl. Phys., 39, 1419

45) Harris, L.A. (1969)
Surface Sci., 15, 77

46) Harting, E. and Read, F.H. (1976)
Electrostatic Lenses, Elsevier, Amsterdam

47) Henderson, R.C., Marcus, R.B. and Polito, W.J. (1971)
J. Appl. Phys., 42, 1208

48) Hirsch, P.B., Howie, A., Nicholson, R.B., Pashley, D.W., and Whelan, M.J. (1965)
Electron Microscopy of Thin Crystals, Butterworths, London

49) Hirsch, P.B., Howie, A. and Whelan, M.J. (1962)
Phil. Mag., 7, 2095

50) Holland, B.W. (1975)
J. Phys. C, 8, 2679

51) Hörnfeldt, O., Fahlman A. and Nordling, C. (1962)
Ark. Fys., 23, 155

52) Houston, J.E., Moore, G. and Lagally, M.G. (1977)
Solid State Commun., 21, 879

53) Howie, A. (1966)
Phil. Mag., 14, 223

54) Jablonski, A. (1979)
ECOSS 2 Cambridge 1979

55) Jenkins, L.H. and Chung, M.F. (1971)
Surface Sci., 24, 125

56) Jennison, D.R. (1978)
Phys. Rev. Letters, 40, 807

57) Jesser, W.A. and Matthews, J.W. (1967)
Phil. Mag., 15, 1097

58) Kowalczyk, S.P., Pollak, R.A., McFeely, F.R., Ley, L. and Shirley, D.A. (1973)
Phys. Rev. B, 8, 2387

59) Kuyatt, C.E. and Simpson, J.A. (1967)
Rev. Sci. Instrum., 38, 103

60) Lander, J.J. (1953)
Phys. Rev., 91, 1382

61) von Laue, M. (1935)
Ann. Phys. Lpz., 23, 705

62) Lindsay, R.N., Kinniburgh, C.G. and Pendry, J.B. (1979)
J. Elec. Spec., 15, 157

63) Lindsay, R.N. and Pendry, J.B. (1978)
J. Phys. C, 11, 1031

64) McDonnel, L., Woodruff, D.P. and Holland, B.W. (1975)
Surface Sci., 51, 249

65) McGuire, E.J. (1971)
Research Report SC-RR-710075, Sandia Laboratories

66) McGuire, E.J. (1977)
Phys. Rev. A, 16, 2365

67) Madden, H.H., Zehner, D.M. and Noonan J.R. (1978)
Phys. Rev. B, 17, 3074

68) Mark, P., Levine, J.D. and McFarlane, S.H . (1977)
Phys. Rev. Letters, 38, 1408

69) Matsudaira, T., Nishijima, M. and Onchi, M. (1976)
Surface Sci, 61, 651

70) Matsudaira, T. and Onchi, M. (1978(a))
Surface Sci., 72, 53

71) Matsudaira, T. and Onchi, M. (1978(b))
Surface Sci., 74, 684

72) Matsudaira, T., Watanabe, M. and Onchi, M. (1974)
Japan. J. Appl. Phys. Suppl. 2 pt. 2, 181

73) Meyer, F. and Vrakking, J.J. (1972)
Surface Sci., 33, 271

74) Moss, H. (1968)
Advances in Electronics and Electron Physics Suppl 3,
Academic Press, New York.

75) Mosser, A., Burgraff, Ch., Goldsztaub, S. and Ohtsuki, Y.H. (1976)
Surface Sci., 54, 580

76) Mosser, A., Shindo, S. and Adachi, Y . (1977)
Phys. Stat. Sol, (a), 43, 295

77) Neave, J.H., Foxon, C.T. and Joyce, B.A. (1972)
Surface Sci., 29, 411

78) Noonan, J.R., Zehner, D.M., and Jenkins, L.H. (1976)
J. Vac. Sci. Technol., 13, 183

79) Noonan. J.R., Zehner, D.M. and Jenkins, L.H. (1977)
Surface Sci., 69, 731

80) Oertel, E. and Weber, E.H. (1977)
Phys. Stat. Sol. (a), 43, 141

81) Palmberg, P.W. (1969)
Appl. Phys. Letters, 13, 183

82) Palmberg, P.W. and Rhodin, T.N. (1968(a))
J. Appl. Phys., 39, 2425

83) Palmberg, P.W. and Rhodin, T.N. (1968(b))
J. Chem. Phys., 49, 134

84) Palmberg, P.W., Bohn, E.K., and Tracy, J.C. (1969)
Appl. Phys. Letters, 15, 254

85) Palmberg, P.W., Riach, E.E., Weber, R.E. and MacDonald, N.C. (1972)
Handbook of Auger Electron Spectroscopy, Physical Electronics
Industries Inc., Edina, Minnesota.

86) Pashley, D.W. (1965)
Advances in Physics, 14, 327

87) Pendry, J.B. (1974)
Low Energy Electron Diffraction, Academic Press, London.

88) Pendry, J.B. (1975)
J. Phys. C, 8, 2413

89) Pendry, J.B. and Gard, P. (1975)
J. Phys. C, 8, 2048

90) Place, J.D. and Prutton, M. (1979)
Surface Sci., 82, 315

91) Powell, C.J. (1973)
Phys. Rev. Letters, 30, 1179

92) Purcell, E.M. (1938)
Phys. Rev., 54, 818

93) Raether, H. (1965)
Springer Tracts in Modern Physics 38, 84

94) Rusch, T.W., Bertino, J.P. and Ellis, W.P. (1973)
Appl. Phys. Letters, 23, 359

95) Rusch, T.W. and Ellis, W.P. (1975)
Appl. Phys. Letters, 26, 44

96) Rye, R.R., Madey, T.E., Houston, J.E. and Holloway, P.H. (1978)
J. Chem, Phys., 69, 1504

97) Sawatzky, G.A. (1977)
Phys. Rev. Letters, 39, 504

98) Seah, M.P. (1972)
Surface Sci., 32, 703

99) Seah, M.P. (1973)
J. Phys. F, 3, 1538

100) Seah, M.P. and Dench, W.A. (1978)
N.P.L. Report Chem. 82

101) Shih, H.D., Jona, F., Jepsen, D.W. and Marcus, P.M. (1976)
Phys. Rev. Letters, 37, 1622

102) Shimizu, R., Aratama, M., Ichimura, S., Yamazaki, Y. and Ikuta, T. (1977)
Appl. Phys. Letters, 31, 692

103) Siegbahn, K., Gelius, U., Siegbahn, H. and Olson, E. (1970)
Physica Scripta, 1, 272

104) Smith, D.K. and Gallon, T.E. (1974)
J. Phys. D., 7, 151

105) Stadler, K. (1972)
Vacuum, 22, 553

106) Stern, R.M. and Taub, H. (1968)
Phys. Rev. Letters, 20, 1340

107) Taub, H. and Stern, R.M. (1966)
Appl. Phys. Letters, 9, 261

108) Taub, H., Stern, R.M. and Dvoryankin, V.F. (1969)
Phys. Stat. Sol. (a), 33, 573

109) Taylor, N.J. (1969)
Rev. Sci. Instrum., 40, 792

110) Tharp, L.N. and Scheibner, E.J. (1967)
J. Appl. Phys., 38, 3320

111) Thomas, S. (1974)
J. Appl. Phys., 45, 161

112) Tolansky, S. (1960)
Surface Microtopography, Longmans, London

113) Tomlinson, P.M. and Howie, A. (1968)
Phys. Lett., 27A, 491

114) Uggerhoij, E. (1966)
Phys. Lett., 22, 382

115) Uggerhoij, E. and Andersen, J.U. (1968)
Can. J. Phys., 46, 543

116) Volmer M. and Weber, A. (1926)
Z. Physik. Chem., 119, 277

117) Voorhoeve,R.J.H. (1976)
in Treatise on Solid State Chemistry 6A ed. N.B. Hannay,
Plenum, New York.

118) Vrakking, J.J. and Meyer, F. (1973)
Surface Sci., 35, 34

119) DeWames, R.E. and Hall, W.F. (1968)
Acta. Cryst., 24A. 206

120) White, S.J., Woodruff, D.P. and McDonnel, L. (1978)
Surface Sci., 72, 77

121) Wolter, A.R. (1968)
J. Appl. Phys., 36, 2377

122) Woodruff, D.P. (1975)
Surface Sci., 53, 538

123) Worthington, C.R. and Tomlin , S.C. (1956)
Proc. Phys. Soc., A69, 401

124) Zehner, D.M., Noonan, J.R. and Jenkins, L.H. (1977)
Phys. Letters, 62A, 267

125) Zehner, D.M., Noonan, J.R. and Jenkins, L.H. (1976)
Solid State Commun., 18, 483